



Study of high damage threshold optical coatings used in environment with very low hygrometry for fusion class laser system

Marine Chorel

► To cite this version:

Marine Chorel. Study of high damage threshold optical coatings used in environment with very low hygrometry for fusion class laser system. Optics / Photonics. Université de Bordeaux, 2019. English. NNT : 2019BORD0188 . tel-02464789

HAL Id: tel-02464789

<https://theses.hal.science/tel-02464789>

Submitted on 3 Feb 2020

HAL is a multi-disciplinary open access archive for the deposit and dissemination of scientific research documents, whether they are published or not. The documents may come from teaching and research institutions in France or abroad, or from public or private research centers.

L'archive ouverte pluridisciplinaire **HAL**, est destinée au dépôt et à la diffusion de documents scientifiques de niveau recherche, publiés ou non, émanant des établissements d'enseignement et de recherche français ou étrangers, des laboratoires publics ou privés.

THÈSE PRÉSENTÉE
POUR OBTENIR LE GRADE DE

DOCTEUR DE
L'UNIVERSITÉ DE BORDEAUX

ÉCOLE DOCTORALE DES SCIENCES PHYSIQUES ET DE L'INGÉNIEUR
SPÉCIALITÉ LASER, MATIÈRE ET NANOSCIENCES

Par Marine CHOREL

**ÉTUDE DES TRAITEMENTS MULTICOUCHES UTILISÉS DANS
UN ENVIRONNEMENT A TRES FAIBLE HYGROMETRIE SUR
LES INSTALLATIONS LASER DE PUISSANCE**

Sous la direction de :

Bruno BOUSQUET, Professeur, Université de Bordeaux

Soutenue le 23 Octobre 2019

Membres du jury :

M. CANIONI, Lionel	Professeur, Université de Bordeaux	Président
M. MELNINKAITIS, Andrius	Associate Professor, Vilniaus Universitetas, Vilnius	Rapporteur
M. UTEZA, Olivier	Directeur de recherché, LP3, Marseille	Rapporteur
M. DEMOS, Stavros	Senior Scientist, LLE, Rochester	Examineur
M. GALLAIS-DURING, Laurent	Professeur, Institut Fresnel, Marseille	Examineur
M. PINARD, Laurent	Directeur du laboratoire des matériaux avancés, Lyon	Examineur
M. LAVASTRE, Éric	Ingénieur de recherche, CEA-Cesta, Le Barp	Examineur
Mme RIGATTI, Amy	Leader of the optical manufacturing at LLE, Rochester	Invitée
M. LANTERNIER, Thomas	Ingénieur de recherche, CEA-Cesta, Le Barp	Invité

Résumé de la thèse (français)

Cette thèse s'inscrit dans le cadre des installations lasers de puissance. Ces installations aux dimensions exceptionnelles permettent d'effectuer diverses expériences dans le domaine de la physique. Augmenter l'énergie et la puissance des lasers reste un enjeu permanent pour atteindre de nouvelles conditions d'interactions laser-matière. Les installations lasers de puissance peuvent être classées dans différentes familles suivant la durée des impulsions laser. Durant cette thèse, nous nous sommes intéressés aux installations du type de Petal (Petawatt Aquitaine Laser) qui opèrent dans le domaine Petawatt avec des durées d'impulsion laser de l'ordre de la picoseconde à la sub-picoseconde (centaines de femtosecondes).

Petal fonctionne sur le principe de l'amplification par dérive de fréquence démontrée par Donna Strickland et Gérard Mourou en 1985 [1]. Cette technique est nécessaire car l'amplification directe d'impulsions courtes (régime picoseconde) est impossible en raison de l'endommagement laser. Elle consiste à étirer dans le domaine temporel une impulsion courte en introduisant un retard de phase sur chaque composante spectrale. L'impulsion étirée dure alors quelques nanosecondes et peut ainsi être amplifiée sans risque d'endommagement laser. Ensuite cette impulsion étirée et amplifiée est finalement compressée en compensant le décalage de phase introduit plus tôt. On obtient ainsi une impulsion courte et très énergétique (Figure 1) qui doit être transportée jusqu'à la cible pour réaliser l'interaction laser-matière souhaitée.

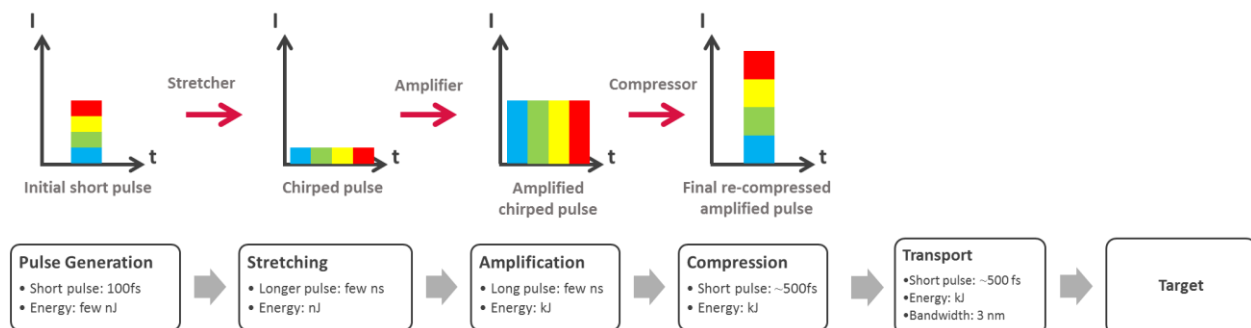


Figure 1. Schéma représentant le principe d'amplification par dérive de fréquence implémenté sur les installations Petawatt

L'amplification par dérive de fréquence a permis de repousser les limites de lasers de puissance et a rendu possible la création de lasers petawatt, tels que Petal. Mais ce qui limite maintenant la montée en puissance de ces installations laser est la résistance à l'endommagement laser des composants optiques utilisés pour le transport du faisceau (Figure 1). En effet, ces composants sont exposés à des fluences (densités d'énergie exprimée en J/cm^2) extrêmement élevées. La Figure 2 est une photo montrant un miroir de transport de Petal endommagé après un tir à plus d'un petawatt [2]. Ces miroirs sont constitués d'empilements multicouches utilisés sous vide et exposés à des impulsions laser variant entre 0,5 et 10 ps sur une bande spectrale de 3 nm centrée à 1053 nm.

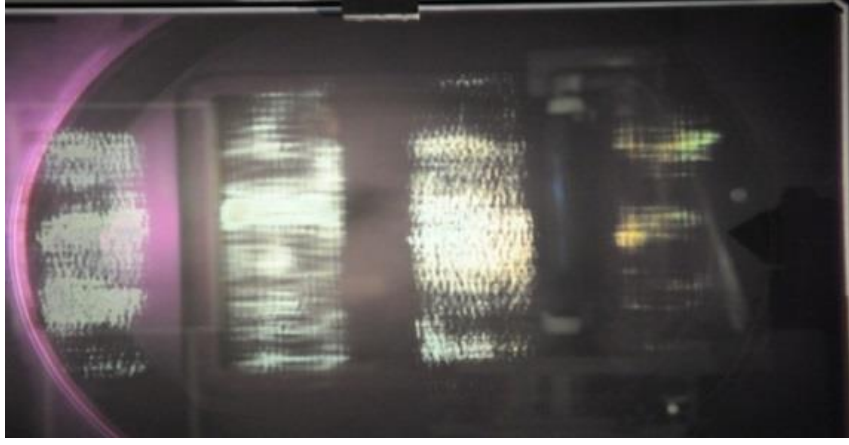


Figure 2. Exemple d'un miroir endommagé sur Petal

L'objectif de cette thèse est d'augmenter le seuil d'endommagement laser des miroirs de transport sous vide de Petal. L'endommagement laser est défini comme toutes modifications irréversibles en surface ou dans le volume d'un composant optique. La résistance à l'endommagement laser peut être caractérisée par une fluence limite appelée la tenue au flux laser du composant (TFL ou LIDT en anglais). En régime picoseconde et sub-picoseconde, ce phénomène est déterministe, ce qui veut dire qu'en dessous de cette fluence il n'y aura pas d'endommagement laser du composant optique. En revanche, au-delà de cette fluence seuil, un dommage pourra être observé à l'endroit du tir laser sous forme d'une décoloration, d'une fracture dans le matériau ou même une délamination des couches.

La façon usuelle de réaliser un miroir est d'alterner des couches minces de deux matériaux d'une épaisseur optique quart d'onde¹ (*quarter-wave optical thickness QWOT*) : un matériau H dit « haut indice » et un matériau L dit « bas indice ». La réflectivité du miroir peut être améliorée en augmentant le contraste d'indice entre les deux matériaux et le nombre de paires de couches.

Pour des empilements multicouches, le seuil de tenue au flux laser est défini comme le minimum du seuil de tenue au flux laser des couches qui le composent :

$$LIDT_{mirror} = \min(LIDT_{layer,H}, LIDT_{layer,L})$$

avec $LIDT_{exp,H}$ tenue au flux laser des couches haut indice (bas indice pour L)

Le seuil de tenue au flux laser d'une couche unique (monocouche ou *single-layer* en anglais) peut être défini de la façon suivante :

$$LIDT_{singlelayer} = \frac{LIDT_{int}}{EFI_{max}}$$

avec $LIDT_{int}$ la tenue au flux laser intrinsèque du matériau et EFI_{max} le maximum de l'intensité du champ électrique au sein de la couche.

Ainsi le seuil d'endommagement laser d'un miroir dépend de la distribution de l'intensité du champ électrique EFI dans les couches (voir Figure 3) et de la tenue au flux laser intrinsèques ($LIDT_{int}$) des matériaux qui le composent. Nous pouvons observer dans l'exemple de la Figure 3 pour un empilement miroir classique les pics de l'intensité du champ électrique sont situés aux interfaces entre les couches et EFI_{max} est situé dans les deux couches supérieures. Ainsi l'endommagement aura lieu dans l'une de ces deux couches.

¹ Epaisseur optique quart d'onde : $\tilde{n}_j d_j \cos(\theta_j) = \frac{\lambda}{4}$ avec \tilde{n}_j l'indice de réfraction de la couche, d_j l'épaisseur physique de la couche, θ_j l'angle d'incidence de la lumière dans la couche et λ la longueur d'onde centrale du miroir

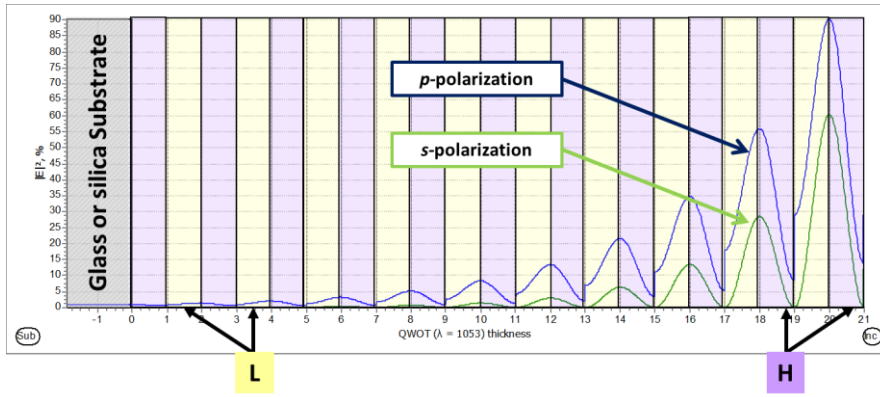


Figure 3. Distribution du champ électrique dans un empilement miroir classique

Grâce à cette définition, nous pouvons identifier 3 stratégies d'amélioration du seuil d'endommagement des miroirs de transport de Petal :

- Changer le design : pour déplacer les pics d'intensité du champ électrique dans le matériau le plus résistant
- Changer les matériaux : pour choisir des matériaux avec des meilleurs seuils d'endommagement intrinsèque
- Changer le procédé de dépôt : pour choisir un procédé induisant moins de défauts et de meilleures performances laser.

Dans un premier temps, nous avons considéré théoriquement les deux premiers axes d'étude pour quantifier numériquement les améliorations potentielles. Les résultats font l'objet du chapitre 3 et sont résumés ci-dessous. Une étude bibliographique a permis de lister les matériaux qui pourraient être intéressants de tester lors de cette étude. Ces matériaux sont pour la plupart des oxydes et quelques fluorides. Les paramètres recueillis sont l'indice de réfraction et la tenue au flux intrinsèque (dans par exemple les références : [3,4]). Le choix de matériaux uniquement basé sur ces caractéristiques est difficile, car nous ne savons pas s'il faut privilégier un bon contraste d'indice ou une bonne tenue au flux intrinsèque. Grâce à une étude numérique, il a été possible d'évaluer les performances des matériaux utilisés par paires dans un empilement multicouche et non individuellement. Dans un premier temps, nous avons évalué l'influence des indices de réfraction des deux matériaux sur l'intensité du champ électrique, ce qui nous a permis de conclure que le choix du matériau bas indice a une influence limitée. Par conséquent, il est préférable de choisir le matériau bas indice avec la tenue au flux laser intrinsèque la plus élevée, c'est-à-dire la silice. Dans un second temps, pour hiérarchiser les matériaux « haut indice », nous avons évalué l'influence des deux caractéristiques des matériaux (indice de réfraction et tenue au flux intrinsèque) sur la tenue au flux d'un empilement classique composé de 37 couches d'un matériau H et de silice, voir Figure 4 gauche. Parallèlement, pour améliorer les seuils d'endommagement, nous pouvons ajuster les épaisseurs des 2 couches supérieures de l'empilement de façon à avoir : $LIDT_{outer\ layer,H} = LIDT_{outer\ layer,L}$ (nous déplaçons l' EFI_{max} dans le matériau qui a la meilleure $LIDT_{int}$), voir Figure 4 droite. Ce type de design est appelé dans ce document le balanced design.

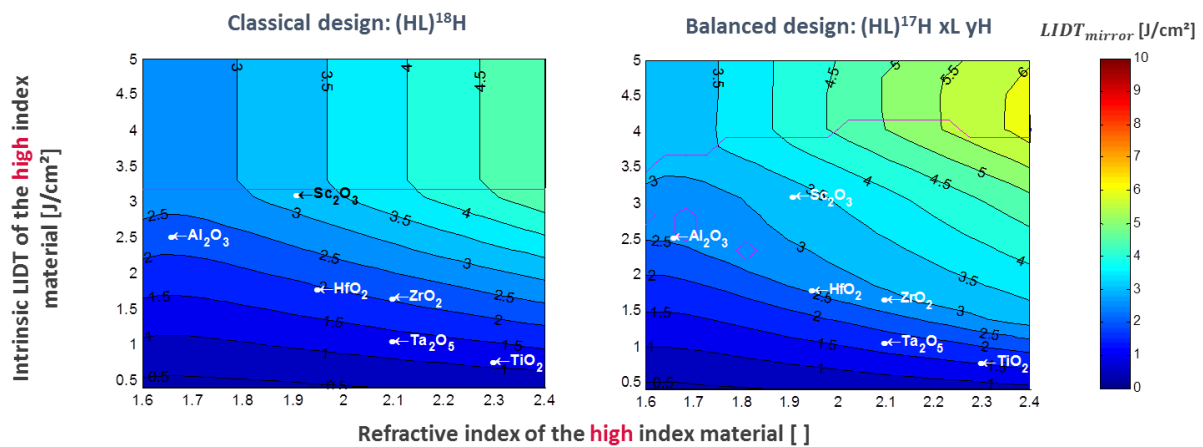


Figure 4. $LIDT_{mirror}$ pour la polarisation p d'un miroir avec $L=SiO_2$ dans un design classique (droite) et un design avec les deux couches supérieures optimisées (gauche)

Avec ces représentations, nous sommes capables de hiérarchiser les matériaux hauts indices. Nous pouvons voir que Sc_2O_3 a un fort potentiel. HfO_2 reste malgré tout un bon candidat, car il est le matériau le plus couramment déposé et produit des performances similaires à celles de Al_2O_3 et ZrO_2 . En comparant les performances d'un balanced design avec celles d'un design classique, nous pouvons voir l'intérêt d'optimiser les empilements.

Pour continuer à explorer ce concept, nous avons développé un algorithme qui optimise un plus grand nombre de couches. Cet algorithme peut être résumé sous la forme schématique suivante, Figure 5.

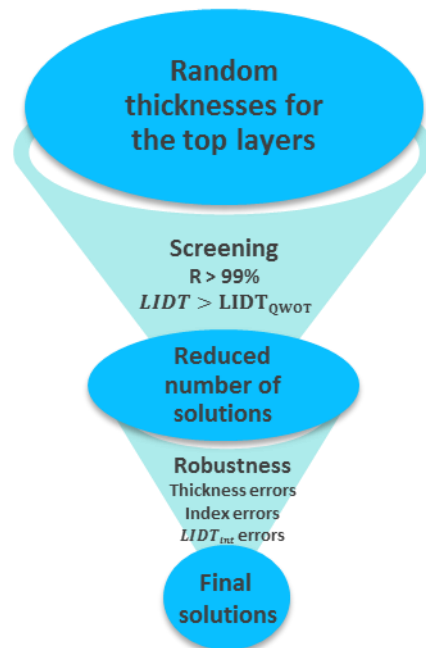


Figure 5. Schéma de fonctionnement de notre algorithme d'optimisation des designs

Le design d'entrée de l'algorithme est un design classique d'un certain nombre de couches (par exemple 37) avec deux matériaux spécifiques dont l'indice de réfraction et la tenue au flux laser doivent être connues. Durant la première étape de l'algorithme, nous avons décidé de faire varier aléatoirement les épaisseurs des 12 couches supérieures entre une valeur d'épaisseur minimale et une valeur d'épaisseur maximale. La génération aléatoire des épaisseurs permet de couvrir une grande variété de solutions et notamment de s'éloigner du design initial qui pour beaucoup de logiciels d'optimisation reste le meilleur. Les valeurs minimale et maximale d'épaisseurs sont choisies en fonction des capacités des procédés de fabrication. Par

exemple, pour de l'e-beam, la gamme d'épaisseurs varie de 20 à 500 nm. A la suite de cette génération aléatoire, les millions de solutions créées sont filtrées avec les critères suivants : une réflectivité supérieure à 99% et une tenue au flux laser supérieure à celle du design initial. A l'issue de cette étape de filtrage, nous avons réduit à quelques milliers le nombre de solutions. Ces solutions peuvent être très bonnes numériquement mais potentiellement non réalisables compte tenue des incertitudes de fabrication. Ainsi pour sélectionner une solution réaliste, une dernière étape de filtrage est appliquée. Cette étape consiste à tester la robustesse des solutions calculées aux incertitudes de fabrication. Ces incertitudes comprennent : les erreurs sur les indices de réfraction, sur les épaisseurs et sur les tenues au flux laser intrinsèque. Elles sont considérées d'abord individuellement puis simultanément dans une erreur cumulative. A la suite de cette sélection sur la robustesse, il ne reste plus qu'un pool de solution avec des performances plus élevées que le design initial. Nous pouvons identifier deux designs intéressants : le « max LIDT design » qui produit les meilleures performances en tenue au flux laser sans erreur cumulative et le « robust design » qui a les performances les plus stables avec ou sans erreur cumulative.

Toutes les simulations du chapitre 3 étant basées sur des valeurs bibliographiques, il est nécessaire de caractériser les indices et les tenues au flux intrinsèque des monocouches afin d'utiliser notre algorithme avec des données d'entrée expérimentales.

Notre méthode de caractérisation des monocouches déposées sur échantillons est présentée dans le chapitre 4 ainsi que les nombreux résultats obtenus.

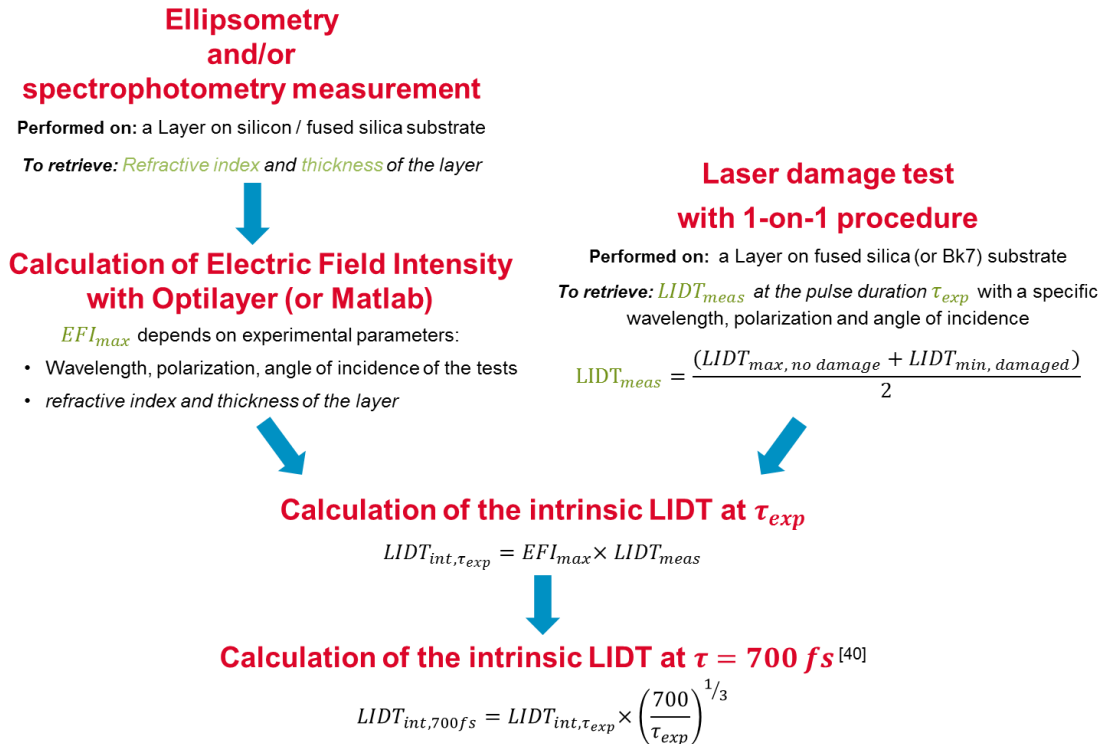


Figure 6. Schéma décrivant notre méthode de caractérisation des matériaux à partir de monocouches

La méthode de caractérisation est résumée dans le schéma ci-dessus. Tout d'abord les indices de réfraction et épaisseurs des monocouches sont déterminés à partir de mesures ellipsométriques et spectrophotométriques. Avec ces données, le maximum d'intensité du champ électrique est calculé pour les conditions des tests d'endommagement laser (angle d'incidence, polarisation, longueur d'onde et environnement). En parallèle de ce calcul, le seuil d'endommagement laser est déterminé sur un banc

d'endommagement. Au cours de cette thèse, deux bancs d'endommagement ont été utilisés : un banc CEA fonctionnant à l'air ambiant ou sec et un banc LLE similaire fonctionnant également sous vide. Ensuite, la combinaison de l' EFL_{max} calculé et de la tenue au flux laser mesurée permet de déterminer la tenue au flux laser intrinsèque. Une loi d'échelle temporelle est ensuite appliquée pour recalculer tous les résultats des tests à la même durée d'impulsion. Une évaluation précise des incertitudes est importante à chacune de ces étapes de caractérisation. Grâce à une étude paramétrique, il a été possible de définir des configurations de test réduisant les incertitudes sur le calcul de l'intensité du champ électrique. Il est préférable de tester des monocouches d'une épaisseur FWOT (*full-wave optical thickness*) en incidence normale ou en polarisation p si l'incidence est différente de 0° .

La méthode de caractérisation a été mise en œuvre sur une grande variété de matériaux d'intérêt sélectionnés au cours de l'étude paramétrique. Les valeurs de seuil de tenue au flux laser intrinsèques sont tracées en fonction des valeurs d'indices de réfraction en Figure 7. Contrairement aux résultats couramment observés dans la littérature [3, 5], nous pouvons observer pour un même matériau une forte dispersion des valeurs suivant leur tenue au flux intrinsèque et une faible dispersion suivant l'indice de réfraction.

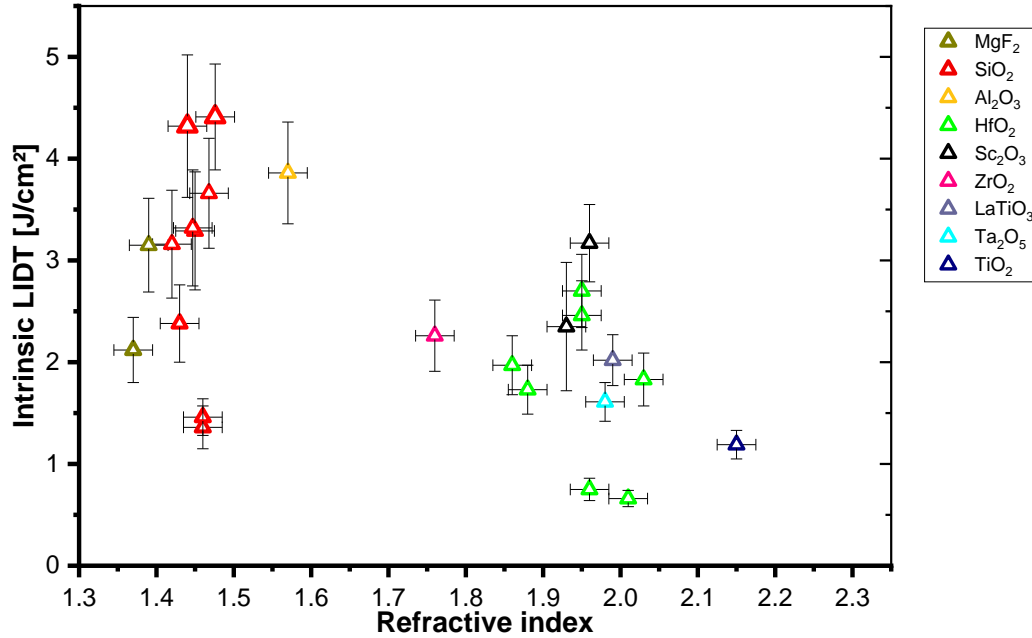


Figure 7. Tenues au flux laser intrinsèque des monocouches caractérisées au cours de cette thèse en fonction de leurs indices de réfraction.

Pour mieux comprendre la source de cette dispersion sur les valeurs de tenue au flux laser intrinsèque, l'énergie de bande interdite a été mesurée sur les échantillons grâce à la méthode de Tauc [6]. En Figure 8 sont tracées les valeurs de tenue au flux intrinsèque en fonction des valeurs d'énergie de bande interdite des monocouches de silice et d'hafnium. Sur cette figure, nous pouvons observer que la dispersion suivant la tenue au flux laser ne peut être expliquée par des variations de l'énergie de bande interdite. De plus, ceci implique que les tenues au flux laser intrinsèque ne peuvent être prédites à partir de la connaissance de l'énergie de bande interdite du matériau déposé. La tenue au flux laser intrinsèque ne dépend pas seulement du matériau mais également du procédé de dépôt (c'est-à-dire méthode de dépôt et fabricant).

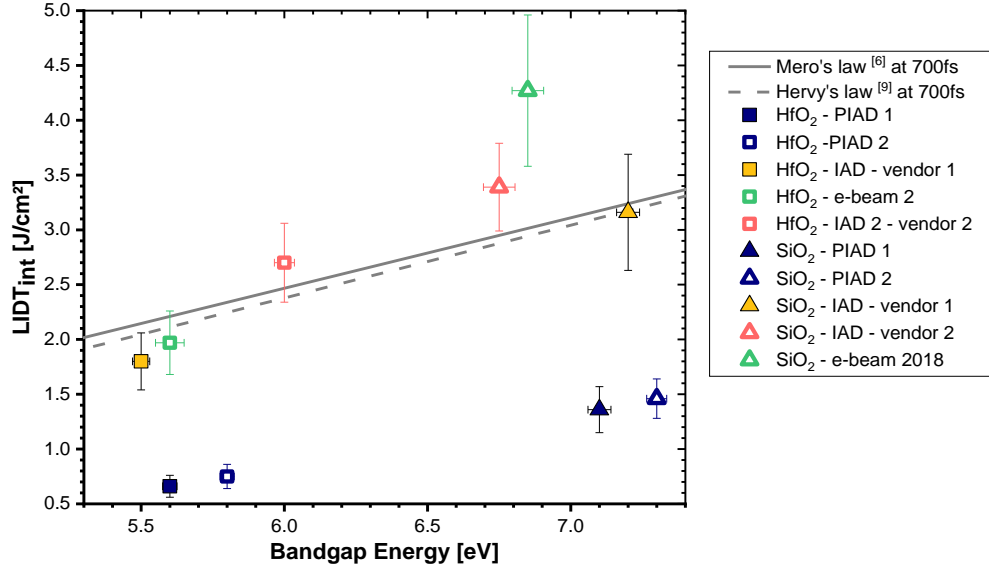


Figure 8. Tenues au flux intrinsèque en fonction des valeurs d'énergie de bande interdite des monocouches de silice et d'hafnium

Pour expliquer la dispersion de ces valeurs nous avons recherché des corrélations avec d'autres grandeurs optiques, notamment avec l'absorption multi-photonique. Pour cela, nous avons mesuré les absorptions des monocouches dans l'ultraviolet. Le détail de cette démarche est présenté en chapitre 5. Le résultat important à retenir est : il existe une bonne corrélation entre l'absorption dans l'ultraviolet et la tenue au flux laser en régime sub-ps dans l'infrarouge (cf. Figure 9).

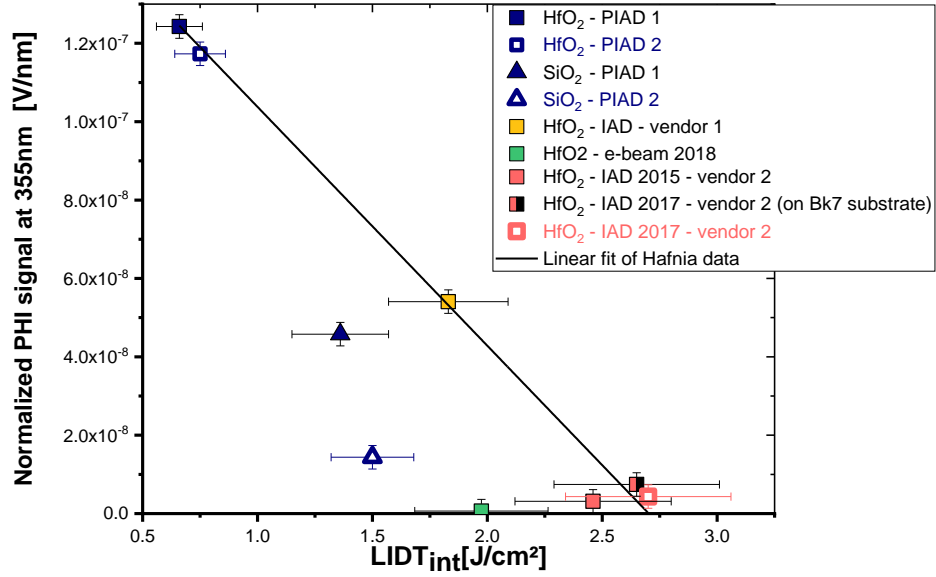
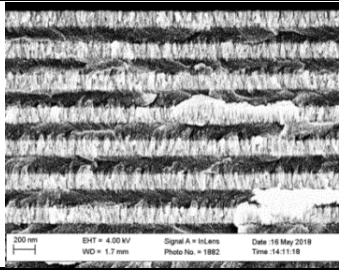
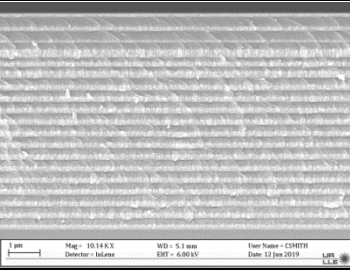
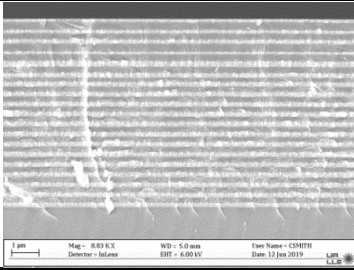


Figure 9. Valeur du signal correspondant à l'absorption des échantillons à 355 nm en fonction des seuils de tenue au flux laser intrinsèque à 1053 nm

Grâce à l'algorithme présenté dans le chapitre 3 et les valeurs expérimentales obtenus dans le chapitre 4, il a été possible de calculer des designs à hautes tenues au flux laser et robustes aux erreurs de fabrications. Les premières caractérisations étant effectuées à l'air ambiant pour des raisons de disponibilité, nous avons validé notre méthode d'optimisation en air ambiant avec une amélioration de l'ordre de 44% de la tenue au flux laser. Ensuite, comme les miroirs de transport de Petal sont utilisés dans le vide, la même démarche a été appliquée pour calculer des designs optimisés sous vide (Cf. Tableau 1).

Tableau 1. Performances des trois designs utilisés sous vide

	Vacuum - Classical design	Vacuum - Robust design	Vacuum - Max LIDT design
			
Reflectivity at 1053 nm <i>p</i>-pol, 45° AOI	99.8%	99.4%	99.5%
Predicted LIDT <i>p</i>-pol [J/cm²]	1.41	2.07	2.53
Measured LIDT <i>p</i>-pol [J/cm²]	1.41±0.08	2.22±0.11	2.44±0.14
Improvement on the LIDT compared to classical design	--	+57%	+73%

Les résultats exposés dans le Tableau 1 montrent que le Max LIDT design produit par notre algorithme d'optimisation fourni une amélioration de la tenue au flux laser de 73% par rapport à un design classique de miroir.

L'objectif de cette thèse a été atteint sur des échantillons. Il reste maintenant à la transposer sur des composants de taille réelle (610 mm x 430 mm x 80 mm). En outre, cette démarche peut être appliquée à d'autres problématique d'empilements multicouches tels que polariseurs, réseaux et miroirs à large bande.

Références du résumé

- [1] D. Strickland and G. Mourou. Compression of amplified chirped optical pulses. *Opt. Comm.*, 55(6):447–449, 1985.
- [2] N. Blanchot, G. Béhar, J.C. Chapuis, C. Chappuis, S. Chavardoine, J.F. Charrier, H. Coic, C. Damiens-Dupont, J. Duthu, P. Garcia, J. P. Goossens, F. Granet, C. Grosset-Grange, P. Guerin, B. Herbard, L. Hilsz, L. Lamaignère, T. Lacombe, E. Lavastre, T. Longhi, J. Luce, F. Macias, M. Mangeant, E. Mazataud, B. Minou, T. Morgaint, S. Noailles, J. Néauport, P. Patelli, E. Perrot-Minnot, C. Present, B. Remy, C. Rouyer, N. Santacreu, M. Sozet, D. Valla, and F. Laniesse. 1.15 PW - 850 J compressed beam demonstration using the PETAL facility. *Opt. Express*, 25(15):16957–16969, 2017.
- [3] L. Gallais and M. Commandré. Laser-induced damage thresholds of bulk and coating optical materials at 1030 nm, 500 fs. *Appl. Opt.*, 53(4):A186–A1966, 2014.
- [4] M. Mende, S. Schrameyer, and H. Ehlers. Laser damage resistance of ion-beam sputtered Sc₂O₃/SiO₂ mixture optical coatings. *Appl. Opt.*, 52(7):1368–1376, 2013.
- [5] B. Mangote, L. Gallais, M. Commandré, M. Mende, L. Jensen, H. Ehlers, M. Jupé, D. Ristau, A. Melninkaitis, J. Mirauskas, V. Sirutkaitis, S. Kicas, T. Tolenis, and R. Drazdys. Femtosecond laser damage resistance of oxide and mixture oxide optical coatings. *Opt. Lett.*, 37(9):1478–1480, 2012.
- [6] J. Tauc, R. Grigorovici, and A. Vancu. Optical properties and electronic structure of amorphous germanium. *phys. stat. sol.*, 15(627), 1966

Acknowledgement

The thesis you are about to read... Yes, because I am hoping that you, dear readers, are about to read the whole thesis and not just this acknowledgement section. I am trusting you, you can do it ! ;-) So let's start again!

The thesis you are about to read presents the work and production of three years of hard work where I was able to express myself, discover and reveal my love for research (especially in the thin films context) and communication. I really enjoyed this experience and all the experiments, simulations, discussions, meetings it required. In the following pages I would like to acknowledge all the people you made this possible.

I would like to begin by thanking the members of my defense committee for accepting to judge my work and be part of the finalization of this thesis. I would like to thank especially Olivier Uteza and Andrius Melninkaitis for reviewing this thesis. All your remarks allowed considering new questions and improving this present paper. I will also acknowledge Lionel Canioni, Stavros Demos, Laurent Gallais-During, Laurent Pinard and Amy Rigatti for reading this thesis and for their comments and questions during the defense.

Then I would like to thank all the people who mentored and guided me during this work. The first two people I am thinking of are Eric and Thomas, my super CEA mentors. You were both very complementary in your daily coaching, thank you for all the things you taught me, all the time we spent working, talking and discussing the way to make/take. Thank you for everything. Thank you Thomas for selecting me for this polarizer's internship that started all.

I would like then to thank my incredible PhD supervisor Bruno. Thank you for your involvement, your outside look that allows to synthesize everything, to fix the goals and to guide this work in the right direction. I would like also to deeply thank you and Eric for all the essential help and corrections during the difficult time of writing this thesis.

Then I wish to acknowledge Jérôme N. & Stavros for creating this collaboration between CEA and LLE on the topic of short pulses laser-induced damage. These exchanges to Rochester undoubtedly broaden my point of view on work, on the world and life. It was a real life experience and I am deeply grateful for this opportunity. You both guided me through this work and helped me synthesize, write and also *rewrite* articles and this thesis as well. All of this taught me a lot.

I would also like to thank Nicolas Bonod for his involvement in my work. The time I spent at Institut Fresnel led to the development of the optimization algorithm as it is. You also helped me a lot on the writing of the two articles published during this thesis. Thank you for that.

Then my thankfulness goes to Denis firstly for accepting my application for this thesis, then for letting me and moreover cheering me to write and defend my thesis in English and also to participate at many contests like "Festival du film (pas trop) scientifique", "Ma thèse en 180s" and finally the L'Oréal award "For women in science". For this latter contest, I would like to thank Claude and Jérôme N., too, for their involvement in

my application and their help in improving it. I wish to thank Stéphane S. too for letting me participate at the “Festival du film pas trop scientifique”. This film contest was the first contest I participated during this PhD and it revealed my love to popularize my Ph.D research. Even though my participation to those contests wasn’t successful I learned a lot and I was very pleased to represent CEA.

Then I wish to thank Bernard, François and both Jérômes (N. and D.) for their overviews on my work as head of the department, service and laboratory. More importantly I would like to thank you all for hiring me after this PhD studies. I am truly appreciative for being able to continue this research as part of my new position and to still be a part of the collaboration between CEA and LLE.

I would like to also thank the CEA communication service (UCAP) for asking me to participate to the interview from “Sciences et Vie Junior” for the article on the LMJ and Petal. I never thought I could be cited and thanked in this magazine that allows young people to discover sciences.

Finally I would like to thank all the people I worked with during these three years: all the people from both LTO and LMO and all the people I met at LLE. You all welcomed me with such kindness and well-meaning that Bordeaux and then Rochester felt almost like home. I am writing almost because everyone should know that Brittany (the place, Bretagne in French) remains the best place on earth.

To the people in LTO, I am thanking each and every one of you: apprentices, interns, post-docs and permanent members of the team for being so nice colleagues. I would like to address special thanks to Daniel for all the board games you made us discover. I only knew Monopoly before coming to LTO.

Among the entire person I met at LLE I am addressing my special thanks to Semyon who taught me a lot and made a considerable number of measurements for me. Your passion to optics and sciences is a real source of inspiration and I really enjoyed talking with you during my stay at LLE. I am also appreciative of all the damage tests performed by Alexeï and all the discussion we had on laser-induced damage, music and anything else. I am also very grateful to Amy and Jim for everything they taught me on coatings and all the discussion we had. Finally, I wish to acknowledge the undeniable involvement of Brittany (the person this time and not the place in France) in this work with all the measurements, observation and everything you have done and also for making me feel comfortable in Rochester. You accomplish an incredible work and you are a great person. I would like to thank Katelynn and Debbie too for their warm welcome at LLE and this week-end in London where we met a backstreet boy. And thank you Katelynn for taking time to correct some spelling and grammar mistakes I made in this thesis. I am looking forward seeing all of you again in Rochester soon.

Among the people from LMO, I directing my special thanks to Nadja for all the damage testing you performed with me, for teaching me how to use DERIC and everything else; to Isabelle for all the measurements you performed for me during this PhD and internship and for teaching me how to use the two spectrophotometers; to Laurent for exchanging about laser-induced damage and advising me on conferences, articles and thesis writing and finally to Stéphane for teaching me a lot about interferometry, power and for your advises.

Finally, I would like to thank all the friends I made when I arrived in Bordeaux: Clémence, Florian, Mathilde, Martin, Mélanie, Nicolas (Bonjour !), Noémie, Pierre-Marie and Roxane. Thank to you all I discovered Bordeaux and spend some incredible times and evenings here. Even though you are not all in Bordeaux anymore, I know we will continue to see each other anywhere in the world. As we experienced

with Nicolas when we travelled on these week-ends to discover the east of the America (Washington, Minneapolis, Rochester, Niagara Falls, Toronto) and the one in New York with Clémence too. It was super and I still remember our songs with a smile. I am sorry because I didn't keep my cape forever and ever like you said you will.

I wish to add some special thanks here to Florian. We both began our thesis almost together and we are finishing them with just 5 days apart. I really enjoyed spending this three years working alongside you, all these shared trainings, all these discussions and laughs exchanged, all of our presentation that followed one another. I would like to thank you, Noémie and my sister, Colette, for this incredible road trip in the west of the USA. We saw the grand Canyon, Las Vegas, the death valley, the Yosemite forest, San Francisco, the quite traumatic Alcatraz, the west coast, Santa Barbara and finally Hollywood. It was great, crazy, tiring (all these miles driving) and unbelievable. I never thought I will be a witness at a wedding in Las Vegas, especially not the wedding of such great friends as you both are. Thank you! Et Bisous !

To finish this section and the writing of this thesis, I wish to acknowledge those you have always been there and always will: ma famille.

Merci !

Table of content

Résumé de la thèse (français).....	i
Acknowledgement	x
Table of content	xiii
Glossaire	xvi
Introduction (français)	1
Introduction	3
Chapter 1 High power facilities: objectives and challenges	5
1.1 High power Laser facilities: Presentation of Petal & LMJ.....	6
1.1.1 High power laser facilities or fusion class laser: purposes and architecture	7
1.1.2 Architecture of Fusion Class Laser: LMJ & Petal example	11
1.2 Laser damage challenges in high power laser facilities	21
1.2.1 Fundamental of laser-induced damage.....	21
1.2.2 Nanosecond facilities.....	23
1.2.3 Pico and sub-picosecond facilities	24
Summary of Chapter 1.....	28
Chapter 2 Multilayer Dielectric coatings	29
2.1 Principle of MLD coatings	30
2.1.1 Dielectrics	30
2.1.2 Single layer example.....	34
2.1.3 Multilayer	36
2.2 Laser damage and MLD	41
2.2.1 Short pulse LIDT on MLD	41
2.2.2 Survey of the models	42
2.3 Fabrication of multilayer dielectric component	46
2.3.1 Survey of thin film manufacturing.....	46
2.3.2 Deposition Methods.....	47
2.3.3 Manufacturing Petal transport mirror.....	51
Summary of Chapter 2.....	54
Chapter 3 Design and optimization of dielectric multilayers with high LIDT in the sub-ps regime	55
3.1 Choice of materials	56

3.1.1	Background on materials.....	56
3.1.2	Numerical parametric study	61
3.2	<i>New Design: Optimization of multilayer stacks</i>	68
3.2.1	Background on design	68
3.2.2	Background on design optimization algorithms.....	71
3.2.3	Presentation of the optimization algorithm.....	72
3.2.4	Example of application of our robust optimization algorithm	73
Conclusion of Chapter 3		78
Chapter 4 Characterization of monolayers.....		79
4.1	<i>Intrinsic LIDT characterization</i>	80
4.1.1	Measurement of the refractive index and thickness.....	81
4.1.2	Calculation of the Electric field intensity	83
4.1.3	LIDT measurement with 1-on-1 procedure	88
4.1.4	Calculation of the intrinsic LIDT	91
4.2	<i>Results: description of the set of samples tested in ambient air</i>	91
4.3	<i>Influence of the environment on monolayers properties</i>	94
4.3.1	Ambient Air Vs Dry Air	94
4.3.2	Vacuum Vs ambient Air	95
Conclusion of Chapter 4		100
Chapter 5 Toward nondestructive characterization of the intrinsic LIDT		101
5.1	<i>Intrinsic LIDT and refractive index comparison</i>	102
5.2	<i>Limits of Mero's Law</i>	104
5.2.1	The Tauc Method.....	104
5.2.2	Results	105
5.3	<i>Correlation to other optical signature</i>	106
5.3.1	Correlation to spectrophotometry measurement.....	107
5.3.2	Correlation to photothermal absorption measurements.....	112
Conclusion of Chapter 5		116
Chapter 6 Design optimization.....		117
6.1	<i>Experimental validation of our algorithm: Optimization for air use</i>	118
6.1.1	Expected numerical LIDT results	118
6.1.2	Results	121
6.1.3	Intrinsic LIDT determination from multilayers	123
6.2	<i>Influence of the environment on multilayers dielectric mirrors</i>	124
6.2.1	Performance of the design for vacuum	125

6.2.2	Study of the potential Influence of the mechanical stress on LIDT	126
6.2.3	Intrinsic LIDT determination in vacuum from multilayers	131
6.3	<i>Optimization of the Final design</i>	131
6.3.1	Expected numerical LIDT results	131
6.3.2	Results	133
Conclusion of Chapter 6		137
Conclusion.....		138
Perspectives on multilayer dielectrics components used in high power laser facility		140
1.	<i>Mirrors</i>	141
1.1.	Petal Transport Mirrors	141
1.2.	Broadband chirped mirrors (15 fs)	142
2.	<i>Other optical functions</i>	142
2.1.	Polarizers	142
2.1.1.	<i>LMJ polarizers specification and designs</i>	142
2.1.2.	<i>Aging effect: irreversible phenomenon</i>	143
2.1.3.	<i>Effect of the relative humidity: reversible phenomenon</i>	144
2.2.	Petal gratings	145
Summary of the perspectives		146
Conclusion (français)		147
References		149

Glossaire

AR : anti-reflective/ anti-reflection

CEA : Commissariat à l'Énergie Atomique et aux Énergies Alternatives *in french to be translated as the French Alternative Energies and Atomic Energy Commission*

CPA : Chirped Pulse Amplification

CTBT : comprehensive test ban treaty

EFI_{max} : maximum of the electric field intensity inside a layer or a multilayer coating

ELI : Extreme Light Infrastructure

FI : fast ignition

FS : fused silica

FWOT : full-wave optical thickness layer

HR : highly-reflective/ high-reflection

HWOT : half-wave optical thickness layer

ICF : inertial confinement fusion

LASER : light amplification by stimulated emission of radiation

LEHs : laser entrance holes in Fig. 5:

LID : laser-induced damage

LIDT : laser-induced damage threshold

$LIDT_{int}$: intrinsic LIDT

LLE : Laboratory for Laser Energetics

LLNL : Lawrence Livermore National Laboratory

LMJ : Laser Mégajoule

MLD : multilayer dielectric

MPA : pre-amplifier module

MPI : multi-photon ionization

NIF : National Ignition Facility

NIF-ARC : National Ignition Facility – Advances Radiographic Capability

PEPC : plasma electrodeless cell

PETAL/Petal : PETawatt Aquitaine Laser

PVD : physical vapor deposition

QWOT : quarter-wave optical thickness layer

SEM : scanning electron microscope

TI : tunnel ionization

Introduction (français)

En 2018, le prix Nobel de physique a été décerné aux professeurs Donna Strickland et Gérard Mourou pour le développement de l'amplification par dérive de fréquence (chirped pulse amplification, CPA). Cette technique a rendu possible la création de Laser Petawatt. Cette récompense a été une grande reconnaissance pour la communauté de la photonique et des lasers.

En effet, depuis la création du premier laser en 1960, les scientifiques ont toujours cherché à atteindre des puissances et des énergies laser plus élevées [1]. Durant les trois dernières décennies, se sont ainsi développées autour du globe de gigantesques installations laser : les installations laser de puissance. Parmi ces installations on peut notamment citer le Laser MégaJoule et Petal implantées près de Bordeaux en France.

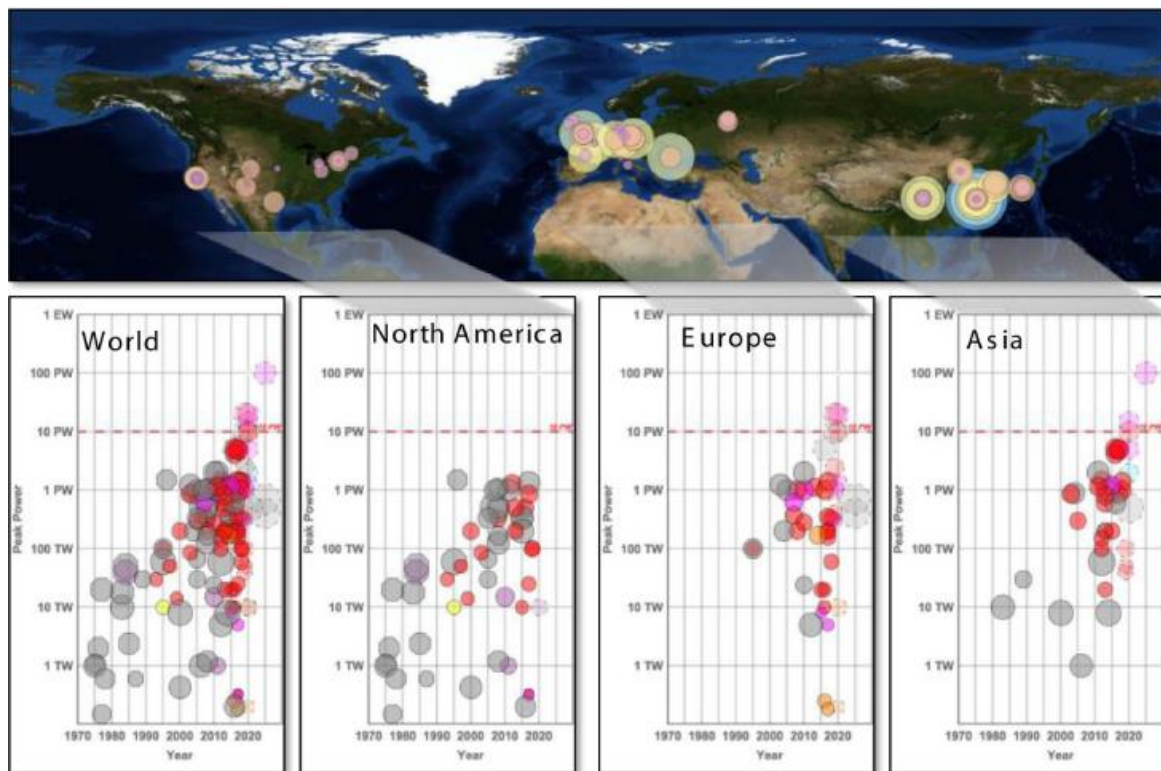


Fig. 1. Répartition géographique des installations laser de puissance dans le monde (haut) et augmentation de la puissance de ces lasers au fil des années (bas). Cette figure est extraite de [1]

L'un des principaux défis de ces installations est de comprendre et d'appréhender l'endommagement laser des centaines de composants contenus dans ces systèmes laser. Plus particulièrement, sur l'installation Petal, le seuil de tenue au flux laser des miroirs de transport est actuellement le facteur limitant de la montée en puissance de l'installation. Ces miroirs de transport sont constitués à partir d'un empilement de couches minces de plusieurs matériaux diélectriques déposés sur des substrats en silice ou verre. La principale motivation de cette thèse est d'augmenter le

seuil de tenue au flux laser (laser-induced damage threshold, LIDT) de ces composants multicouches (MLD) utilisés en régime sub-picoseconde. Les stratégies d'amélioration de cette tenue au flux laser consistent en la recherche de meilleurs designs, matériaux et/ou techniques de fabrication.

Ce travail de thèse s'appuie sur une approche numérique originale ainsi que sur une solide validation expérimentale. Tout d'abord, nous avons développé notre propre algorithme d'optimisation des empilements multicouches permettant de concevoir des empilements performants et robustes aux erreurs de fabrication. Ensuite, des matériaux soigneusement sélectionnés ont été caractérisés puis testés vis-à-vis de leur tenue au flux laser. La présentation des méthodes employées et résultats obtenus est organisée comme suit.

Le contexte général dans lequel s'inscrit ce travail est présenté dans le premier chapitre à travers une vue d'ensemble sur les installations laser de puissance dans le monde. Ensuite les installations Laser MégaJoule (LMJ) et Petal sont présentées plus en détails. Pour finir ce chapitre introductif, les principaux mécanismes à l'origine de l'endommagement laser sont présentées puisque comprendre et surpasser l'endommagement laser reste un des défis principaux de ces installations.

Le chapitre suivant présente les connaissances nécessaires à l'étude des empilements multicouches de matériaux diélectriques en décrivant comment l'intensité du champ électrique est calculée à l'intérieur de la structure multicouches, et comment sont conçus et fabriqués les empilements multicouches. Au travers de cette présentation, les trois axes d'amélioration de la tenue au flux laser cités ci-dessus seront dégagés. Le premier consiste à considérer de nouveaux matériaux, le second porte sur l'amélioration des empilements *via* de nouveaux designs optimisant la distribution du champ électrique. Le dernier axe d'amélioration porte sur la recherche de nouvelles techniques de dépôts.

Ensuite dans le troisième chapitre, les deux premières stratégies d'optimisation seront examinées numériquement et les améliorations seront quantifiées. Cette étude théorique basée sur un calcul numérique a mené au développement d'un algorithme d'optimisation robuste qui sera présenté au cours de ce chapitre.

L'application de cet algorithme requiert la caractérisation préalable de matériaux. Les matériaux à fort potentiel repérés au cours de l'étude théorique ont donc été caractérisés et les résultats de ces divers matériaux associés à différentes méthodes de dépôt, présentés dans le chapitre 4, seront analysés pour remettre en cause certaines corrélations entre paramètres physiques publiées bien avant ce travail.

Dans le chapitre 6, l'algorithme d'optimisation est appliqué en utilisant les résultats expérimentaux présentés dans le chapitre 4. En concevant un empilement multicouche il est important de maintenir la réponse spectrale souhaitée suivant l'environnement et au cours du temps. L'influence de l'humidité relative et du vide sur les performances en tenue au flux laser des traitements a ainsi été étudiée.

Pour finir, en dernière partie de cette thèse, seront présentées les perspectives de recherche pouvant s'appuyer sur ce travail et les améliorations futures qui pourraient être apportées à notre algorithme de conception de structures multicouches optimisées pour qu'il puisse être utilisé à l'amélioration et au développement d'autres composants multicouches utilisés sur les installations laser de puissance.

Introduction

In 2018, the Nobel Prize in physics was awarded to Professor Donna Strickland and Gerard Mourou for the development of the technique of chirped pulse amplification (CPA), which made possible the creation of ‘Petawatt Class Lasers’. This award was a great achievement for the laser research community.

Indeed, since the invention of laser in the 1960, scientists have been working at always reaching higher energies and higher power [1]. The past decades have seen the development of several gigantic laser facilities around the world: the high power facilities. Among those, one can cite the LMJ and Petal facilities installed near Bordeaux in France.

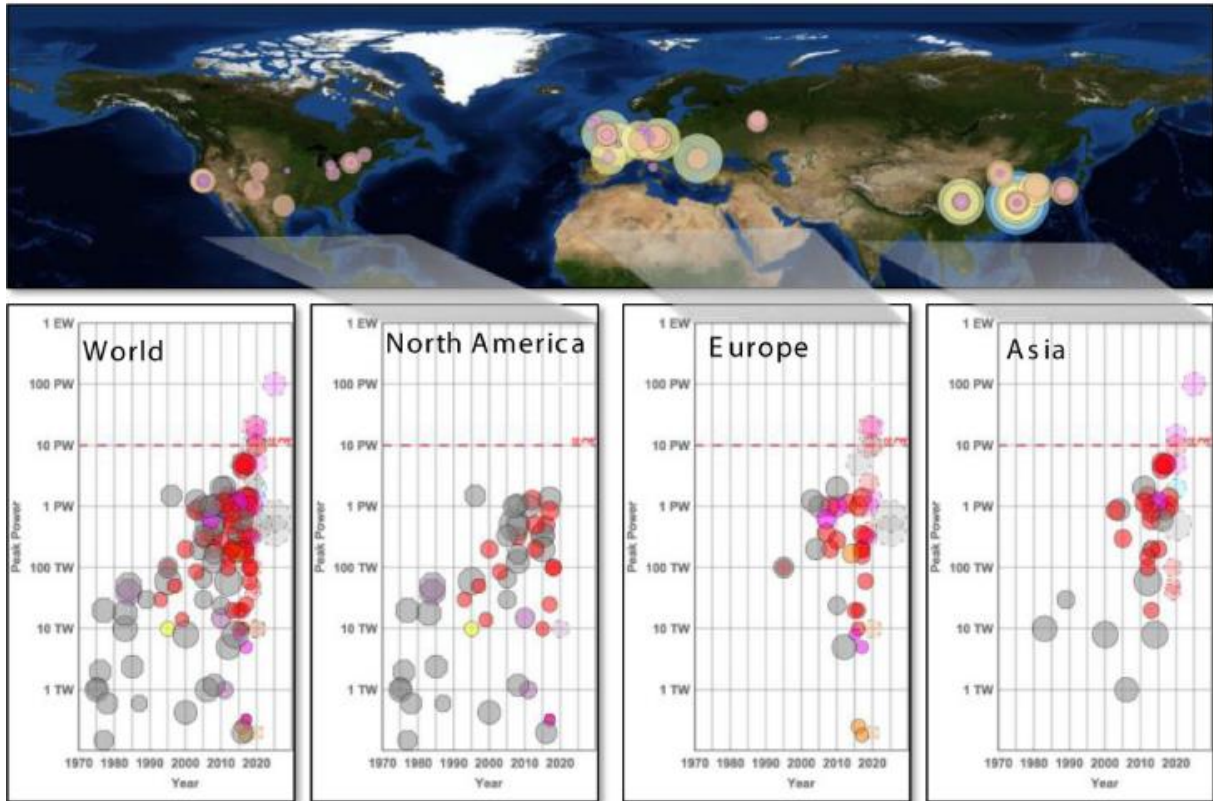


Fig. 2. Geographic distribution of high-peak-power lasers (top) and increase of power of those lasers regarding the years (bottom). This figure is taken from [1]

One of the main challenges of those facilities is to understand and overcome laser-induced damage on the thousands of optical components in the laser system. Especially, on the Petal laser facility, the laser-induced damage threshold of the transport mirror is currently limiting the overall power of the laser. Those transport mirrors are made of coatings manufactured by stacking a multitude of thin films of various dielectric materials on a fused silica or glass substrate. The main motivation of this PhD study is to develop methods to increase the laser-induced damage threshold (LIDT) of such multilayer

dielectrics (MLD) mirrors used in sub-picosecond regime. The paths considered to achieve this goal are:

- Improving/changing the materials,
- Improving/changing the designs
- or optimizing/changing the manufacturing process.

This PhD work combines a specific and innovative numerical approach with extensive experimental validation. Firstly, we developed our optimization algorithm is robust to manufacturing errors. Secondly, an array of materials was considered and characterized with a spectrophotometer and an ellipsometer, and were finally laser damage tested throughout of this work.

The presentation of methods and results is organized as follows.

In a first chapter, the general context in which this work takes place is presented by first giving an overview of the high power lasers in the world. Then the LMJ/Petal facilities are presented in more details. To finish, we present the main mechanism at the origin of laser-induced damage, since one of the main challenges of these facilities is to understand and manage the laser-induced damage to optical material.

The following chapter presents the background necessary to study MLD components, explaining how to calculate the electric field intensity in a MLD structure, and how to design and manufacture MLDs. Throughout this presentation, the three axes of improvement of the mirrors LIDT, cited above, will be disclosed. The first one considers new materials exhibiting higher intrinsic LIDT than the reference materials. The second one improves the design by re-engineering the near electric field distribution. The last one investigates other deposition methods than the one currently used.

In Chapter 3, we examine the two first paths of increasing the LIDT theoretically and calculate the improvement those change can bring. This theoretical study led to the development of a robust optimization algorithm, presented within this chapter.

To apply this algorithm, the materials with high potential highlighted in Chapter 3 have been characterized. Those materials associated with various deposition process and their characterizations are presented in Chapter 4. They lead to reconsider the model establishing a link between the bandgap energy and the intrinsic LIDT on MLD, in Chapter 5.

In Chapter 6, the robust algorithm is applied using the values determined in the Chapter 4. When designing optical multilayer dielectric component, it is important to obtain and maintain the desired spectral response. The influence of the environment has been assessed throughout this work.

Finally, in the last part of this thesis we will discuss the future prospects of research brought by this present work and the future improvement that could be performed on the algorithm so it can be applied to improve other MLD coatings used on high power laser facilities.

Chapter 1 High power facilities: objectives and challenges

1.1	<i>High power Laser facilities: Presentation of Petal & LMJ</i>	6
1.1.1	High power laser facilities or fusion class laser: purposes and architecture	7
1.1.1.1	Overview of high power laser facilities	7
1.1.1.2	Military applications.....	8
1.1.1.3	The Civilian Applications	9
1.1.2	Architecture of Fusion Class Laser: LMJ & Petal example.....	11
1.1.2.1	Establishment of LMJ and Petal	11
1.1.2.2	Architecture of LMJ Beam Line [29]	14
1.1.2.3	Architecture of PETAL	17
1.2	<i>Laser damage challenges in high power laser facilities</i>	21
1.2.1	Fundamental of laser-induced damage	21
1.2.2	Nanosecond facilities	23
1.2.3	Pico and sub-picosecond facilities	24
1.2.3.1	Mechanisms during laser damage in short pulses regime	25
1.2.3.2	Laser damage on Petal	26
	Summary of Chapter 1	28

This chapter provides an overview of high power laser facilities that are operating or under development around the world and some of their main goals. This PhD thesis is specifically carried out in the framework of the LMJ/PETAL facilities. Therefore, a second part of this chapter presents the architecture of both LMJ and PETAL lasers in more details. The objective of high power laser facilities is to push forward the limits of laser power and energy. However, this challenge requires overcoming laser-induced damage. This issue limits laser power and plays a key role in all high power laser facilities. The physical mechanisms at the origin of laser-induced damage will be discussed in this chapter.

1.1 High power Laser facilities: Presentation of Petal & LMJ

Since its creation in the sixties [2] and with the development of the semi-conductor industry, lasers tend to become always smaller with the rise of semi-conductor laser diodes. This miniaturization has brought lasers into daily life and industry. They are widely used in telecommunications, telemetry, surgery, fabrication by laser processing, LIDAR, laser pointers, LIBS among many other applications. Still, the past few decades have seen the development of extraordinary large lasers, the size of high power laser facilities becoming comparable with the size of buildings. This development was motivated by the need to reach higher energies and higher powers (see Fig. 3). High power lasers open new fields of investigation for physicists and bring light matter interactions to high field and relativistic optics. One of the main outcomes of high power lasers is to foster thermonuclear fusion.

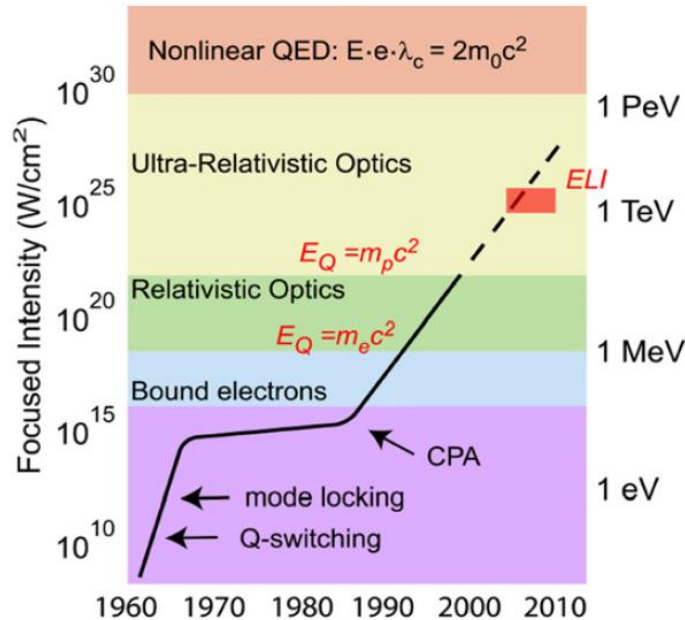


Fig. 3. Rise of focused intensities achieved by laser facilities of the last decades, taken from [3].

1.1.1 High power laser facilities or fusion class laser: purposes and architecture

High power lasers aim at yielding extraordinarily high temperatures and pressures onto a very small volume. The laser facilities will foster unprecedented electric fields in a short time and a confined space and this will open novel routes in high field physics. Although laser facilities share the same objective to achieve strong light-matter interactions, they feature different characteristics and target different applications. Among the wide variety of goals, the generation of X-rays and gamma rays, neutrons and electrons are highly needed. Some of the applications of those facilities will be more detailed in this section.

1.1.1.1 Overview of high power laser facilities

High power laser facilities are developed in different regions of the world [1, 4], see Fig. 1. Two different laser facility families can be distinguished: the nanosecond facilities (10^{-9} s) and the pico/sub-picosecond facilities (10^{-12} s and $<10^{-12}$ s). Nanosecond facilities were the first to be developed. The National Ignition Facility (NIF) is the largest mega-joule facility. Its construction started in 1997 at Lawrence Livermore National Laboratory (LLNL, USA). NIF was inaugurated in 2009 and designed to reach 1.8 MJ and 500 TW at 351 nm with 192 laser beams [5]. Another American nanosecond laser facility called OMEGA was developed at the Laboratory for Laser Energetics (LLE) at the University of Rochester (NY, USA). Construction and commissioning of OMEGA were in 1995 [6]. It hosts 60 laser beams that can focus up to 40kJ in the UV (351 nm). In France, the Megajoule Laser (LMJ) started to operate in 2014 while still being under construction. When the LMJ construction reaches completion in 2022, LMJ will host 176 laser beams and will deliver 1.4 MJ at 351 nm [7]. One can also cite the SG-IV project (SG stands for Shengguang which means Divine Light) in China, that follows the success and specification validation of the SG-III which counts 48 laser beams designed to deliver up to 200 kJ [8]. Considering the size and complexity of those facilities, an important effort was made first to design the architecture of the facility and to select the specifications of the optical components and tooling from “smaller” projects. Then those facilities were constructed and inaugurated several years later.

The pico/sub-picosecond facility family was developed later using the chirped pulse amplification (CPA) method proposed in 1985 by Donna Strickland and Gerard Mourou [9]. CPA will be presented in more detail in the following paragraph when describing the architecture of Petal. Pico/sub-picosecond lasers present a large variety of pulse-time duration, and therefore a wide variety of energies and powers, see in Fig. 4.

In the kJ-ps range, for petawatt to multi-petawatt facilities, one can cite Omega EP (Extended Performance) at LLE [10, 11] and NIF-ARC (Advances Radiographic Capability) at LLNL in the USA [5], Gekko and LFEX in Japan [12], Orion and Vulcan in the United Kingdom [4] and finally Petal in France [7, 13, 14]. In May 2015, the Petawatt Aquitaine Laser, named Petal, demonstrated to be one of the most powerful single beam in operation with a 1.15 PW shot at 850 J and 1053 nm [14]. As presented in Fig. 4, Petal aims at further increasing its power and energy from 1.15 PW and 1 kJ to

5 PW and 4 kJ. This significant increase will strongly challenge the resistance of optical components to laser damage. This issue of laser damage resistance in the context of the Petal project motivated this PhD thesis.

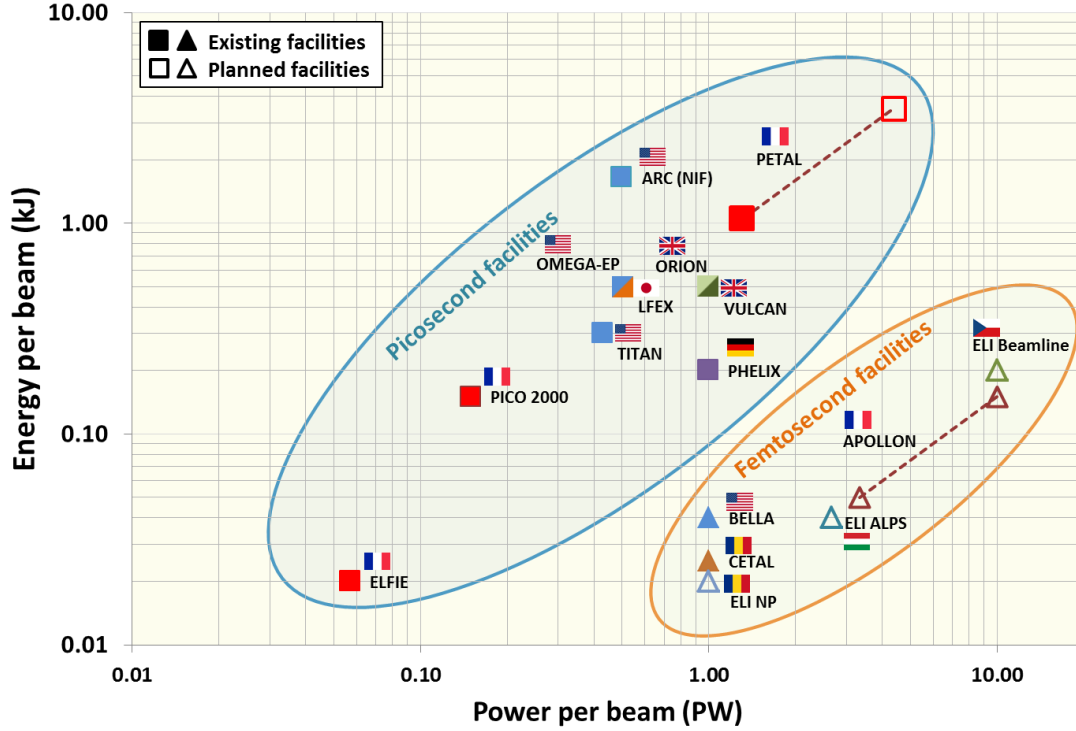


Fig. 4. Petawatt class lasers in the world: energy per beam with respect to the power per beam. Figure taken from [15]

Also installed in France, but with much shorter pulses of 15 fs, the Apollon laser [16] was inaugurated in 2015. The Apollon laser was designed to be the most powerful laser to deliver initially 5 PW pulses and then increasing this power up to 10 PW. These performances are now surpassed by the Thales laser of ELI-NP facility, which stands for Extreme Light Infrastructure - Nuclear Physics. Indeed, in March 2019, Thales reported a 10 PW laser shot [17]. ELI-NP is part of the European project ELI [3, 18]. This project consists of three laser facilities located in 3 different countries: ELI-ALPS (Attosecond Light Pulse Source) in Hungary aims at delivering ultrashort pulses from the femtosecond (10^{-15} s) to the attosecond (10^{-18} s) domains [19], ELI-Beamlines in Czech Republic will be a high-energy beam facility delivering short pulses, and finally ELI-NP (Nuclear Physics) in Romania will couple two 10 PW laser beams with a brilliant gamma source. The ELI facilities aim to be fully operational in 2020.

Many of these facilities aim to produce thermonuclear ignition for military and/or civilian applications. The Laser MégaJoule (LMJ) in France and National Ignition Facility (NIF) in the USA share that objective for both military and civilian applications.

1.1.1.2 Military applications

These two national high power laser facilities ensure nuclear deterrence. Since the opening of signature of Comprehensive Test Ban Treaty (CTBT) in September 1996, 162 countries have signed and ratified the engagement to not carry out any nuclear weapons test explosion, and to prohibit and

prevent any such nuclear explosion at any place under its jurisdiction or control [20]. To deter nuclear threats, it is necessary to assess the reliability of the stockpile of the nuclear weapons without testing them.

For that purpose, France launched an ambitious program called “Simulation” that aims to numerically model nuclear weapons. This requires additional knowledge in high energy physics and to get additional experimental data. This program combines the use of an original set of computation and experimental facilities. The computational facility located at Bruyère-Le-Châtel (32km southwest of Paris) hosts the Tera-1000-2 center. Tera-1000-2 is the most powerful computer in France and the sixteenth in the world according to the TOP500 of November 2018 [21]. The experimental facilities are the X radiography generator, Airix installed in the Epure facility, located in Salives (45km north of Dijon) [22] and the laser facility, LMJ, located in Le Barp (20km south of Bordeaux). Both facilities assess specific portion of the functioning of the nuclear weapons. LMJ allows the study of the behavior of matter in extreme conditions similar to the thermonuclear fusion happening during the final stage of the explosion of nuclear bomb.

1.1.1.3 The Civilian Applications

Civilian applications for thermonuclear ignition are the production of electricity and a better understanding of high energy physics.

By inflicting high temperature and high pressure onto a small target filled with lightweight atoms like deuterium (D) and tritium (T), they will fuse into heavier atoms such as helium and release neutrons, as shown in Eq. (1.1):



Thermonuclear fusion is associated with a creation of a neutron and a strong release of energy. This energy will lead to a huge rise of the temperature that can be used to produce electricity.

Two methods use lasers to achieve thermonuclear fusion: inertial confinement fusion (ICF) and fast ignition (FI).

Inertial Confinement Fusion [23] consists of heating and compressing a very small fuel target (smaller than a centimeter: Fig. 5) enclosing a capsule containing a mixture of deuterium and tritium (D-T) with multiple very high energy laser beams. Fig. 5 shows a schematic of a classical ICF target where the D-T capsule is inside a cylindrical gold hohlraum. The capsule is supported by a thin membrane (15-100 nm) called the tent.

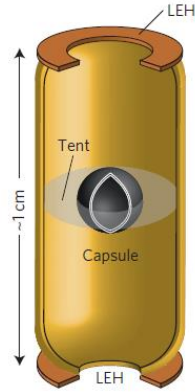


Fig. 5. Schematic of a classical ICF target. The cylindrical hohlraum encloses the ICF capsule supported by a thin (15-100 nm) membrane (the tent). Laser beams enter the hohlraum through the laser entrance holes (LEHs). Figure taken from [23]

The different laser beams are uniformly spread around the target and focused on it. They enter the target through two opposite holes (called laser entrance holes in Fig. 5: LEHs). The inner surface of the target is heated by the laser-matter interaction (Fig. 6(b1)). The strong local electric field of the laser beam accelerates the electrons of the gold capsule which produces X-rays (Fig. 6(b2)). The X-rays generated by the laser beams focused on the gold capsule will compress and heat the core of the target (Fig. 6(b3)) until the target implodes (Fig. 6(b4)). This implosion will create temperature of billions of degrees allowing the fusion of the D-T mixture. This ICF concept is being explored with nanosecond megajoule facilities.

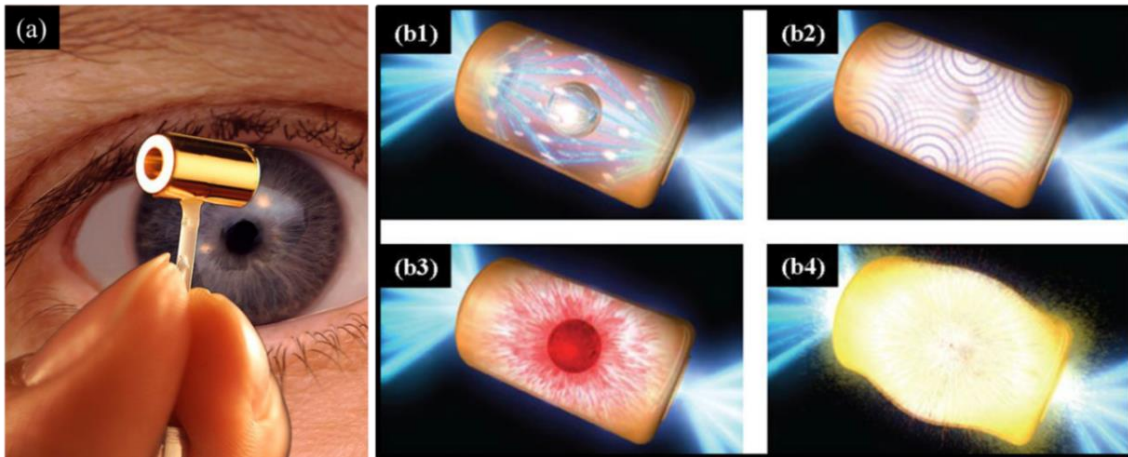


Fig. 6. **(a)** picture of a gold target-**(b1-b4)**: Illustrations of the gold target and principles of Inertial Confinement Fusion. Figures taken from [24] based on [5] resources

Fast ignition is a variant of ICF principles. The difference between the two techniques is that with the fast ignition, the compression phase is separated from the ignition phase of a D-T capsule. In other words, in this technique, the target is first compressed with a conventional high-energy laser driver (similar laser beams to the ICF technique) and then the compressed core is ignited with a short-pulse laser beam (also called shock wave) working as a “spark” [23, 25]. Fig. 7 is an example of fast-ignition target, cone-in-shell target, designed for the OMEGA/OMEGA EP facility at the Laboratory of Laser Energetics in Rochester (NY, USA). In this example of fast-ignition experiment the UV

nanosecond laser beams from OMEGA are focused onto a deuterated-plastic (CD) shell containing the D-T mixture to heat the target. Then the fast laser pulse from Omega EP is focused onto the center of the gold cone to ignite the target. Symmetry requirements with this kind of cone-in-shell target are less strict than with ICF target. This is a considerable advantage for the fast-ignition technique.

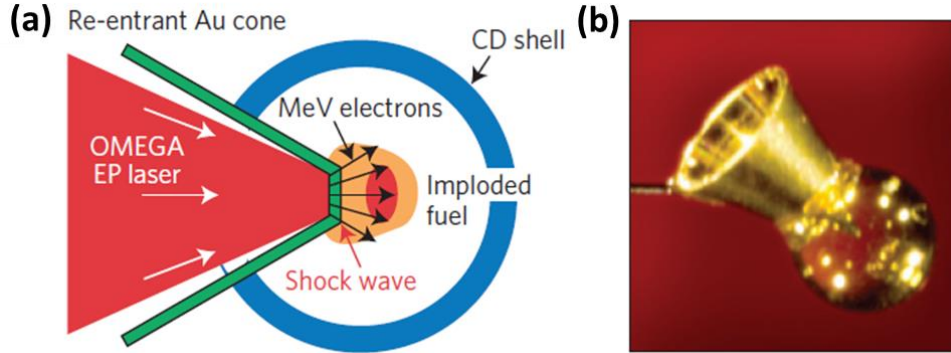


Fig. 7. OMEGA fast-ignition targets. **(a)** Schematics of the cone-in-shell electron-fast-ignition experiments on the OMEGA laser facility. **(b)** The cone-in-shell target used in integrated FI experiments on OMEGA. Figure extracted from [23] which is reproduced from [26].

Let us mention that another method of thermonuclear fusion, based on magnetic-confinement fusion [27], is currently followed for civilian applications with the construction of the ITER fusion (Cadarche, France) and Z-pinch that is operated in Sandia (USA).

Generating thermonuclear reactions is comparable to reproducing a star in a laboratory [5]. It requires very energetic and powerful lasers when considering the ICF or FI approach. For that purpose, high power laser facilities need to meet very specific requirements. Thus the architecture of the high power laser facilities is not left to chance and must follow strict specification. As this PhD thesis has been carried out in CEA Cesta in the framework of the LMJ/Petal program, the LMJ and Petal facilities will be described more precisely in the following section.

1.1.2 Architecture of Fusion Class Laser: LMJ & Petal example

1.1.2.1 Establishment of LMJ and Petal

The construction and operation of the LMJ and Petal programs is managed by CEA (French Alternative Energies and Atomic Energy Commission). They are both located in the same building to share the target chamber. Petal is a pico- to sub-picosecond facility funded by European, national and regional funds. It consists of one laser beam located in the south-east laser hall of the LMJ/Petal building.

The LMJ/Petal building is 300 m long and 100 m wide (Fig. 8). It consists of one 38 m tall experiment hall surrounded by 4 laser halls. Those laser halls contain 5 or 6 laser beamlines each for a total of 22 laser beamlines. Each LMJ laser beamline is made of 8 beams. So at the completion of LMJ construction, the LMJ/Petal building will host 176 nanosecond laser beams in the UV plus one laser short-pulse beam in the IR (Petal).

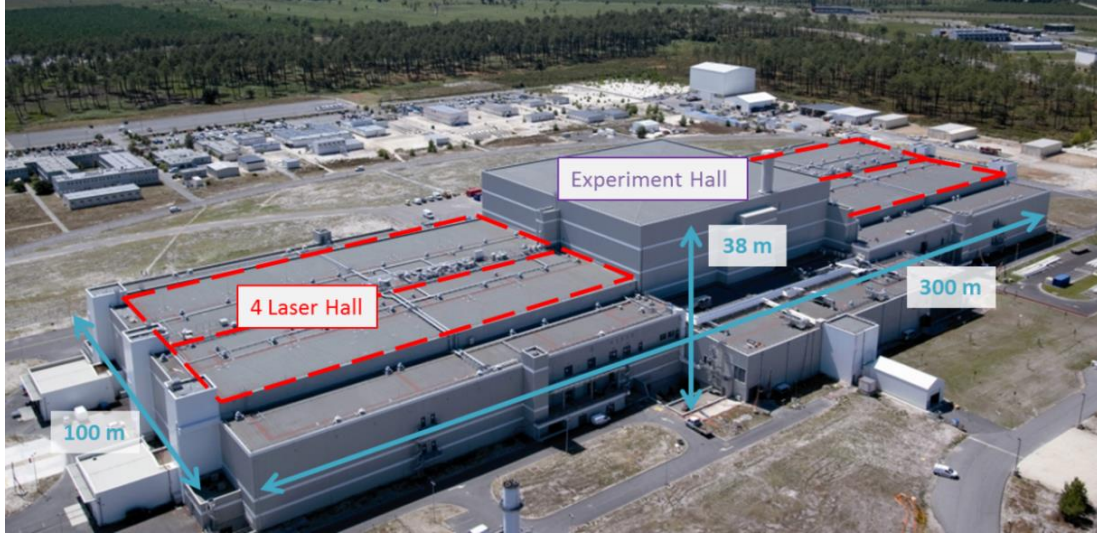


Fig. 8. Aerial view from the LMJ-PETAL building with dimensions and positions of the 4 Laser Halls and the Experiment Hall containing the target chamber

The experiment hall contains the target chamber, a 10m diameter sphere made of aluminium and concrete. Fig. 9(a) shows a picture of the outside of the chamber taken from the bottom of the experiment hall. The square metallic plates are where the fused silica windows will be placed. The 176 laser beams will enter the chamber through those windows. Four beams are passing through each opening containing 4 windows. Fig. 9(b) shows the inside of the chamber, placed under vacuum, with the three telescopic arms used to place the millimetric target at the center of the chamber where the 176 beams will be focused. One of those three telescopic arms is the target holder and the other two are only used for the alignment.

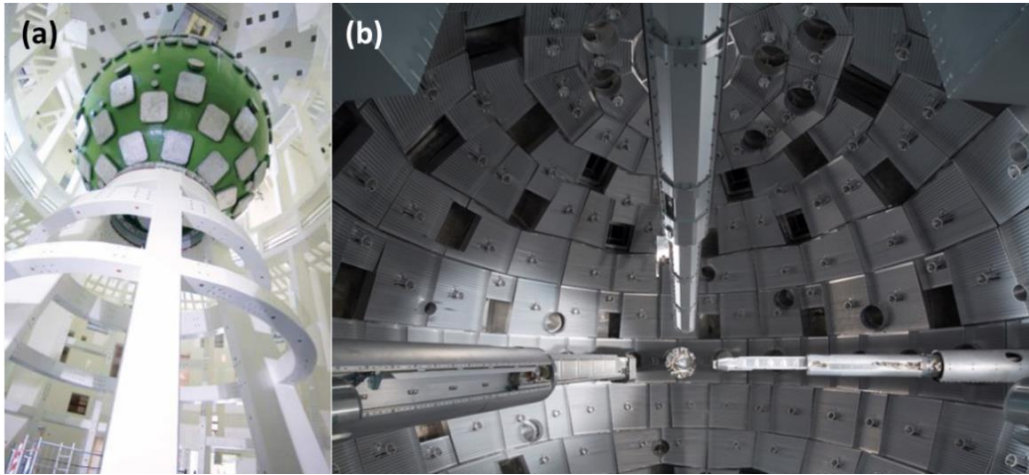


Fig. 9. Pictures of the target chamber: (a) below/outside and (b) inside.

Around the chamber and inside the experiment hall are placed a wide variety of diagnostic and measurement devices to measure and study the phenomenon occurring inside the chamber and also controlling the condition/state of the entrance windows and other optics.

Fig. 10 summarizes the end of the LMJ laser beamlines and their transport toward the target chamber. The transport of the beams is carefully calculated so the optical path of each beam is identical. The Petal beam enters the chamber at the equatorial plane of the sphere.

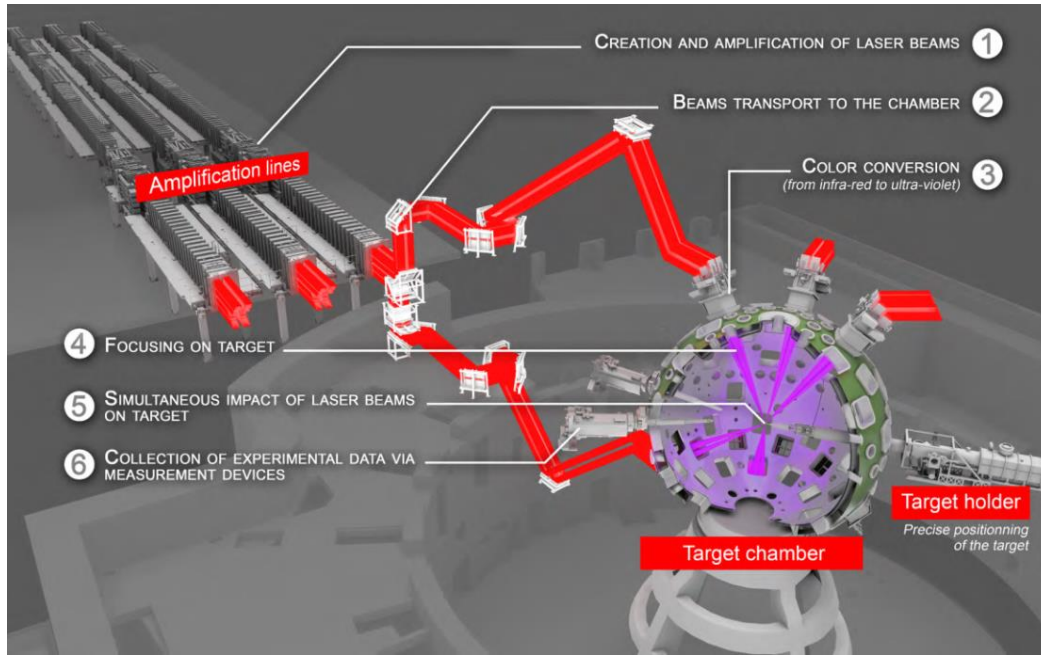


Fig. 10. Schematic of the end LMJ amplification lines and their transport toward the target chamber taken from [28]

Petal and LMJ share the same target chamber so they can be use together. Such implementation could serve to create fast ignition for example. The purpose of the Petal beam is to probe at different times the plasma created by the LMJ pulses on the target. This feature has many applications in various areas of physics, so the Petal facility is available for use by the scientific community [15]. An example of an experiment carried out with Petal is the validation of the model of the magnetic field amplification and turbulences in galaxies, which is displayed in Fig. 9.

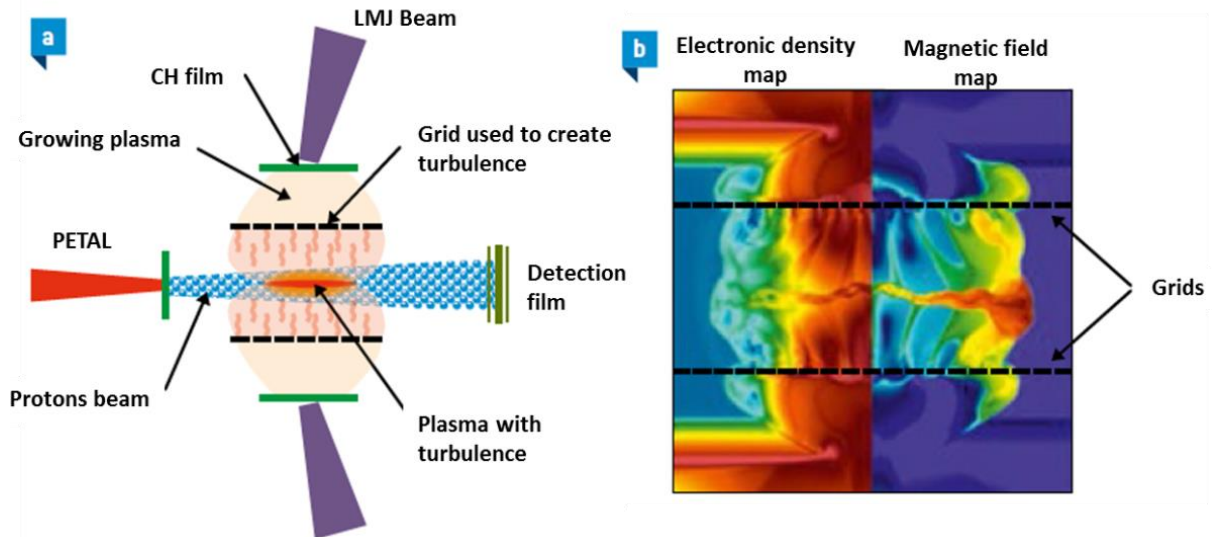


Fig. 11 Principle of the magnetic field amplification **(a)** two plasmas propagating toward one another are generated by irradiating two plastic films (CH) with LMJ beams. Two grids are placed so turbulences are generated. The magnetic field created by the collision of the two plasmas is observed by protons generated by Petal Beam **(b)** simulation of the electronic density and the associated magnetic field. Figures taken from [15]

The use of the nanosecond facilities together with pico- to sub-picosecond facilities allows for a wide variety of experiments in astrophysics, physics of the matter and/or medical sciences. For the same reasons, NIF/NIF-ARC and OMEGA/OMEGA EP shares the same building and target chamber.

The architecture of one LMJ beamline and Petal are detailed in the following subsections.

1.1.2.2 Architecture of LMJ Beam Line [29]

Fig. 12 presents the architecture of one of the 176 LMJ beams. The beamline consists of four sections (see Fig. 12):

- The front-end section
- The amplification section
- The transport, frequency conversion and focusing section
- The target chamber

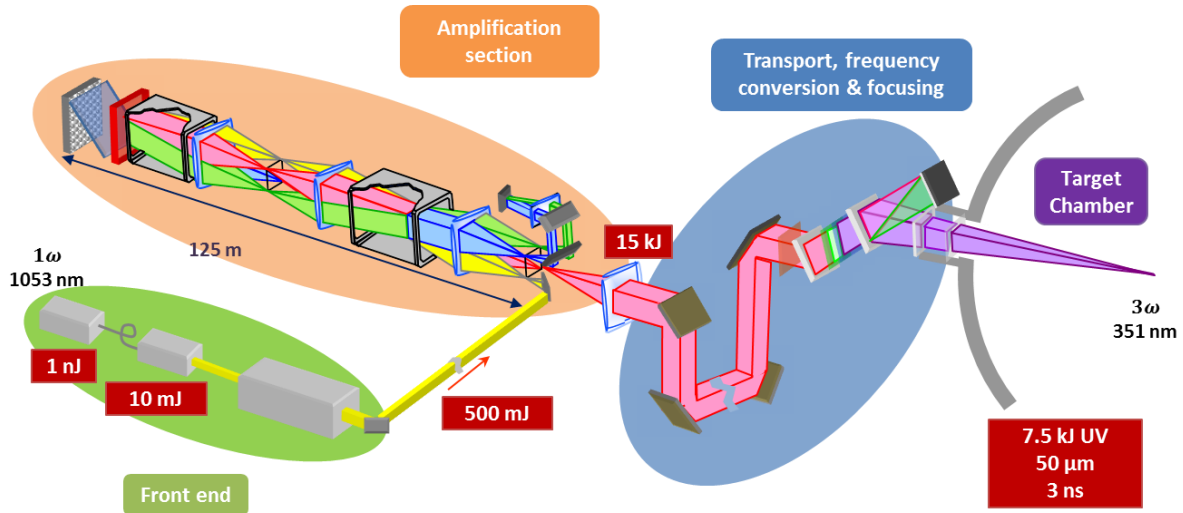


Fig. 12. Schematic of one LMJ beam with the 4 different sections of the beam line.

The 3ns laser pulse at 1053 nm is generated in the front-end by a fiber source. After its generation, the 10 mJ pulse is amplified to 500 mJ by the Pre-Amplifier Module (MPA) before being transported to the amplification stage.

When entering the amplification stage, the beam is expanded into a $400 \times 400 \text{ mm}^2$ square. This expansion allows for a larger amplification without reaching the laser-induced damage threshold (fluence, energy density¹ in J/cm²) of the optical components involved in the amplification section. The beam makes four laps in the amplification section in order to reach energy of 15 kJ. At each passing through the amplification stage, the beam travels 125 m and propagates through laser amplifier slabs. These amplifier slabs are made of phosphate glass doped with neodymium and are pumped by flash lamps. The amplification spectrum of these slabs is centered at 1053 nm. These amplifier slabs are sensitive to the humidity, so the whole amplification section is placed in dry air.

¹ The reader should note that in the manuscript all the values of fluence are given in terms of normal beam fluences, meaning that the fluence is calculated with the surface of the beam in a plane normal to the propagation axis and not the surface projected at the angle of incidence on the optical component.

In order to avoid the amplification of spontaneous emission in the amplifier slabs, an optical switch is positioned at the end of the amplification stage. This optical switch is composed of a Plasma Electrode Pockels Cell (PEPC), a polarizer and absorbers see Fig. 13. A deformable mirror is added after this optical switch to reinject the beam in the amplification stage for the 2nd or 4th passage, and thus to close the laser cavity. The fact that this mirror is deformable enables to spatially reshape the beam and to improve the wavefront of the beam in the 400x400 mm² square.

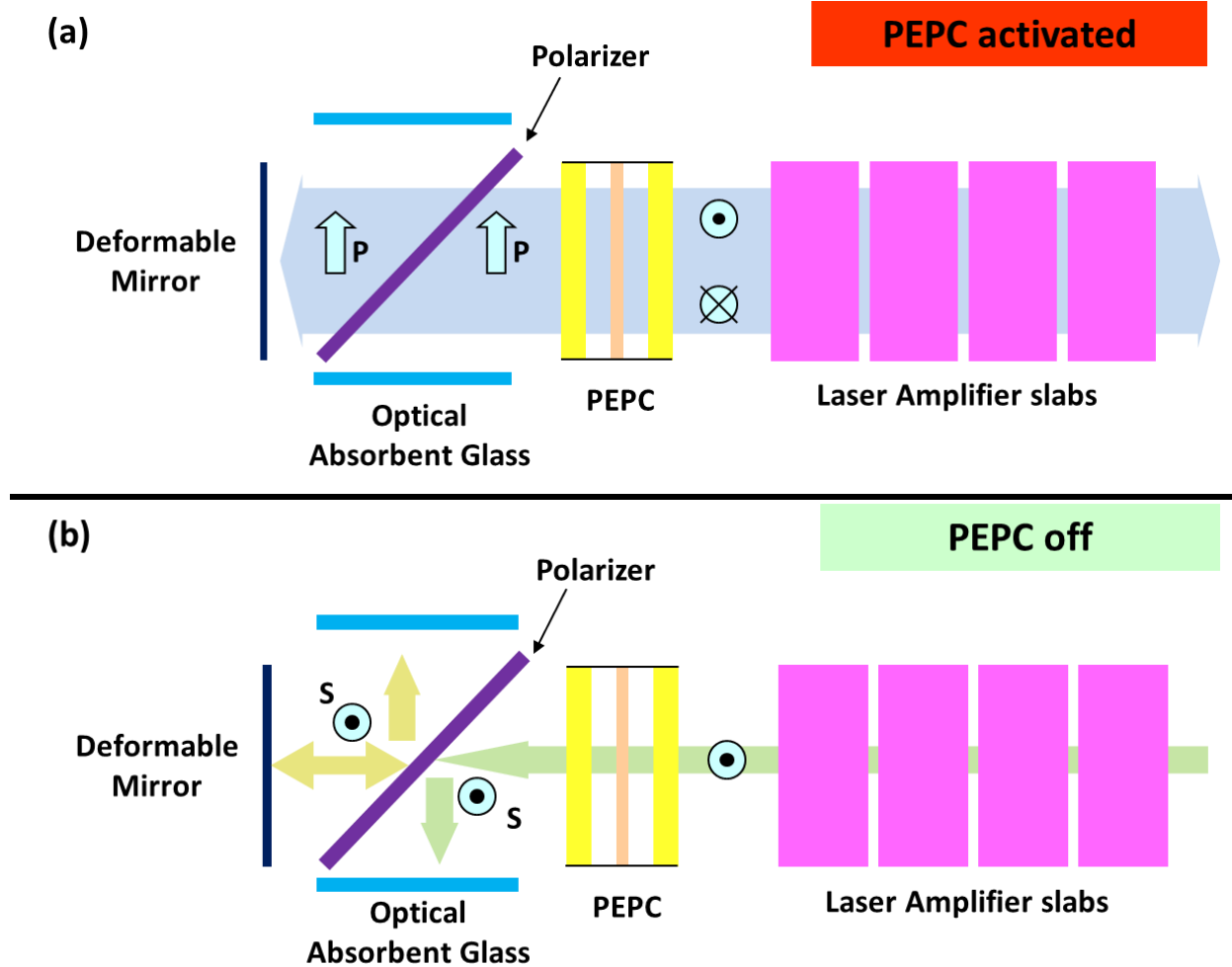


Fig. 13. Schematic of the optical switch placed at the end of the laser cavity. **(a)** PEPC is activated when the amplified laser beam is passing through the optical switch. Indeed the polarization is turned into *p*-polarization and the beam is completely transmitted through the polarizer. **(b)** In all other circumstances, the PEPC is passive. The *s*-polarized beam will be then reflected by the polarizer toward absorbent glass. Consequently, spontaneous emitted light (in other word the parasite beams) are absorbed by the optical absorbent glass.

The polarizer involved in the optical switch operates at the Brewster angle which suppresses the reflection for the *p*-polarization². This polarizer is designed to be transparent for the *p*-polarized beam and highly reflective for the *s*-polarized beam. Both the deformable mirror and polarizers are multilayer dielectric coatings. Their layers are porous because of the deposition method (which will be

² *p*-polarization corresponds to the transverse magnetic polarization (TM). *s*-polarization to the Transverse Electric (TE). These notations will be detailed in the next chapter.

presented in the next chapter). This porosity makes stress and spectral response of the multilayer coating sensitive to the environment (more details will be provided in the presentation of the fabrication method in chapter 2). As the polarizer features a narrow spectral range (see the example of transmission of the p -polarization of polarizer in Fig. 14, it is very sensitive to spectral shift which can induce transmission loss. Aging of the coating, as exposed in the example in Fig. 14, can lead to a spectral shift and a loss of transmission.

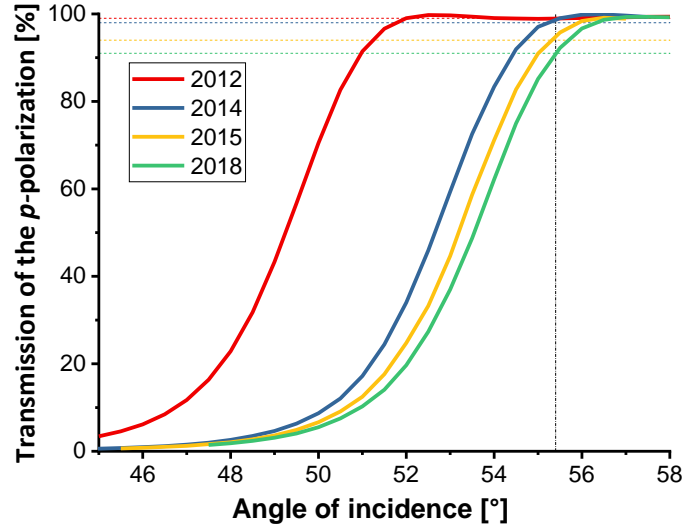


Fig. 14. Example of Spectral Shift of the p -polarization transmission of the same LMJ polarizer in 2012 (red), in 2014 (blue), in 2015 (yellow) and in 2018 (green) measured with CEA photometer Symphonia. The black dotted symbolized the classical angle of incidence of use of the polarizers. The colored dotted lines are guide for the eye to facilitate the reading of the loss of transmission through the years.

Because the beams propagate 4 times in the polarizers, even a small loss on the transmission can have dramatic consequence on the final energy arriving on the target. The optical switch is designed as follows. When the amplified beam propagates through the PEPC, the Pockels Cell is activated, Fig. 13(a). The beam polarization is changed from s to p . the amplified beam reflected on the deformable mirror and is reinjected in the amplification section. Otherwise, when the cell is off (Fig. 13(b)), the parasite beams polarization remains unchanged (s -polarization). The parasitic beams are reflected with the polarizer toward optical absorbent glass. The system is conceived to allow four paths of the main beam through the amplifier slabs. This optical switch system ensures that a parasitic beam cannot make more than one passage in the amplification section without being cut off.

After the amplification, each beam is carried along different paths to reach the target chamber at different locations. The challenge is to spread the different beams uniformly around the target chamber while preserving the same optical path. The different beams enter the experiment chamber through thick fused silica windows protected by two debris shields.

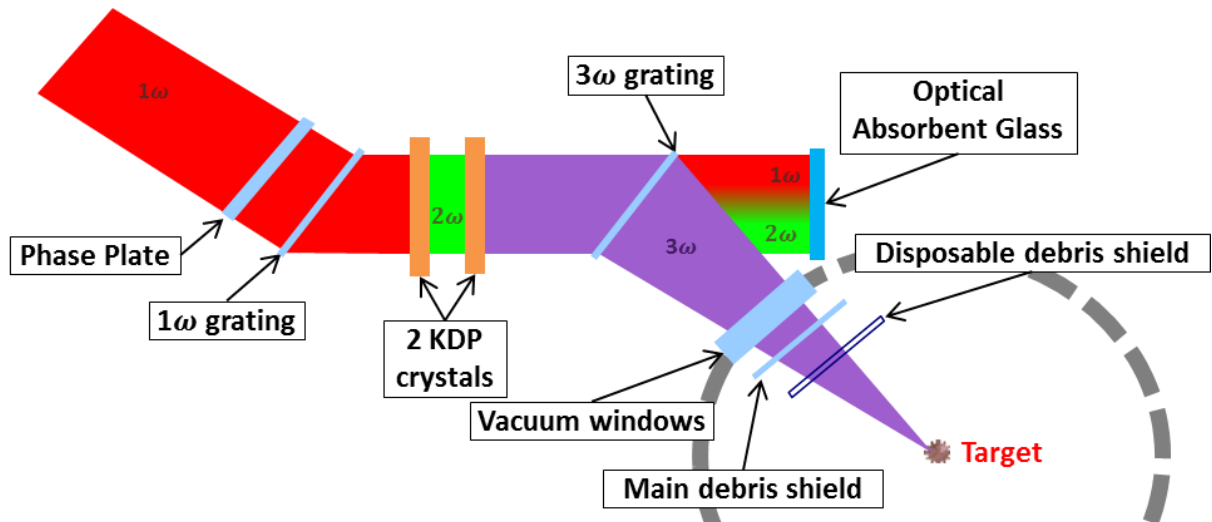


Fig. 15. Schematics of the Frequency conversion and focusing section

Frequency conversion is needed between the amplification stage and the target chamber because the wanted laser-matter interaction is more efficient with short wavelength, meaning wavelength in the UV. A diffraction grating operating at 1053 nm deviates the 1ω beam toward two KDP crystals that yield the $3\omega = 351$ nm frequency with an efficiency of 50%, see Fig. 15. The first KDP crystal doubles the frequency with an efficiency of 50%. The second KDP crystal receives half of the energy at $1\omega = 1053$ nm and this other half at $2\omega = 526.5$ nm and sums these two frequencies to get the $3\omega = 351$ nm final beam. A second diffraction grating focuses the 3ω beam toward the target and deviates the 1ω and 2ω beams toward absorbent glass located outside the target chamber. The 3ω beam is focused on the target in the center of the experiment chamber at a final energy of 7,5 kJ, see Fig. 12.

1.1.2.3 Architecture of PETAL

The architecture of the Petal beamline consists of 4 sections in addition to the experiment chamber which is shared with LMJ:

- The front end section
- The amplification section
- The compression section
- The transport and focusing
- The target chamber shared with LMJ

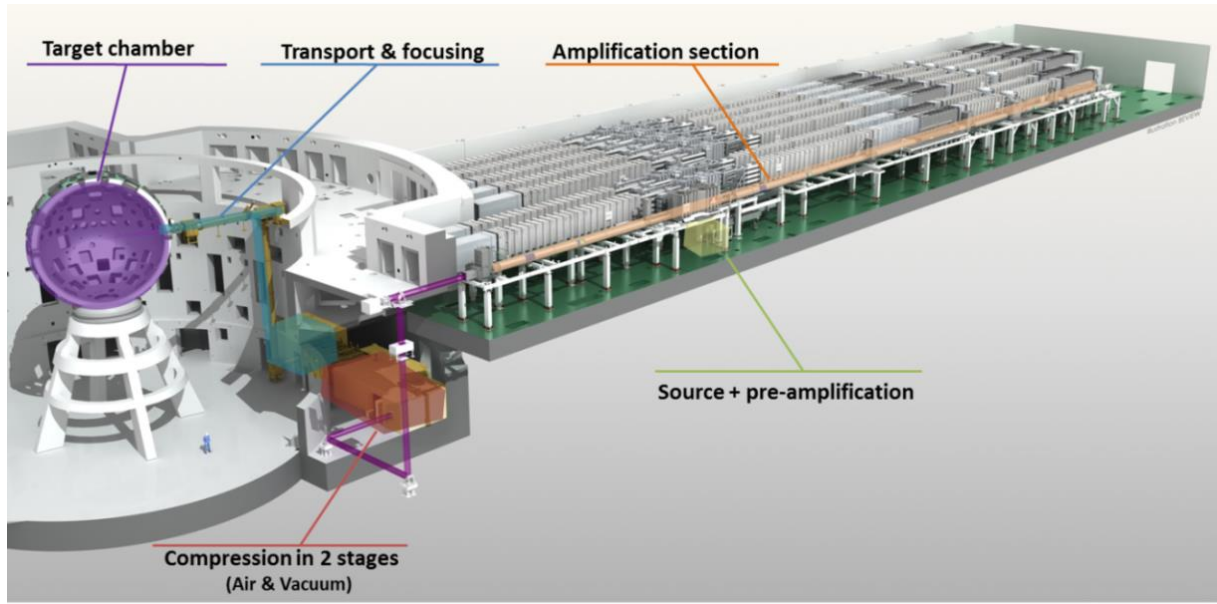


Fig. 16. Schematics of Petal inside the LMJ building. Petal laser beamline is implanted in the south-east laser hall of the LMJ building next to LMJ lines.

The major differences between one LMJ beam and the Petal beam are their time duration (3 ns for LMJ versus 500 fs for PETAL), their frequency focused on the target (351 nm for LMJ versus 1053 nm for PETAL) and pulse power. Short pulse amplification is not possible due to non-linear effects and laser-induced damage threshold reached by high power short pulses. As stated before, an outcome in the generation of high energy short-pulses was obtained in 1985 with the development of chirped pulse amplification (CPA) by Donna Strickland and Gerard Mourou [9]. CPA is possible thanks to the spectral bandwidth $\Delta\nu$ is linked to the pulse length Δt as stated by the Heisenberg inequality:

$$\Delta\nu\Delta t \geq K \quad (2)$$

where K is a constant depending on the time shape of the beam. For example, for a Gaussian beam $K=0.441$ and for a hyperbolic secant beam $K=0.315$.

CPA, presented in Fig. 17, occurs by first reducing the power of short-pulses by a stretch in the time domain. This stretch is performed by introducing a different phase shift on each spectral component of the pulse. The pulse power being strongly decreased by this stretch, it is then possible to amplify this pulse. After the amplification stage, the pulse is temporally compressed by compensating the phase shift introduced by all the optical components present in the front end and amplification sections (stretcher...).

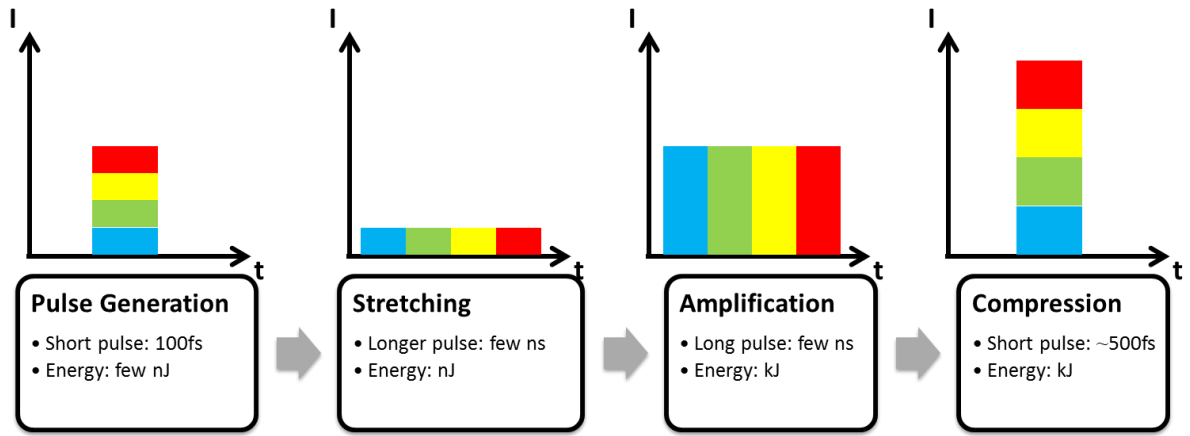


Fig. 17. Principle of chirped pulse amplification. The CPA principle is applied to Petal in order to generate high energy short pulses.

The first section of Petal is the front end where the 100 fs laser pulse is generated at 1053 nm with an energy of 3 nJ. Then this pulse is stretched by a pair of gratings to have pulse duration of 3 ns before being amplified to 100 mJ by the pre-amplifier module. Then the beam is amplified in an amplification section similar to a LMJ one with a $400 \times 400 \text{ mm}^2$ square beam.

After this amplification, the pulse is compressed in a compression section consisting of 2 stages, see Fig. 18. The first compression stage operates in ambient air and reduces the pulse duration from few nanoseconds (1,7 ns in the example shown in Fig. 18) to few hundreds of picoseconds (350 ps in the example shown in Fig. 18). The second compression stage operates in vacuum in order to avoid non-linear effects (e.g. self-focusing effects). The few-hundred picosecond pulse duration will be reduced around the picosecond or under (500 fs in the Fig. 18 example). The final pulse duration in the Petal beamline can be tuned from 0.5 to 10 ps depending on the need and requirements of the experiments.

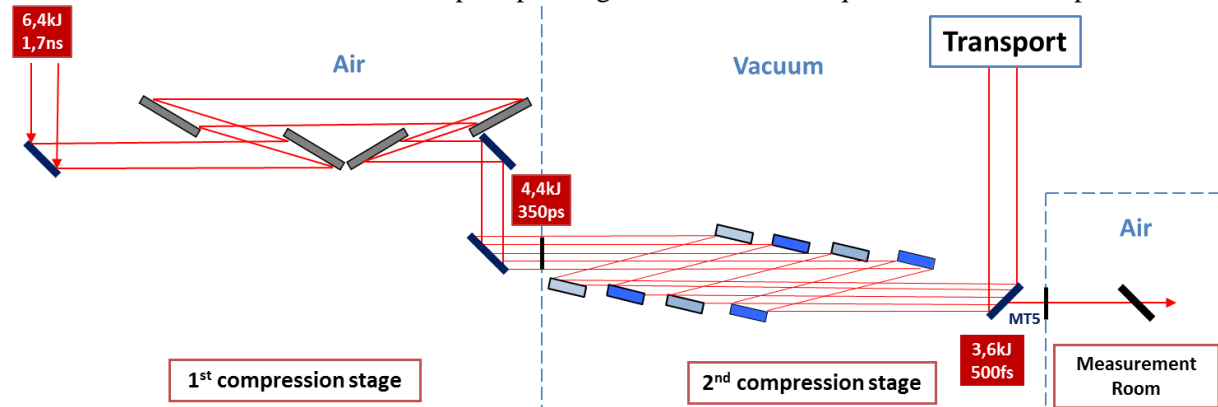


Fig. 18. Schematic of the 2 different Petal compression stages.

This second compression involves four pairs of gratings placed at 77.2° of incidence. The laser beam is divided into four sub-apertures that are recombined in one beam on the leaky mirrors MT5, see Fig. 18. The use of a single pair of gratings would require very large gratings, approximatively 1.80 m wide, while gratings used in this compression stage including the four sub-apertures are 450 mm wide and 420 mm high. These gratings are made of dielectric multilayers deposited on 43 mm thick substrates with the periodic pattern etched onto the outer layer.



Fig. 19. Picture of three out of four full size multilayers diffraction gratings facing their paired gratings implemented in the final (vacuum) compression stage

The leaky mirror, MT5, transmits part of the beam (at 0° incidence and 1050 nm) toward the measurement room where the laser is characterized; pulse duration, contrast measurement, energy, spatial profile and beam phasing are all analyzed. The rest of the beam is reflected toward the transport section. The specific spectral response featured by the MT5 mirror makes it more sensitive to possible spectral shift (environment or aging effect) and requires a specific design of the multilayered mirror

The transport is composed of 6 multilayer dielectric mirrors that reflect and focus the beam to the target chamber. This transport is also performed in vacuum to avoid non-linear effects. Fig. 20 shows a 3D schematic of the transport with in the insets the representation, placement and identification of the mirrors involved in the transport. The polarization of the beam is well-defined but the plane of incidence on each mirror depends on the orientation of the mirror with respect to the beam propagation. Therefore, each mirror can operate under a specific *s* or *p* incident polarization. On the left inset is the aforementioned MT5 mirror illuminated with an *s*-polarized beam and the MT6 mirror placed perpendicular to MT5 and illuminated with a *p*-polarized beam. Those two mirrors allow the beam to exit the compression vessel and direct it up toward the target chamber. When the beam reaches the height of the equatorial plane of the target chamber, it is redirected toward the target chamber with a set of three mirrors, the MT7 used in *s*-polarization, MT8 used in *s*-polarization, and MT9 used in *p*-polarization, see left bottom inset. The laser beam is finally focused with a parabola and reflected with the MT10 final mirror (see inset in Fig. 17). The parabola and mirrors MT5 to MT10 are multilayered dielectric mirrors to minimize their absorption and to maximize their reflection³. They are 610 mm wide, 430 mm long and 80 mm thick and require high reflection at 45° and 1053 nm. The parabola is distinguishable from the other mirrors because of its concave fused silica substrate. The rest of the mirrors are deposited on BK7 planar substrates. In addition to this specification, MT5 requires a specific transmission at 0° incidence and 1050 nm for the measurements.

³ Multilayer dielectrics theory, advantages and disadvantages will be presented in detail in the next chapter

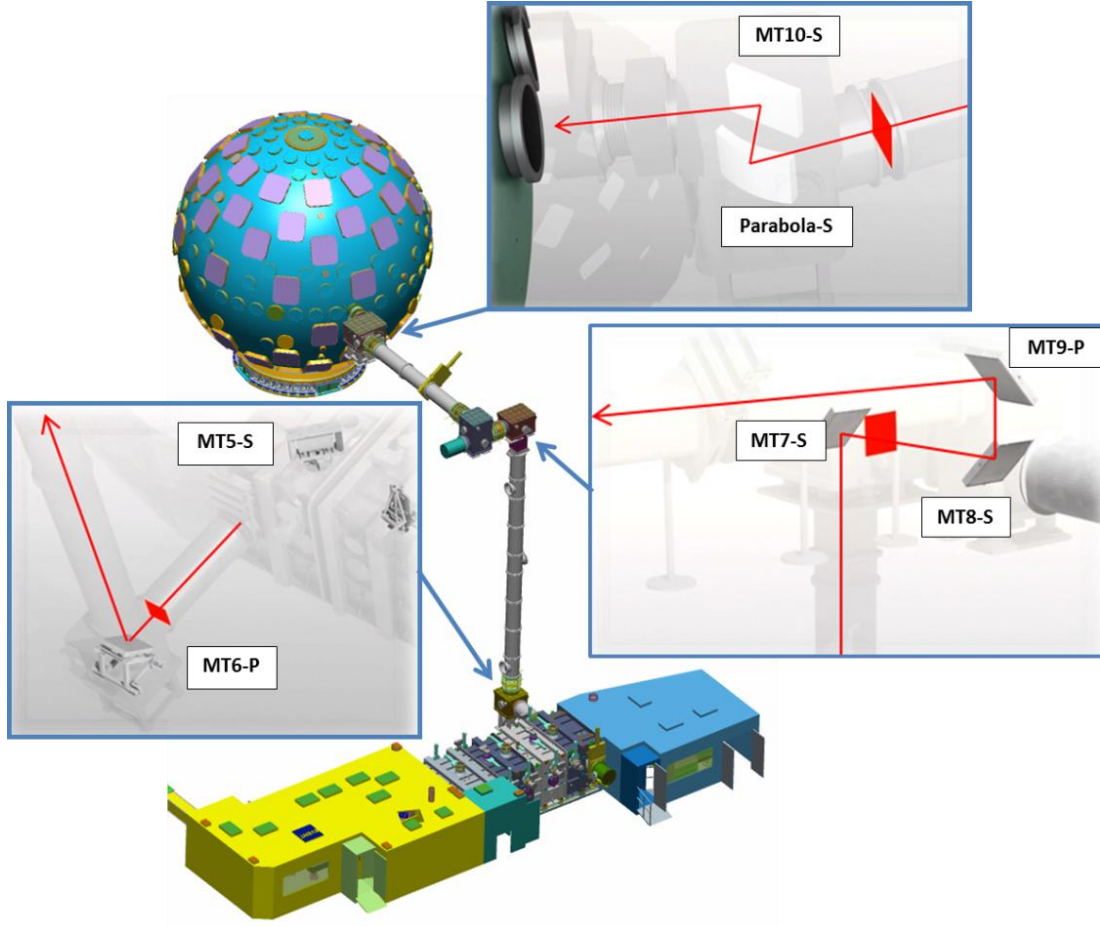


Fig. 20. 3D schematics of the compression vessel, the transport section and target chamber with in the insets the location, identification and polarization of use of the transport mirrors and focusing parabola

All these mirrors, placed after the final compression stage, are exposed to the highest laser peak power of the Petal facility. Their resistance to laser damage limits the overall power of Petal. Improving the laser damage resistance of the final components is a crucial challenge. This challenge will be more widely exposed in the next section.

1.2 Laser damage challenges in high power laser facilities

In the previous section, high power laser facilities were presented and it was shown that they include a wide variety and number of optical components. The main challenge of those laser facilities is to reach high energy and/or power. For that purpose, the optical components need to have high laser-induced damage threshold (LIDT).

1.2.1 Fundamental of laser-induced damage

Laser-induced damage (LID) is defined by the ISO 21254-1 standard [30] as any irreversible modification on the surface or in the volume of a material that can be observed with a DIC (Differential Interference Contrast also called Nomarski) microscope. Fig. 21 is an illustration of the observation with a Nomarski microscope. The three pictures are taken on the same hafnia monolayer deposited onto a fused silica substrate with the same objective and same scale. This figure is just presented here as an illustration of laser damage. Further description of the morphologies of the

damage will be exposed in chapter 2 in the state of the art of laser damage of thin films in the sub-ps regime and later in chapters 4 and 6.

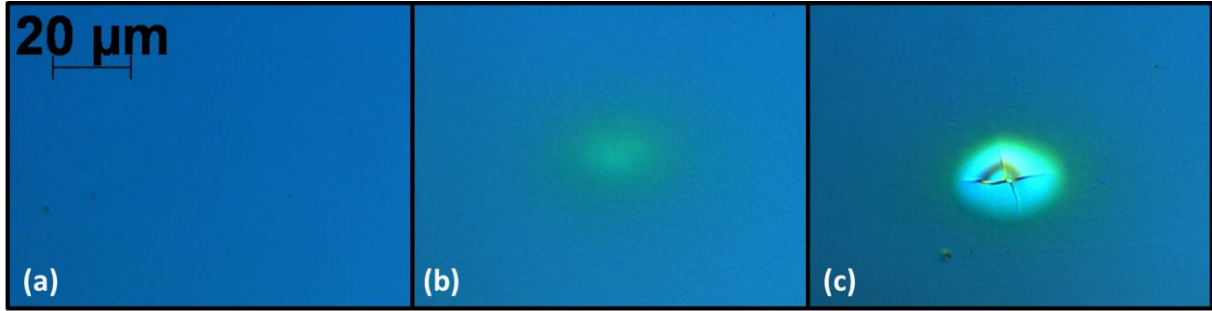


Fig. 21. Pictures of Nomarski observations of (a) an undamaged area and (b) and (c) two damage sites on the same sample, a hafnia single layer. The (b) picture shows a discoloration and in the (c) picture the monolayer is cracked. The microscope objective used for those pictures and their scale are identical for the three images. Wavelength of the laser damage test $\lambda=1053$ nm and pulse time duration $\Delta t=800$ fs.

The first studies of the laser-induced damage quickly followed the invention of laser in 1960 [2]. Indeed, the first laser damage symposium was held in 1968 [31]. This is due to the fact that the laser cavities were made of absorbing metallic layers that damaged after short time of utilization [32, 33]. This laser damage limitation pushed the thin-film industry to develop and manufacture multilayer dielectric coatings (this will be presented in the next chapter). Laser damage was first studied for continuous wave (CW) lasers and then nanosecond pulse lasers. The study of laser damage in shorter pulses arrived later with the development of CPA. Improvements in manufacturing of the components or in the LID characterization made in the nanosecond regime were directly transferred to the sub-picosecond regime. For that reason, even if the present study is focused on sub-ps laser-induced damage, it is interesting to present shortly laser-induced damage in nanosecond. This is, for example, in the nanosecond context that all the characterization procedures were developed.

The first way considered to manage LIDT problems is to reduce the fluence by simply expanding the laser beam. This approach is at the origin of the impressive size of those laser facilities. But as this approach has its limits in terms of size and cost, it is important to understand the physical process of the LIDT to develop accurate characterization of the damage and to develop novel optical materials and manufacturing process that will maximize the laser damage resistance [32].

The laser damage threshold can be characterized with a 1-on-1 procedure and/or procedure like the R-on-1 and N-on-1 based on the 1-on-1 procedure. The 1-on-1 procedure is detailed in [34] and the ISO 21254-1 norm [30]. They characterize the threshold on small areas of samples or optical components. This determined threshold results from laser damage initiated because of the intrinsic properties of the materials (fusion temperature, young modulus, electronical properties...).

On the high power laser facilities the laser damage threshold of optics will be lower than the one characterized with the previously cited techniques, because these meter scale optics contains defects that are missed on small areas tested by the 1-on-1 procedure. To consider this *defect-induced laser* damage [35] the rasterscan procedure is to be preferred. *Rasterscan* procedure consists in scanning wide areas of the optical components with a laser at a specific fluence. These values will be linked to

the defect density. There are many kinds of defects with different origins: polishing scratch and digs, cracks in the materials, nodules in a coating materials and so on... The presence of these defects creates intensification of light. This intensification leads to laser damage at the defect location or/and further on propagation. This latter effect is called the *fratricidal effect*. The fratricidal effect can happen either on the other face of the optical component or on downstream optical components.

Two aspects of laser-induced damage are to be distinguished: the laser-induced damage initiation and the growth. Once damage is initiated further illumination of this damage site (comparable to a defect) will make it grow in size.

The following section will give a quick overview of laser damage on high power laser facilities and describe the main mechanisms causing laser-induced damage initiation in the specific context of our study, where the laser shots are spaced with enough time that all the components of the laser beamline can completely cool down between two consecutive shots. Then we can restrict ourselves to single shot laser damage phenomena and not consider the influence of a repetition frequency.

1.2.2 Nanosecond facilities

Laser pulses are defined as *long* pulses when the time duration is longer than the relaxation time of the irradiated material, or in other words, when the time duration is longer than the time required for the energy to be released from the excited electrons toward the lattice of the material. In this case, the laser damage is linked with thermal effects and/or shock waves. The material absorbs light through free electrons excited by the first photons. These electrons relax *via* electrons-phonon relaxation and their energy is released to the material lattice while still being irradiated by the laser pulse. A thermal equilibrium is rapidly reached. If the excitation is sufficient, the irradiated area of the material will be heated until reaching a critical temperature (fusion or sublimation temperature). Damage is then a consequence of the melting or vaporization of the material. The energy is spread outside the focal point by the thermal diffusion in the material.

Thus the intrinsic properties driving the laser damage are the absorption and the melting temperature of the material. For dielectric materials, the absorption is low (especially true in the IR) and the fusion temperature is high (approx. 1400°C for silica). So in that case, for long pulses, the material LIDT is very high. The laser damage for the nanosecond regime is mostly driven by the defects. The defects can be nanometer scaled particles or structural defects. These defects can either be absorbers that can induce thermal phenomenon (melting, evaporation) and/or mechanical failure or they can lead to local light intensification that will generate damage further in the material. More details on the thermal and mechanical phenomena driving the Defect-induced damage can be found in [35].

Laser-induced damage in nanosecond regime relies on non-deterministic phenomenon (presence of defects) and thus requires statistical analysis to determine the LIDT. LIDT determination procedures such as 1-on-1 (developed in the nanosecond pulse duration context) include this kind of analysis.

LIDT for LMJ and other nanosecond facilities components is mostly limited by the density of defects. Then the challenges on manufacturing those optical components is to improve the fabrication,

polishing, cleaning processes of the fused silica in order to reduce the number and size of the scratches [24]. These problems are especially important on the entrance windows of the target chamber that receive the highest fluence in UV of the laser beamline. The material of these windows must be completely non-absorbent for those wavelengths (that is why they are in fused silica) and have a number of defects as low as possible. Other challenges reside on the coating to reduce the number and size of the defects in the Anti-Reflective single layer coatings, to evaluate their impacts toward fratricidal effect [36] and also the effect of the contamination in and on these coatings. For multilayer coatings the presence of nodules in the layer limits their laser-induced damage threshold. It has been shown that using reactive deposition reduces their number and adding a thick silica overcoat⁴ reduces the occurrence of damage without changing the spectral requirement (absentee layer presented in the next chapter).

1.2.3 Pico and sub-picosecond facilities

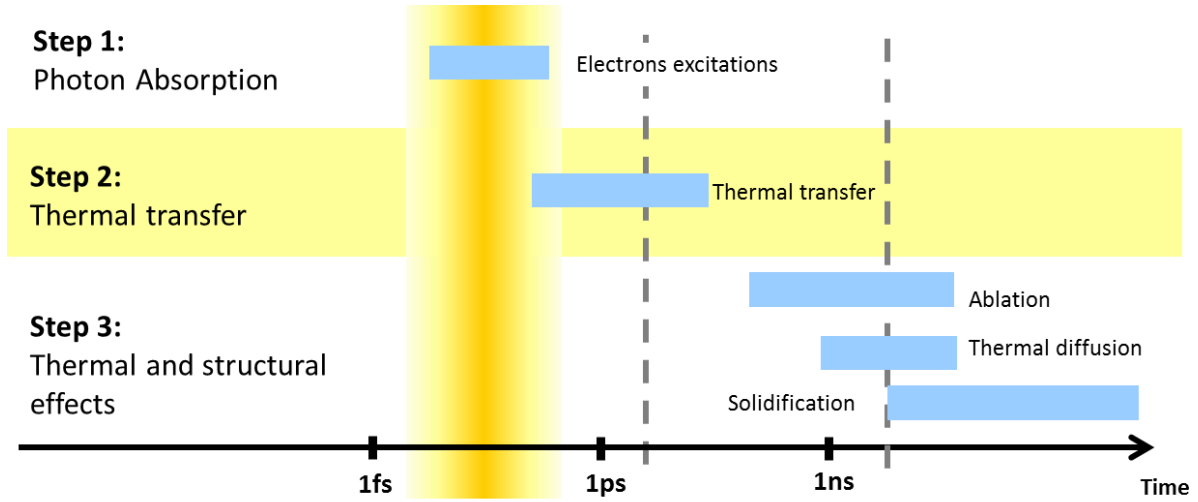


Fig. 22. Different steps occurring during the laser damage process with respect to time.

The *short* pulse laser-matter interaction regime corresponds to conditions when the heat conduction time exceed significantly the pulse duration [37]; see Fig. 22. For dielectrics this duration is of the order of the picosecond or even shorter.

In this case of short pulse duration, the laser damage results from the formation of a plasma due to the excitation of electrons whose mechanism is detailed in the following sub-section. The laser-induced damage threshold of optical components is mostly driven by the material limitation and marginally from the presence of defects [38].

For those short pulse ranges, a linear scaling between the laser-induced damage threshold and the *Electric Field Intensity* (EFI) enhancement has been widely reported [39, 38, 40], allowing establishing a model that can predict the LIDT of optical components [38, 41, 42]. This model allows calculating the measured LIDT as the product between some intrinsic properties of the materials,

⁴ This overcoat layer is often referred as a 2L layer. The terminology of L and H will be presented in the next chapter.

named hereafter *intrinsic or internal LIDT*⁵ and noted $LIDT_{int}$, and the maximum of the electric field intensity⁶, noted EFI_{max} . To a first approximation, the damage threshold of the tested optical component ($LIDT_{meas}$) is determined by the damage threshold of each material within the coating ($LIDT_{int}$) normalized by the peak electric-field enhancement (EFI_{max}): $LIDT_{int} = LIDT_{meas} \times EFI_{max}$.

What is now designated as the intrinsic LIDT is varying with the pulse duration [43]. At damage-threshold conditions, the material volume exposed to a narrow range of peak electric-field intensities (that can support plasma formation) is superheated. The generated pressure in this volume must also be sufficient to support shear fracture and detachment of the overlying layer in the case of multilayer [40].

This dependence of the LIDT on intrinsic electronic parameters and the electric field intensity makes the laser-induced damage in short pulse a deterministic phenomenon. Therefore the LIDT determination procedure developed in the nanosecond context based on statistical analysis can be adapted and simplified in the sub-ps regime.

1.2.3.1 Mechanisms during laser damage in short pulses regime

Damage initiation with short pulses is associated with the formation of a plasma in the form of a sufficient electron density in the conduction band⁷ to facilitate superheating of the affected volume. Assuming a crystalline material, this excitation would result from nonlinear electron excitation between the ground state and the conduction band.

The electron excitation from the ground state to the conduction band, a phenomenon called photoelectric effect, requires the absorption by the electron of photons with total energy higher than the bandgap energy. The linear excitation will correspond to the absorption of a single photon with very high energy for dielectric materials⁸. In our context, with pulse excitation in the near IR (Petal wavelength is 1053 nm), the electron excitation will result from non-linear excitations (Fig. 23). These can be either due to multiphoton ionization (MPI) or tunnel ionization (TI). The probability for a phenomenon to occur can be calculated from the Keldysh model [44]. The multiphoton ionization results from the absorption of a few photons by one single electron. The cumulative energy of these photons is higher than the gap energy. The tunnel ionization is when a high electric field transiently lowers the Coulomb barrier that links an electron to the atom allowing the electron to have a high enough probability to tunnel through the barrier. Once the electrons are in the conduction band, they can still absorb photons, bringing them to higher energy states. This absorption can lead to other nonlinear excitations resulting from the electron-to-electron relaxation: impact ionization and then avalanche effect. Once an electron from the conduction band has absorbed enough energy (Keldysh criteria), the impact ionization phenomenon is possible. This additional energy is released and

⁵ In the present document, only the terminology *intrinsic LIDT* will be used.

⁶ The electric field intensity is the square norm of the electric field normalized by the incident intensity. It is expressed as follows: $\frac{|E|^2}{|E_0|^2}$. The calculation of the EFI in the case of multilayer will be detailed in chapter 2.

⁷ More detailed on the solid state representation of dielectric will be given in the following chapter with the definition of dielectric material.

⁸ The order of magnitude of that photon for dielectric material will be discussed in the chapter 2.

reabsorbed by a valence electron. Both electrons are at the bottom of the conduction band. The repetition of this impact ionization leads to the avalanche effect. All these electron excitation processes are described the following sketch in Fig. 23.

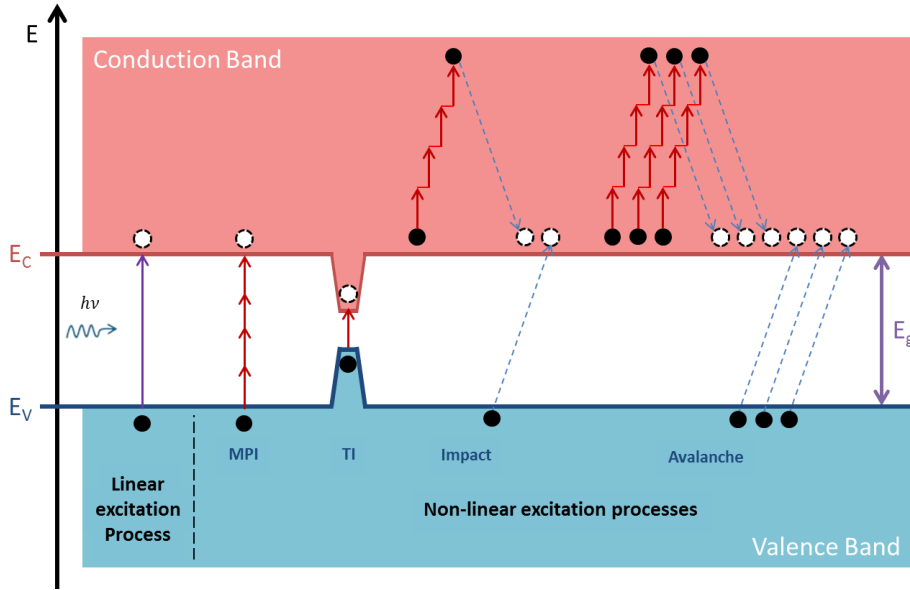


Fig. 23. Representation of the different electron excitation and relaxation processes in dielectric materials at thermal equilibrium

The probability of a given phenomenon to occur depends on the laser intensity and pulse duration. This representation points out a way to increase the LIDT by choosing materials with higher bandgap energies. A model that establishes a linear relationship between the bandgap energy and the intrinsic LIDT, the measured LIDT normalized by the Electric Field Intensity, has been proposed and exploited in refs [43, 45, 42, 46]. This model has been established in the context of multilayered thin films and will then be more detailed in chapter 2. Moreover, in chapter 5, we will discuss the validity of these models and search for other description of the intrinsic LIDT.

1.2.3.2 Laser damage on Petal

In the previous section was given an overview of the mechanism causing laser damage in the case of short pulse regime. In practice, on Petal, the most vulnerable optical components are the ones placed at the end of the beamline, after the pulse compression because they are exposed to the highest peak intensity. Those components are the transport mirrors presented in section 1.1.2.3 and displayed in Fig. 22. The LIDT of these transport mirrors is currently the limiting factor of the overall power of Petal [14]. Fig. 24 is a picture of a damaged Petal transport mirror. In this picture, one can observe four whitish rectangular areas. Those areas correspond to each sub-aperture generated by a pair of gratings. The damaged areas are discolorations, small pits or delamination of the coatings.

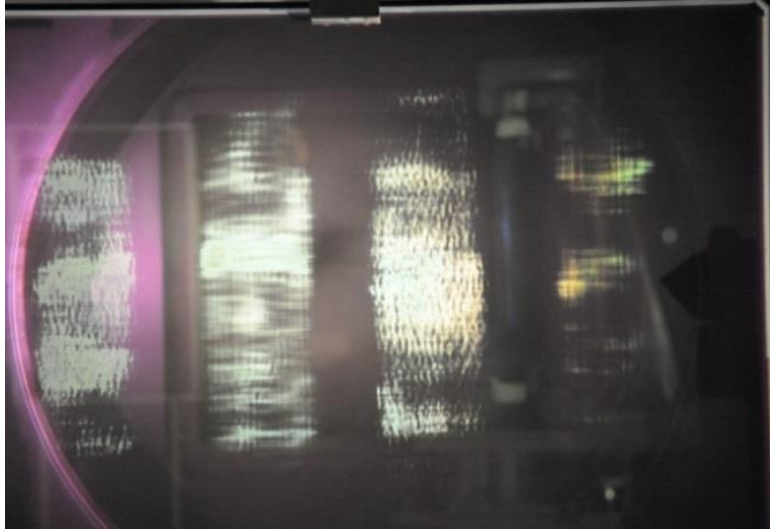


Fig. 24. Picture of a damaged Petal transport mirror

Increasing the LIDT of these mirrors is the main goal of the present work. To this end, we first need to know how the mirrors are designed and manufactured (chapter 2), then how the LIDT in short pulses on multilayer dielectric is modeled and can be improved (chapter 2 and 3) and finally how one can characterize the materials LIDT (chapter 4 and 5) and apply our optimization method (chapter 6).

Summary of Chapter 1

In this chapter we presented the general context in which present work takes place, by first giving an overview of the high power lasers facilities around the world and presenting the main objective of such incredible laser facilities.

This present PhD is undertaken at CEA Cesta (20km south of Bordeaux in France) where are implanted LMJ/Petal facilities which are important actors in this general context. The architecture of both facilities was presented with emphasis on the critical multilayer dielectric components involved. More generally, Laser-induced damage threshold is an important issue to overcome in order for high power facilities reaching higher power. Laser damage is caused by different physics phenomenon depending on the pulse duration. For short pulses, laser damage is the result from the formation of a plasma due to the excitation of electrons.

In the future, Petal aims at increasing its energy and power performances. The current critical components are the transport mirrors placed after the compression stage; they receive the highest fluence (density of energy). The motivation of this PhD work is thus to increase the LIDT of these multilayer dielectrics (MLD) mirrors. In the following chapter, we will present how the principles of MLD together with the models of laser-induced damage threshold in short pulse and their fabrication methods.

Chapter 2 Multilayer Dielectric coatings

2.1	<i>Principle of MLD coatings</i>	30
2.1.1	Dielectrics	30
2.1.1.1	Definition.....	30
2.1.1.2	Light propagation in dielectric media	32
2.1.1.3	Interface	33
2.1.2	Single layer example	34
2.1.2.1	Anti-Reflective layer	36
2.1.2.2	Absentee layer	36
2.1.3	Multilayer.....	36
2.1.3.1	Electric field calculation: matrix formalism	37
2.1.3.2	Bragg mirrors.....	40
2.2	<i>Laser damage and MLD</i>	41
2.2.1	Short pulse LIDT on MLD.....	41
2.2.2	Survey of the models	42
2.3	<i>Fabrication of multilayer dielectric component</i>	46
2.3.1	Survey of thin film manufacturing	46
2.3.2	Deposition Methods	47
2.3.2.1	Electron-beam evaporation (E-beam): without assistance.....	48
2.3.2.2	Ion Assisted Deposition (IAD).....	49
2.3.2.3	Plasma Ion Assisted Deposition (PIAD)	50
2.3.2.4	Ion Beam Sputtering (IBS)	50
2.3.3	Manufacturing Petal transport mirror	51
2.3.3.1	Specifications	51
2.3.3.2	Material, deposition method and design	52
	Summary of Chapter 2	54

This Chapter presents the principles of multilayer dielectric by first introducing the definitions of a dielectric and light propagation in such medium. The conception of multilayer is based on interference. To present this concept we present how to engineer an anti-reflective and neutral spectral response with a single layer. Adding layers allows designing more complex spectral responses such as mirrors. Multilayer dielectric mirrors are of interest for high power laser facilities because they ensure high reflectivity and low absorption. We saw in the first chapter that laser damage in short pulse is linked with electron excitation process. We will present the matrix formalism used to calculate their electric field enhancement in the structure. We will detail the model describing laser-induced damage threshold on multilayer in the sub-picosecond regime. To finish we will present how those mirrors can be manufactured and the technical solution currently used for Petal transport mirrors.

2.1 Principle of MLD coatings

Let us start by the definition of a dielectric and the equations that ruled the light propagation in such a medium.

2.1.1 Dielectrics

2.1.1.1 Definition

The material equations can describe its properties especially in electromagnetics. If the material is homogenous and isotropic these equations can be simplified and written as follow¹:

$$\mathbf{D} = \epsilon \mathbf{E} \quad (2.1)$$

$$\mathbf{B} = \mu \mathbf{H} \quad (2.2)$$

And finally, the Ohm's law $\mathbf{j} = \sigma \mathbf{E} \quad (2.3)$

Where:

- \mathbf{D} is the *electric displacement*
- $\epsilon = \epsilon_0 \epsilon_r$ is the *dielectric permittivity*
- \mathbf{E} is the *electric field vector*
- \mathbf{B} is the *magnetic induction*
- $\mu = \mu_0 \mu_r$ is the *magnetic permeability*
- \mathbf{H} is the *magnetic field vector*
- \mathbf{j} is the *electric current density*
- σ is the *conductivity* of the medium

A *dielectric* material, also called *insulator*, is defined by a conductivity σ equal to zero and does not contain isolated charges ($\rho=0$). On the opposite a material with its conductivity different from zero is a *conductor*. There is a third class of material, called *semi-conductor*, for which the conductivity increases with temperature. The electric conductivity results from the movement of electrons between

¹ The quantities marked in bold are vectors.

their energy bands, more precisely the movement between the valence band toward the conduction band.

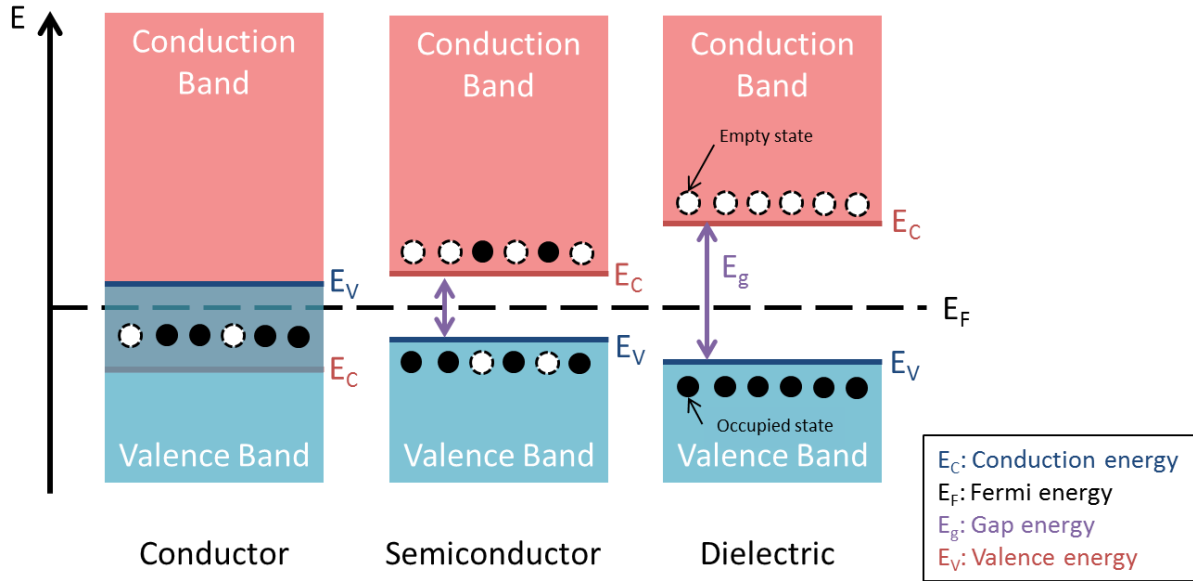


Fig. 25. Schematic of the conduction, gap and valence band of conductors, semiconductors and dielectric at thermal equilibrium

Conductors have their valence and conduction bands overlapping. In this overlap are found the occupied (electrons) and empty (holes) states. On the opposite the semiconductors and dielectric have an energy gap between these two bands. This energy separation (or difference $E_C - E_V$) is called the **gap energy** E_g . This gap energy, also called **bandgap**, is a characteristic of a material. Semiconductor bandgaps are small $E_g < 100k_B T$ (with k_B the **Boltzmann's constant** $\sim 8.617 \times 10^{-5} \text{ eV} \cdot \text{K}^{-1}$ and T the temperature in Kelvin, approximately below 2.5 eV at room temperature). In certain conditions (absorption of a photon², for example), electrons can easily travel from the valence band to the conduction band. The fact that the conduction band is partially filled and the valence band is partially empty makes this transfer possible. This is different for dielectrics, the gap energy is higher $E_g > 200k_B T$ (approximately 5 eV at room temperature). A 5 eV gap energy corresponds to the energy of a photon at $\sim 248 \text{ nm}$: the wavelength of a photon needs to be shorter than 248 nm, deeper in the UV, for this photon to be absorbed alone by a valence electron and excite this electron from the valence band into the conduction band.

Moreover in the case of dielectrics the valence band is completely filled with bound electrons. The absence of electron in the upper band (the conduction band) results in a positive real part of the dielectric permittivity. The **Fermi level** $f(E)$ is the probability for a state to be occupied by electrons. This probability varies with the temperature, but when the temperature is 0 K at the thermodynamic equilibrium, it can be considered as a constant and called **Fermi Energy**, E_F . The Fermi energy is then

² The **energy of a photon** is $E = h\nu = h\frac{c}{\lambda}$ with $h \simeq 6.62 \times 10^{-34} \text{ J} \cdot \text{s}^{-1} \simeq 4.13 \times 10^{-15} \text{ eV} \cdot \text{s}$ the **Planck's constant**. For examples, the energy of a 1053 nm photon is 1.17 eV and a 351 nm photon is 3.53 eV.

the highest occupied quantum state at 0 K. The Fermi Energy is placed in the gap between the two bands for both semiconductors (near the center between E_C and E_V) and dielectrics.

Let us remind that metals are characterized by a Fermi level inside the conduction band, which means that this band is partially filled. Electrons in the upper and partially filled band are classically called free electrons. The dielectric permittivity of metals can be easily described by the Drude-Lorentz model. This model predicts a negative real part of the dielectric permittivity. The imaginary part of dielectric permittivity dielectric material is always positive (equal to zero for lossless materials).

All these information are summarized in Fig. 25. This representation of the energy band is the one used to describe the excitation processes in the first chapter.

2.1.1.2 Light propagation in dielectric media

The *refractive index of dielectrics* is the ratio between the celerity c (*speed of light in vacuum*) by the velocity v of the light in the dielectric. Dielectrics are non-magnetic $\mu = \mu_0$, so the refractive index equals the square root of the dielectric permittivity $\varepsilon = \varepsilon_0 \varepsilon_r$ (combination of vacuum ε_0 and relative ε_r dielectric permittivity). Therefore the index is positive and higher than 1. The imaginary part k is either null for lossless materials or positive for lossy materials.

$$\tilde{n} = \frac{c}{v} = \sqrt{\varepsilon \mu_0} = n + ik \quad (2.4)$$

Light propagation is described by Maxwell equations (eq. 2.5 to 2.8) that can be reduced into Helmholtz equations (2.11). These essential equations were enounced in 1865 by James Clark Maxwell (1831-1879) [47] and can be cast as following in a linear, isotropic dielectric and non-magnetic medium [48]:

$$\text{Maxwell-Faraday} \quad \mathbf{curl}(\mathbf{E}) = -\frac{\partial \mathbf{B}}{\partial t} \quad (2.5)$$

$$\text{Maxwell-Ampère} \quad \mathbf{curl}(\mathbf{B}) = \varepsilon \mu \frac{\partial \mathbf{E}}{\partial t} \quad (2.6)$$

$$\text{Maxwell-Gauss} \quad \mathbf{div}(\mathbf{E}) = 0 \quad (2.7)$$

$$\mathbf{div}(\mathbf{B}) = 0 \quad (2.8)$$

By using the relation $\mathbf{curl}(\mathbf{curl}(\mathbf{A})) = \mathbf{grad}(\mathbf{div}(\mathbf{A})) - \Delta(\mathbf{A})$, one can obtain the propagation relations for \mathbf{E} and \mathbf{B} :

$$\Delta \mathbf{E} - \varepsilon \mu_0 \frac{\partial^2 \mathbf{E}}{\partial t^2} = 0 \quad (2.9)$$

$$\Delta \mathbf{B} - \varepsilon \mu_0 \frac{\partial^2 \mathbf{B}}{\partial t^2} = 0 \quad (2.10)$$

In the following, we consider the harmonic Maxwell equations at a given ω frequency. The harmonic \mathbf{B} and \mathbf{E} field components are simply the Fourier components of the $\mathbf{E}(\mathbf{r}, t)$ and $\mathbf{B}(\mathbf{r}, t)$. Solutions of the equation (2.9) and (2.10) can be obtained in the form $\mathbf{E}(\mathbf{r}) = \mathbf{E}_0 \exp(i(\omega t - \mathbf{k} \cdot \mathbf{r}))$ and $\mathbf{B}(\mathbf{r}) = \mathbf{B}_0 \exp(i(\omega t - \mathbf{k} \cdot \mathbf{r}))$. Therefore Helmholtz equations are written as following:

$$\Delta \mathbf{E} + k^2 \mathbf{E} = 0 \quad (2.11)$$

with this description one can remark that \mathbf{B} , \mathbf{E} and \mathbf{k} forms a direct trihedron.

2.1.1.3 Interface

A major interest of Maxwell equations is to predict the behavior of waves propagating through interfaces. At each boundary between two materials, the incident wave splits into the reflected wave and the transmitted wave. The determination of the direction and amplitude of those waves requires first the knowledge of the continuity. Maxwell's equations predict that tangential part of the fields must be continuous propagating across the interface.

The plane containing the normal to the surface between the two media and the direction of propagation \mathbf{k} is the *plane of incidence*. The *polarization* is the direction in which the electric field oscillates. This polarization can be circular, elliptic or linear. In the case of a linear polarization, when the polarization is contained in the plane of incidence, the polarization is called *p*. When the polarization is perpendicular to the plane of incidence the polarization is called *s*. This terminology is coming from German in which *Parallel* means parallel and *Senkrecht* means perpendicular. It will be largely used in the present work as presented it were for example in the 1.1.2.3 architecture of Petal paragraph to describe the polarization of use of each mirror. Another terminology to describe linear polarization is *TM* for *Transverse Magnetic* corresponding to the *p* polarization and *TE* for *Transverse Electric* corresponding to the *s* polarization. This latter terminology is not used in this present work.

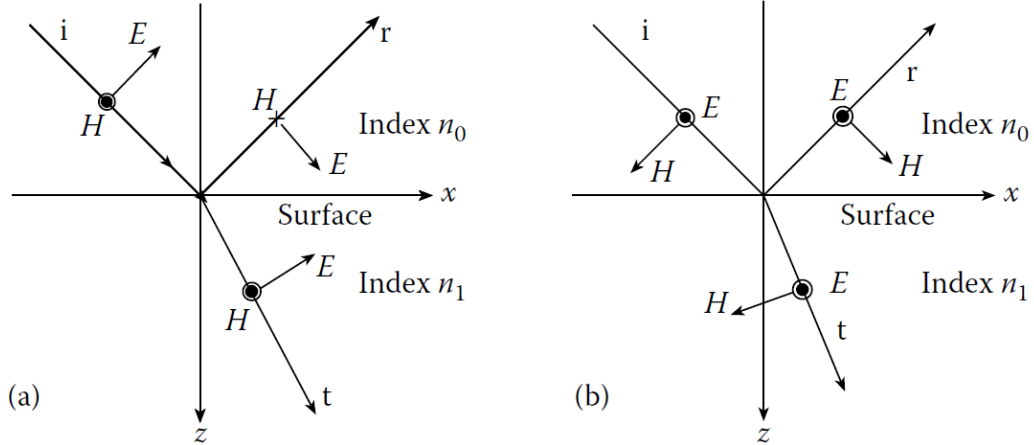


Fig. 26. (a) Convention defining the positive directions of H and E for *p*-polarization (b) Convention defining the positive directions of H and E for *s*-polarization. Figure extracted from [49] page 27

With the continuity relations, one can express the Reflectance and Transmittance at the interface (diopter) for both cases of polarizations as the square norm of the Fresnel formulae; see development and calculation in [48].

$$\left. \begin{aligned} T_p &= |t_{p\ 0 \rightarrow 1}|^2 = \left| \frac{2 \tilde{n}_0 \cos(\theta_0)}{\tilde{n}_0 \cos(\theta_1) + \tilde{n}_1 \cos(\theta_0)} \right|^2 \\ T_s &= |t_{s\ 0 \rightarrow 1}|^2 = \left| \frac{2 \tilde{n}_0 \cos(\theta_0)}{\tilde{n}_0 \cos(\theta_0) + \tilde{n}_1 \cos(\theta_1)} \right|^2 \end{aligned} \right\} \quad (2.11)$$

$$\left. \begin{aligned} R_p &= |r_{p\ 0 \rightarrow 1}|^2 = \left| \frac{\tilde{n}_0 \cos(\theta_1) - \tilde{n}_1 \cos(\theta_0)}{\tilde{n}_0 \cos(\theta_1) + \tilde{n}_1 \cos(\theta_0)} \right|^2 \\ R_s &= |r_{s\ 0 \rightarrow 1}|^2 = \left| \frac{\tilde{n}_0 \cos(\theta_0) - \tilde{n}_1 \cos(\theta_1)}{\tilde{n}_0 \cos(\theta_0) + \tilde{n}_1 \cos(\theta_1)} \right|^2 \end{aligned} \right\} \quad (2.12)$$

At normal incidence these formulae are simplified into $R = \left(\frac{\tilde{n}_0 - \tilde{n}_1}{\tilde{n}_0 + \tilde{n}_1}\right)^2$ and $T = \left(\frac{2\tilde{n}_0}{\tilde{n}_0 + \tilde{n}_1}\right)^2$. As example, for a air/fused silica (FS) interface ($\tilde{n}_0 = n_0 = 1$ and $\tilde{n}_1 = n_1 = 1.45$ in the visible range), the reflection at normal incidence is approximatively 3.37%.

We can apply the reflection formulae (2.12) to a few examples and calculate the reflectance of three different interfaces between air ($n_0 = 1$) and silica ($n_1 = 1.45$), or air and hafnia ($n_1 = 1.95$).

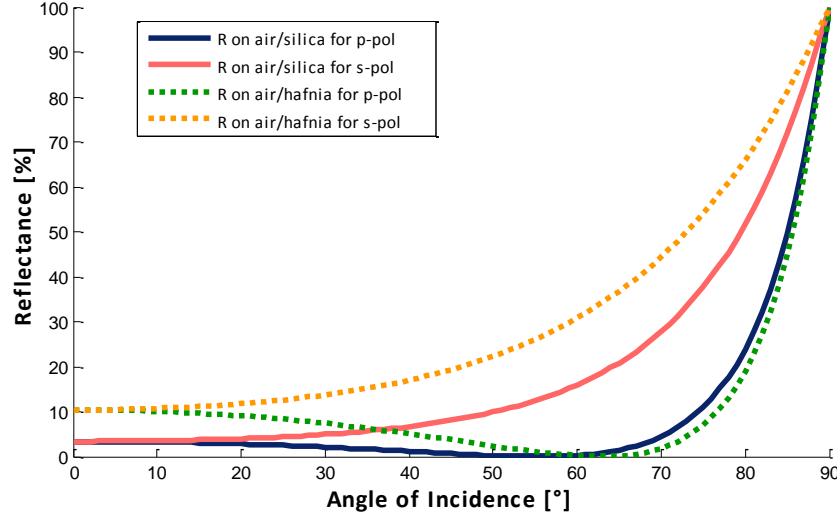


Fig. 27. Reflectance for p - and s -polarization for two different types of interfaces. **Nota on Fig. 27:** The hypothesis taken for this figure and the rest of this description are for a monochromatic plane wave for which the group delay dispersion is neglected. The nonlinear effects and the secondary reflection are also neglected.

With these three examples we can see that naturally for a given angle (Brewster angle³) the reflectance for p -polarization is completely suppressed. One of the main motivations for the development of thin films is to modify this behavior. To illustrate the principle of thin film, we will in the following paragraph describe how to obtain an Anti-Reflective or neutral layer.

2.1.2 Single layer example

In this paragraph, we introduce the concept of thin films with the example of a single layer that can be anti-reflective (AR) or neutral for a given wavelength. This presentation of single layers is important to understand the logic behind multilayer coatings and also because all the material characterization realized in this present work was performed on a wide variety of single layer samples. The results of these characterizations will be presented in the chapter 4.

A single layer (see Fig. 28), also called monolayer, is a media characterized with a **physical thickness** d and a **refractive index** of \tilde{n}_1 deposited on a semi-infinite substrate characterized with a refractive index of \tilde{n}_2 . The incident media, also called **superstrate**, is characterized with an index of \tilde{n}_0 . \tilde{n}_1 is different from \tilde{n}_0 and \tilde{n}_2 , so the two interfaces exist. An important quantity to describe a layer is its **optical thickness** which is the path of the incident light through the layer: $\tilde{n}_1 d \cos(\theta_1)$

³ Brewster's angle was first noted by David Brewster (1781-1868) in 1815. $\theta_B = \arctan(\frac{\tilde{n}_1}{\tilde{n}_0})$ For an interface between FS and air the Brewster's angle is 55.4°.

with θ_1 the refractive angle given by the *Snell-Descartes 3rd law* as a function of the angle of incidence θ_0 and the refractive index of the substrate and layer: $\widetilde{n}_0 \sin(\theta_0) = \widetilde{n}_1 \sin(\theta_1)$

At each interface one part of the light will be reflected and a second part will be transmitted (see Fig. 28). The superposition of all the reflected and transmitted parts will create interferences that can either be constructive or destructive depending on the *optical path difference* δ . This can keep intact, modulate or suppress the amplitude (and thus intensity) of the reflected or transmitted wave.

For example the reflected intensity in Fig. 28 is the combination of two beams and can be written $I_R = I_{R_{01}} + I_{R_{02}} + 2\sqrt{I_{R_{01}}I_{R_{02}}}\cos(\frac{2\pi\delta}{\lambda})$. The last term of this expression is the *interference coefficient*.

In reality, there is infinity of beams to combine to have the reflected or transmitted light. The intensity of the beams is decreasing with the order of the reflection of the beam ($I_{R_{01}} > I_{R_{02}} > \dots > I_{R_{0n}}$). In a first approximation, to introduce the concept of interference, we can restrict the number of beams to consider to two. The main characteristics announced on the optical path difference to obtain constructive or destructive interferences when considering two will remain true with more beams considered.

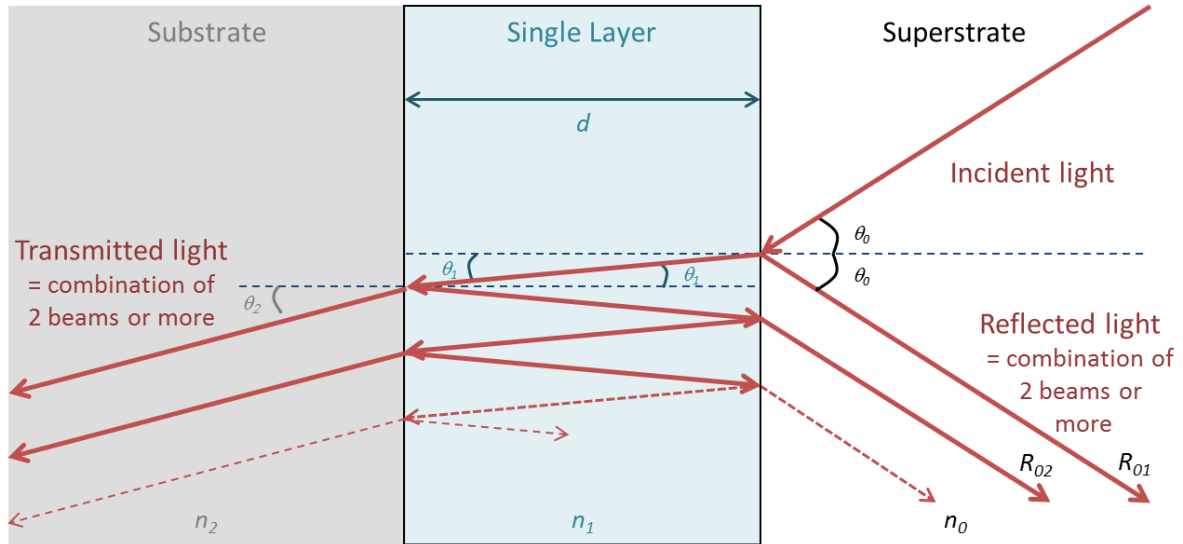


Fig. 28. Schematic of the incident, reflected and transmitted light through a single layer

Nota on the Fig. 28: the direction of propagation of the light in this figure is from the right to the left (the opposite of the reading direction). I chose this direction so this is in accordance with Optilayer software representation and figures. All the figures representing single layer, multilayer structure or electric field intensity distribution will follow the same convention.

The interferences are constructive (and respectively destructive) when the cosine $\cos(\frac{2\pi\delta}{\lambda})$ in the interference term is maximized, meaning $\delta = m\lambda$ (respectively minimized, meaning $\delta = (m + \frac{1}{2})\lambda$) with $m \in \mathbb{N}$. The optical path difference for the reflected beams is twice the optical thickness of the layer: $\delta = 2\widetilde{n}_1 d \cos(\theta_1)$. The interference will be constructive (respectively destructive) for an optical thickness $\widetilde{n}_1 d \cos(\theta_1) = m\frac{\lambda}{2}$ (respectively $\widetilde{n}_1 d \cos(\theta_1) = m\frac{\lambda}{4}$).

2.1.2.1 Anti-Reflective layer

Applying this thought it is possible to design Anti-Reflective (AR) single layer. A layer will be AR if its total reflectance is equal to zero when the reflection of both interfaces of the layer are equals and the interferences on the reflected part are destructive [50].

To design AR layer at normal incidence (more details in chapter 4 of [49]), the equality of the interfaces reflections $R_{0 \rightarrow 1} = R_{1 \rightarrow 2}$ is equivalent to $\frac{\tilde{n}_1 - \tilde{n}_2}{\tilde{n}_1 + \tilde{n}_2} = \frac{\tilde{n}_0 - \tilde{n}_1}{\tilde{n}_0 + \tilde{n}_1}$ which requires $\frac{\tilde{n}_1}{\tilde{n}_0} = \frac{\tilde{n}_2}{\tilde{n}_1}$. This final equality can be written $\tilde{n}_1 = \sqrt{\tilde{n}_0 \tilde{n}_2}$. The destructive characteristic of the interferences gives a condition on the physical thickness $d = m \frac{\lambda}{4 \tilde{n}_1}$ with $m \in \mathbb{N}$.

As an application of this example, if $n_0 = 1$ and $n_2 = 1.45$, the refractive index of the anti-reflective layer needs to be equal to $n_1 \simeq 1.204$. For a wavelength of 1053 nm, the physical thickness of the AR layer should be $d \simeq 218 \text{ nm}$.

Following this technique, a sol-gel single AR layer is coated on the LMJ transmission optical components that cannot be used at Brewster angle (Vacuum windows, gratings, KDP crystals, lens...).

2.1.2.2 Absentee layer

The interference coefficient is modulated by the cosine of the phase shift $\cos(\frac{2\pi\delta}{\lambda})$, the cosine function is periodical with a 2π period. When transposed on the optical path difference δ , this periodicity is λ . This is equivalent to a periodicity of $\lambda/2$ on the optical thickness. This means that with a period of $\lambda/2$ on the optical thickness the interference coefficient will be identical. Thus the reflection and transmission will be identical for a $\lambda/2$ optical thickness layer (also called a half-wave optical thickness layer, HWOT) and a $m\lambda/2$ optical thickness layer (with $m \in \mathbb{N}$). So, a HWOT layer has no effect on the reflectivity and transmittivity for the given wavelength λ and is called an *absentee layer*. With or without the layer, the reflection and transmission of the optical component remains the same. An absentee layer can be used as a protective overcoat to a substrate or a coating. This overcoat layer is currently used on MLD coating (mirrors and polarizers) of nanosecond facilities.

These two iconic examples show how a single layer can drastically affect the optical propagation of a beam. We now aim at going further by designing complex optical responses to obtain highly efficient anti-reflective (AR) coatings, highly-reflective (HR) mirrors, filters or also polarizers. For that purpose, we need to engineer the optical response of the coatings by increasing the degrees of freedom to achieve the targeted spectral feature. This can be achieved by increasing the number of layers.

2.1.3 Multilayer

To describe the thin-film optical coatings, three parameters are important to know the structure of the multilayer stack called hereafter *design*:

- **Materials:** refractive index n
- **Thicknesses:** physical thickness d of each layer
- **Sequence of the coating:** number of layers and order of deposition

The *optical thickness* defined previously is simply equal to the product between the refractive index n and the propagation length $d \cos(\theta)$.

The optical responses will be optimized for a given set of polarization, wavelength and angle of incidence with respect to the thickness and refractive index of each layer. Tuning the refractive index of dielectric layers can be considered when considering mixtures of dielectrics or textured films with engineered void or porosity.

However, one usually works with pairs of high and low refractive index materials. In this PhD thesis, emphasis will be placed on oxide materials since they feature excellent optical (low absorption, k) and mechanical properties.

2.1.3.1 Electric field calculation: matrix formalism

Even in the case of single layer, it has been shown that depending on the number of reflection considered, the model can easily become complicated. The model of adding multiple reflection or transmission became impractical in the case of multilayer. A matrix approach, involving 2×2 matrices, helps to calculate the effect of a boundary and the propagation through a film more easily.

This matrix formalism is a very convenient and compact form to describe light propagation in stratified media. It has been first introduced and discussed by Florin Abelès in 1948 [51], where both the electric field E and magnetic field H are calculated at different depth of a stratified media. The Abelès's matrix method [52, 53] allows the calculation of the electric field intensity distribution at any depth of a stratified media using the amplitude of the forward-travelling electric field E^+ and backward-travelling electric field E^- as basis vector for the reflection and transmission calculation. Heavens, later, described the matrix formalism in [54, 55]. Since that presentation, Azzam and Bashara have reformulated the equations [56] to isotropic stratified planar structure. This latter formalism will be the one used in the present work. It is more concisely presented in [57].

Other matrix formalism using the column vector $\begin{bmatrix} E(z) \\ H(z) \end{bmatrix}$ instead of $\begin{bmatrix} E^+(z) \\ E^-(z) \end{bmatrix}$ can be found as presented in [49]. They will not be presented here because we need to express the electric field intensity only as we have no requirement on the magnetic field.

Fig. 29 represents a multilayer consisting in m layers and the propagation of an incident monochromatic plane wave through the structure. Moreover other assumptions for those calculations are that the group delay dispersion (GDD), secondary reflections and propagation effect related to nonlinear refractive index are neglected. The figure is placed in an orthogonal direct system of coordinates $(\vec{x}, \vec{y}, \vec{z})$ where the z -axis is normal to the layers interface. Each interface is either in or parallel to the (\vec{x}, \vec{y}) plane. The plane of incidence is (\vec{x}, \vec{z}) . The incident wave propagates in the direction of increasing z . The superstrate is the 0 medium. The substrate is the $m+1$ medium and all the layers in between are numbered from 1 (outer layer) to m (layer closest to the substrate). All media are homogenous, isotropic, non-magnetic and characterized with a complex refractive index \tilde{n}_j and a physical thickness of d_j . The optical thickness of each layer is $N_j d_j \cos(\theta_j)$. The total field inside the j th layer, which is excited by the incident plane wave, consists in two plane waves: a forward-travelling plane wave denoted E_j^+ and a backward-travelling plane wave E_j^- .

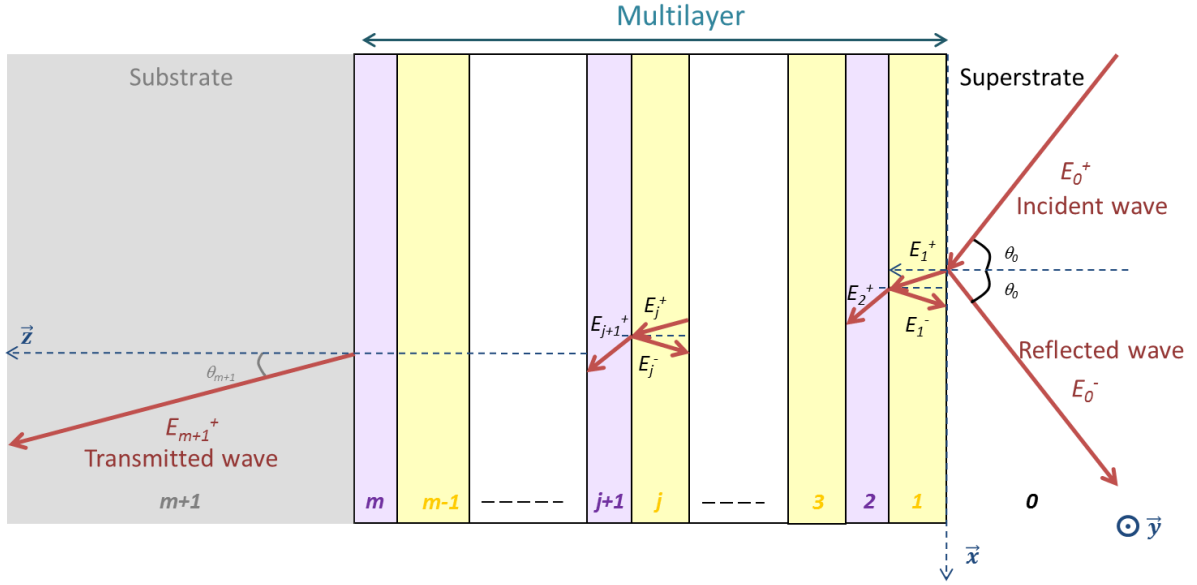


Fig. 29. Schematic of a multilayer and an incident monochromatic plane wave propagating through the stratified structure

The total field at any depth z in the stack can be described as following:

$$\mathbf{E}(z) = \begin{bmatrix} E^+(z) \\ E^-(z) \end{bmatrix} \quad (2.13)$$

where $E^+(z)$ and $E^-(z)$ are the complex amplitude of the forward- and backward-travelling plane waves at an arbitrary plane z . The incident wave, the reflected wave and the transmitted wave are expressed as follows:

$$\begin{bmatrix} E_0^+ \\ E_0^- \end{bmatrix} = \begin{bmatrix} S_{11} & S_{12} \\ S_{21} & S_{22} \end{bmatrix} \begin{bmatrix} E_{m+1}^+ \\ E_{m+1}^- \end{bmatrix} \quad (2.14)$$

The \mathbf{S} matrix is called the *scattering matrix* in [56] page 334 (often this matrix is called Transmission matrix and noted \mathbf{T}) which represents the overall transmission and reflection properties of the stratified structure. \mathbf{S} can be expressed as the product of *interfaces matrices* \mathbf{I} and *layer matrices* \mathbf{L} :

$$\mathbf{S} = \mathbf{I}_{0 \rightarrow 1} \mathbf{L}_1 \mathbf{I}_{1 \rightarrow 2} \mathbf{L}_2 \cdots \mathbf{I}_{(j-1) \rightarrow j} \mathbf{L}_j \mathbf{I}_{j \rightarrow (j+1)} \cdots \mathbf{L}_m \mathbf{I}_{m \rightarrow m+1} \quad (2.15)$$

An interface matrix between two media a and b can be described as follows, using Fresnel formulae:

$$\begin{bmatrix} E_a^+ \\ E_a^- \end{bmatrix} = \begin{bmatrix} I_{11} & I_{12} \\ I_{21} & I_{22} \end{bmatrix} \begin{bmatrix} E_b^+ \\ E_b^- \end{bmatrix} = \frac{1}{t_{a \rightarrow b}} \begin{bmatrix} 1 & r_{a \rightarrow b} \\ r_{a \rightarrow b} & 1 \end{bmatrix} \begin{bmatrix} E_b^+ \\ E_b^- \end{bmatrix} \quad (2.16)$$

$r_{a \rightarrow b}$ and $t_{a \rightarrow b}$, the Fresnel coefficients at each boundary between a and b can be calculated with (2.11) and (2.12) for both cases of polarization.

The \mathbf{L}_j matrix describes the propagation of the wave through the layer j from the beginning of the layer z_0 to the end $z_0 + d_j$. Therefore it can be written:

$$\begin{bmatrix} E_j^+(z_0) \\ E_j^-(z_0) \end{bmatrix} = \begin{bmatrix} L_{j11} & L_{j12} \\ L_{j21} & L_{j22} \end{bmatrix} \begin{bmatrix} E_d^+ \\ E_d^- \end{bmatrix} = \begin{bmatrix} e^{i\beta_j} & 0 \\ 0 & e^{-i\beta_j} \end{bmatrix} \begin{bmatrix} E_j^+(z_0 + d_j) \\ E_j^-(z_0 + d_j) \end{bmatrix} \quad (2.17)$$

$\beta_j = \frac{2\pi \tilde{n}_j d_j}{\lambda} \cos \theta_j$ being the phase shift of the layer.

Then the scattering matrix can be rewritten as in [57]:

$$\mathbf{S} = \frac{\mathbf{C}_1 \mathbf{C}_2 \dots \mathbf{C}_j \mathbf{C}_{j+1} \dots \mathbf{C}_{m+1}}{t_{1 \rightarrow 2} t_{2 \rightarrow 3} \dots t_{j \rightarrow j+1} \dots t_{m \rightarrow m+1}} \quad \text{with} \quad \mathbf{C}_{j+1} = \begin{bmatrix} e^{-i\beta_j} & r_{j \rightarrow j+1} e^{-i\beta_j} \\ r_{j \rightarrow j+1} e^{i\beta_j} & e^{i\beta_j} \end{bmatrix} \quad (2.18 \text{ \& } 2.18')$$

Then, with:

$$\mathbf{C}_1 \mathbf{C}_2 \dots \mathbf{C}_j \mathbf{C}_{j+1} \dots \mathbf{C}_{m+1} = \begin{pmatrix} a & b \\ c & d \end{pmatrix} \quad (2.19)$$

the amplitude reflectance and transmittance of the overall stack can be expressed as:

$$r = \frac{E_0^-}{E_0^+} = \frac{c}{a} \quad \text{and} \quad t = \frac{E_{m+1}^+}{E_0^+} = \frac{t_{1 \rightarrow 2} t_{2 \rightarrow 3} \dots t_{j \rightarrow j+1} \dots t_{m \rightarrow m+1}}{a} \quad (2.20 \text{ \& } 2.20')$$

Now based on this formalism we can calculate the electric field intensity of each component at an arbitrary depth z .

$E^+(z)$ and $E^-(z)$ are expressed as follows with the amplitude at the interface E_j^+ and E_j^- :

$$\mathbf{E}(z) = \begin{bmatrix} E^+(z) \\ E^-(z) \end{bmatrix} = \begin{bmatrix} E_j^+ \exp(iK_{zj}\Delta_z) \\ E_j^+ \exp(-iK_{zj}\Delta_z) \end{bmatrix} \quad (2.21)$$

with $K_{zj} = 2\pi\tilde{n}_j \cos \theta_j$ the z -component of the wave vector and $\Delta_z = z - \sum_{k=1}^{j-1} d_k$ the distance from the j -th boundary.

Based on this description, we can define each component of the electric field as follows:

$$\begin{cases} E_x(z) = [E_p^+(z) - E_p^-(z)] \cos(\theta_j) \\ E_y(z) = [E_s^+(z) - E_s^-(z)] \\ E_z(z) = [E_p^+(z) + E_p^-(z)] \sin(\theta_j) \end{cases} \quad (2.22)$$

Then, the electric field intensities $EFI(z)$ is the ratio of the square of the amplitude of the field $|E(z)|^2$ to that of the incident field $|E_0^+|^2$ of each polarization: $|E_{0p}^+|^2$ and $|E_{0s}^+|^2$.

$$\begin{cases} EFI_x(z) = |E_x(z)|^2 / |E_{0p}^+|^2 \\ EFI_y(z) = |E_y(z)|^2 / |E_{0s}^+|^2 \\ EFI_z(z) = |E_z(z)|^2 / |E_{0p}^+|^2 \end{cases} \quad (2.23)$$

Finally, the electric field intensity for each polarization can be expressed:

$$\begin{cases} EFI_s(z) = EFI_y(z) \\ EFI_p(z) = EFI_x(z) + EFI_z(z) \end{cases} \quad (2.24)$$

This matrix formalism is central to this study as it enables the use of numerical calculation for the electric field intensity within the stack which is required to engineer mirrors with optimized EFI distribution in the structure. As stated in the first chapter and described later in this chapter, the laser-induced damage threshold in short pulses depends on the electric field intensity. The required parameters to do this EFI calculation are the refractive index of the materials involved in the design and the number and thickness of the layers. Then in order to modify the EFI there are two paths: considering other refractive index meaning other material or other thicknesses. In addition to changing

the refractive index, considering new materials will bring different $LIDT_{int}$. The optimization of the thicknesses and number of layer will aim at shifting the EFI peaks (location where the damage is more likely to happen) into the more resistive material. These two paths which required the electric field intensity calculation will be explored theoretically in Chapter 3.

2.1.3.2 Bragg mirrors

Using what is presented above, the designing method is very versatile and a wide variety of spectral functions can be obtained with engineered stratified media [50]: anti-reflective, dielectric mirrors, polarizers, edge filters, beam splitters, narrow-band interferences filters...

Previously, we presented how an antireflective coating can be designed with a single layer. The AR characteristic forces the layer to have a specific refractive index and thickness. By adding layers, it is possible to create an AR coating even when the condition on the matching refractive index of the layer with the substrate cannot be satisfied. The addition of layers also allows the reduction of transmission for a specific wavelength or the creation of broadband AR coatings.

The simplest design to achieve a High Reflection (HR) with multilayer dielectric coating for a given wavelength λ consists of the alternation of quarter-wave optical thickness (QWOT) layers $\lambda/4$ of a pair of high and low index materials. This design, also known as *Bragg mirrors* as it has been developed by William Lawrence Bragg, is the solution that can be determined analytically to engineer HR multilayer.

A common notation to describe multilayer coating consists in calling *H* a quarter-wave optical thickness layer of the high index material and *L* a quarter-wave optical thickness layer of the low index material. With this notation a Bragg mirrors are described as: $(HL)^n$, n being the number of pair of layers.

With the increase of n , the number of pairs of layers, the reflection will increase up to almost 100%. The final reflection will be only limited by the losses through absorption and scattering of the materials, while the transmission falls down to 0%. The highest reflections achievable with MLD mirrors are higher than with metallic layers, because dielectrics unlike metals have very low absorption. This reflection will differ with respect to the polarization, see example in Fig. 30. The reflectivity maximum at the central wavelength and the reflectance band is higher for s -polarization than for the p -polarization. It is then easier to design a mirror for s -polarization than p -polarization. In terms of electric field intensity, this property gives that the electric field intensity within the structure for the s -polarization is lower than the one for the p -polarization.

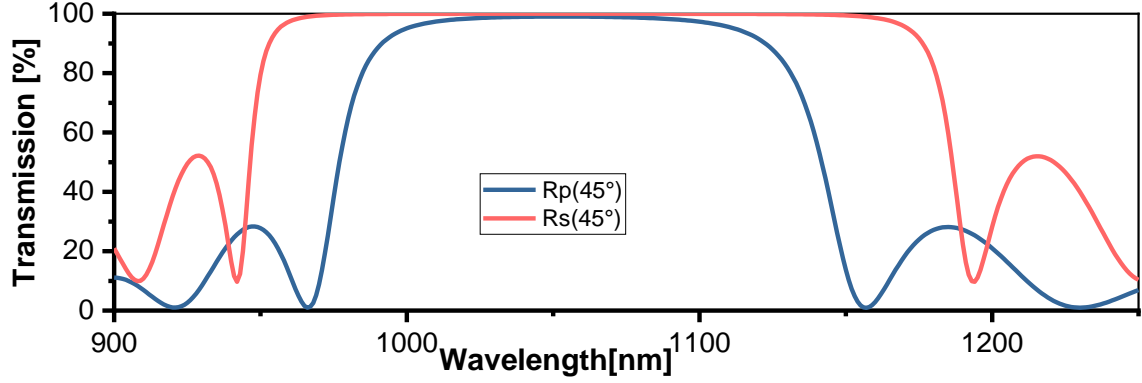


Fig. 30. p - (blue) and s -polarization (red) reflectance of Bragg mirror with (HL)14H2L design for a wavelength of 1053 nm and 45° incidence. Here H is hafnium HfO_2 and L is silica SiO_2

The higher the *index contrast* n_H/n_L between the two materials used in the coating, the higher will be the coating reflectivity and wider will be the reflectance band for both polarizations. So, by choosing the materials wisely, a given reflectivity can be achieved with a smaller number of pair of layers.

In this work, we focus our attention on the development of all-dielectric mirrors. We will consider multilayer coatings made of 2 different materials with low and high refractive index.

2.2 Laser damage and MLD

At this stage, we presented separately high power laser facilities and MLD coatings. However, the two topics are intrinsically combined as optical coatings have been long recognized as a key challenge in the Fusion class laser systems [58, 59]. Laser-induced damage on thin-films optical coating is different from bulk material laser-induced damage threshold. The models need to be investigated and adapted at MLD components. Structure of the materials will vary between bulk and thin film. Moreover depending on the deposition method, the density and the electronic intermediate states of the material will change. The deposition method is then not a neutral choice and need to be done carefully. Deposition methods that reduce the density of defects, especially nodules, are to be preferred. The choice of deposition method will be the subject of the next section.

For long pulse, the laser-induced damage threshold is mostly due to the presence of defects like nodules. The morphologies of damage in this regime are mostly nodular ejection pits, plasma scalds, flat bottom pits and delamination. The addition of a thick silica overcoat (like an absentee layer: 2L) on MLD optical components reduces the risk of delamination and more generally damage [60]. This type of design with an overcoat is commonly used on nanosecond laser facilities. At first, their use was transferred to pico/sub-picosecond laser facilities even if it is not ideal considering the model of laser damage in short pulse regime.

2.2.1 Short pulse LIDT on MLD

LIDT is governed in the short-pulse regime (*i.e.* picosecond to sub-picosecond) by electron excitation processes as explained in 1.2.3.1.

It has been shown in 1976 by Apfel [61] that there is a relationship between the LIDT (for a pulse of 30 ps at 1064 nm) and the electric field intensity inside multilayer coatings by comparing the damage results of four designs with widely different electric field enhancement but manufactured together (in one single run).

As presented in 2.1.3.1, the Electric Field Intensity (EFI) is the square of the time-average electric field $|E|^2$ normalized by the incident electric field $|E_0|^2$. The electric field intensity values are expressed in relative units to the incident field $|E_0|^2/|E_0|^2=100\%$. The values are quadratic and can reach 400%. The maximum enhancement of the electric-field intensity $|E|^2/|E_0|^2$ in each layer is denoted by EFI_{max} .

This intensity of the electric field within each layer varies significantly, depending on the design of the multilayer, giving rise to a distribution of enhanced electric-field intensity within each layer structure. For example, Fig. 31 presents the electric field intensity distribution with a Bragg mirror design with a silica absentee layer as an overcoat. In other words this mirror is composed of an alternation of quarter-wave optical thickness layers of high and low refractive index with a thicker low refractive index layer as outer layer. Using the representation presented in the chapter 2, the design is $(HL)^{10}H2L$. On Fig. 31, the electric field intensity values are above 100% in the overcoat and the EFI_{max} in this layer is around 140% for the p -polarization. The electric field intensity values at each interface of the absentee layer are equal which is representative of its absentee characteristic. Therefore, with the dependence of the LIDT on the electric field intensity this overcoat might weaken the general LIDT of multilayer without bringing any spectral modification.

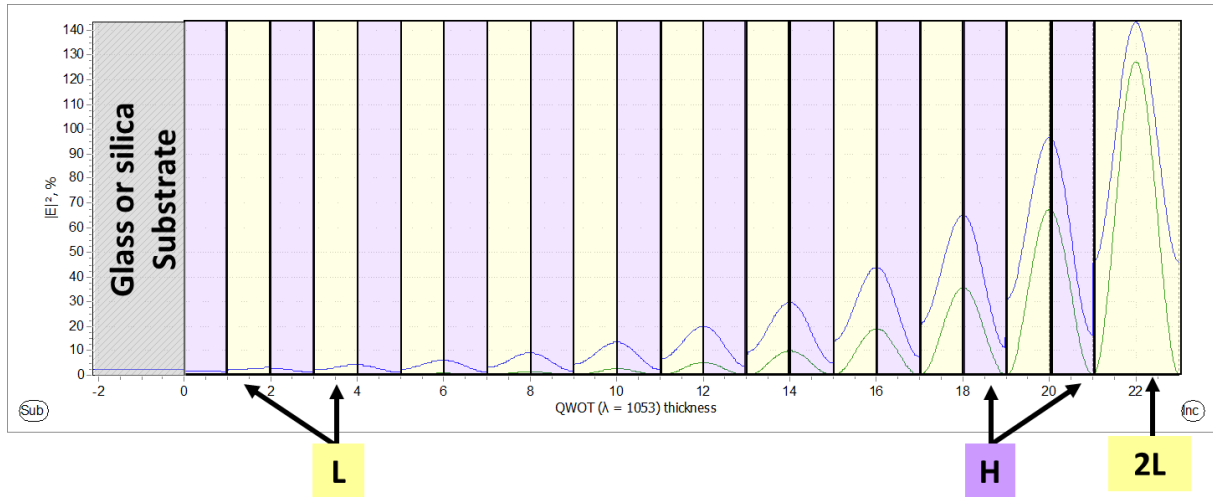


Fig. 31. Electric field intensity distribution for p -polarization (blue) and s -polarization (green) within a $(HL)^{10}H2L$ mirror stack at 45° incidence. H and L designate quarter-wave optical thickness (for a 1053 nm wavelength at 45° incidence) layers of either high or low refractive index. The 2L layer which is twice the thickness of an L layer is a protective overcoat to laser-induced damage in nanosecond regime.

2.2.2 Survey of the models

In 2001, Jasapara *et al.* confirmed Apfel observation [38] and observed that breakdowns of a Ta_2O_5 single layer and Ta_2O_5/SiO_2 multilayer for pulses from 10 fs to 100 fs were highly deterministic and can be explained by multiphoton absorption and impact ionization when local electric field intensities

enhancements are taken into account. The laser damage is then determined by intrinsic properties rather impurities. Moreover, Jasapara announced that LIDT could be predicted from the multiphoton absorption coefficient and impact ionization. Later, in 2005, Mero *et al.* extended the study of laser damage threshold to other oxides deposited with IBS [43] and found out a linear scaling of the breakdown fluence with bandgap energy. This can be explained by invoking the bandgap dependence of the multiphoton absorption coefficient from Keldysh photoionization theory [44]. Mero finally establish the following phenomenological law:

$$LIDT_{meas} = (C_1 + C_2 E_g) \tau_p^\kappa \quad (2.25)$$

with τ_p the pulse duration in fs, $C_1 = -0.16 \pm 0.02 \text{ J} \cdot \text{cm}^{-2} \cdot \text{fs}^{-\kappa} \cdot \text{eV}^{-1}$, $C_2 = 0.074 \pm 0.004 \text{ J} \cdot \text{cm}^{-2} \cdot \text{fs}^{-\kappa} \cdot \text{eV}^{-1}$ and $\kappa \sim \frac{1}{3}$

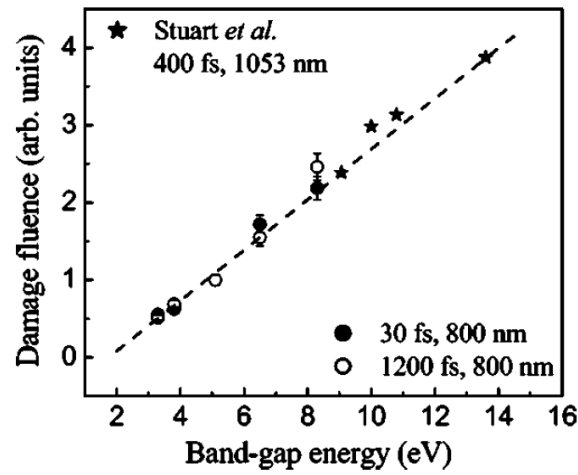


Fig. 32. Experimental breakdown fluence as a function of bandgap energy obtained with 30 fs (solid circles) and 1.2 ps (open circles) laser pulses. The data points are normalized to the damage fluence at $E_g=5.1$ eV. The data shown by asterisks were taken from [62]. The figure is taken from [43] and illustrate the (2.25) formulae

In this law, the threshold fluence is determined by the sole bandgap energy of the material, with a possible additional factor that depends on the material type and growth process. Using mixture materials Melninkaitis *et al.* [63] reported deviation from the LIDT-Bandgap model proposed by Mero, see Fig. 33.

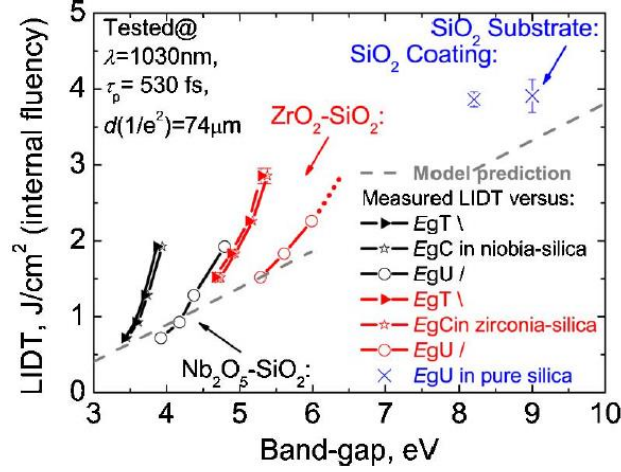


Fig. 33. Comparison of experimentally obtained LIDT data (3 different colors) and model prediction (gray dashed line) with respect to different bandgap definitions (different shapes of points). Figure taken from [63]

In 2011, Mangote used the following description of the measured LIDT normalized by the maximum of the electric field intensity to compare performances of different materials called internal LIDT [64, 45] (here referred as intrinsic LIDT). One can consider the following model to predict the damage threshold of a tested monolayer ($LIDT_{meas}$) by the damage threshold of the layer material ($LIDT_{int}$) normalized by the peak electric-field enhancement (EFI_{max}) :

$$LIDT_{int} = LIDT_{singlelayer} \times EFI_{max} \quad (2.26)$$

With this description, the damage is initiated when the electric field intensity (localized laser fluence) reaches a value above the threshold value of one of the materials (referred to as “intrinsic” damage threshold). The intrinsic LIDT allows performance comparison of materials even when they are deposited with different thicknesses on different substrates. The experimental determination of the intrinsic LIDT and what is influencing its values will be investigated and discussed in chapters 4 and 5. Since then this description has been widely used to compare materials to one another: [41, 65, 42, 46]. This will be more detailed chapter 3. Consequently, the LIDT of the entire multilayer is taken equal to the minimum value between the $LIDT_{meas}$ of each constituent layer of the stack:

$$LIDT_{mirror} = \min(LIDT_{singlelayer,H}, LIDT_{singlelayer,L}) \quad (2.27)$$

Damage can be initiated at different depths and/or layers within the same optic, depending on the irradiation parameters such as angle of incidence and polarization state of the laser beam. At damage-threshold conditions, the material volume exposed to a narrow range of peak electric-field intensities (that can support plasma formation) is superheated.

In 2017, Sozet *et al.* used this model in the description of the laser damage growth in short pulse regime (500 fs) on engineered circular defect. The prediction of damage and growing damage are in very good agreement [66]. The growth is linearly scaled with the number of laser illumination. Starting damage sites were initiated at fluence higher than the laser-induced damage threshold. As first approximation, the growth effect will not be considered in this present work.

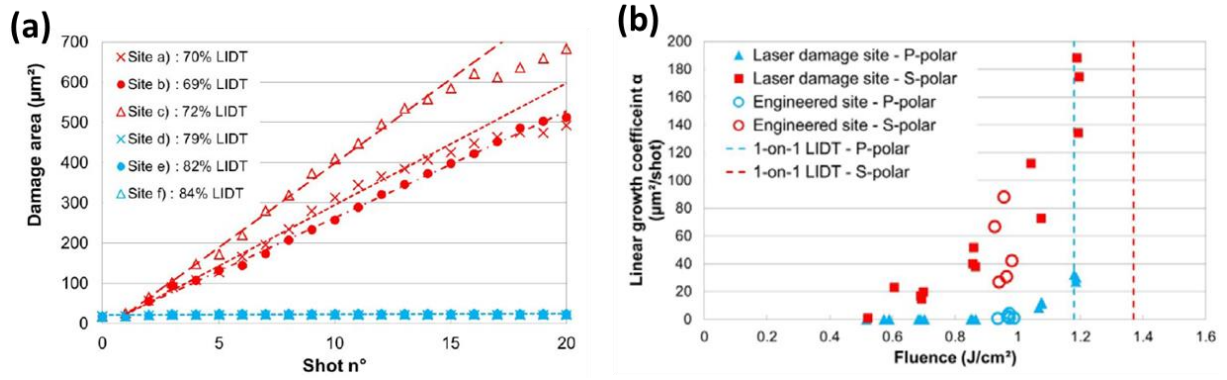
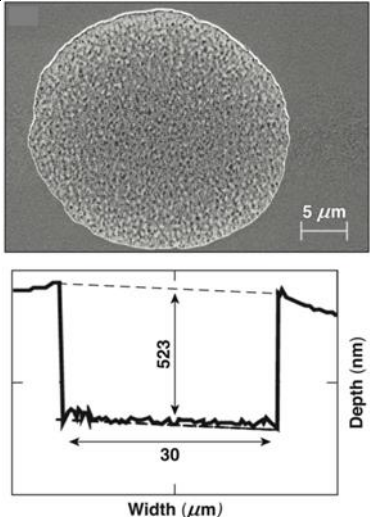
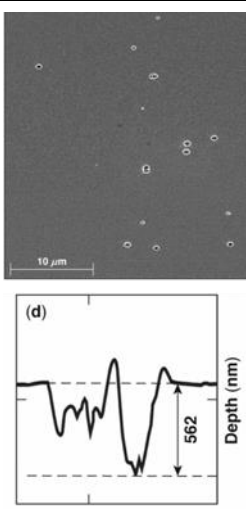
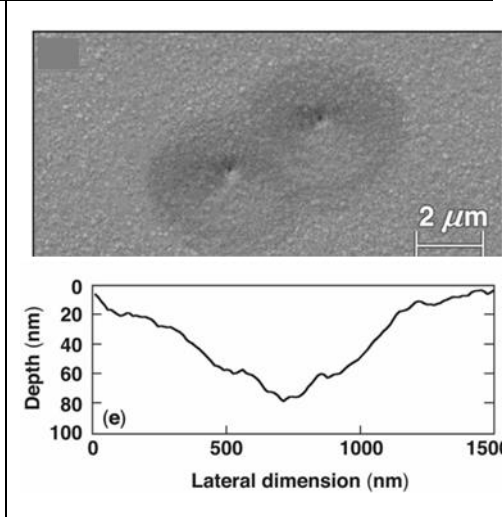


Fig. 34 **a)** Damage area evolution as a function of the shot number for the 6 sites the red sites are irradiated with a s-polarized beam and the blue sites with a p-polarized beam, Linear regressions are performed to extract the growth coefficient α . **b)** Linear growth coefficient α as a function of fluence. Comparison between results obtained on engineered damage sites (empty circles) and on laser damage sites (triangle and square) for P and S beam polarization. Intrinsic LIDT are also reported (dashed lines). Both figures are taken from [66]

Recently, in 2019, Kozlov *et al.* reported three types of laser damage morphologies on MLD mirrors made of HfO_2 and SiO_2 associated with specific pulse duration and physical phenomena, reported in Table 1 [40]. They showed that in order for damage to occur the generated pressure in this volume must also be sufficient to support shear fracture and detachment of the overlying layer [40]. In this present work, the pulse duration considered relate to the Type I damage where the crater formation is dominated by pressure-induced mechanical ejection of overlying material following plasma formation at the depth of peak electric-field intensity. This suggests that burying the electric field intensity peaks deeper in the structure might increase the general LIDT of the multilayer dielectric mirror. This recent observation is not considered as first approach in this present work.

Table 1. Three types of laser damage reported for short pulse in [40] with 1-on-1 procedure

Name	Type-I	Type-II	Type-III
Pulse duration	600 fs to 2.5 ps	2.5 ps to 100 ps	
Mechanism	Non-defect driven initiation	Defect-driven damage initiation	
SEM picture of the damage sites & depth profiles			

By considering this model (2.26) and (2.27), what has been exposed earlier, we can distinguish two complementary trends in the enhancement of damage performance of dielectric mirrors in short pulse regime:

- **identifying materials** with high damage resistance and improved refractive index (electric field intensity reduces with higher indexes, number of layer reduces with higher index contrast)
- **working on stack designs** with adapted electric field intensity distribution by shifting the peaks into the most resistant material and/or burying the electric field intensity to diminish the probability of reaching the sufficient pressure to initiate damage

In the next chapter, the strategies of optimization are considered theoretically and the experimental validation is presented in chapters 4 and 6.

2.3 Fabrication of multilayer dielectric component

As stated in the previous paragraph, the deposition method induces different properties in the films, which may lead to different damage threshold. Moreover an important manufacturing expertise is required to deposit multilayer with low density of damage and respecting the other high power laser specifications.

2.3.1 Survey of thin film manufacturing

The first optical function ever to be developed with thin films coatings is mirrors with its creation in the antiquity [67]. According to Pliny the Elder, the first metal-coated glass mirrors were fabricated in Sidon in the first century AD. Those mirrors were made by first depositing a molten lead film on a blown glass bubble, and then cutting off a small circular section (approx. 13-20 cm) of the round glass, making the mirrors either convex or concave. Pliny also reported on glass mirrors backed with gold leaves⁴. Due to their distorted images, fragileness and a very high cost, solid-metal-mirrors (made of polished steel) were preferred to those early metal-coated mirrors [68]. Since that time the mirrors made of metallic layer have evolved into those we use daily at homes, in cars or on optical set-ups in Laboratories. The use of mirrors in our daily lives probably makes them the most common optical components, but this is impossible to quantify.

The first trigger to the development of thin-films manufacturing was World War II [33]. During the war the need of high transmission on optical instrument (binocular telescope especially for use at sea) drove the research on manufacturing of anti-reflective coatings.

Later in the sixties with the creation of laser appears the need to fabricate mirrors with low losses. First, the need of lossless-mirrors was for the resonators of the lasers and then to direct the laser beams. But metals in UV, visible and near infrared spectra exhibit losses. The high absorption of the

⁴ The metal chosen were gold and lead to prevent oxidation of the films and provide a longer durability of the mirrors.

light with long pulse can cause as presented in Chapter 1: Laser damage. Thus the first metallic-layer resonators exhibited laser damage and needed to be changed often. That explained that the study of laser damage started almost at the same time as the creation of laser. The development of laser forced companies and research laboratories to make progress in the deposition of multilayer dielectric mirrors. Then after the development of multilayer dielectric mirrors raised the need of designing and manufacturing optical components that could manipulate laser beams such as: narrowband interference filters, beams splitters and so on.

Nowadays what is mostly triggering the progress of thin films industry is the mobile phone industry [69]. There were more than 4 million phones sold each day in 2018 with all cameras incorporated. The miniaturization of the cameras and the development of spectral analysis (to transform phones into portative spectrometers for food safety applications, for example) required new deposition technologies and design of filters.

In the actual thin film context, designing and depositing mirrors may seem unchallenging as the design of standard MLD mirrors is of the simplest in theory and very common. But the high Power Lasers, presented in Chapter 1, bring such high energies and powers that the fabrication of mirrors and more widely MLD components is challenging regarding spectral requirements, precision, planarity, homogeneity, rugosity and especially laser damage [59]. To meet all this specifications, the deposition methods of all the MLD components used in high Power Laser have to be carefully chosen.

2.3.2 *Deposition Methods*

In this section, we present the deposition techniques of interest for this project. The choice of the deposition method depends on the properties needed for the coating and the environment of use. The components involved in this study are used either in vacuum or in dry air. These environments induce a higher level of stress on the coatings. Therefore to avoid crazing or delamination, one needs to choose a deposition method inducing a low level of intrinsic stress. The coatings used in high power lasers need to have a high LIDT which requires a low density of defects and low absorbing materials. Another particularity of optical components used in high power laser lines is their sizes. Mirrors in the PETAL beamline have a size of $61 \times 43 \text{ cm}^2$. Compared with the wavelength, this size is extremely large and the challenge is to warrant a physical thickness of the deposited layer mastered at a scale much smaller than the wavelength, typically a few nanometers, over the whole surface of the component. We here restrain ourselves to the techniques that respect the high power laser requirements on stress, stoichiometry, defects density, intrinsic laser damage, homogeneity and uniformity for large components with a reasonable cost of fabrication.

One should note that it exists a vast number of deposition methods. More generally for vapor deposition, two groups of deposition techniques can be distinguished: (i) the Physical Vapor Deposition (PVD) methods where the material is evaporated using a physical phenomenon, namely thermally evaporation and sputtering; and (ii) the Chemical Vapor Deposition methods where the film is formed from the reaction of the constituent of a vapor in heterogeneous reaction sequences [70]. CVD techniques run at much higher temperatures this is not ideal for glass substrates and for the stress

induced during cooling of the substrate. These techniques are often used in the micro-electronic area and with semi-conductor. In high power laser facilities, the most ubiquitous techniques are PVD techniques based on electron beam evaporation with or without assistance. We will present the most commonly used techniques and also the IBS technique that has high potential for sub-picosecond LID application.

2.3.2.1 Electron-beam evaporation (E-beam): without assistance

Electron beam evaporation without assistance is a conventional PVD technique. In this technique, the coating material in the crucible is sublimated by electron beam obtained either with deflection gun or tele-focus gun [70]. A plume of vaporized material is then formed above the crucible. Molecules in this vapor condensate onto the substrates placed at the top of the coating chamber (cf. Fig. 35a)). The substrate carrier rotates to improve the uniformity of the coating on all the substrates mounted on the chamber [59]. Masks can also be added to improve the uniformity of the deposited films [59]. The gas backfill is used to keep the optimal partial pressure and to keep the stoichiometry in case of reactive evaporation of metal oxides. Reactive evaporation of metal oxides consists in using the metal in the crucible as starting targets and oxidizing the films with O_2 presence in the chamber. The oxidation of the oxides is made during the condensation on the substrate by keeping a partial pressure of the reactive gas here dioxygen O_2 in the coating chamber. This reactive deposition improves the LIDT [71] and the quality of the coating by reducing the number of nodules [72].

The e-beam technique is used to deposit transport mirrors and small polarizers of the LMJ facility. Those components are made of the alternation hafnia and silica layers. The hafnia is deposited through a reactive deposition method.

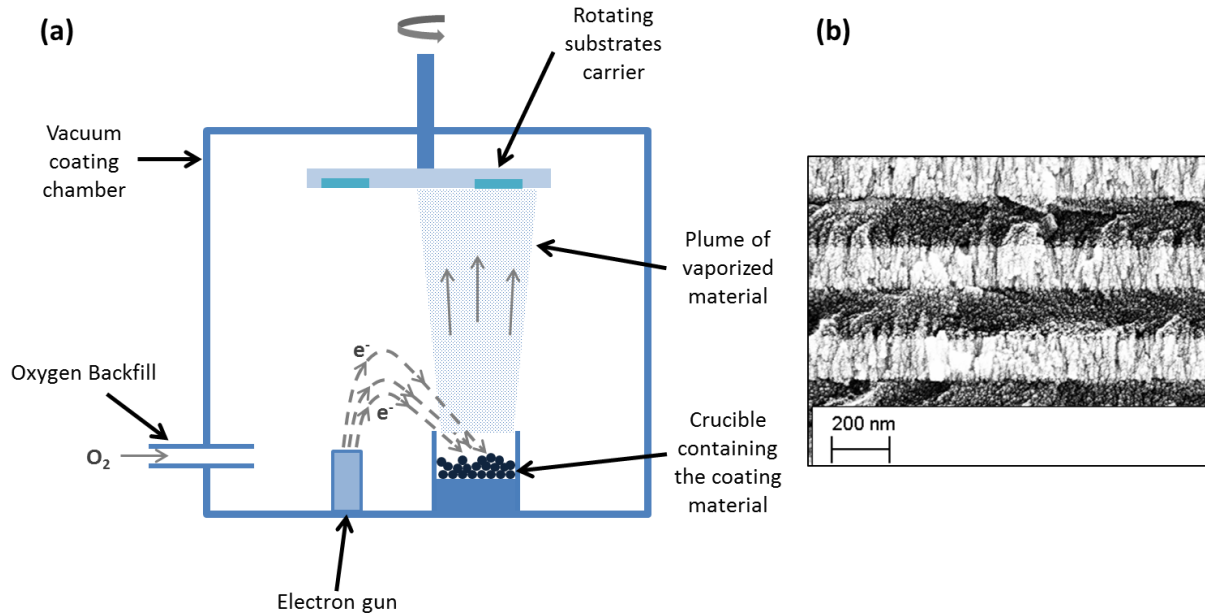


Fig. 35. **(a)** Schematic of an e-beam coater and **(b)** SEM picture of a coating composed of alternating quarter-wave optical thickness layers of Hafnia and Silica deposited with e-beam deposition method. The columnar structure is clearly visible for the Hafnia layers. For the silica layers, the structure is less visible but one can see the porosity of the coating.

The films deposited with this technique have an open columnar microstructure; see Fig. 35b), which causes a low density, low tensile intrinsic stress and porosity [73, 74]. This porosity induces a dependence of the film effective refractive index⁵ and stress on the environment of use. The *effective refractive index* is defined by the refractive index of the material, the environment and the porosity. It can be calculated with different models. Those models are valid for specific shape and size of porosity [75].

Indeed in ambient air, the pores will be partially filled with humid air and water molecules. In dry air, the coating will dry and the pores will empty from the water. This will change the effective refractive index of the films in the coating (this will be just a combination of the refractive index of the air and the material instead of the air, water and material) and the final power of the wavefront and stress of the coating. Finally, in vacuum, this is exacerbated and the pores will be emptied as much as possible changing the power and inducing a stronger stress that can lead to crazing. More dangerously than just water, other molecules like non-stoichiometric material, contamination can be trapped in those pores. Because of this, the influence of the environment will be an important topic in this work and porosities of different deposition methods will be measured in the chapter 4.

2.3.2.2 Ion Assisted Deposition (IAD)

The ion assisted deposition is the same principle as with classical e-beam deposition except that the growing film is bombarded by either neutral ions (like argon ions) just to densify the film or with reactive ions (like oxygen ions) to both densify the film and ensure the stoichiometry of the film. Those ions are bombarded with energies up to several hundreds of electron volts. This ion assistance improves the stoichiometry, morphology and density of films [70]. It helps also to change the stress from tensile to compressive which is required to avoid crazing [74].

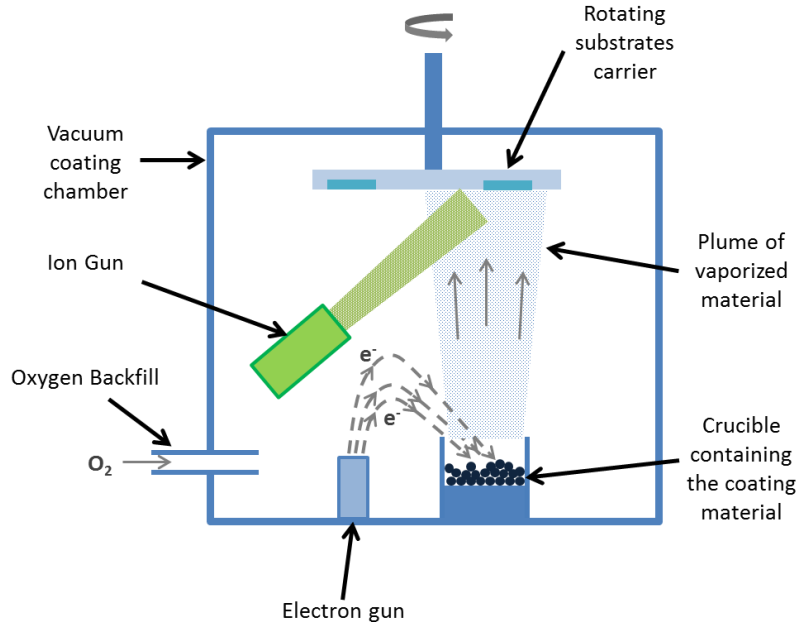


Fig. 36. Schematic of an IAD coater

⁵ In this manuscript this effective refractive index of the layer might be referred just as refractive index of the layer to simplify.

One disadvantage of the technique is that some ion guns contain a grid through which the ions are sputtered. This grid may introduce contamination inside the deposited film as residue of the grid can be sputter with the flow of ions.

This deposition method is the one currently used to manufacture Petal transport mirrors.

2.3.2.3 Plasma Ion Assisted Deposition (PIAD)

In this technique the assistance is realized with a plasma of Argon ions, as illustrated in Fig. 37, instead of the ion gun in the previously presented technique. This technique is used to overcome some of the structural disadvantages of evaporated layers at low or medium substrate temperatures. The advantage of the plasma assistance instead of the ion gun assistance is the absence of grid reduces the risk of contamination. By proper optimization of the deposition parameters, dense, water-free and low absorption oxide films with amorphous structure, smooth interfaces and low scatter losses can be deposited.

This deposition method is used to manufacture LMJ polarizer and deformable mirrors placed in the optical switch described in chapter 1.

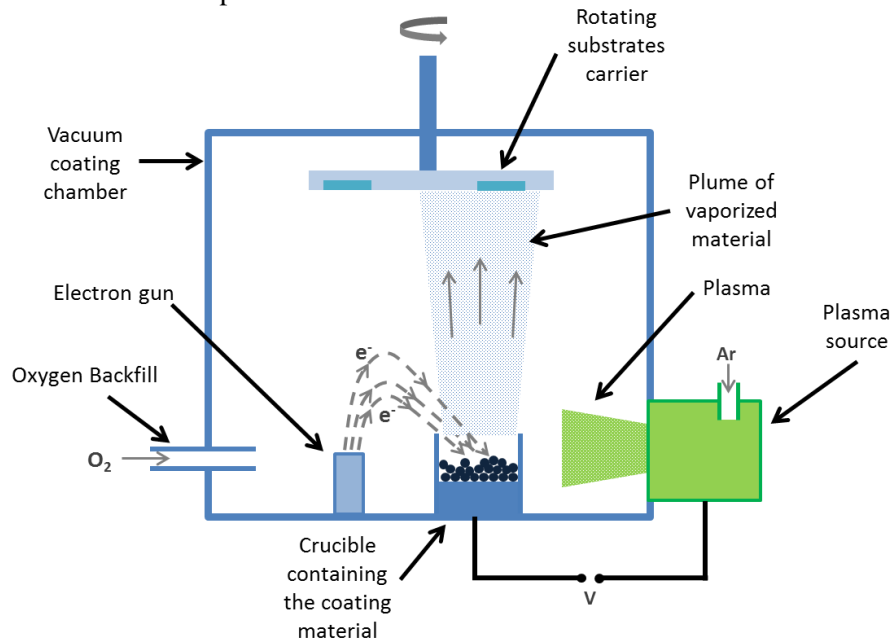


Fig. 37. Schematic of a PIAD coater

2.3.2.4 Ion Beam Sputtering (IBS)

In the Ion Beam Sputtering technique, argon ions are sputtered onto the target to dislocate lattice of the coating material and form a plume of detached molecules. Those molecules have then a very high kinetic energy and are projected toward the substrate where they will condensate. A secondary ion gun can be used to further densify the growing film; this is then Dual Ion Beam Sputtering (DIBS). The carrier rotates to improve uniformity and homogeneity and additional masks can be placed in front of the substrate carrier. The fact that IBS films are very dense (as dense as bulk material) limits the influence of the environment (and potentially the aging effect), but it induces a larger stress.

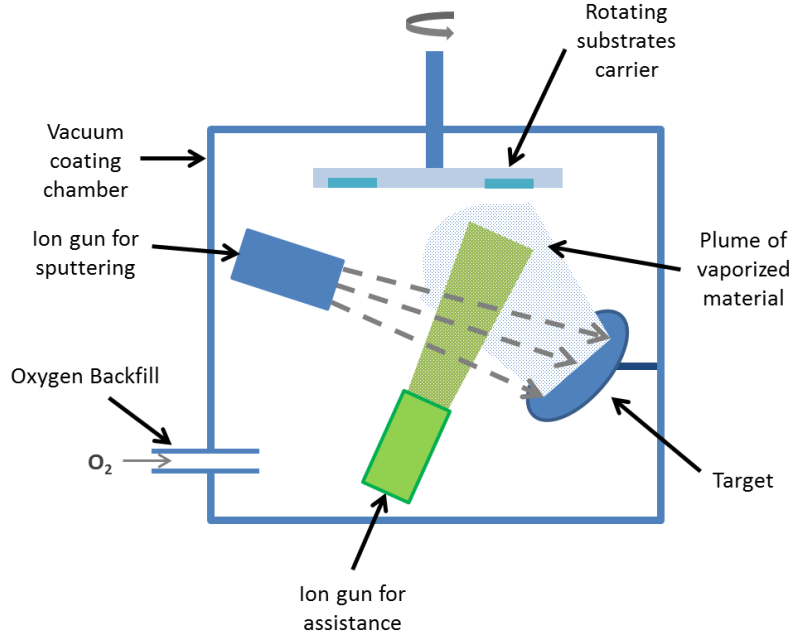


Fig. 38. Schematic of an IBS coater

This method is of interest in the context of high power laser beams since it has been noticed that high density films such as IBS coatings exhibit higher potential LIDTs for sub-picosecond applications [76]. Moreover IBS enables the deposition of mixture by using a target made of the different composite materials. Mixtures can be beneficial to improve the LIDT in sub-ps regime [41] and they will be presented in more details in chapter 3.

Large coatings are difficult to manufacture with IBS especially with strict specification on the uniformity and stress [77]. It requires an important expertise and has higher cost than more usual technique. This is why nowadays mirrors for pico-second laser facilities are not manufactured with IBS. But it is important to evaluate the potential of this technique and the improvement it can bring in the future.

2.3.3 Manufacturing Petal transport mirror

As stated at the end of the first chapter, our main concern is on Petal transport mirrors and how to improve their LIDT. Through this chapter we saw that spectral response, LIDT and stress of the Multilayer coatings depends on the materials, the design and/or deposition method. So in this sub-section, we present the specification of both Petal transport mirrors and how they are designed.

2.3.3.1 Specifications

The main specifications of Petal transport mirrors are listed in the following Table 2.

Table 2. Specification of the Petal transport mirrors

Substrate	Angle of incidence	Size [mm]	Spectral specification for		LIDT* [J/cm ²]	Pulse length	Environment of use
			p-polarization	s-polarization			
Boro-silicate BK7	45°	610x430x80	>99% Reflectivity from 1045 nm to 1061 nm for p- or s-pol**		4	700 fs	Vacuum

* In this table and throughout this manuscript, the Laser-Induced Damage Threshold (LIDT), in J/cm², is given in terms of normal beam fluences, meaning the fluence is calculated with the surface of the beam in a plane normal to propagation axis and not the surface projected at the angle of incidence on the sample.

** As exposed in the section presenting the architecture of Petal the Polarization of use of the transport mirrors is different depending on their position in the transport section. Therefore specification is either for one or the other polarization.

The quality of the coating must be very good regarding uniformity, rugosity and density of defect. The density of defect needs to be low to avoid damage initiation and then growth. For that same reason, the substrate polishing and cleaning requirements are very high.

The stress specification on the Petal mirrors coatings deposited onto BK7 substrates is that the coatings must not induced more than 1μm change of power on the wavefront: the integrate stress of the coating σe must be under 1 GPa/μm

2.3.3.2 Material, deposition method and design

The most ubiquitous materials chosen in optical coatings for high power Laser are the pair HfO₂ & SiO₂. Those materials have been chosen because of their high intrinsic LIDT in the nanosecond context. Through the years, manufacturers gain expertise in the deposition of those two materials. Thanks to that expertise, those two materials remain the one preferred in the industry as reported in [76] and that were naturally used in the sub-picosecond regime too. So, Petal transport mirrors (and LMJ mirrors/ polarizers) consist in an alternation of hafnia and silica layers. Those layers are deposited with Ion assisted e-beam deposition which made those layers relatively dense and reduce their sensitivity to environment without inducing to high stress that would risk crazing when used in vacuum.

Following that same trend of transferring the expertise acquired in nanosecond to sub-picosecond facility, the first design of Petal transport mirrors was a design similar to LMJ transport mirrors: a Bragg mirror design with a 2L overcoat of silica. But as exposed with the electric field enhancement in a structure similar to this design in Fig. 31, the overcoat contains a very high electric field intensity peak. Since laser damage in short pulse is associated with the electric field distribution, it is of interest to remove this overcoat that does not impact the reflectivity of the mirrors. We will then consider design based of the alternation of hafnia and silica quarter-wave optical thickness layers, with the first and last layer being a hafnia layer: (HL)ⁿH (with $n \in \mathbb{N}$). This Bragg based type of design will be referred either as QWOT design or reference design in the rest of this manuscript. The electric field intensity distribution in a QWOT design counting 21 layers is plotted in Fig. 39. The electric field

intensity distribution of Petal transport mirrors will be similar. The electric field maxima are located at the interfaces between each layer.

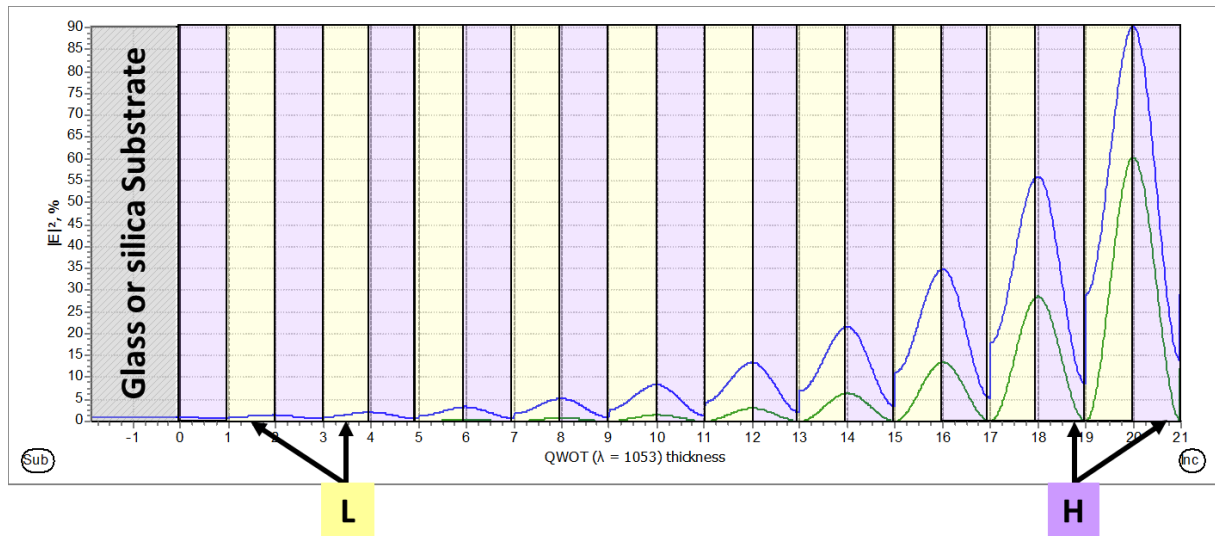


Fig. 39. Electric Field Intensity distribution for s (green) and p (blue) polarization in a $(HL)^{10}H$ stack where H is the high index material and L is the low index material. The incident medium, air, is located on the right of the stack and the substrate on the left.

Summary of Chapter 2

In this chapter, we introduced the basics needed to design multilayer dielectric coatings by first, defining what is a dielectric material. We then presented the principle of the thin-film coating with two iconic examples of single layers: an AR layer and absentee layer. The degree of liberty to engineer the spectral response can be increased by stacking multiple pairs of layers on one another. Such complex systems can be described by the matrix formalism inspired by Abelès work. Quarter-wave optical thickness (QWOT) of high and low refractive index materials multilayers provide an elegant analytic solution that warrants a high reflectivity. The matrix formalism enables the use of numerical software to calculate the electric field intensity distribution in the multilayer structure, which is required to predict the laser-induced damage threshold in short pulse of multilayer dielectric coatings using the following model:

$$LIDT_{mirror} = \min(LIDT_{singlelayer,H}, LIDT_{singlelayer,L}) \quad (2.27)$$

Where each layer is defined by

$$LIDT_{int} = LIDT_{singlelayer} \times EFI_{max} \quad (2.26)$$

With $LIDT_{int}$ the intrinsic LIDT and peak electric-field enhancement (EFI_{max})

This representation and throughout this chapter we identified the first two path of improvement of the initiation LIDT:

- **identifying other materials** with better refractive index and/or intrinsic LIDTs
- **working on new stack design** with engineered distribution of the electric field inside the dielectric layers

Finally, we presented the fabrication method of multilayer dielectric coating together with the specifications and technical solution of Petal transport mirrors. The choice of the deposition method is not neutral, because deposition method influences the films properties. A third path of improvement would be to consider other or improve deposition method of the Petal transport mirrors.

Petal transport mirrors are currently deposited using ion assisted deposition method. Their design is based on $(HL)^nH$ (with $n \in \mathbb{N}$) with hafnia as H and silica as L. For these designs, the electric field maxima are located at the layer interfaces.

As exposed in chapter 1, this current mirrors laser-induced damage threshold limits the overall power of Petal and need to be improved. In the following chapter, we will explore the first two path of improvement with a numerical approach to evaluate the potential of the materials and designs.

Chapter 3 Design and optimization of dielectric multilayers with high LIDT in the sub-ps regime

3.1	<i>Choice of materials</i>	56
3.1.1	Background on materials	56
3.1.1.1	Oxides & Fluorides	56
3.1.1.2	Other types of materials	59
3.1.1.2.1	Mixtures.....	59
3.1.1.2.2	Metals and semiconductors	61
3.1.2	Numerical parametric study	61
3.1.2.1	Influence of material index on the maximum of electric field intensity	62
3.1.2.2	Laser-induced damage threshold (LIDT) of multilayer mirror.....	63
3.1.2.3	Optimization of the two outer layers.....	66
3.2	<i>New Design: Optimization of multilayer stacks</i>	68
3.2.1	Background on design.....	68
3.2.1.1	Design with 3 different dielectric materials: ternary mirror stack.....	69
3.2.1.2	RISED	69
3.2.1.3	Metal Multilayer Dielectric (MMLD)	71
3.2.2	Background on design optimization algorithms	71
3.2.3	Presentation of the optimization algorithm	72
3.2.4	Example of application of our robust optimization algorithm.....	73
	Conclusion of Chapter 3	78

This chapter presents the theoretical study led to explore two different paths of improvement of the LIDT of multilayer dielectric mirrors. The numerical approach presented here is dedicated at evaluating the potential use of different materials and/or designs to increase the laser-induced damage threshold of multilayer mirrors.

3.1 Choice of materials

The previous chapter highlighted that the choice of material influences the mirror LIDT through their values of the intrinsic LIDT and refractive index. Indeed the refractive index modifies the electric field intensity values and distribution and also the spectral response. We demonstrated that with a higher index contrast, the mirror could reach the same reflectivity with fewer layers. This is due to the fact that the interfaces have higher reflectivity, which leads to lower electric field intensity values within the structure.

The present numerical study starts from a background about materials used in IR applications and their laser damage threshold. This will emphasize the difficulty to select a material based on its sole properties, namely without taking into account the stack design performance. In order to select adequate materials, we implemented a parametric numerical approach by considering the materials arranged within a multilayer stack built from a reference design, namely a design already adopted for the manufacturing of existing mirrors. The aim of our parametric numerical approach is thus to identify the best materials to make a mirror with the highest laser-damage threshold. And we will thus also present the criteria we consider as relevant to achieve this selection.

3.1.1 Background on materials

The materials used for building multilayer mirrors for high power ultrashort laser applications are typically the same as those developed in the context of nanosecond high threshold coatings, mainly oxides and fluorides [76].

3.1.1.1 Oxides & Fluorides

There are several reports suggesting a linear dependence between the intrinsic LIDT and the optical bandgap energy [43, 45, 42, 46], for different materials, as discussed in Chapter 2. When establishing this representation the authors presented and compared the performances of different materials. For example, Mero *et al.* [43] compared the measured LIDT value at 800 nm of 5 different oxides deposited by IBS, namely TiO_2 , Ta_2O_5 , HfO_2 , Al_2O_3 and SiO_2 , in sub-picoseconde regime. Their results displayed in Fig. 40 highlight this interest of the pair of low and high refractive index materials: silica and hafnia. Al_2O_3 which has an intermediate refractive index exhibits higher results than the HfO_2 .

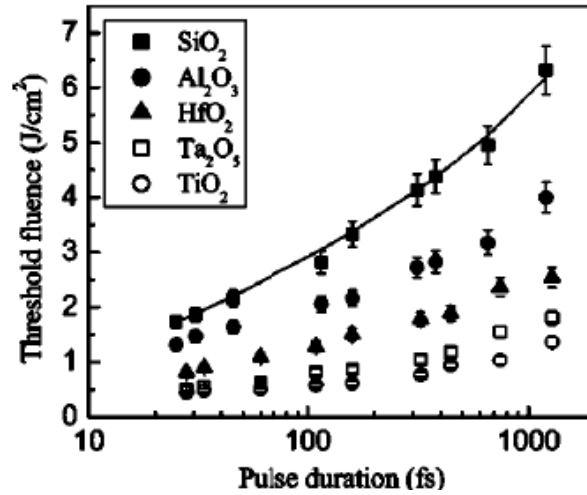


Fig. 40. Laser-induced damage threshold of monolayers (made of 5 different oxides) as function of the pulse duration. This figure extracted from [2] highlights the ranking among 5 oxides regarding their LIDT in sub-picosecond regime.

In 2014, Gallais *et al.* [42] led a larger study comparing what is called here “intrinsic LIDT” at 1030 nm for 500 fs pulse of bulk materials, oxide and fluoride single layers and mixtures of materials. This work includes results from thin films deposited with various deposition methods among which one can find the deposition methods described in chapter 2. They compared different materials via two plots giving the intrinsic LIDT, referred as “LIDT_{internal}”, as a function of the bandgap energy (cf. Fig. 41a) and the refractive index (cf. Fig. 41b). Both plots exhibited linear trends also observed in [46] on oxides deposited by e-beam.

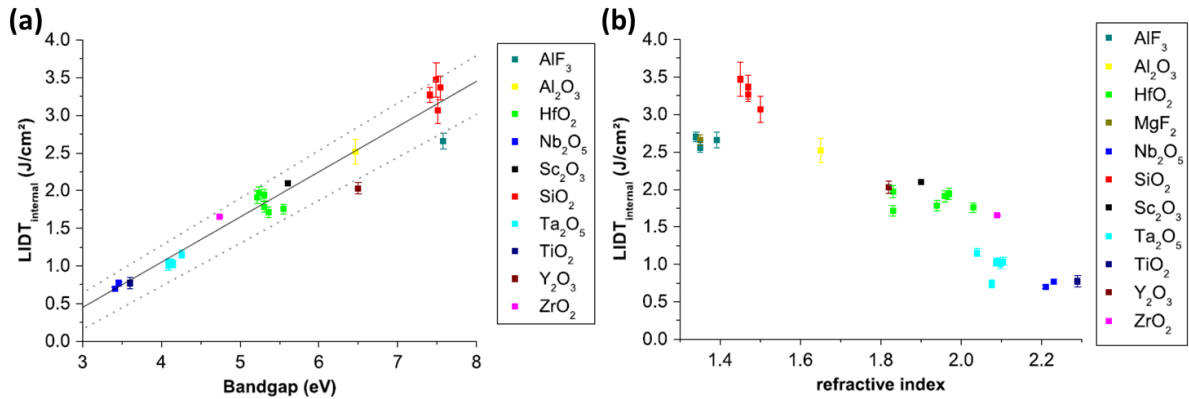


Fig. 41. (a) Intrinsic LIDT of a series of ten optical thin film materials tested in single-shot at 500 fs and 1030 nm as a function of the measured optical bandgap. Each point corresponds to a different sample. (b) Intrinsic LIDT of a series of eleven thin film materials tested in single-shot at 500 fs and 1030 nm, as a function of the refractive index at 1030 nm. Both figures are extracted from [42].

Nota on the Fig. 41: the plain and dotted lines in Fig. 41(a) correspond to the plot of the phenomenological law with its error margin established by Mangote *et al.* in [45], which is adapted from the Mero’s law. Fig. 41(b) includes MgF_2 samples for which the optical bandgap was not determined, and thus not displayed in Fig. 41 (a).

Table 3 reports the values of refractive index at 1030 nm, bandgap, and intrinsic LIDT for the materials presented in Fig. 41(b) (except AlF_3), together with the deposition method. For each material, we selected the best average layer (the layer with the most average properties).

Table 3. Optical constant of material thin films at 1030 nm with intrinsic LIDT determined from 1-on-1 procedure with 500 fs pulses (from [42] otherwise specified)

	Material	Refractive index (at 1030 nm)	Bandgap [eV]	Intrinsic LIDT [J/cm ²]	Deposition method
Low refractive index materials (L)	SiO_2	1.46	7.49	3.15±0.35	E-Beam
	MgF_2	1.35	unknown	2.66±0.07	not specified
	Al_2O_3	1.65	6.46	2.52±0.16	not specified
	Y_2O_3	1.82	6.5	2.03±0.08	E-Beam
	Sc_2O_3 _a	1.9	5.6	2.1±0.02	not specified
High refractive index materials (H)	Sc_2O_3 _b [41]		5.7	3.1	
	HfO_2 _a	1.94	5.31	1.78±0.07	E-Beam
	Ta_2O_5	2.09	4.10	1.05±0.04	Dual Ion Beam Sputtering
	ZrO_2	2.09	4.74	1.66±0.02	E-Beam
	Nb_2O_5	2.23	3.46	0.77±0.02	IBS
	TiO_2	2.29	3.6	0.77±0.08	E-Beam

Fig. 41 and Table 3 indicate that low refractive index materials tend to exhibit high intrinsic LIDT values and reciprocally except for MgF_2 . Indeed MgF_2 has lower refractive index and higher bandgap (approx. 10 eV) [42] than SiO_2 and exhibit lower intrinsic LIDT.

Concerning the high refractive index materials, Sc_2O_3 exhibits relatively high intrinsic LIDT values of 2.1 J/cm² or 3.1 J/cm² according to [41] and a refractive index around 1.9. The values related to HfO_2 are very close to those of Sc_2O_3 . The other materials with higher values of the refractive index such as Nb_2O_5 and TiO_2 exhibit lower values of intrinsic LIDT, namely around 1 J/cm² or lower.

Finally, Al_2O_3 exhibits an intermediate value of the refractive index and can be thus considered either as a high or low refractive index material. Its value of intrinsic LIDT of 2.52 J/cm² can be considered as high if Al_2O_3 is included in the group of high index materials and a low in the other case.

Recently in June 2019, Stolz [76] presented at the *Optical Interference Coating* conference the trends observed during the last ten years in the context of thin film laser damage competition, it was noticed that $\text{SiO}_2/\text{HfO}_2$ was the best pair of low and high refractive index materials in picosecond regime. More generally this pair is also the preferred one for Near Infra-Red high power laser application. However, it is worth noticing from Table 4 that SiO_2 and HfO_2 exhibit weak and intermediate mechanical properties, respectively. Based on this observation Stolz concluded that the

selection of HfO₂ among the high refractive index materials was questionable: has HfO₂ the right combination of mechanical and thermal properties or is its deposition better mastered and controlled?

Table 4. Materials properties of the oxides used in the context of thin film laser damage competition. Table extracted from [76]

Material property	SiO ₂	Al ₂ O ₃	Y ₂ O ₃	Sc ₂ O ₃	HfO ₂	ZrO ₂	Ta ₂ O ₅	Nb ₂ O ₅	TiO ₂
Refractive index	1.45	1.64	1.77	1.8	1.89	2.03	2.1	2.25	2.3
UV cutoff	160	180	225	230	250	300	300	320	350
Poisson ratio	0.17	0.27	0.31	0.30	0.29	0.27	0.27	0.34	0.28
Fracture toughness (Mpa)	0.6	4.1	2.5	1.5	2.3	4.5	3.5	3.0	2.9
Hardness (Gpa)	7	10.5		8.9	9.5	10.6	11.3	10.6	9.8
Shear Modulus (Gpa)	30	127	67	79	99	70	71	48	101
Bulk Modulus (Gpa)	35	230	136	168	205	142	129	139	214
Young's modulus (Gpa)	71	314	160	206	255	175	180	131	259
Melting temperature (deg C)	1710	2323	2425	2485	2900	2823	1872	1512	2103
Thermal Expansion (μ/m-K)	0.65	9.6	8.1	7.3	6	7.25	5	5.6	10.1
Specific Heat (J/kg-K)	705	950	135	130	120	480	133		690
Thermal Conductivity (W/m-K)	1.4	25.2	13.6	16.5	1.1	2.2	0.45	1	0.45

From this background on materials, one can notice that **SiO₂ and HfO₂** remain the **preferred pair of materials** to design multilayers dielectric components used **in high power lasers**.

3.1.1.2 Other types of materials

3.1.1.2.1 Mixtures

Other studies [63, 45] demonstrated that significant increase of bandgap and laser damage resistance could be obtained by choosing specific mixtures.

These mixtures are manufactured with IBS by using targets made of multiple pure materials. Gallais *et al.* reported in [42] on several of these mixtures, see Fig. 42 and concluded that the mixture providing the highest LIDT value was made of Al₂O₃ and AlF₃. The Sc₂O₃ - SiO₂ mixture is finally considered to be a perfect candidate for the high refractive index material since it exhibits the highest LIDT value (see grey dots in Fig. 42 (b)).

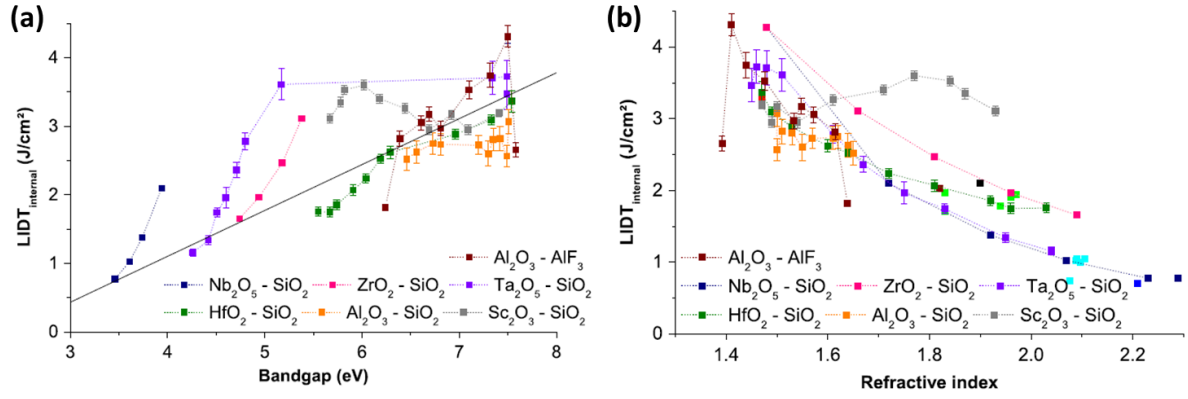


Fig. 42 (a) Intrinsic LIDT values of thin films made of seven binary mixtures and tested in single-shot at 500 fs and 1030 nm as a function of the measured optical bandgap. Each point corresponds to a different sample. The labels are an indication of the composition of the film (e.g., $\text{Nb}_2\text{O}_5 - \text{SiO}_2$ indicates a co-deposition of silica and niobia). (b) Intrinsic LIDT values of thin film made of seven binary mixtures and tested in single-shot at 500 fs and 1030 nm, as a function of their refractive index at 1030 nm. Both figures are extracted from [42]

Nota on Fig. 42: The dotted lines are guides for the eyes and they link the samples of the same set of deposition. The black line corresponds to the trend observed for pure materials established in [45]. This figure also includes some samples for which the optical bandgap was not determined.

Mende *et al.* [41] reported on that the right proportion of the $\text{Sc}_2\text{O}_3 - \text{SiO}_2$ mixture can drive to LIDT value higher than those obtained from each single pure material in Fig. 43, the mixture with 75% Sc_2O_3 and 25% SiO_2 exhibits the highest LIDT value; with an intrinsic LIDT around 3.5 J/cm².

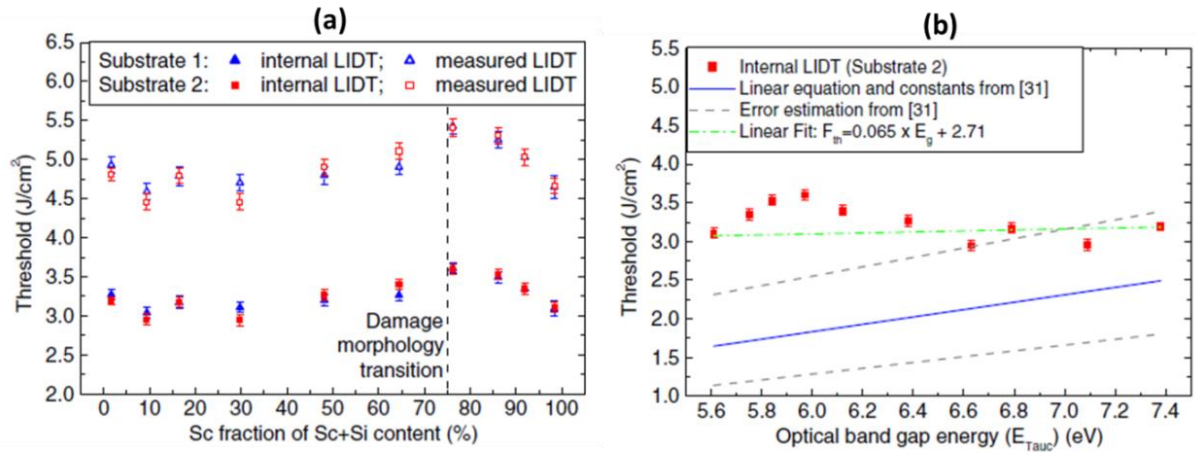


Fig. 43. (a) Measured and intrinsic (here referred as internal) 1-on-1 LIDT at 1030 nm as a function of the Sc fraction of the Sc+Si content for two types of substrate. The layers are deposited in a reactive deposition process which means that the target materials are metals that are oxidized during the deposition. (b) Comparison between the internal LIDT values as function of the optical bandgap energy and the values calculated from the numerical model (eq. 2.25). Both figures are taken from [41].

This intrinsic LIDT value of this mixture, 3.5 J/cm², is higher than all the intrinsic LIDT of the pure material thin films reported in Table 3 which points out the interest of considering mixtures.

3.1.1.2.2 Metals and semiconductors

The previously presented mixtures are obtained from the oxides or fluorides materials classically considered for those IR. Their properties vary but remains in the same order of magnitude.

More exotic materials such as metals and semi-conductors can be considered in this study. Those exotic materials have completely different properties which can be interesting. For example, semiconductors exhibit very high real part of refractive index. This could help reducing considerably the electric field intensity in a mirrors stack.

Gallais *et al.* [42] reported some intrinsic LIDT values of semiconductors in bulk materials and metals in thin films summarized in Table 5.

Table 5. Optical constants of material from [42] at 1030 nm and intrinsic LIDT determined with 1-on-1 procedure for 500 fs pulses

	Material	Refractive index (at 1030 nm)	Bandgap [eV]	Intrinsic LIDT [J/cm ²]	Deposition method
Semi-conductors	Germanium (Ge)	4.42 + 0.15 i	0.7	0.031±0.005 0.043±0.003	*From [78]
	Silicon (Si)	3.5	1.1	0.91±0.05 0.55±0.04	*From [78]
Metals	Silver (Ag)	0.28 + 7.5 i [78]		0.094±0.011	RF sputtering
	Platinum (Pt)	3.55 + 5.92 i		0.015±0.001	RF sputtering
	Gold (Au) [79]	0.08-4.6 i		0.025 (Measured LIDT at 400 nm and 200 fs)	

The values presented in the Table 5 shows that these materials alone are not well suited for our application. They required specific design (Metal Multilayer Dielectric design for example) and adaptation in order to be used to design mirrors for high power laser applications.

Nota about metals and semiconductors: During this PhD study, Silicon, Germanium and Chromium single layers were laser damage characterized. The final intrinsic LIDT values were 0.041 J/cm² for silicon, 0.012 J/cm² for germanium and 0.006 J/cm² for Chromium. These results are lower than the one presented in the Table 5 which reduced even more the potential interest of metals and semiconductors. These results are so low that they will not be further developed in the rest of this manuscript and the metal based designs will not be considered in this work. Still in order to perform a more exhaustive background on designs the principles of MMLD will be presented later in 3.2.1.3.

3.1.2 Numerical parametric study

This parametric study is performed in three steps. The first step is focused on evaluating the influence of the refractive indexes of both materials on the electric field intensity maximum in a classical design. The following step aims at judging the influence of the parameters of the high index material on the laser-induced damage threshold. The final step of this parametric study includes a first step toward optimizing the design and the influence of this optimization on the choice of material.

In Chapter 2 was presented the matrix formalism to calculate the electric field intensity in a MLD structure. Here, we consider a reference design counting 37 QWOT layers deposited on a fused silica substrate illuminated by a 1053 nm collimated beam under an angle of incidence of 45° and with air as superstrate. The design can be described as follows $(HL)^{18}H$. It counts enough layers to ensure a sufficiently high reflectivity compared to the specifications of the mirrors dedicated to the beam transport.

3.1.2.1 Influence of material index on the maximum of electric field intensity

In the first step of this numerical parametric study, the electric field intensity is calculated for different values of the low and high refractive index varying with 20 steps from 1.3 to 1.55 and from 1.65 to 2.2 respectively. Then the maxima of the electric field intensity in each material are retrieved at each step from the electric field intensity calculation in the whole structure. One should note that the optical thickness of each layer of the design is varying when changing the values of the refractive indices.

In a QWOT design the maximum of electric field intensity is located at the interface between the two outer layers, as demonstrated in Chapter 2 (Fig. 39). Therefore the value of EFI_{\max} becomes the same for both materials. The calculated EFI_{\max} values are displayed in Fig. 44 as a function of the high refractive index (horizontal axis) and low refractive index (vertical axis) for both p - (Fig. 44(a)) and s - (Fig. 44(b)) polarization states. The coordinates of a few pairs of high / low refractive index materials are superimposed to the density plot of electric field intensity.

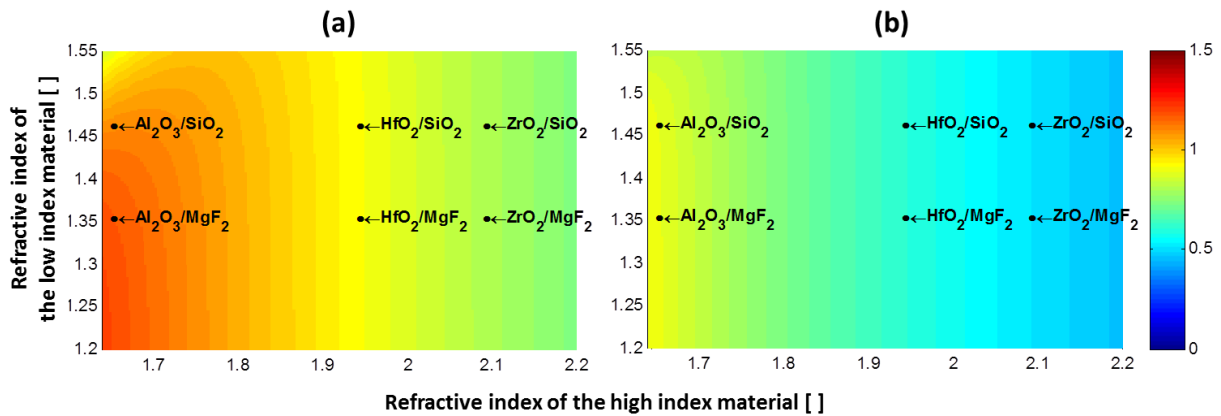


Fig. 44. Maximum of the Electric Field Intensity (EFI_{\max}) calculated in the reference QWOT stack composed of two materials under the design $(HL)^{18}H$ for the p - (a) and the s - (b) polarization states as a function of the high (x axis) and low (y axis) refractive index.

The values of refractive index explored in this numerical simulation are including most of the values corresponding to the pure materials already presented in the Table 3. The value of the refractive index of a given binary mixture is then expected to be found between the values of each pure materials, its exact value depending on the proportion of each material to compose the binary mixture. Consequently, the range of refractive index values displayed in Fig. 44 allows also taking into account the case of binary mixtures. To facilitate the reading of the Fig. 44 only a short selection of pairs of pure materials is shown.

The density plot exhibits vertical colored patterns indicating that for this type of QWOT design characterized by a high refractive index material for the outer layer, the EFI_{\max} is mainly influenced by the high refractive index. Moreover one can note that the EFI_{\max} is minimized for the highest values of the high refractive index. Indeed, with the highest values of the high refractive index on the outer layer, the index contrast between the incident medium (air) and the first layer is maximized, which induces a high reflectivity at the first interface and means that fewer portion of the electric field is entering the stack. Based on the results of numerical simulation displayed in Fig. 44, one can conclude that the high refractive index should be as high as possible, while no specific recommendation can be given about the low refractive index. Finally, the best candidates to build multilayer mirrors with reduced EFI_{\max} are either ZrO_2 / SiO_2 or ZrO_2 / MgF_2 . At the opposite, the pairs Al_2O_3 / SiO_2 and Al_2O_3 / MgF_2 are giving the highest values EFI_{\max} and should be excluded from the selection. Let us point out that, based on the intrinsic LIDT values given in Table 3 only, Al_2O_3 should have been selected among the list of high refractive index materials. The difference between the results provided by Table 3 (individual $LIDT_{\text{int}}$) and Fig. 44 (EFI_{\max}) highlights the fact that the whole stack of layers must be considered instead of individual layers separately, to select the best materials.

To conclude, the LIDT of the entire mirror depends not only on the EFI_{\max} but also on the intrinsic LIDT of each layer. Thus we need to also consider the intrinsic LIDT of the materials.

3.1.2.2 Laser-induced damage threshold (LIDT) of multilayer mirror

The objective of this section is to consider the influence of the intrinsic LIDT on the LIDT of the mirror. As the high index materials modify the most the electric field intensity values, we will first evaluate the advantage of considering other high refractive index values in the reference QWOT design (HL)¹⁸H for a fixed low index value. Thus, the LIDT values of the entire mirror are calculated as a function of both the high refractive index n_H and the intrinsic LIDT value of the high refractive index material, hereafter denoted $LIDT_{\text{int,H}}$. We did the calculation for two different types of low refractive index materials, namely SiO_2 and MgF_2 as they exhibit different LIDT values, hereafter denoted $LIDT_{\text{int,L}}$. This calculation allowed assessing the influence of the low refractive index material on the LIDT performance of the whole mirror.

Practically, the values of the high refractive index n_H were tuned from 1.6 to 2.4 while the values of the intrinsic LIDT were tuned from 0.5 J/cm² to 5 J/cm² in order to take into account all the materials presented in Table 3 and even more. Then, the electric field intensity was calculated within the multilayer stack and the two maxima $EFI_{\max,H}$ and $EFI_{\max,L}$ in the high and low refractive index materials respectively were recorded. Finally, the LIDT of the high and low refractive index materials denoted respectively $LIDT_H$ and $LIDT_L$ were evaluated by calculating the ratio between the intrinsic LIDT and the EFI_{\max} in each material, meaning $LIDT_H = LIDT_{\text{int,H}} / EFI_{\max,H}$, and $LIDT_L = LIDT_{\text{int,L}} / EFI_{\max,L}$ (cf. model presented in Chapter 2). The LIDT of the entire multilayer is finally considered to be equal to the minimum value between $LIDT_L$ and $LIDT_H$ and is displayed as a density plot for a multilayer with either SiO_2 (Fig. 45) or MgF_2 (Fig. 46) as the low refractive index

material. Below the horizontal purple lines, $LIDT_L > LIDT_H$ so the laser damage occurs in the high refractive index material, and reciprocally.

Fig. 45 and Fig. 46 show that the calculated LIDT values are significantly different for the two states of polarization. For example, with HfO_2 and SiO_2 , the LIDT performance is 1.93 J/cm^2 for the p -polarization (Fig. 45(a)) and 2.90 J/cm^2 for the s -polarization (Fig. 45(b)). This result indicates it might be more efficient to specifically design a multilayer mirror depending on the polarization. However, one can notice that the values of LIDT for the entire mirror evolve in roughly the same way according to the two states of polarization.

Finally, it is interesting to notice from Fig. 45 that two materials such as Al_2O_3 and ZrO_2 characterized by very different values of refractive index, namely 1.65 and 2.09, respectively, and intrinsic LIDT (2.52 J/cm^2 and 1.66 J/cm^2 respectively) provide similar values of LIDT for multilayer mirrors made of silica as the low refractive index material. However, let us point out that these two materials were identified in Table 3 as the best for Al_2O_3 and almost the worst candidates for ZrO_2 , when considering only the intrinsic LIDT values. At the opposite, Al_2O_3 was considered as the worst and ZrO_2 as almost the best candidates when considering the EFI_{max} values in the reference stack (cf. Fig. 44).

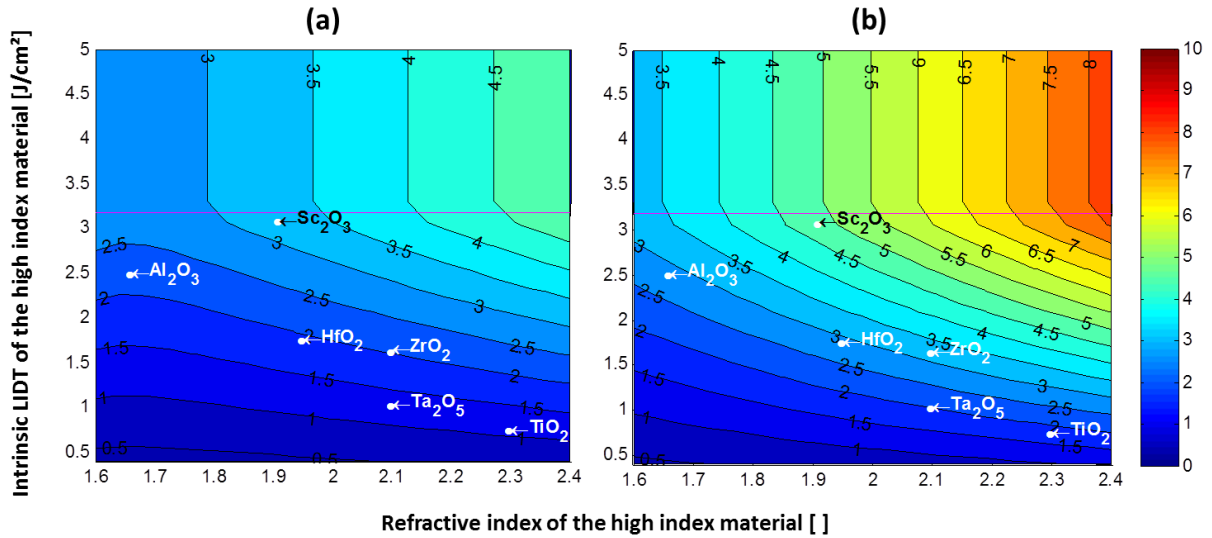


Fig. 45. Calculated LIDT values of the reference QWOT multilayer mirror $(HL)^{18}H$ (colors) for the (a) p - and (b) s -polarizations as a function of the high refractive index values (x axis) and intrinsic LIDT values of the high refractive index materials (y axis). The low refractive index is silica. Below the horizontal purple line (resp. above) laser-damage occurs within the high (resp. low) refractive index material.

Based on the results displayed in Fig. 45, the pair Sc_2O_3 / SiO_2 features the highest LIDT values for the entire mirror, namely 3.25 J/cm^2 for the p -polarization (Fig. 46(a)) and 4.82 J/cm^2 for the s -polarization (Fig. 45(b)). Sc_2O_3 consequently represents the best compromise between the value of the high refractive index and those of the intrinsic LIDT. Finally, based on Fig. 45, it is possible to compare the high refractive index materials and then select one of them through its influence on the general LIDT of silica-based multilayer mirrors of the same architecture.

The relative position of the materials is similar when the low refractive index material is MgF_2 (Fig. 46) or SiO_2 (Fig. 45) but the calculated LIDT values are different. In addition, the limit displayed by the horizontal purple line is 2.66 J/cm^2 for the stacks composed of MgF_2 , to be compared to 3.15 J/cm^2 for the stack composed of SiO_2 . The intrinsic LIDT of MgF_2 is lower than the one of SiO_2 and so are the calculated values of LIDT of the whole stacks using magnesium fluoride as low index material.

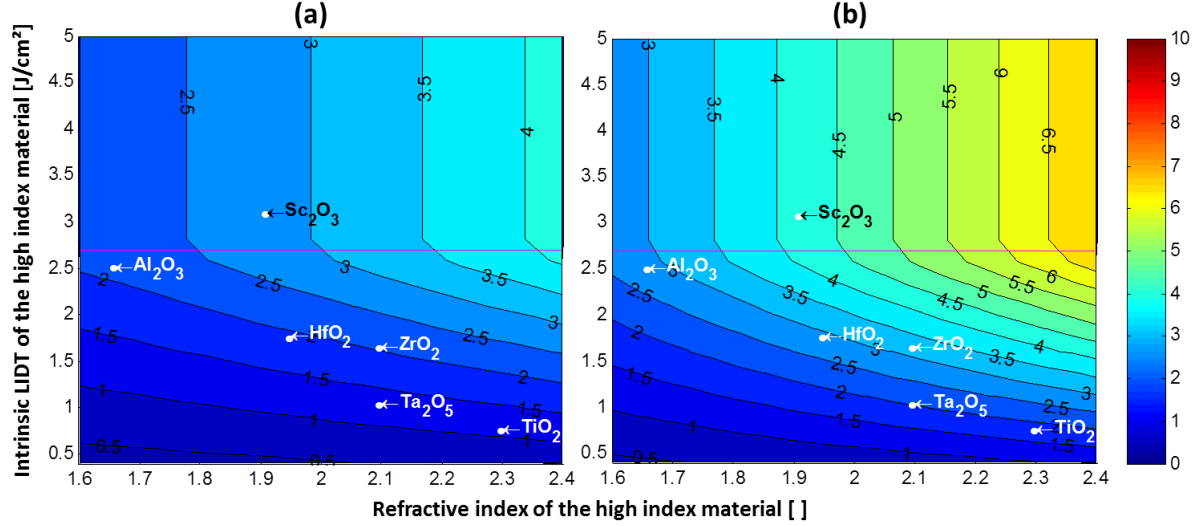


Fig. 46. Calculated LIDT values of the reference QWOT multilayer mirror (HL)¹⁸H (colors) the (a) *p*- and (b) *s*-polarizations as a function of the high refractive index values (*x* axis) and intrinsic LIDT values of the high refractive index materials (*y* axis). The low refractive index is magnesium fluoride. Below the horizontal purple line (resp. above) laser-damage occurs within the high (resp. low) refractive index material.

As presented in Fig. 41(b), a dependency of the intrinsic LIDT with the refractive index has been observed in [42, 45, 46] which means that high refractive index materials tend to exhibit low intrinsic LIDT. Thus the upper right quarter of these density plots presents performance of materials with for now unwitnessed combination of refractive index and intrinsic LIDT, LIDT_{int} . It is interesting to consider those potential performances in the eventuality of engineering new materials with tunable refractive index or intrinsic LIDT such as mixture. Properly proportioned mixture of materials [41] such as Sc_2O_3 with ZrO_2 or TiO_2 can produced hybrid materials with properties placing them in this upper right quarter of those abacuses. The aim of these mixtures will be to increase the refractive index of the material compared to Scandia without degrading the intrinsic LIDT. For example, a mixture of Sc_2O_3 and TiO_2 will have a high refractive index (between 1.9 and 2.3) and could exhibit an intrinsic LIDT around (or even higher than) 3.1 J/cm^2 which is the intrinsic LIDT of Sc_2O_3 pure material. With such a high refractive index material, the final mirror could exhibit LIDT higher than 3.5 J/cm^2 for *p*-polarization and 5 J/cm^2 *s*-polarization.

These density plots will be used as abacus to evaluate potential of high index materials. One only required the knowledge of the refractive index and intrinsic LIDT of the material to superimpose it on the abacus.

3.1.2.3 Optimization of the two outer layers

Fig. 39 reveals that the two outer layers of a (QWOT design) mirror are exposed to the highest electric field intensity values. It is then possible to improve the LIDT of the entire mirror by optimizing the thicknesses of these two outer layers as proposed by Apfel *et al.* in [39] who presented how to improve the laser damage threshold of multilayer mirrors by shifting the EFI_{\max} position inside the material exhibiting the highest intrinsic LIDT value. We thus applied this optimization method not only by shifting the EFI_{\max} position to the most resistant material but also by equalizing the LIDT value to the previous calculation: $\frac{LIDT_{int,L}}{EFI_{\max,L}} = \frac{LIDT_{int,H}}{EFI_{\max,H}}$. This strategy allowed to optimize the design of multilayer mirror, hereafter referred as the **balanced design**. The new results deduced from this design are displayed in Fig. 47 and Fig. 48.

Fig. 47 displays the LIDT values of a multilayer mirror with the balanced design characterized by $(HL)^{17}H \times L y H$ with silica as the low refractive index material for different values of high refractive index and for the p - (a) and s -polarization (b). The balanced design was calculated by using a Matlab function that minimized the difference between the LIDT of the low and high refractive index materials: $LIDT_L - LIDT_H$. The final LIDT value of this optimized design (color level in Fig. 47) is equal to the minimal values between $LIDT_L$ and $LIDT_H$. With this optimization, when $LIDT_L > LIDT_H$, the thickness of the outer high refractive index layer, denoted y in the design representation, is reduced and those of the adjacent low refractive index layer, denoted x in the design representation, is increased, and reciprocally.

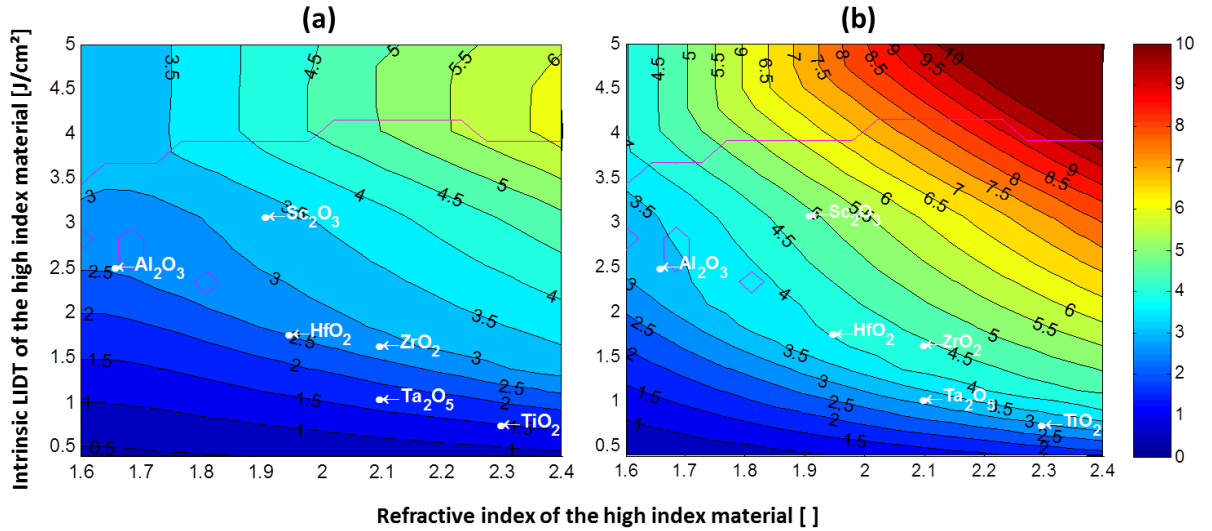


Fig. 47. Calculated LIDT values of multilayer mirrors based on a balanced design, namely the reference QWOT design modified, with the two outer layer thicknesses optimized, (colors) for (a) p - and (b) s -polarization as functions of high refractive index values (x axis) and intrinsic LIDT values of the high refractive index materials (y axis) for the p (left) and the s (right) polarizations. The low refractive index material is silica. Below the horizontal purple line (resp. above) laser-damage occurs within the high (resp. low) refractive index material.

The relative position of the materials is almost unchanged between the balanced and reference designs, but all the LIDT values are higher with the balanced design, see Table 6. More precisely, the

HfO₂ / SiO₂ pair, the overall LIDT is thus increased by 31% for the *p*-polarization (see Fig. 45 (a) and Fig. 47 (a)) and by 33% for the *s*-polarization (see Fig. 45 (b) and Fig. 47 (b)).

Table 6. Comparison of the LIDT of the reference and balanced design for different pair of materials

Pair of materials (H / L)	LIDT in [J/cm ²] for the <i>p</i> -polarization		Improvement of the LIDT between the two designs
	For the reference design (HL) ¹⁸ H	For the balanced design (HL) ¹⁷ H xL yH	
Sc ₂ O ₃ / SiO ₂	3.2	3.4	6%
Al ₂ O ₃ / SiO ₂	2.25	2.6	15%
ZrO ₂ / SiO ₂	2	2.7	35%
HfO ₂ / SiO ₂	1.9	2.5	31%
Ta ₂ O ₅ / SiO ₂	1.2	1.6	33%
TiO ₂ / SiO ₂	1.1	1.5	36%

Table 6 highlights that the improvement between the two designs is not the same for all the pair of materials. A balanced design (and so is an optimized design) is specific to a pair of material. The improvement of the design is depending on the ratio of the two intrinsic LIDT values: $LIDT_{int,L}/LIDT_{int,H}$. Higher this ratio is, higher the change of design will be beneficial.

The same calculation was run in the case of magnesium fluoride as the low refractive index and the results are displayed in Fig. 48, driving to the same conclusion, meaning that the balanced design does not change the relative position between the materials, but increases the LIDT values. More precisely, when considering Scandia as the high refractive index material, the overall LIDT value increases from 2.7 J/cm² (cf. Fig. 46 (a)) to 3.2 J/cm² (cf. Fig. 48 (a)) for the *p*-polarization and from 4.25 J/cm² (cf. Fig. 46 (b)) to 4.75 J/cm² (cf. Fig. 48 (b)) for the *s*-polarization.

The density plots presented in Fig. 47 and Fig. 48 allow evaluating the resistance to laser damage of some selected materials in the case of the balanced design. They also allow evaluating the limits of the improvement approach of changing the materials involved in the mirror stack. With the only characterization of the materials based on single layers we will be able to superimpose its characterized values on these abacuses. This will allow judging and quantifying the improvement brought by considering these materials rather than the reference pair of materials.

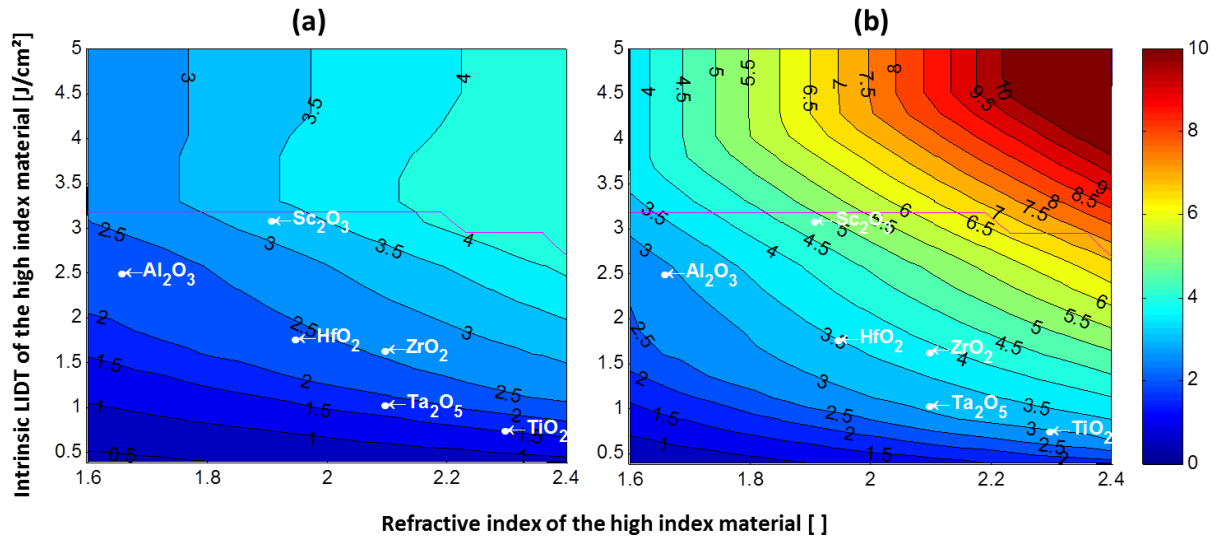


Fig. 48. Calculated LIDT values of multilayer mirrors based on a balanced design, namely the reference QWOT design with the two outer layer thicknesses optimized, $(HL)^{17}H \times L yH$, (colors) for (a) p - and (b) s -polarization as functions of high refractive index values (x axis) and intrinsic LIDT values of the high refractive index materials (y axis) for the p - (left) and the s - (right) polarizations. The low refractive index material is magnesium fluoride. Below the horizontal purple line (resp. above) laser-damage occurs within the high (resp. low) refractive index material.

To conclude, the highest LIDT values presented in this section were based on the balanced design composed of a QWOT stack of layers except for the two outer layers for which the thickness has been optimized to enhance the LIDT value. This approach is the current state of the art. However, there is still room for improvement. Firstly, the robustness of the solution toward manufacturing errors (variation of the deposited thicknesses and refractive index) is not taken into account. Secondly, there is no demonstration that it is the best possible design. This point is addressed in the next section.

3.2 New Design: Optimization of multilayer stacks

3.2.1 Background on design

Considerable work has been reported on the engineering of the electric field intensity on multilayer coatings. On binary mirror stacks, Apfel modified the upper layers to reduce the electric field intensity in the most vulnerable to laser damage material: the high refractive index material [39].

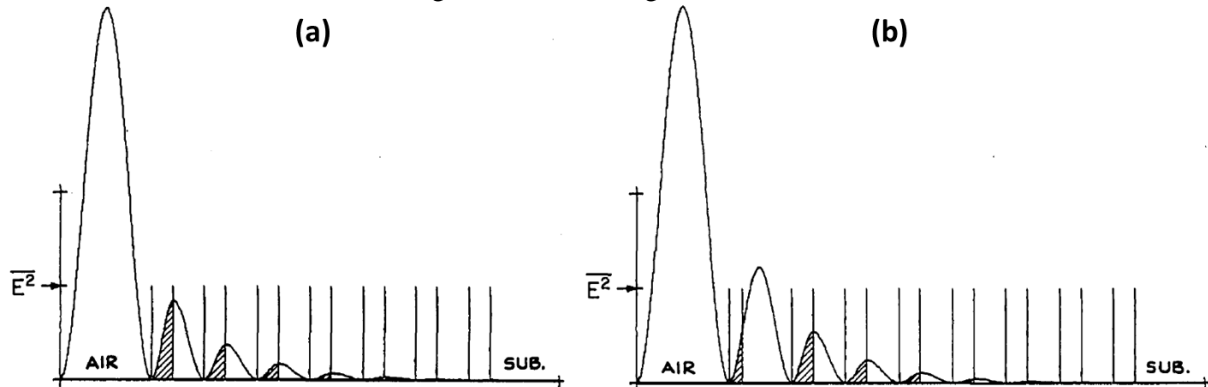


Fig. 49. (a) Electric field intensity distribution in a $(HL)^6H$ design and (b) Electric field intensity distribution in Apfel design. The high refractive index layers are indicated by cross-hatch shading. Figure taken from [39].

This approach, illustrated with Fig. 49, and formulated by Apfel in 1977, has allowed reaching significant improvement, as illustrated in the previous paragraph with Table 6 and the balanced design performance. These improvements were sufficient so this topic has not been further investigated for years or simply by following the same approach [80]. This approach has been extended to a higher number of layers (also called reduced standing wave design), it was proved to improve the LIDT in the short pulse regime [81, 82, 83, 84]. However, the experimental results were not always in good agreement with the theoretical predictions, probably due to manufacturing errors [85]. Indeed, a slight variation of thickness or refractive index of the deposited materials is expected to change the position of the peaks of the electric field intensity within the stack and thus strongly influence the LIDT performance of a given design.

In the quest of improving the laser damage threshold of mirrors, before optimizing further binary stacks other types of designs could be considered.

3.2.1.1 Design with 3 different dielectric materials: ternary mirror stack

Firstly, one could consider advanced designs based on more than two dielectric materials. This strategy has been adopted by Bellum *et al.*, Patel *et al.* and Schiltz *et al.* [83, 86, 80]. They proposed ternary mirrors stacks where the pursued idea is to use high refractive index materials with higher intrinsic LIDT where high electric field intensities could not be avoided, and a higher index material (albeit less damage resistant) elsewhere to reduce the number of pairs necessary to reach the desired reflectivity. Their conclusion is that hafnium dioxide layers should be preferred to titanium or tantalum oxide layers to compose the outer layers. Hafnium dioxide is already considered here as our standard the high refractive index material. Consequently, even if the use of more than two materials could potentially improve the stress properties [87], this approach displays limited interest in our present study.

Moreover, these ternary based designs are in fact two binary structures stacked on one another. Developing a method to optimized binary structure could then be easily adapted to this type of binary designs. In consequence, designs including more than two materials will not be discussed in this thesis and the following developments will concern only binary stacks made of sequence of high and low refractive index materials.

3.2.1.2 RISED

Increasing the LIDT value of a mirror can also be achieved by using the *RISED* (Refractive Index StEps Down) designs [88], which consists in using differently proportioned mixtures in the layers affected by the highest field strength. The layers with the higher electric field intensity peaks will have the highest proportions of the low refractive index material and the layers closest to the substrates with the lowest electric field intensity enhancement will have higher proportions of the high refractive index materials with a lower intrinsic LIDT. Looking at the refractive index profile of the coating helps understanding the RISED principle.

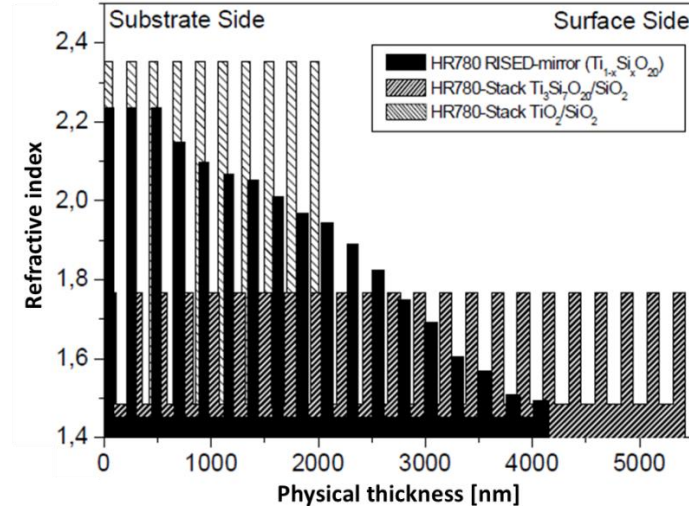


Fig. 50. Refractive indexes profiles of three different designs: two classical binary designs and a RISED design (black profile). The figure is extracted from [88]

In Fig. 50 extracted from [88], refractive indexes profiles of three different designs are presented. Two of these designs with the stripped design are classical binary stacks. The third design in black is the *RISED* design with its outer high refractive index layers exhibiting different refractive indexes.

Jupe *et al.* [88] reported that the damage threshold for a 150 fs pulse of TiO_2 and Ta_2O_5 optics could be multiplied by two by using mixture of metal oxides and silica in a *RISED* structure, see Fig. 51.

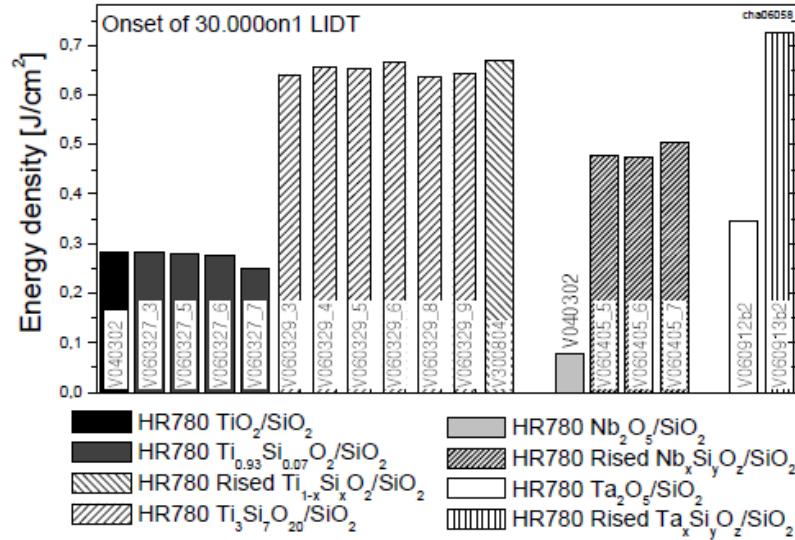


Fig. 51. Overview of the LIDT values for a 150 fs pulse at 780 nm in the case of a high reflector made of stacks of oxide material or mixture or RISED designs. Figure taken from [88]

Applying the same strategy to mirror designs at 355 nm, Jensen *et al.* [89]. showed that mixing silica and hafnia within *RISED* structures could improve the laser damage threshold of the mirror. However, the *RISED* [89] structures are specific to the use of mixtures and will thus not be considered as first approximation, but the algorithm developed and presented in this chapter could be adapted to *RISED* structures in the future.

3.2.1.3 Metal Multilayer Dielectric (MMLD)

Finally, another path to improve LIDT of mirrors could be to consider Metal Multilayer Dielectric (MMLD) mirrors rather than MLD mirrors. MMLDs consist of a dielectric stack deposited onto a metallic layer coated directly on the substrate. This path is explored theoretical in [79] by inserting a gold layer under HfO_2 and SiO_2 dielectric stack, see Fig. 52. The metallic layer ensures a high reflectivity and allows reducing the number of dielectric bi-layers. The structure is designed to have electric field strengthened in the MLD part of the stack, so laser damage is not located in the metallic layer but in the MLD part. In order to improve the laser damage of MMLD components designed as such, it is necessary to improve the MLD structure. Then, the method developed and presented in what follows could be adapted to MMLD structure. We will not detail MMLD structure more here since the manufacture of this kind of thin-film coatings is difficult because of the low adherence of the dielectric stack on the gold layer. The low adherence is even more critical when those coatings are used in vacuum which is required here.

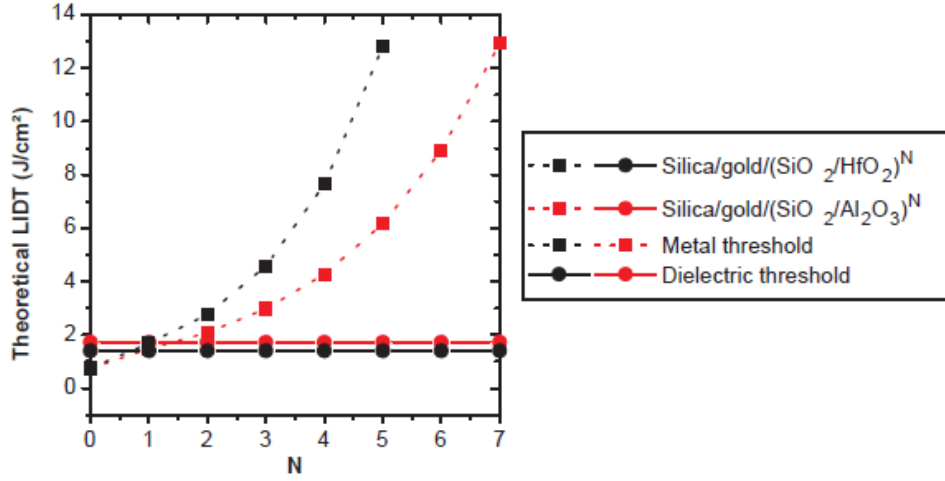


Fig. 52 Case of MMLD mirrors with different high index materials: calculation of the fluence needed to reach the melting point of the gold film (dotted lines) and comparison to the fluence needed to initiate damage in the high index material (plain line). Figure taken from [79]

3.2.2 Background on design optimization algorithms

For this purpose, optimization algorithms such as the gradient optimization proposed by Demichelis *et al.* [90] or the needle optimization [91, 92] provided for example in the Optilayer software [93] can be used. More recently memetic algorithm [94] based on a genetic algorithm to generate new designs have shown interesting results in the design optimization for broadband applications and could be transposed to the context of laser-induced damage.

Those algorithms operate by minimizing a function of merit to be defined depending on the parameters to optimize: such as reflectivity, group delay dispersion, spectral width, electric field, etc. Taking into account the different and sometimes conflicting goals, it can be difficult for the algorithm to converge toward a minimum of the function of merit. And when a minimum is found it can be only one of the local minima of the function and not the global minimum.

The final solution derived from these algorithms might be either impossible to manufacture or simply not sufficiently robust to manufacturing errors. Some commercially available algorithm, such as the one provided in OptiLayer, propose robustness tests. But those robustness tests are not implemented as part of the solution selection but designed as a post treatment process.

In most of the commercial solutions, the optimization algorithm does not provide satisfying optimization of the design based on the electric field intensity distribution consideration which is central in this study. For example, in Optilayer, the electric field targets are either minimize or maximize and are affected by materials and not specific to a layer position. When the E-field targets of both materials are set to minimize the final solution proposed by OptiLayer is a classical QWOT design.

For all these reasons, we decided to develop our own optimization algorithm aimed at optimizing the electric field distribution in the outer layers and including the robustness as a criterion of selection of the best solution.

In what follows, we present a method to obtain a design related to a “global optimum” for a given pair of materials taking into account reflectivity, LIDT and robustness to manufacturing variations and to uncertainties on the physical parameters of the materials.

3.2.3 Presentation of the optimization algorithm

The objective is to find the optimal solution by considering every combination of layers. The random generation of the layers thickness based on the Monte-Carlo approach, allows considering a wide range of combinations in order to retrieve the most interesting designs.

Thus the first step of the algorithm is to randomly generate a series of layer's thickness for either all the layers or a subset of specific layers in the stack. The random values of thickness are uniformly distributed within a range of values realistic for manufacturing. After this random generation, billions of solutions are examined thanks to pre-selected criteria, namely high reflectivity, and higher overall LIDT value than the one related to the reference design. The last step consists in testing the feasibility and robustness of the solutions of the algorithm to face possible manufacturing difficulties. We have thus considered uncertainties concerning i) the refractive index, ii) the thickness of the deposited layers, and iii) the determination of the intrinsic LIDT. A sketch describing our algorithm is presented in Fig. 53.

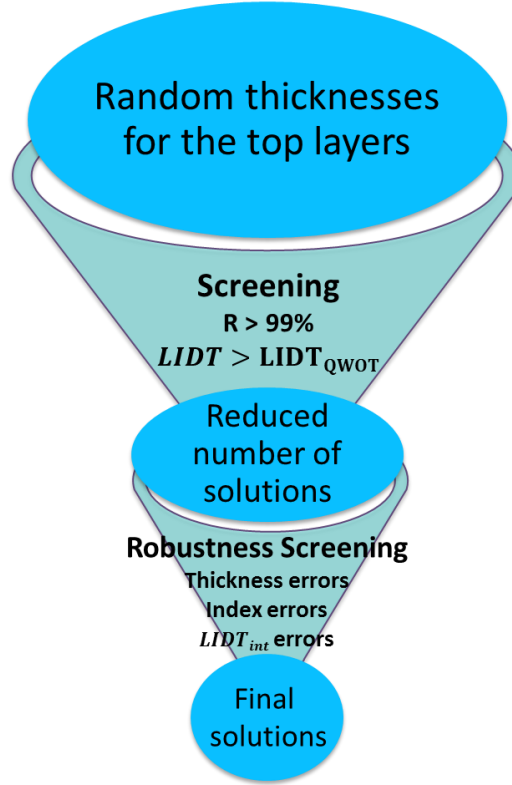


Fig. 53. Schematic of our Monte-Carlo optimization algorithm dedicated to the identification of new designs for multilayer mirror, and taking into account potential errors during the manufacturing.

3.2.4 Example of application of our robust optimization algorithm

Here we detail an application of our algorithm to optimize - for the p -polarization - a 37-layer design composed of the HfO_2 and SiO_2 from Table 3. We chose HfO_2 and SiO_2 , as they are the most ubiquitous materials for high power laser applications.

Since the outer layers of a mirror are exposed to the highest electric field intensity (see Fig 37), we decided to modify only the thicknesses of the 12 outer layers while the 19 inner layers guaranteed reflectivity values of $>99\%$ for the s -polarization and $>95\%$ for the p -polarization.

Regarding the range of thickness, the minimal value had to be realistic regarding the thinnest layer that can be achieved by the deposition process. Based on technical considerations, this minimum value was set to 20 nm. As the electric field intensity varies periodically inside a layer with a period of half-wave optical thickness, the range of variation needs to be higher or equal to a half-wave optical thickness. So the maximum thickness was set to 500 nm for both materials which corresponds to almost 3.5 QWOT for a high index layer and less than 2.5 QWOT for a low index layer.

At the first step, 9 billion combinations of values of thickness within the interval 20-500 nm were randomly generated. The second step consists in keeping only the solutions satisfying screening conditions, namely $>99\%$ reflectivity at 1053 nm and $> 2 \text{ J/cm}^2$ LIDT for the p -polarization. Applying these criteria, the number of solutions was reduced by 99.93% (down to 6067 solutions). The distributions of the remaining solutions are displayed in Fig. 54 with respect to the thickness of the 4 outer optical layers. The number of solutions is clearly higher for thickness of layers 3 and 4 close to

the QWOT, according to the criterion high reflectivity, and it is interesting to mention that the layers 5 to 12 exhibited the same histograms as the layers 3 and 4. For the first layer, the distribution of thicknesses exhibits a maximum of the histogram around 0.8 QWOT. For the second layer, the largest number of solutions is obtained around 1.4 QWOT. From these results, we can conclude that the final design should exhibit a thin high refractive index outer layer (the least resistant material to laser-induced damage) and a thicker low refractive index adjacent layer (the most resistant). This conclusion is in good agreement with the results reported by Apfel *et al.* [39]. Moreover, the most obtained thicknesses for the two outer layers are comparable to the thicknesses of the two optimized layers of the balanced design.

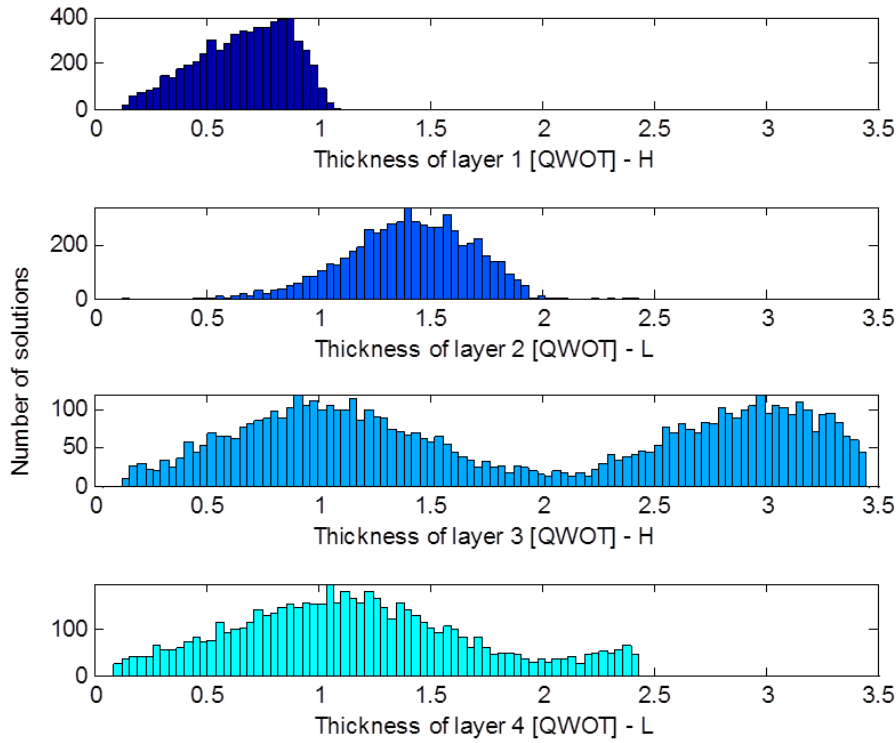


Fig. 54. Distribution of the 6067 solutions satisfying the two criteria: reflectivity > 99%, LIDT > 2 J/cm² as a function of layer thickness normalized to QWOT (quarter-wave optical thickness) for the 4 outer layers. Layer 1 corresponds to the outer layer and the thickness is given in units of QWOT.

Then in the third step, several robustness tests are run. We first modified the thickness of the 12 outer layers of ± 3 nm for each of the 6067 designs. This error corresponds to a possible modification of around 3% of the thicker quarter-wave optical thickness [95]. Again, only the solutions satisfying the conditions about reflectivity and LIDT were kept. Then, we modified the values of the refractive index by ± 0.03 , considering this level of uncertainties overestimates the real variations of the refractive index potentially due to either the layer porosity or the measurement fluctuations.

Let us remember that the intrinsic LIDT is defined as the product of the EFI_{max} and the experimental LIDT ($\text{LIDT}_{\text{int},i} = \text{EFI}_{\text{max},i} \cdot \text{LIDT}_i$ with $i = \text{L,H}$). Errors on the EFI_{max} have already been evaluated with the potential error on thickness and uncertainties on the refractive index. Regarding the errors on the experimental LIDT, we consider that we are able to determine the intrinsic LIDT with a 5% precision leading to a variation of LIDT of ± 0.08 J/cm² in this test.

The first and second robustness tests on thickness and refractive index drastically decreased the number of solutions to only 84. As expected, this value stayed unchanged after applying the test of robustness related to the potential variations of intrinsic LIDT.

Finally, the 84 mirror designs obtained from the simulation exhibited all higher reflectivity values than the minimum required value of 99%, and higher LIDT values than those of the reference design. Among this set of 84 solutions compatible with manufacturing tolerance, the solution exhibiting the highest LIDT, named hereafter the “**LIDT Max Design**”, is characterized by a LIDT value of 2.73 J/cm² and a reflectivity value of 99.37% for the *p*-polarization (Table 7).

Let us emphasize that this value of LIDT=2.73 J/cm² is 41% higher than the one obtained from the reference design (1.93 J/cm²) and still 9% higher than the one obtained from a balanced design for which only the two outer layers are optimized (2.54 J/cm², see Fig. 47).

All the results presented until now have been obtained after considering the manufacturing errors separately for each factor. To go further into this study, let us now apply the effect of possible cumulative errors to the set of 84 solutions presented above. We thus simultaneously reduce all the thickness values by 3 nm, refractive index by 0.03 and intrinsic LIDT by 0.08 J/cm² as it corresponds to the worst possible case. With this cumulative error, there are only 2 designs with a reflectivity higher than 99% and LIDT higher than 2 J/cm². This best design after this final robustness evaluation is designated as **Robust Design**. The Robust design exhibit a LIDT value of 2.08 J/cm² with the cumulative errors and a LIDT value of 2.22 J/cm² considering the nominal values of thickness, refractive index and intrinsic LIDT.

Table 7. Best LIDT performance and related designs

	LIDT under nominal conditions [J/cm ²]	LIDT under cumulative errors [J/cm ²]
Classical design	1.93	1.71
Balanced design	2.54	1.89
LIDT Max design	2.73	1.75
Robust Design	2.22	2.08

In our previous calculation considering the manufacturing errors step by step, the best solution exhibited an LIDT value of 2.73 J/cm². This value dropped to 1.75 J/cm² when considering potential cumulative errors. Note also that when applying the approach of cumulative errors to our reference design, the LIDT value decreased from 1.93 J/cm² to 1.71 J/cm². Finally, the LIDT values of the design with the two outer layers optimized dropped from 2.54 J/cm² to 1.89 J/cm². Table 6 summarizes these results.

Fig. 55 and Fig. 56 exhibit the electric field intensity across the corresponding stack (a) with and (b) without the cumulative errors for respectively the LIDT Max design and the Robust design.

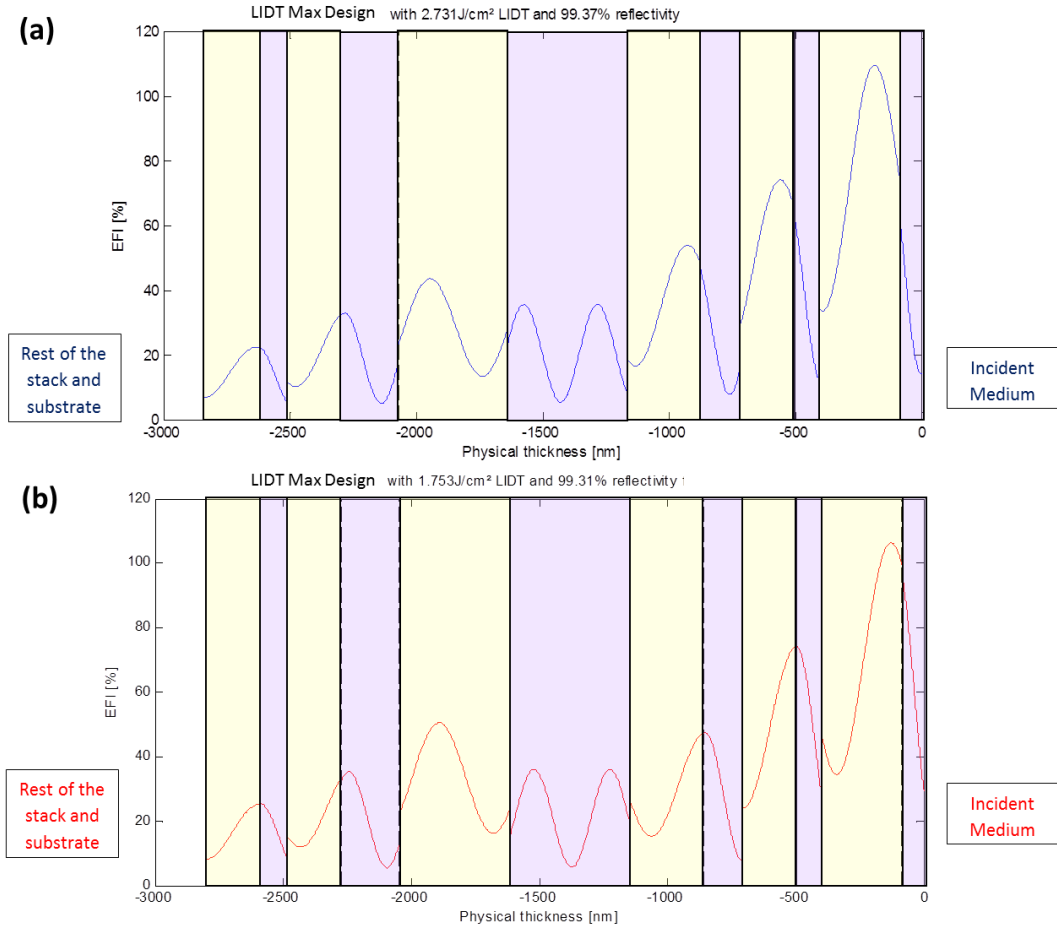


Fig. 55 Electric field intensity distribution for *p*-polarization in the 12 outer layers of the LIDT Max Design in nominal conditions **(a)** (blue) LIDT=2.73 J/cm² and with cumulative errors on the thicknesses, index and intrinsic LIDT **(b)** (red) LIDT=1.75 J/cm²

Fig. 56 reveals that for the robust design in the nominal conditions the damage occurs in layer 3. With the cumulative errors, the damage will occur at the interface between layers 1 and 2. So the most stable design will not always damage at the interface between the two outer layers. At the opposite Fig. 55 reveals that for the LIDT Max design the damage will occur between the first and the second outer layer in both nominal and under cumulative error. The optimized thicknesses of the two designs given by our algorithm the highest LIDT and most stable design are detailed in the Table 8.

Table 8. Thickness of the two designs obtained with the optimization algorithm

	Physical thickness [nm] of layers											
	12	11	10	9	8	7	6	5	4	3	2	1
LIDT Max Design	218	108	213	228	434	475	289	156	208	108	313	89
Robust Design	420	40	141	428	198	169	207	109	230	151	342	54

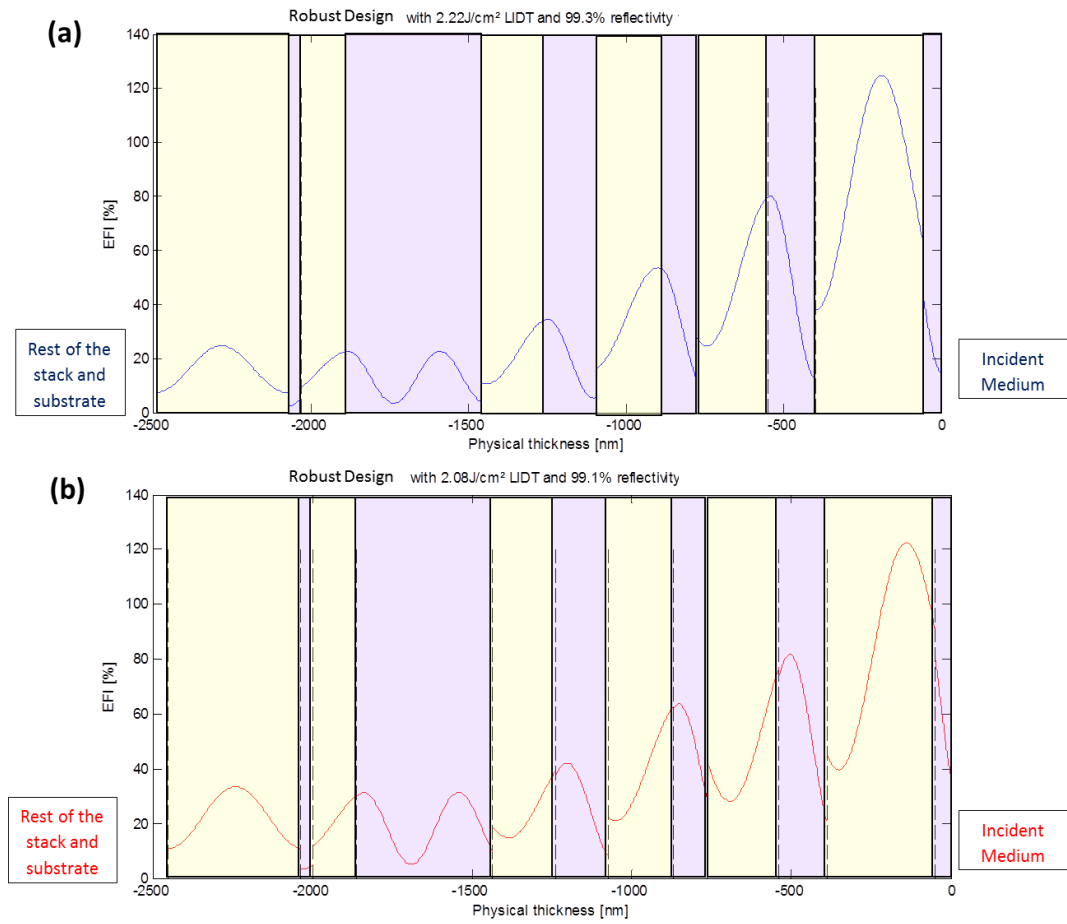


Fig. 56. Electric field intensity distribution for *p* polarization in the 12 outer layers of the Robust Design in nominal conditions **(a)** (blue) LIDT=2.22 J/cm² and with cumulative errors on the thicknesses, index and intrinsic LIDT **(b)** (red) LIDT=2.08 J/cm²

Conclusion of Chapter 3

In this chapter, we numerically showed how to increase the LIDT of multilayer mirrors (i) by identifying designs with alternative materials to the conventional $\text{HfO}_2/\text{SiO}_2$ pair and (ii) by investigating designs using those materials deviated from quarter-wave optical thickness layers. Dielectric materials are ranked after a parametric study on the electric field intensity and LIDT. Scandia appears to be a good candidate for the high refractive index material and silica for the low refractive index one. This numerical approach disclosed that materials with very different properties (refractive index and intrinsic LIDT) such as Al_2O_3 and ZrO_2 can exhibit similar LIDT performance when stacked within a multilayer mirror. The abacuses developed during this numerical study highlighted the need to characterize the refractive index and intrinsic LIDT of the materials to predict the performance in a multilayer and choose alternative materials.

Lack of robustness in a design manufacturing can lead to actual performance being not as good as expected [65, 85], we then present a method to obtain an optimal design taking into account (i) reflectivity, (ii) LIDT and (iii) robustness to manufacturing variations and to uncertainties on the physical parameters of the materials. This robust optimization algorithm has been carried out in the framework of improving the LIDT of the PETAL transport mirrors, but the method reported here is general and can thus be applied to other kinds of coatings, other cases and other laser facilities. In order to apply this algorithm and verify its experimental validity, one needs to introduce the values of the refractive index and intrinsic LIDT of the pair of materials. In the next chapter, we will thus describe how to deduce the material's characteristics from the characterization of monolayers and presents the results obtain from our set of samples. Finally, in chapter 6, we will apply this algorithm to design two optimized mirrors, one for air use and the other for vacuum use.

Chapter 4 Characterization of monolayers

4.1	<i>Intrinsic LIDT characterization</i>	80
4.1.1	Measurement of the refractive index and thickness	81
4.1.1.1	Preferred method: determination on single layer deposited on silicon wafer and fused silica substrate	81
4.1.1.2	Second method for confirmation or additional samples	82
4.1.2	Calculation of the Electric field intensity	83
4.1.2.1	Case of high refractive index layer	85
4.1.2.1	Case of low refractive index layer	87
4.1.3	LIDT measurement with 1-on-1 procedure	88
4.1.4	Calculation of the intrinsic LIDT	91
4.2	<i>Results: description of the set of samples tested in ambient air</i>	91
4.3	<i>Influence of the environment on monolayers properties</i>	94
4.3.1	Ambient Air Vs Dry Air	94
4.3.2	Vacuum Vs ambient Air	95
4.3.2.1	Index variation & porosity	97
4.3.2.2	Intrinsic LIDT comparison	98
Conclusion of Chapter 4		100

The numerical approach described in the previous chapter leads to the development of a robust optimization algorithm. To apply this algorithm and this method, one needs to know the two relevant parameters of each material, namely the refractive index and the intrinsic LIDT, with good accuracy. This chapter presents the procedure to characterize the intrinsic LIDT from single layers. By explaining how to estimate the uncertainties on each value used in the intrinsic LIDT calculation, we present a test configuration that reduces uncertainties and allows for determining accurately the intrinsic LIDT. Then the results from the set of selected samples are presented and compared to the *LIDT/Eg* models previously presented in the literature. Characterizations were performed in ambient air and then in other environmental conditions (dry air at ambient pressure and vacuum) to assess the impact of the environment. The understanding on the damage of single layers and impact of the environment can help to understand the phenomena observed later in stacks.

In the next section, we present the procedure that we have developed to quantify the value of the intrinsic LIDT from single-layer samples in air under ambient pressure, and the results obtained on a selected set of samples will be presented in the following section.

4.1 Intrinsic LIDT characterization

The intrinsic LIDT of a monolayer material is defined as the product of the maximum of the electric field intensity within the layer and the measured LIDT of the layer (sample): $LIDT_{int} = LIDT_{meas} \times EFI_{max}$ (2.26). Therefore, one needs to perform not only a series of laser damage tests on the sample of interest but also to calculate the maximum of the electric field intensity distribution. The electric field intensity calculation requires the knowledge of the refractive index of the material and the thickness of the monolayer. In the case of a single layer, there is just one value of thickness and one value of refractive index to take into account in the calculation. Finally, the only parameters required to determine the intrinsic LIDT value of a monolayer sample are the refractive index of the material, and the thickness and measured LIDT of the layer. The procedure we propose to determine intrinsic LIDT is described in Fig. 57, and starts by fitting the refractive index and thickness of the layer from either ellipsometry and/or spectrophotometry measurements. With these measured values, the electric field intensity distribution is calculated at the wavelength, angle of incidence and polarization of the laser damage test. In parallel to this calculation, the laser-induced damage threshold is measured with a 1-on-1 procedure [34]. The intrinsic laser-induced damage threshold can be calculated at the pulse duration corresponding to the laser pulses used for the tests. Finally, considering that the pulse durations differ between the laser damage set-ups exploited for these types of characterization, all the values of intrinsic LIDT are scaled to 700 fs using the Mero's scaling law [43].

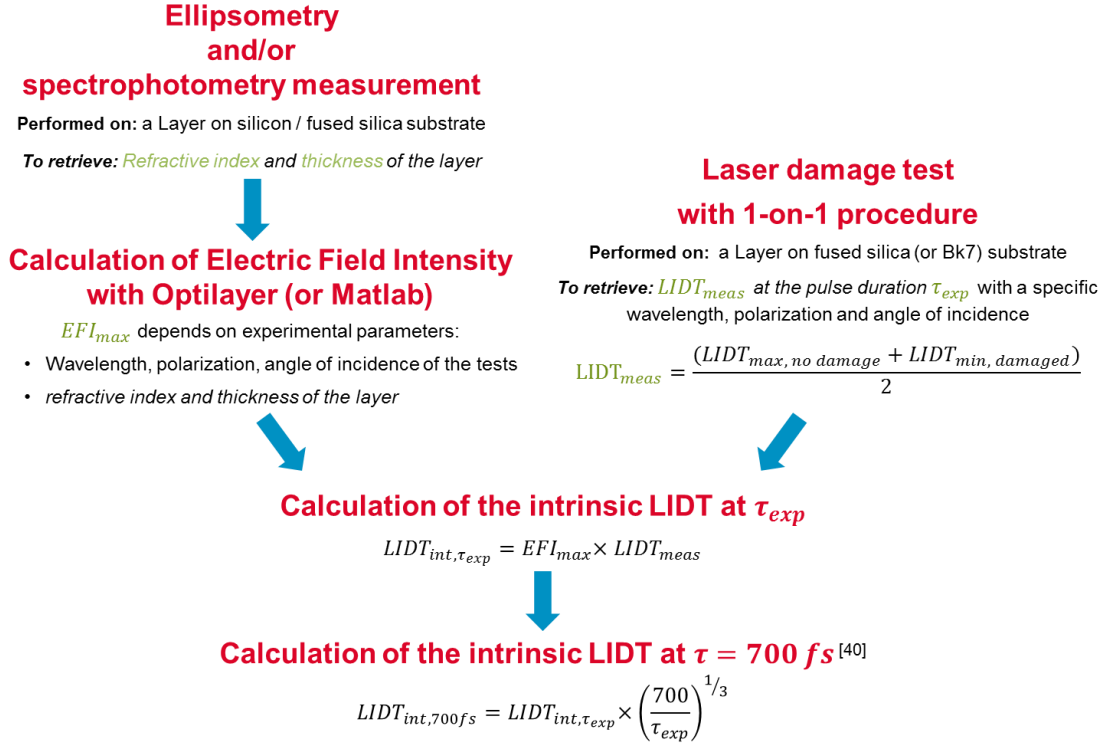


Fig. 57. Schematic of our procedure to determine the intrinsic LIDT from monolayers samples

Each step of the procedure described in Fig. 54 is detailed below, together with the characterization methods and the determination of the uncertainties following the formalism described in [96, 97].

4.1.1 Measurement of the refractive index and thickness

The values of the refractive index and thickness of a monolayer must be accurately determined. Such data can be provided by the vendors. It is assumed that the layer deposition is controlled with less than 5% uncertainties on the thickness and refractive index. However these values of uncertainties were too high for the present study and we decided to measure by ourselves these two parameters following two different methods depending on the available substrates for the samples. Indeed all the single layers samples ordered during this PhD were deposited simultaneously onto silicon wafers, fused silica and BK7 substrates. But the samples prior to 2016 were not deposited on all those substrates disabling the ellipsometry characterization.

4.1.1.1 Preferred method: determination on single layer deposited on silicon wafer and fused silica substrate

In a first method, the refractive index and physical thickness of each monolayer material deposited on silicon wafers were first determined by ellipsometry. In this technique, the ellipsometric angles Ψ and Δ of the reflected wave (with a 70° angle of incidence) are determined for a set of wavelengths, where $\tan(\Psi)$ is the ratio of the p - and s -polarized amplitude reflectance and Δ is the reflected phase shift. With OptiChar it is possible to fit the ellipsometry and spectrophotometry measurements simultaneously [18]. In addition to the ellipsometric measurements, reflection spectra of the same samples were acquired with a spectrophotometer (Perkin Elmer lambda 950 Flex System) at 8° (minimal angle for reflection spectra acquisition with our spectrophotometer) and 45° , angle of

incidence for which the optical thickness of most of the samples were matched for both polarizations. Reflection spectra and ellipsometric angle measurements were fit simultaneously to retrieve the refractive index and the physical thickness of the monolayer material.

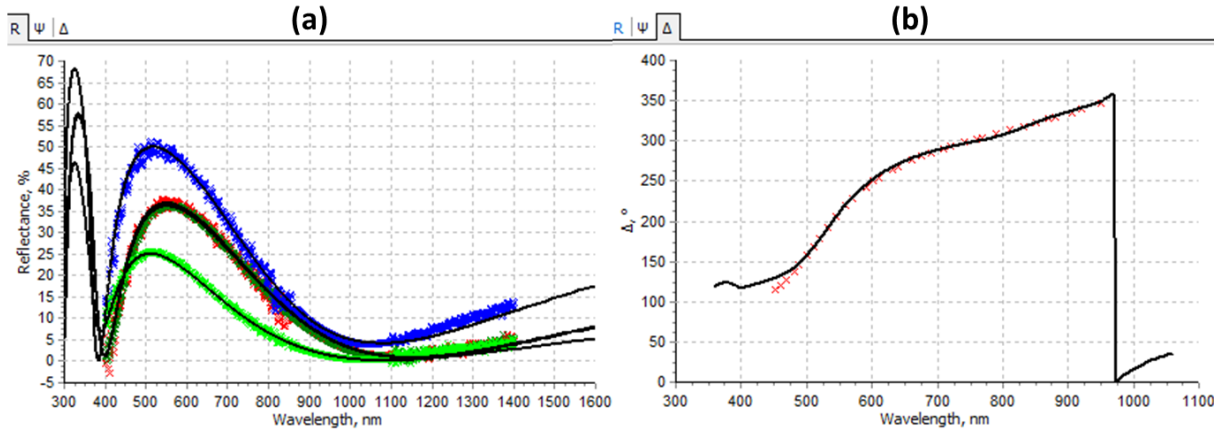


Fig. 58. Example of fitted curves (black lines) of **(a)** measured reflection spectra at two angles of incidence 8° (red and dark green) and 45° (blue and light green) for both s - and p - states of polarizations and **(b)** measured ellipsometric angles Δ (red crosses) on a HfO_2 single layer deposited with IAD by vendor1 on a silicon wafer

Uncertainties on the determination of the layer thickness and refractive index are due to experimental parameters such as measurement offset and noise. In order to evaluate the impact of these parameters on the measured values of the refractive index and thickness, we have used the following numerical method.

- The reflection spectra $R(\lambda)$ at 8° and 45° and ellipsometric angles $\Psi(\lambda)$ and $\Delta(\lambda)$ at 70° of a theoretical monolayer (defined by refractive index n and thickness h) of either hafnia or silica on a silicon wafer were first calculated.
- Then, a white noise mimicking an experimental noise monitored by the spectrophotometer or ellipsometer was added to the calculated spectra. Note that the amplitude of this noise was set to the maximum value of the noise observed on our experimental data.
- The noisy spectra were then fitted with the OptiChar software with respect to the refractive index (n) and thickness (h) of the monolayer.
- The uncertainties u_n and u_h were obtained by calculating the maximal difference between the initial numerical values and fitted values of the refractive index n and thickness h .

Based on this method, the uncertainty was reduced to $\pm 2.5 \times 10^{-2}$ for the refractive index (which corresponds to less than 2% of uncertainty) and to ± 5 nm for the thickness (which corresponds to less than 3.5% of uncertainty for all the samples). The refractive index and thickness of each layer are determined simultaneously by fitting measurements, and, therefore, their uncertainties (u_n and u_h , respectively) are correlated.

4.1.1.2 Second method for confirmation or additional samples

In this case, silica substrates are used instead of silicon wafers. The reflection and transmission spectra of the monolayers were acquired at 8° and 45° and then fitted using OptiChar to calculate the

refractive index values and physical thickness. This technique was either used to confirm the results previously obtained or to determine the refractive index and thickness from layers only deposited on silica.

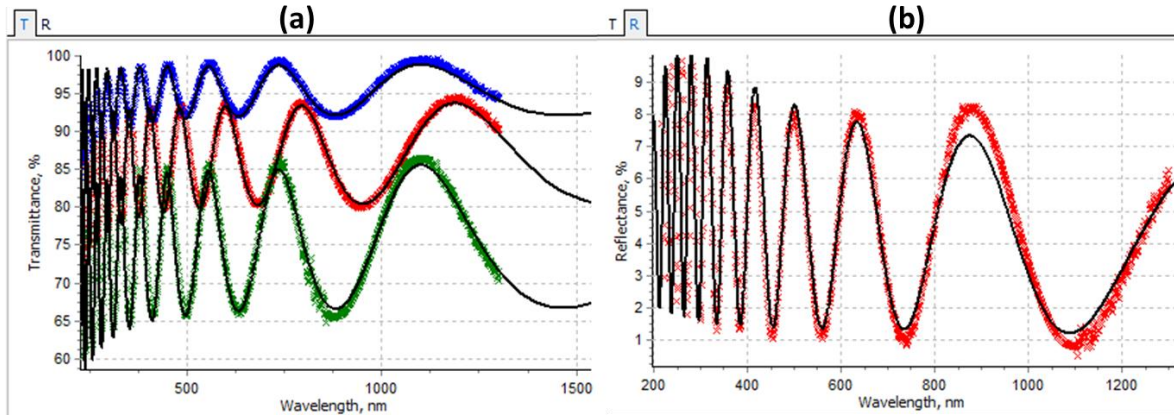


Fig. 59. Example of fit curves (black lines) of the second method on **(a)** measured transmission spectra at 0° incidence (red dots) and at 45° incidence for *s*-polarization (green dots) and *p*-polarization (blue dots) and **(b)** measured reflection spectrum at 45° incidence for *p*-polarization (red dots) of the HfO₂ single layer deposited with e-beam in 2018 on fused silica substrates

The uncertainties related to this second method were derived from a similar numerical method as the one described in the frame of the previous technique. In the present case, we calculated reflection and transmission spectra at 8° and 45° incidence and for both polarizations of a theoretical single layer (characterized by its refraction index and thickness). The calculation was made for either high or low refractive index monolayer materials deposited on fused silica windows. The maximum uncertainty was obtained in the case of a silica monolayer deposited on fused silica window because of the weak refractive index contrast between the layer and the substrate. In this case, the uncertainty related to the refractive index was similar to those obtained with the previous method. However, the thickness was more difficult or even impossible to determinate with this method. When the fit of the thickness was not possible, we considered the thickness given by the vendor.

For this reason, the first method was always preferred to the second one, which was only applied to only 8 specific cases for which no silicon wafers were available. Among these 8 samples only 3 of them were silica layers onto silica substrates. Among these 3 samples, the thickness was impossible to fit only for the silica layer deposited with IAD by vendor 2 in 2015. Consequently, the thickness in Table 10 is then the one given by the manufacturer with adapted uncertainties.

4.1.2 Calculation of the Electric field intensity

The measured values of the refractive index and thickness (cf. previous section) are used to calculate the electric-field intensity distribution within the sample of interest. The electric-field intensity was calculated using two independent approaches, the OptiLayer software, and a home-made software developed via MATLAB that incorporates the matrix formalism described in chapter 2. The sample is modeled as a monolayer deposited on a semi-infinite substrate (either fused silica or BK7

depending on the sample used during the laser damage test) and the superstrate of air with a refractive index approximated to 1. The sample is illuminated at normal incidence from the superstrate with a plane wave linearly polarized at the wavelength $\lambda = 1053$ nm. The maximum enhancement of the electric-field intensity in the layer, denoted by EFI_{\max} , is estimated and reported in Table 9 for hafnia samples, Table 10 for silica samples and Table 11 for other materials samples.

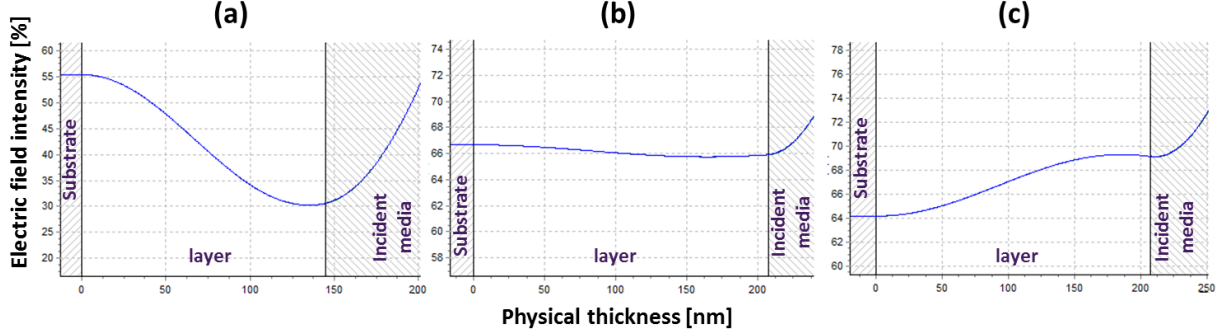


Fig. 60 Electric field intensity distribution at near normal incidence, 1053 nm and for both polarization within (a) a high refractive index layer ($n_H=1.95$) on a fused silica substrate ($n_S=1.45$), (b) a silica layer ($n_L=1.44$) on a fused silica substrate ($n_S=1.45$) and (c) a silica layer ($n_L=1.44$) on a BK7 substrate ($n_S=1.50$)

The electric-field distribution depends on several variables: laser wavelength λ and bandwidth, angle of incidence θ , polarization, refractive index n , and thickness h of the layer; consequently, the evaluation of the uncertainty on the EFI_{\max} must include all these sources of uncertainty. The laser used in the Deric laser damage set-up (presented in [98]) is operating with a 2.8 nm bandwidth centered at $\lambda = 1053$ nm, which is comparable to the spectral bandwidth on the transport section of Petal [14]. The influence of the spectral bandwidth on the EFI_{\max} can be safely neglected (the EFI variation with ± 3 nm on the wavelength is under 10^{-3}). Fig. 60 presents the electric field distribution within three different QWOT (at 45° , 1053 nm) single layers: (a) high refractive index layer ($n_H=1.95$) on a fused-silica or BK7 substrate, (b) low refractive index material layer n ($n_L=1.44$) on a fused-silica substrate, and (c) low refractive index material layer ($n_L=1.44$) on BK7 substrates.

To evaluate the standard uncertainty on the EFI_{\max} , we first calculate the maximum of the electric-field intensity (Fig. 61) inside a layer of refractive index n_L deposited on a substrate of refractive index n_S as a function of the angle of incidence (y axis) for both polarizations states and the layer's physical thickness (x axis). We applied this technique to the three kinds of samples as already presented in Fig. 60, namely a high refractive index layer on fused-silica substrate (Fig. 61(a)), a low refractive index layer on fused-silica substrate (Fig. 61(b)), and low refractive index layer on BK7 substrate (Fig. 61(c)). Results displayed in Fig. 60 and Fig. 61 show that the EFI_{\max} depends mostly on the refractive index contrast between the layer and the substrate. For high refractive index layers, the refractive index contrast is big while for the low refractive index layers, it is weak. Thereby, the choice of the substrate significantly affects the uncertainty. For example, in Fig. 60(b), the refractive index of layer and the substrate are similar and the EFI_{\max} is weakly varying. Differently in Fig. 60(c), the refractive index of the layer is lower than the one of the substrate. This induces the location of the electric field intensity maximum at the interface between the layer and the superstrate. This is not the case for Fig.

60(a) and (b) where the refractive index of the layer is higher than the substrates and the maxima are located at the interface between the substrate and the layer.

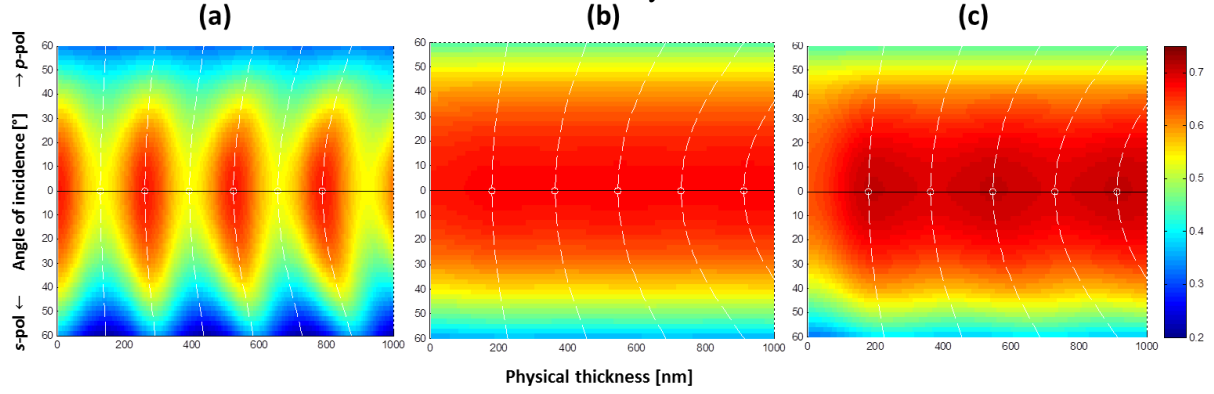


Fig. 61. EFI_{max} (color scale) as functions of the layer thickness (x axis) and the angle of incidence (y axis) for p (positive y) and s (negative y) polarization for **(a)** a high index layer ($n_L=1.95$) on a fused silica substrate ($n_S=1.45$), **(b)** a silica layer ($n_L=1.44$) on a fused silica substrate ($n_S=1.45$) and **(c)** a silica layer ($n_L=1.44$) on a BK7 substrate ($n_S=1.50$). Dashed white lines are the multiple of $\lambda/4$ optical thicknesses.

According to [16], the uncertainty of the EFI_{max} , $u_{EFI_{max}}$, can be calculated as a combined standard

uncertainty:

$$u_{EFI_{max}}^2 = \left[\frac{\partial (EFI_{max})}{\partial h} \right]^2 \times u_h^2 + \left[\frac{\partial (EFI_{max})}{\partial n} \right]^2 \times u_n^2 + \left[\frac{\partial (EFI_{max})}{\partial \theta} \right]^2 \times u_\theta^2 + 2 \frac{\partial (EFI_{max})}{\partial h} \frac{\partial (EFI_{max})}{\partial n} \times u_h u_n \times r(n, h) \quad (4.1)$$

with h the thickness of the layer, n the refractive index of the layer, θ the angle of incidence of the test and $r(n, h)$ the correlation factor between the refractive index and the thickness.

4.1.2.1 Case of high refractive index layer

Let us start this parametric approach with the first kind of sample (see Fig. 55.(a) and 56. (a)): a hafnia layer ($n_L = 1.95$) on a fused-silica substrate ($n_S = 1.45$).

To apply the formula (4.1), the derivative of the electric field, shown in Fig. 62, is considered for the three sources of uncertainty: the angle of incidence of the laser damage test (Fig. 62.(a)), refractive index (Fig. 62.(b)) and physical thickness (Fig. 62.(c)) of the layer.

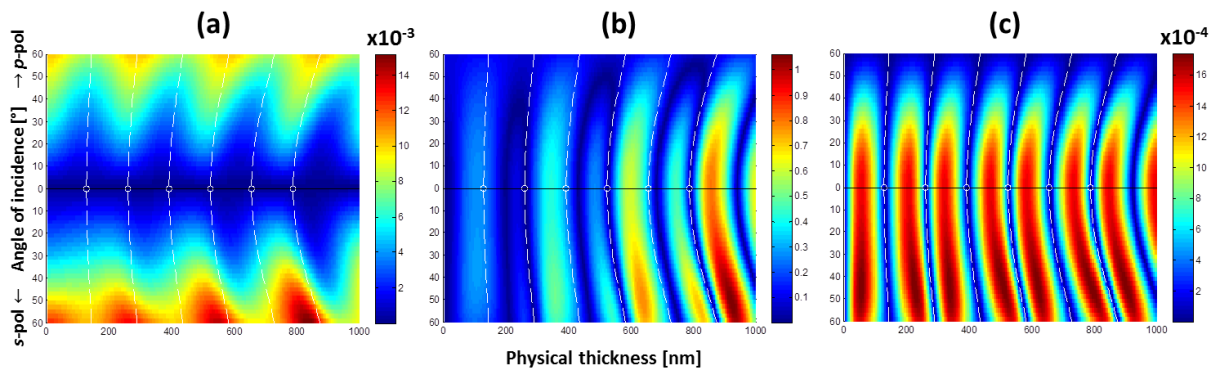


Fig. 62. Squared derivative of the electric-field maximum regarding **(a)** angle of incidence of the laser damage test $[\partial(EFI_{max})/\partial \theta]^2$, **(b)** refractive index $[\partial(EFI_{max})/\partial n]^2$ and **(c)** the thickness of the monolayer $[\partial(EFI_{max})/\partial h]^2$ for a hafnia layer ($n_L = 1.95$) on a fused-silica substrate ($n_S = 1.45$).

Fig. 62(a) displays the derivative of the EFI_{max} regarding the angle of incidence of the test, and highlights the importance of doing the damage tests at normal incidence to reduce the uncertainties coming from the angle of incidence. The derivative regarding the refractive index, Fig. 62(b), indicates that the uncertainty is wider with samples thicker than FWOT. But the uncertainty coming from the index will be higher with a QWOT sample around 0.3 than with a FWOT less than 0.1. The last derivative regarding the physical thickness of the monolayer, Fig. 62(c), shows that it is preferable to have a thickness that is a multiple of a quarter-wave optical thickness at the angle of the test.

The impact of the partial derivative on the general $u_{EFI_{max}}$ is weighted with the uncertainties: u_θ , u_n and u_h which are estimated to: $u_\theta = 0.1^\circ$, $u_n = 2.5 \times 10^{-2}$ and $u_h = 5 \text{ nm}$. The maximal contribution of the angle of incidence will be around 1.4×10^{-3} while it will be around 2.5×10^{-2} for the refractive index and around 8×10^{-3} for the thickness. With these considerations, one can see that the uncertainty on the refractive index is the largest, followed by the uncertainty on the thickness and finally the uncertainty on the angle of incidence. This observation confirms the need to precisely measure the refractive index as well as the thickness of the layer.

As the uncertainties on the thickness and refractive index are correlated due to the fact that these two parameters are obtained from the same measurements, a correlation factor $r(n, h)$ must be taken into account. The physical determination of this correlation factor is too difficult and time consuming, so to evaluate the uncertainty on the EFI_{max} we consider the extreme values of the correlation factor: -1, 0 and 1 and do the calculation for these three values. The final uncertainty on the EFI_{max} is defined as the worst case of the three calculations. With this parametric approach adapted to all the layers the standard uncertainties on the EFI_{max} for each sample are evaluated and reported in the Results section.

The relative uncertainty on the EFI_{max} , meaning $u_{EFI_{max}}/EFI_{max}$, is plotted in Fig. 63. This representation eases the readability of the best configuration of damage test: the configuration that brings the smallest uncertainty and facilitates the comparison between the three kinds of samples. Indeed, this figure shows how testing samples at **normal incidence** reduces the relative uncertainty on the determination of the electric field enhancement. If samples are to be tested **with an angle of incidence, the p -polarization** should be preferred, because the uncertainty levels are lower with p -polarization. Moreover half-wave optical thickness or **full-wave optical thickness sample** should be preferred, because they are local minima.

As an example, in Fig. 63 are placed two hafnia samples with a refractive index equal to 1.95 involved in this study. Their respective relative uncertainties are 0.025 for the IAD 1 (designated the layer deposited in 2015) and 0.028 for IAD 2 (designated the layer deposited in 2017).

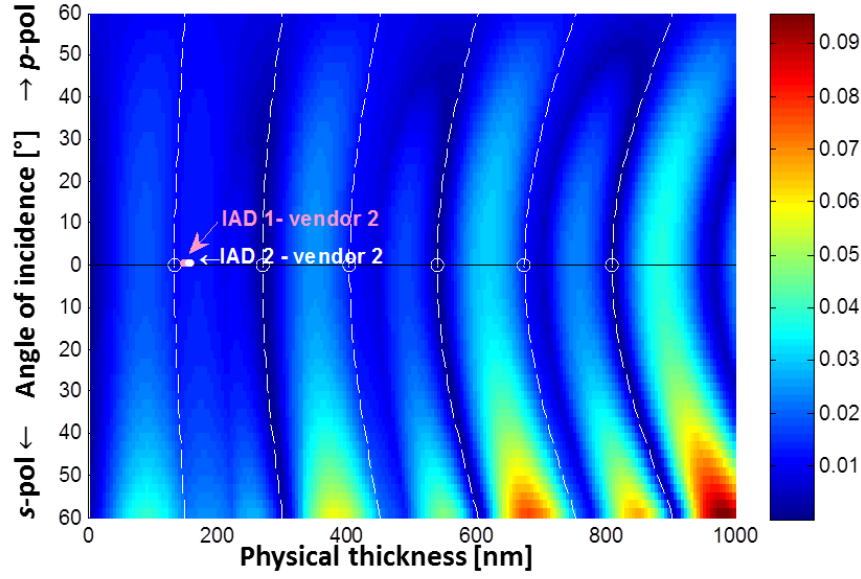


Fig. 63. Relative uncertainty on the maximum electric field intensity for a hafnia layer ($n_L=1.95$) on a fused silica substrate ($n_S=1.45$). The two samples corresponding to this index and damage test configuration are placed so their relative uncertainty on the EFI_{max} can be read.

4.1.2.1 Case of low refractive index layer

We applied the same procedure on the other two kinds of samples, low refractive index layer ($n_L=1.45$) on either a **(a)** fused silica or **(b)** BK7 substrates, and obtain the respective final relative uncertainties plotted in Fig. 64. These uncertainties are calculated as a combination of the uncertainties on the angle of incidence, the refractive index and the thickness with $u_\theta = 0.1^\circ$, $u_n = 2.5 \times 10^{-2}$ and $u_h = 5 \text{ nm}$.

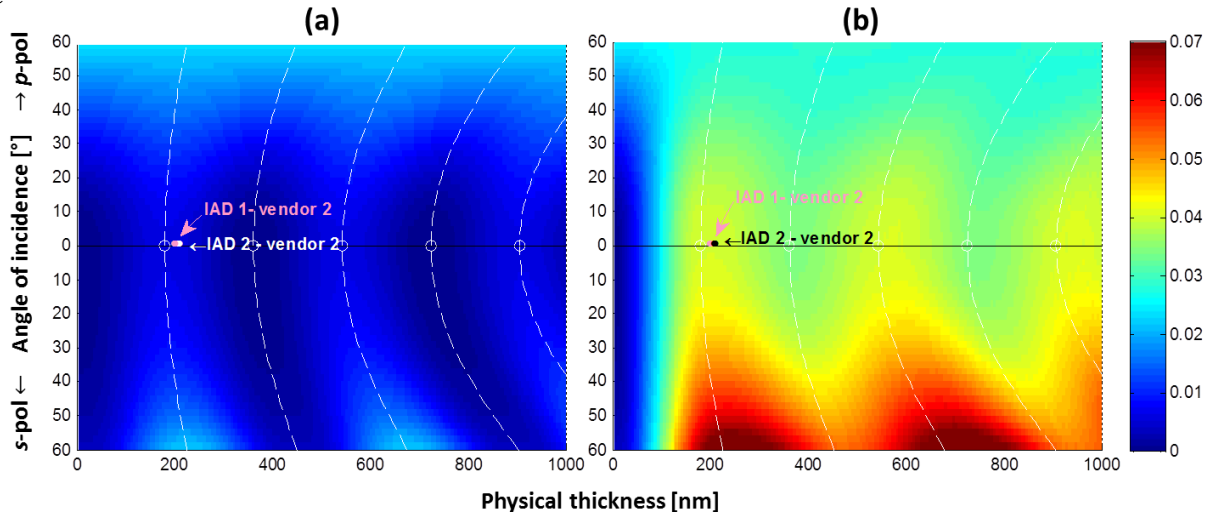


Fig. 64. Relative uncertainty on the maximum electric field intensity for a silica layer ($n_L=1.45$) on a **(a)** fused silica substrate ($n_S=1.44$) or a **(b)** BK7 substrate ($n_S=1.50$). As an example, the two samples corresponding to this index and damage test configuration are placed so their relative uncertainty on the EFI_{max} can be read.

IAD 1 corresponds to the layer deposited in 2015 and IAD 2 corresponds to the layer deposited in 2017.

The uncertainties on the EFI_{max} for a silica layer deposited on a fused silica substrate are very small compared to the other kinds of samples, because for this kind of layer, the electric field is almost a constant throughout the layer (see Fig. 60(b)). But, as previously mentioned, the refractive index and

thickness determination from the method based on silica instead of silicon wafer is difficult and almost impossible. For these samples, the uncertainties on the thickness provided by the manufacturer were considered.

To **conclude**, the configuration that minimizes the uncertainties consists in performing the laser damage tests at **near normal incidence** (strictly normal incidence is too risky for the experimental set-up due to backward reflection) **with a p -polarized beam** on a sample characterized by a **full-wave optical thickness (FWOT) layer**.

Nota on the set of samples: Thanks to these conclusions the damage tests of our whole set of samples were performed at normal incidence or at oblique incidence with a p -polarized beam when the normal incidence was impossible. For example, with very low LIDT samples (like metal or semi-conductor samples) the incidence is needed to reduce the EFI_{max} . Or when damage testing some samples under vacuum on LLE damage set-up, incidence was preferred so the damage detection system could be used. The orders of some samples involved was prior to this PhD and/or the discovery of this recommendation on the thickness. That is why not all the samples are FWOT single layers.

4.1.3 LIDT measurement with 1-on-1 procedure

Laser damage in sub-picosecond regimes is a deterministic phenomenon. Therefore to characterize the LIDT with the 1-on-1 procedure [34], only one shot per fluence is required. Or it is even possible to characterize the LIDT with a single Gaussian shot following the mono-shot procedure described in [99]. In this procedure, the fluence distribution of the Gaussian beam is correlated with the damage morphology after only one shot. To determine the LIDT with the adapted 1-on-1, we irradiate 1 independent site per fluence. An example of laser damage test results of the PIAD 2 HfO_2 layer is provided in Fig. 64. A step between each tested site is introduced to avoid cooperative effect (incubation [100] of the next site or ejection of particles) and to guarantee that the LIDT is established on pristine locations. This step is chosen to be four times the beam diameter as suggested by ISO standards [30]. The LIDT is defined as the mean between (i) the lowest fluence where damage is detected and (ii) the highest fluence where no damage occurs. The uncertainty of the measured u_{meas} is set to be the mean absolute deviation between these two fluences. Thus the uncertainty of the measurement can be reduced by testing more fluence values around the damage threshold fluence.

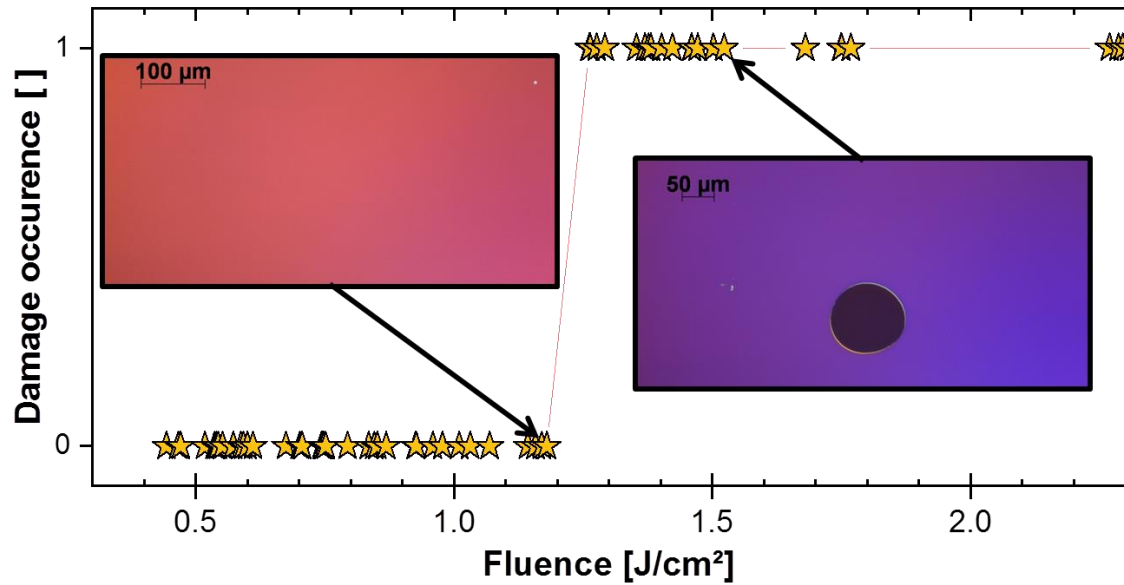


Fig. 65. Example of laser damage threshold determination: The damage occurrence corresponds to a value of 1 and when no damage appears the fluence sites is designated as 0. Two pictures corresponding to one site without damage and one site with damage are provided as an illustration of the *post mortem* observation performed with Nomarski microscopy.

During the present study, laser damage tests were performed first on Deric which is the short-pulse laser damage set-up installed at CEA Cesta [98] and then on the laser damage set-up installed at LLE [101]. Both set-ups operate on the same principle described by the schematics given in Fig. 66. A 1053 nm laser with tunable pulse duration is used.

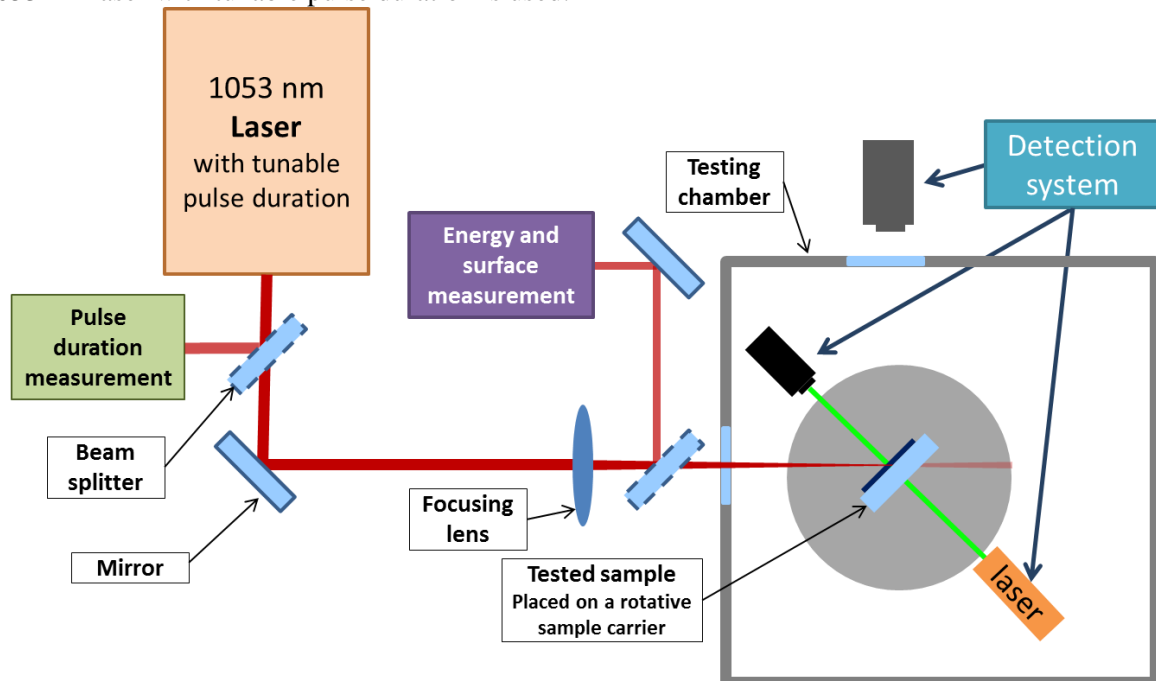


Fig. 66. Schematic of the principle of a Laser damage set-up

The pulse duration can be controlled on a first sampling path with an auto-correlator or the use of Frog devices. Then the beam is focused toward the sample with a focusing lens. Before entering the testing chamber (to perform damage test in a dry air environment on Deric at CEA Cesta or in vacuum

at LLE), the beam is split in two parts. A small portion of the beam is directed toward a second sampling path to determine the energy density that is focused on the sample. The energy measurement is performed with a pyrometer and the surface measurement is made with a camera. The optical path toward the camera is equivalent to the optical path toward the sample, so the surface is correctly determined. The retrieved surface is given in terms of normal beam, which means that it is the surface of the beam in a plane normal to the propagation axis and not the surface of laser-matter interaction at the sample surface due to the angle of incidence. The sample is mounted on a rotative sample carrier with its rotation center placed at the waist of the Gaussian beam. The sample carriers are placed inside testing chambers. At CEA, the testing chamber has no window to avoid leaks. It is designed to operate with dry air (approx. 5% relative humidity at 20°C at the location of the sample) with a constant flow of dehydrated air with 0% of relative humidity or in ambient air with a laboratory humidity regulated at 50% relative humidity at 20°C. The relative humidity is verified with a hygrometer placed under the sample on the sample carrier. At LLE, the testing chamber operates with a vacuum with a partial pressure of 10^{-6} Torr.

The detection systems differ at CEA and LLE. The *in-situ* detection at CEA is done by analyzing the variation of the scattered light from the surface of the sample at the focal spot. To do so a probe laser beam (green beam in Fig. 66) is focused on the damage test site facing a photodiode with a blind so only the scattered light is recorded by the photodiode. When a damage is formed the scattered light increases. The detection at LLE is performed with a camera by comparing *pre*- and *post*-shot pictures. These detection systems are used only as an indicator of the damage during the 1-on-1 procedure and not as a damage determination. The final damage determination is performed with Nomarski observations.

Both set-ups are described with more details in [98, 101]. At the Deric set-up, the laser damage can either be performed in ambient or dry air. At LLE, the sample carrier is implanted in a vacuum chamber thus the laser damage tests can be performed in vacuum or in ambient air.

The round-robin started during this PhD thesis highlighted a difference between the measurements of the final LIDT values. The laser-induced damage threshold values vary depending on the two set-ups, but the general trend of threshold and ranking of the samples remains identical. The observed differences opened the path to a larger round-robin involving other members of the laser damage fellowship [102]. In this present work, we do not further discuss this pending question.

The results presented here are then given for a specific set-up (which will be specified when giving the results) and we did not apply any conversion on the LIDT values from a set-up to another. Generally the given LIDT values are the one determined on DERIC (Chapter 4.1 & Chapter 5) except when considering LIDT in vacuum and the comparison of LIDT values performed in ambient air and vacuum (Chapter 4.2 & Chapter 6).

The measured LIDT depends on the evaluation of the damage threshold described above and the performance of the laser damage test bench. The uncertainties coming directly from the laser damage system are due to the calibration of the set-up which is at: $u_{set-up} = x\% \times fluence$ and the day-to-

day repeatability of tests which is estimated at $u_{repeat} = y\% \times fluence$. The values x and y are linked to each laser damage set-up precision and must be determined with the knowledge of the set-up. The final uncertainty on the LIDT determination $u_{LIDT_{meas}}$ is deduced from the formula:

$$u_{LIDT_{meas}} = \sqrt{u_{meas}^2 + u_{set-up}^2 + u_{repeat}^2} \quad (4.2)$$

4.1.4 Calculation of the intrinsic LIDT

As presented before, the intrinsic LIDT value of the coating material in each sample is estimated by calculating the product between the measured LIDT of the sample and the maximum of the electric-field enhancement, $LIDT \times |E/E_0|^2$, within the monolayer. We use the scaling law¹, $LIDT_{int}(700 \text{ fs}) = LIDT_{int}(\tau_{exp}) \times (700/\tau_{exp})^{1/3}$, established by Mero *et al.* [43] to normalize the intrinsic LIDT at the same pulse duration (700 fs) to compare them safely. Table 9, Table 10 and Table 11 given in section 4.2 provide the intrinsic LIDT ($LIDT_{int}$) obtained for the different samples.

The intrinsic LIDT of each material depends on the EFI_{max} and the measured LIDT of the corresponding sample, which means its uncertainty, can be described as:

$$u_{LIDT_{int}} = \sqrt{(LIDT_{meas} \times u_{EFI_{max}})^2 + (EFI_{max} \times u_{LIDT_{meas}})^2} \quad (4.3)$$

The expanded *or overall* uncertainty of $U_{LIDT_{int}} = k \times u_{LIDT_{int}}$ is calculated by multiplying with the coverage factor k taken here to be equal to 2 [96, 97].

4.2 Results: description of the set of samples tested in ambient air

The background on material and the numerical approach performed in the last chapter highlighted the interest for oxides. We then ordered a series of monolayers made of different oxides: HfO_2 , SiO_2 , Sc_2O_3 , Al_2O_3 , ZrO_2 , TiO_2 and Ta_2O_5 . As presented in chapter 3, mixtures with the right proportion of each component can exhibit higher LIDT performances than pure materials. To verify this assertion, we ordered a mixture composed of 25% SiO_2 and 75% Sc_2O_3 . In addition to these oxides we ordered single layers of MgF_2 in order to consider another low refractive index material. We ordered several samples of HfO_2 and SiO_2 deposited by different deposition methods and/or by different manufacturers. A deposition technique achieved by a given manufacturer will be referred hereafter as a manufacturing process. The deposition methods involved here are presented and described in Chapter 2. We also ordered samples at different times to assess the stability in time of some deposition processes. Other material such as metals and semi-conductors were damage tested and characterized during this PhD, but the results, not reported here, were very poor and not further exploited.

The single layers were deposited simultaneously on three kinds of substrates: silicon wafers, fused silica and BK7 substrates. The fused silica (FS) and BK7 substrates had laser damage polishing and cleaning requirements. The silicon wafers were used for ellipsometry and spectrophotometry measurements. But some layers, already ordered before the beginning of the present study, were not deposited on silicon wafers and their characterization induced higher values of uncertainty.

¹ With τ_{exp} the pulse duration of the laser damage test

The measured parameters in ambient air, their deposition method and substrates are reported in Table 9 for hafnia layer, in Table 10 for silica layers and in Table 11 for other materials.

Table 9. Measured parameters for the hafnia samples.

Manufacturing process	Substrate	Refractive index at 1053 nm	Physical thickness of layer [nm]	EFI _{max} [%]	LIDT measured at 800 fs [J.cm ⁻²]	LIDT _{int} 700 fs [J.cm ⁻²]
PIAD 1	FS / Si wafer	2.01	142.7	53.9±1.66	1.28±0.08	0.66±0.11
PIAD 2	FS / Si wafer	1.96	527.2	66.4±0.88	1.22±0.08 (870 fs)	0.75±0.11
e-beam 2017	FS	1.88	607.2	64.43±1.15	2.80±0.18	1.73±0.24
IAD – vendor 1	FS / Si wafer	2.03	138.4	53.4±1.58	3.59±0.28	1.83±0.26
e-beam 2018	FS / Si wafer	1.86	522.2	59.33±1.50	3.37±0.20	1.92±0.26
IAD – vendor 2 - 2015	FS	1.95	142.2	55.35±1.41	4.78±0.28 (870 fs)	2.46±0.34
IAD – vendor 2 - 2017	FS / Si wafer	1.95	149.5	55.56±1.65	5.08±0.28	2.70±0.36
	BK7 / Si wafer			54.14±1.54	5.11*±0.29	2.65±0.36

* LIDT measured on the layer deposited on BK7 substrate

The results from the sample set used in this study, summarized in Table 9, Table 10 and Table 11, evidence the significant variation of the intrinsic LIDT with the deposition/fabrication process for both silica and hafnia. The materials in Table 9 and Table 10 are sorted by increasing intrinsic LIDT. For hafnia, while low LIDT_{int} values are reported with PIAD samples (0.66 J/cm²), much larger values are measured with IAD layers deposited by vendor 1 (1.83 J/cm²) and with e-beam (1.73 J/cm² or 1.92 J/cm²) and even larger for the IAD 2 layer from vendor 2 (2.70 J/cm²). The refractive index of the hafnia layers are varying with the deposition process. Processes with assistance exhibit higher refractive index than the classical e-beam deposition.

Table 10. Measured parameters for the silica samples.

Manufacturing process	Substrate	Refractive index at 1053 nm	Physical thickness of layer [nm]	EFI _{max} [%]	LIDT measured at 800 fs [J.cm ⁻²]	LIDT _{int} 700 fs [J.cm ⁻²]
PIAD 1	FS / Si wafer	1.46	204	66.5±0.63	2.19±0.16 (870 fs)	1.36±0.21
PIAD 2	FS / Si wafer	1.46	972.9	66.6±0.43	2.36±0.14	1.46±0.18
IAD - vendor 3	FS / Si wafer	1.43	291.6	68.65±2.58	3.73±0.24 (870 fs)	2.38±0.38
IAD - vendor 1	FS / BK7 / Si wafer	1.42	321.8	68.95±3.81	4.6*±0.33	3.16±0.53
IAD - vendor 2 - 2017	FS / Si wafer	1.45	202.8	67±4.07	5.06±0.30	3.25±0.58
IAD – vendor 2 - 2015	FS	1.447	195	67.06±4.08	5.18±0.29	3.32±0.57
e-beam 2017	FS	1.468	818.2	66.88±0.49	5.71±0.40	3.66±0.58
e-beam 2018	FS / Si wafer	1.44	795.6	67.9±3.63	6.57±0.37	4.27±0.69
IBS 2015	FS	1.476	269.4	66.87±0.22	6.90±0.39	4.41±0.52

* LIDT measured on the layer deposited on BK7 substrate

For silica, PIAD samples also exhibit the weakest intrinsic LIDT ($\text{LIDT}_{\text{int}} = 1.46 \text{ J/cm}^2$ and 1.36 J/cm^2). E-beam ($\text{LIDT}_{\text{int}} = 4.27 \text{ J/cm}^2$) and IAD layers by vendor 2 are seen to offer higher intrinsic LIDTs than those deposited with IAD by vendor 1. The best samples for silica are obtained here with the ion beam sputtered layer ($\text{LIDT}_{\text{int}} = 4.41 \text{ J/cm}^2$). For silica layers, the refractive index are also varying but with fewer amplitude between 1.42 for the IAD by vendor 1 to 1.476 with IBS which is the most densifying coating technique.

Table 11. Measured parameters for the other materials samples.

Material	Manufacturing process	Substrate	Refractive index at 1053 nm	Physical thickness of layer [nm]	EFI _{max} [%]	LIDT measured at 800 fs [J.cm^{-2}]	LIDT _{int} 700 fs [J.cm^{-2}]
Low refractive index Materials							
MgF ₂	IAD - vendor 4	FS / Si wafer	1.37	213.4	75.9±3.14	3.01±0.17 (870 fs)	2.12±0.32
MgF ₂	e-beam - vendor 5	FS / Si wafer	1.39	243.2	73.27±3	4.50±0.26	3.15±0.46
High refractive index Materials							
TiO ₂	IAD - vendor 1	FS / Si wafer	2.15	126	50.31±0.72	2.47±0.14	1.19±0.14
Ta ₂ O ₅	IAD - vendor 1	FS / Si wafer	1.98	139.6	54.69±0.66	3.07±0.17	1.61±0.19
ZrO ₂	IAD - vendor 3	FS / Si wafer	1.76	242.8	64.84±0.29	3.75 ±0.27 (870 fs)	2.26±0.35
Sc ₂ O ₃	IBS 2015	FS	1.93	137.7	55.76±0.61	4.4±0.56	2.35±0.63
Sc ₂ O ₃	IBS 2014	FS	1.96	179.02	58.08±0.74	5.72±0.32	3.17±0.38
Intermediate refractive index Materials							
Al ₂ O ₃	IAD - vendor 1	FS / Si wafer	1.57	194	64.84±0.52	6.23±0.38	3.86±0.50
Mixture 75% Sc ₂ O ₃ - 25% SiO ₂	IBS 2015	FS	1.77	150.2	59.95±0.59	8.31±0.55	4.76±0.66

The different materials listed in Table 11 exhibit various intrinsic LIDT. Even a given material from the same deposition process presents significant variations of the intrinsic LIDT values, as illustrated by the two Sc₂O₃ samples deposited by IBS in 2014 and 2015. The mixture composed of 25% SiO₂ and 75% of Sc₂O₃ suggested in [41] presents indeed higher intrinsic LIDT ($\text{LIDT}_{\text{int}} = 4.76 \text{ J/cm}^2$) than the pure materials, namely $\text{LIDT}_{\text{int}} = 2.35 \text{ J/cm}^2$ for Sc₂O₃ and $\text{LIDT}_{\text{int}} = 4.41 \text{ J/cm}^2$ for SiO₂. The ZrO₂ has a lower refractive index than expected, 1.76 while a index higher to 2 was expected. This might suggest a default of fabrication. The TiO₂ and Ta₂O₅ samples exhibit lower refractive index than those ones reported in Table 3, but at the opposite higher intrinsic values. Moreover, the common assertion that the refractive index is decreasing while the intrinsic LIDT is increasing is not confirmed from our set of measurements with our selection of samples (see in chapter 5 Fig. 68). Further discussions of the variation of the intrinsic LIDT with the manufacturing process and their correlation to other optical signature are provided in chapter 5.

4.3 Influence of the environment on monolayers properties

All the results reported in Table 9 to Table 11 were obtained under ambient air, with 50% relative humidity. However, the transport mirrors of the Petal facility are used in vacuum and the multi-layer dielectric coatings can be sensitive to the environment. Consequently, it is of major importance to assess and understand the influence of the environment to design a mirror operating under vacuum.

In the following paragraph we thus compare the laser damage results obtained under ambient air, dry air or vacuum. The comparison ambient/dry air is done using laser damage tests performed on Deric at CEA and the comparison ambient/vacuum is done using the LLE laser damage set-up. We then interpret the results after considering the porosity determined by ellipso-porosimetry, to be compared to the effective refractive index² variation using the Maxwell-Garnett model [75] defined in the section 4.3.2.

This investigation on the influence of the environment on single layers allows discussing if laser damage tests performed in laboratory can be representative of what does occur in the Petal facility.

4.3.1 *Ambient Air Vs Dry Air*

As presented before, laser damage tests on DERIC can be either in dry air or in ambient air. Testing samples in dry air is meant to avoid self-focusing effects and be more representative of a vacuum environment than ambient air.

Dry air laser damage tests required drying the samples for at least three hours. This increases considerably the testing time and thus reduces the number of samples to test. The assessment of the influence of the dry versus ambient air will then help judge on the necessity to perform tests in dry air.

To do so, we compare LIDT results obtained in ambient air and in dry air with silica and hafnia single layers representative of the materials currently used for the Petal transport mirrors. Both types of single layer were damage tested on DERIC at CEA at near normal incidence with a 1053 nm *p*-polarized beam and at 800 fs. Results are reported in Table 12. The decrease of the LIDT from ambient to dry air is barely noticeable for the hafnia layer but becomes visible for the silica layer, despite remaining within the uncertainties interval.

Both the refractive index and thickness are fitted simultaneously from ellipsometry and spectrophotometry measurements performed in ambient air for layers deposited on silicon wafers. Then, spectrophotometry measurements were performed under dry air, meaning that the samples are dried for at least three hours before being measured. During that drying time, repetitive scans of the spectral response of the sample are performed to certify that the sample exhibits stabilized properties. The value of the thickness remains identical under the different environment conditions and only the refractive index changes. For the hafnia layer, the effective refractive index of the layer in ambient air is lower than in dry air. For the silica layer, the opposite trend is observed but with an amplitude of

² The *effective refractive index* has been defined in chapter 2 with the presentation of the deposition methods. It depends on the refractive index of the material, the porosity of the coating and the refractive index of environment.

variation one order of magnitude lower. Thus the environmental conditions seem to affect differently the two materials. In dry air, it is possible that when the pores of the hafnia layer are emptied, the layer bends and densifies which increases the effective refractive index of the layer. For the silica layer the water filling some pores could be replaced by air lowering the overall refractive index of the layer.

The electric field intensity is finally calculated for both environments (ambient and dry air) and their maximum values are calculated and reported in Table 12 with their related uncertainties. With a constant thickness of the single layer, the maximum of the electric field intensity is varying inversely from the refractive index. Finally, the intrinsic LIDT of the two single layers in each environment are calculated from the maximum of the electric field intensity within the layer and the measured LIDT of the layer and the results are also reported in Table 12, indicating that the final intrinsic LIDT of a given layer can be considered as constant considering either dry or ambient air. Indeed the decrease of the intrinsic LIDT, when the layer is dried, are found to be equal to 0.05 J/cm² for the silica layer and 0.09 J/cm² for the hafnia layer, and these values are smaller than the uncertainties estimated around ± 0.3 J/cm² for hafnia and above ± 0.5 J/cm² for the silica layer.

Table 12. Measured values of a hafnia and silica layers representative of the Petal transport mirrors for ambient air dry air.

Material	Environment	Refractive index at 1053 nm	Physical thickness of layer [nm]	EFI _{max} [%]	LIDT measured at 800 fs [J.cm ⁻²] CEA	LIDT _{int} 700 fs [J.cm ⁻²] CEA
HfO ₂	Ambient Air	1.93	149.9	54.14±1.60	5.11±0.29	2.67±0.35
	Dry Air	1.96		54.09±0.47	5.06±0.28	2.62±0.31
SiO ₂	Ambient Air	1.447	194.3	68.9±0.4	5.59±0.35	3.68±0.66
	Dry Air	1.446		70.12±0.99	5.35±0.39	3.59±0.55

To conclude, the intrinsic LIDT characterization in ambient air is sufficient to extrapolate the LIDT performances in dry air. But in order to apply the algorithm presented in chapter 3, one needs to characterize accurately the second input parameter: the refractive index in both environments. Indeed variations of the refractive index with the environmental conditions are different for each material and unpredictable.

This comparison authorizes to characterize the LIDT in ambient air, which makes the damage tests significantly easier and faster. We now need to assess that the characterization in ambient air is representative of the characterization in vacuum. In the next paragraph, we then aim at going further and assessing the influence of the vacuum onto the LIDT of 5 single layers of hafnia and silica deposited with different manufacturing process.

4.3.2 Vacuum Vs ambient Air

All the samples considered for this comparison were laser damage tested at LLE with a 1053 nm *p*-polarized beam at 800 fs. The angle of incidence of the test (AOI) was first set to 45° to be able to

operate the detection system in vacuum. The samples were placed under vacuum overnight prior to laser damage tests. Then, for the measurements under ambient air, the angle of incidence (AOI) was set to 1° to reduce the uncertainties. Switching the angle of incidence between 1° and 45° drives a change of the EFI_{\max} values. It allows verifying the repeatability and reliability of the measurements. For two kinds of samples, the PIAD 2 and the e-beams samples were damage tested at one single angle of incidence, respectively tested at 45° and 1° incidence. Results are reported in Table 13.

Table 13. Measured parameters for the hafnia samples in ambient air and similar to vacuum environment

Manufacturing process	Environment	Refractive index at 1053 nm	Physical thickness of layer [nm]	EFI _{max} [%]	LIDT measured at 800 fs [J.cm ⁻²] LLE	AOI	LIDT _{int} 700 fs [J.cm ⁻²] LLE	Open Porosity [%]
Hafnia layers								
PIAD 1	Air	2.010	142.7	53.9±1.66	0.95±0.06	1°	0.49±0.07	2.5
	Vacuum	2.005		41.45±0.45	1.4±0.08	45°	0.56±0.07	
PIAD 2	Air	1.960	527.2	45.3±0.21	1.32±0.08	45°	0.57±0.07	1.5
	Vacuum	1.946		45.11±0.22	1.38±0.08	45°	0.6±0.07	
IAD – vendor 1	Air	2.030	138.4	53.41±1.58	2.23±0.14	1°	1.11±0.16	0
	Vacuum	2.050		38.89±0.43	3.483±0.2	45°	1.33±0.16	
e-beam 2018	Air	1.860	639.9	59.39±1.50	1.92±0.13	1°	1.09±0.16	7.5
	Vacuum	1.827		60.17±1.34	2.06±0.12	1°	1.19±0.16	
IAD - vendor 2 - 2017	Air	1.952	149.5	55.56±1.65	2.67±0.16	1°	1.38±0.19	3
	Vacuum	1.955		42.46±0.47	4.20±0.24	45°	1.71±0.2	
Silica layers								
PIAD 1	Air	1.46	204	66.56±0.63	1.39±0.08	1°	0.89±0.11	2.5
	Vacuum	1.468		55.4±0.97	1.94±0.12	45°	1.03±0.14	
PIAD 2	Air	1.46	972.9	55.41±0.98	1.76±0.1	45°	0.93±0.12	1.2
	Vacuum	1.457		55.41±0.98	1.81±0.11	45°	0.96±0.13	
IAD – vendor 1	Air	1.420	321.8	71.71±3.81	2.23±0.14	1°	2.0±0.332	11.9
	Vacuum	1.439		56.97±1.69	4.16±0.23	45°	2.26±0.3	
e-beam 2018	Air	1.438	795.6	70.20±2.46	3.90±0.22	1°	2.62±0.37	8.8
	Vacuum	1.430		70.94±2.44	3.89±0.22	1°	2.64±0.37	
IAD - vendor 2 - 2017	Air	1.448	202.8	69.98±4.06	2.98±0.21	1°	2.0±0.38	11.2
	Vacuum	1.446		56.66±1.71	4.58±0.26	45°	2.48±0.33	

The LIDT values of the samples tested at the same angle of incidence, the PIAD 2 and e-beam samples can be directly compared. The LIDT of both hafnia layers and the silica PIAD 2 layers exhibit higher LIDT in vacuum than in ambient air. For the silica PIAD layer the LIDT in vacuum is practically not varying.

For the other samples, in order to compare the effect of the environment, the intrinsic LIDT should be considered. To do so, one needs to calculate the electric field intensity. As stated before, the layers

can be sensitive to the environment through their porosity. We then fit the refractive index and thickness of each layer from spectrophotometry measurement and compare these variations with open porosity measurements retrieved from ellipso-porosimetry. An *ellipso-porosimeter* is an ellipsometer where a solvent is saturated into the pores. The sample is placed in a vacuum chamber. The measurement of the refractive index and thickness is realized through ellipsometry for different portions of solvent saturation into the pores. The solvent volume fraction and relative pressure of the solvent is tracked. With the exact knowledge of the refractive index of the solvent, one can retrieve from the index and thickness variation the open porosity of the film. Those measurements are performed on layers deposited onto silicon wafers.

4.3.2.1 Index variation & porosity

First, we performed spectrophotometry measurements in dry air following the same procedure as presented in the last paragraph. We were not able to perform these measurements in vacuum with our spectrophotometer. Consequently, we have approximated the refractive index and thickness in vacuum from the values obtained in dry air. Results are listed in Table 13 for hafnia and silica layers. The fitted thickness variations are so low when changing the environment that we consider the thickness to stay unchanged. For hafnia layer, the larger refractive index variation is observed for the e-beam deposited layer. The index dropped from 1.86 in ambient air to 1.827 in dry air. For silica layers, the wider variation is observed for the layer deposited by IAD by vendor 1. It spans from 1.42 in ambient to 1.439 in dry air.

Then we compare these refractive index variations with porosity measurements. The porosity is retrieved from the fit of ellipso-porosimetry measurements.

The results are reported in Table 13. The hafnia layers have smaller open porosity measured (between 0 to 7.5%) than the silica layers (between 1.2% and 11.9%). Both materials deposited with PIAD have their open porosity percentage diminishing with the thickness of the layer. The most porous hafnia layer is the one deposited by e-beam as expected since it is a low densifying process (no assistance). The most porous silica layers are the ones deposited with IAD, which is surprising because the ionic assistance should increase the densification of the layer. These last results highlight the importance of considering not only the deposition method by itself but the deposition method achieved by a specific manufacturer as a whole: referred here manufacturing process. One should remark that the behavior of the samples when changing the environment are very different for each manufacturing process and no general law or trend can be observed. This indicates that accurate characterization as a function of the environment for each manufacturing process and material is necessary.

It should be emphasized that if the only phenomenon occurring during the drying of a layer is that the pores emptied, the effective refractive index of the layer should always decrease between ambient air and dry air. The effective refractive index of a layer can be described with the Maxwell-Garnett model:

$$n_{eff}^2 = n_c^2 \left(1 - \frac{3\phi(n_c^2 - n_d^2)}{2n_c^2 + n_d^2 + \phi(n_c^2 - n_d^2)} \right) \quad (4.4)$$

In the latter expression, n_{eff} is the effective refractive index of the layer, n_c the refractive index of the bulk material, n_d the refractive index of the pores and finally ϕ the porosity of the material. Using this model the refractive index of a hafnium dioxide layer is 1.97 in dry air with $n_c = 2.08$ [103], $n_d = 1$, and a porosity of $\phi = 10\%$. And in ambient air, with half of the pores filled with ($n_d = (1.33 + 1)/2 = 1.165$) water the effective refractive index is 1.988.

Let's consider another example: a silica layer for which the refractive index of the bulk material is $n_c = 1.45$ [103] and a porosity of $\phi = 15\%$. In dry air $n_d = 1$ the effective refractive index of the layer is 1.38 and in ambient air with only half of the pores filled with water ($n_d = 1.165$) the effective refractive index becomes 1.40.

The porosity in these two examples overestimates the open porosity results. So the variation of the refractive index is overestimated.

As a conclusion, one can note that the refractive index variations for silica layers are more important than for hafnia layers oppositely to their open porosity (silica layers exhibit higher open porosity values than hafnia layers). Based solely on the porosity measurement and the basic model of pores filled with water, one should expect a larger refractive index variation for the silica layers than for the hafnia layers. Moreover, one should always observe higher refractive index in ambient air than in dry air. But the reality doesn't match with this description and consequently, the refractive index variation is not only due to the proportion of filled or empty pores. Thus, characterizing the refractive index in the adequate environment is required and much more relevant than considering the open porosity.

4.3.2.2 Intrinsic LIDT comparison

From the values of refractive index and thickness previously fitted for both ambient and dry air, we have calculated the electric field intensity and the associated uncertainties, considering that dry air could be considered as similar to vacuum. With these electric field intensity maxima and the measured LIDT, we have calculated the intrinsic LIDT values. The results are reported in Table 13 and plotted in Fig. 67(a) for hafnia layers and in Fig. 67(b) for the silica layers. The error bars are calculated as described in the first paragraph of this chapter.

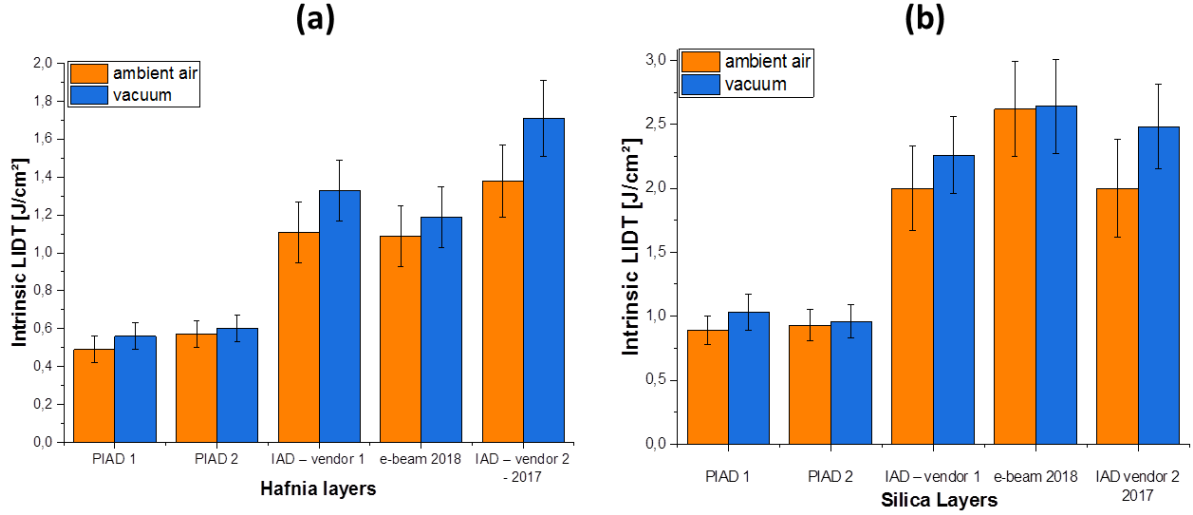


Fig. 67. Intrinsic LIDT in ambient air and vacuum for 5 hafnia layers and 5 silica layers

One can see in Fig. 67 that all the LIDT variations are included in the error bars meaning that the variations of the intrinsic LIDT are not significant when changing the environment. Furthermore the values of the intrinsic LIDT appear to be unchanged for the PIAD 2 layers as well as the silica e-beam layer. One should also remind that the laser damage tests were performed at the same angle of incidence for these samples. Consequently, the larger variations of the intrinsic LIDT observed for other samples could be attributed to the change of the angle of incidence which can be expected to generate uncertainties in the measurements. Moreover, the observed variations cannot be simply linked to the open porosity. Indeed, the hafnia layer deposited with IAD by vendor 1 has no open porosity but a large (even not significant) variation of the intrinsic LIDT. Symmetrically, the hafnia layer deposited with e-beam has the most important open porosity of all hafnia layers but smaller intrinsic LIDT variation compared to the previous one. To push further the discussion, one may take into account the fact that the refractive indexes of dry air and vacuum are not identical. Moreover, in chapter 2, it was presented that the change of environment does not only affect the refractive index but also the stress of the coating, especially in vacuum. As it is difficult to track the stress for single layer deposited onto thick substrates (necessary for the damage test), further investigation on the potential effect of stress will be studied in chapter 6 on multilayer instead of monolayer dielectric components.

To conclude, we have demonstrated that the variation of the LIDT can be mostly linked to the variation of the refractive index of the layer. The use of dry air instead of vacuum for the determination provides a good approximation. The refractive index and LIDT variations cannot be directly linked to the coating open porosity. Further analyses are required to model more precisely the refractive index variation taking into account the water affinity of the material and the size and shapes of the pores. Finally, even if the intrinsic LIDT values are not significantly different for the different environments being ambient air and vacuum, we recommend to always characterizing the material in the final environment of use.

Conclusion of Chapter 4

In this chapter, we presented and detailed our home-made procedure to characterize the intrinsic LIDT of materials on single layers. The determination of the refractive index is the first step of this procedure. A fine estimation of the uncertainties allowed us to select the optimum laser damage test configuration. It consists in using a p -polarized beam at near normal incidence on full-wave optical thickness single layers.

Then through the results obtained from a set of samples including a wide variety of oxide materials deposited with different deposition methods and various manufacturers, in other words multiple manufacturing processes, we demonstrated that the intrinsic LIDT depends on the manufacturing process (deposition method + vendor/manufacturer). Therefore in order to optimize a design, one needs to characterize the materials deposited with the specific manufacturing process involved in the design. Further discussion of these intrinsic LIDT variations will be provided in the following chapter.

Finally, we have assessed the influence of the environment onto the intrinsic LIDT by damage testing a series of samples under various environments. By providing refractive index measurement in ambient and dry air, we showed that the environment has a limited impact on the final intrinsic LIDT. The refractive index and LIDT variations of the set of samples have no general trend and cannot be directly linked to the coating open porosity. These variations consequently cannot be modelled or predicted and thus need to be characterized accurately. Therefore it will be preferable to characterize the materials in the final environment of use.

The procedure to determine the intrinsic LIDT presented here is destructive and time consuming especially because of the LIDT characterization. In the next chapter, we will present our research toward nondestructive and quicker characterization of the LIDT by correlating the intrinsic LIDT with optical signatures of the layer.

Chapter 5 Toward nondestructive characterization of the intrinsic LIDT

5.1	<i>Intrinsic LIDT and refractive index comparison</i>	102
5.2	<i>Limits of Mero's Law</i>	104
5.2.1	The Tauc Method	104
5.2.2	Results	105
5.3	<i>Correlation to other optical signature</i>	106
5.3.1	Correlation to spectrophotometry measurement	107
5.3.1.1	Procedure to determine the absorption coefficient spectra	107
5.3.1.1.1	Case of hafnia single layers	107
5.3.1.1.2	Extension to other studied materials	108
5.3.1.1	Discussion	110
5.3.2	Correlation to photothermal absorption measurements	112
5.3.2.1	Set-up description	112
5.3.2.2	Results	113
Conclusion of Chapter 5		116

It has been observed, in the previous chapter, that a given material deposited by various deposition methods and/or manufacturer exhibits very dispersed intrinsic LIDT and refractive index values [42, 104]. To choose the best manufacturing process it is essential to understand the source of the intrinsic LIDT dispersion.

Considering that the procedure described in the previous chapter to determine the intrinsic LIDT value is based on multiple steps and is time-consuming, we focus our attention in the present chapter on exploring fast and reliable nondestructive techniques allowing a fast selection of the pair material/manufacturing process. These techniques could also help understanding the precursor mechanisms of laser damage.

5.1 Intrinsic LIDT and refractive index comparison

To start this chapter we list the layers of interest use throughout this chapter and their properties of interest: refractive index, intrinsic LIDT and optical bandgap energy. Most HfO_2 and SiO_2 layers were deposited with the same manufacturing process and are listed in the Table 14.

Table 14. Measured parameters for the HfO_2 and SiO_2 samples.

Manufacturing process	Refractive index at 1053 nm	LIDT _{int} 700 fs [J.cm^{-2}]	Optical bandgap [eV]	Refractive index at 1053 nm	LIDT _{int} 700 fs [J.cm^{-2}]	Optical bandgap [eV]
	HfO_2 layers			SiO_2 layers		
PIAD 1	2.01	0.66±0.11	5.5±0.025	1.46	1.36±0.21	7.6±0.04
PIAD 2	1.96	0.75±0.11	5.75±0.025	1.46	1.46±0.18	7.4±0.035
IAD - vendor 3		--		1.43	2.38±0.38	Unknown
e-beam 2017	1.88	1.73±0.24	Unknown	1.468	3.66±0.58	Unknown
IAD - vendor 1	2.03	1.83±0.26	5.5±0.03	1.42	3.16±0.53	7.2±0.04
e-beam 2018	1.86	1.92±0.26	5.6±0.05	1.44	4.27±0.69	6.85±0.55
IAD - vendor 2 - 2015	1.95	2.46±0.34	Unknown	1.447	3.32±0.57	Unknown
IAD - vendor 2 - 2017	1.95	$\frac{2.70\pm0.36}{2.65\pm0.36}$	6±0.035	1.45	3.25±0.58	6.75±0.55
IBS 2015		--		1.476	4.41±0.52	Unknown

The results of the rest of our set of samples are listed in Table 15. Each manufacturing process is associated with a specific color. The four different IAD deposition processes, two e-beam, one PIAD and one IBS. For some manufacturing process, multiple samples were ordered to assess the variation of the manufacturing process with the thickness of the layer or through the years.

Table 15. Measured parameters for the other materials samples.

Manufacturing process	Refractive index at 1053 nm	LIDT _{int} 700 fs [J.cm ⁻²]	Optical bandgap [eV]	Manufacturing process	Refractive index at 1053 nm	LIDT _{int} 700 fs [J.cm ⁻²]	Optical bandgap [eV]
High refractive index				Low refractive index material			
LaTiO ₃ - IAD - vendor 4	1.99	2.02±0.25	Unknown	MgF ₂ - IAD - vendor 4	1.37	2.12±0.32	Unmeasurable
TiO ₂ - IAD - vendor 1	2.15	1.19±0.14	3.33±0.03	MgF ₂ - e-beam - vendor 5	1.39	3.15±0.46	Unmeasurable
Ta ₂ O ₅ - IAD - vendor 1	1.98	1.61±0.19	4.24	Intermediate index materials			
ZrO ₂ - IAD - vendor 3	1.76	2.26±0.35	Unknown	Al ₂ O ₃ - IAD - vendor 1	1.57	3.86±0.50	6.56
Sc ₂ O ₃ - IBS 2015	1.93	2.35±0.63	Unknown	Mixture 75% Sc ₂ O ₃ - 25% SiO ₂ - IBS 2015	1.77	4.76±0.66	Unknown
Sc ₂ O ₃ - IBS 2014	1.96	3.17±0.38	Unknown				

In all the figures of this chapter, each material is matched with a specific symbol:

- HfO₂ layers are symbolized by squares
- SiO₂ layers are represented by triangles
- LaTiO₃ layer by diamond
- TiO₂ layer by a tilted triangle
- Ta₂O₅ layer by an hexagon
- ZrO₂ layer by a reverse triangle
- Sc₂O₃ layers by 8-branch crosses
- MgF₂ layers by circles
- Al₂O₃ layer by a star
- mixture layer by a simple cross

As stated before, the results from our pool of samples exhibit a wide dispersion regarding their refractive index and intrinsic LIDT. To make this ascertainment more visible we plot in Fig. 68 the intrinsic LIDT as function of the refractive index of the materials, both properties were acquired through the procedures described in chapter 4. Gallais *et al.* [42] reported that the intrinsic LIDT of various materials deposited with different manufacturing process is inversely linear dependent to the refractive index (see Fig. 41(b) in chapter 3). When considering each manufacturing process separately (in other word each color), Fig. 68 mostly confirms this general trend that high refractive index tend to have lower intrinsic LIDT values than low refractive index. One exception to this trend, when observing only the samples deposited IAD by vendor 1 manufacturing process, is the SiO₂ layer that exhibits a lower refractive index and intrinsic LIDT than the Al₂O₃ layer. Another exception can be noticed with the mixture deposited with IBS. This last discrepancy could be expected: as mixtures can exhibit higher intrinsic LIDT values than the pure materials they are made of, but they have an averaged refractive index [41].

Otherwise, when considering the results from the entire pool of samples, the previously observed trend [42, 45, 46] is not confirmed here. Our SiO₂ have refractive indexes included between 1.42 and

1.476 but their intrinsic LIDT values vary between 1.36 J/cm² (for the PIAD1 layer) and 4.41 J/cm² (for the IBS layer). The intrinsic LIDT dispersion cannot be link to refractive index variations.

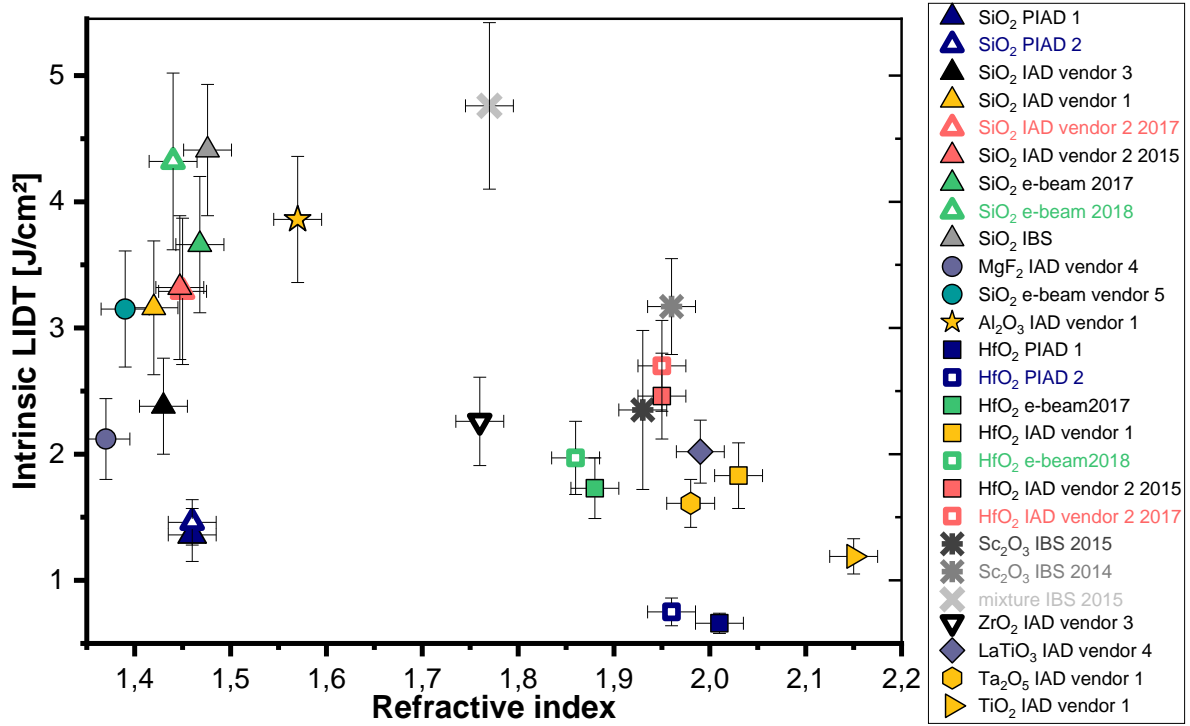


Fig. 68. Intrinsic LIDT as a function of the refractive index at 1053 nm for various materials (shapes of the symbols) deposited with various manufacturing process (colors)

5.2 Limits of Mero's Law

It is commonly also accepted that the intrinsic LIDT has a linear relationship with the band-gap energy [43, 45, 42, 46]. The next investigation axis to explain the intrinsic LIDT dispersion is to finely observe the link between the intrinsic LIDT to the bandgap energy.

5.2.1 The Tauc Method

We have employed the Tauc method [105] using ultraviolet ellipsometry measurements on silicon wafer witnesses to estimate the optical bandgap energy for each material. The results are reported in Table 14 and Table 15. In the Tauc method, the value of $\sqrt{\alpha h\nu}$ is plotted against the photon energy $h\nu$, where α is the absorption coefficient. A portion of this curve can be linearly fitted. The intersection of this linear fit with the x axis gives the optical bandgap energy in eV. This method of determination is illustrated for the two IAD samples from vendor 1 in Fig. 69. One should note that the ellipsometer used for this measurement has a maximal value of 8 eV. It thus excludes high bandgap materials such as MgF₂.

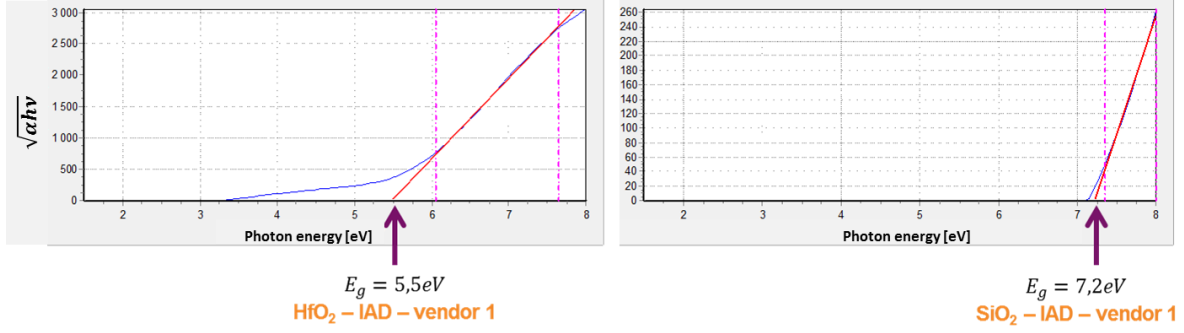


Fig. 69. Example of Tauc method application on a hafnia and silica single layers deposited with IAD by vendor 1

The uncertainties on the final bandgap energy result from the interval of energy linearly fitted. The final uncertainty for a Tauc energy determination is defined as the mean deviation between the lowest value and the highest value that can be retrieved after the values have been reasonably fitted. In Fig. 70 is presented an example of two boundary fits realized to evaluate the uncertainty on the determination of the optical bandgap of the TiO_2 layer deposited by IAD by vendor 1 which is finally estimated at 3.33 eV. From this example the resulting uncertainty is then ± 0.03 eV. The same method has been applied to determinate the uncertainties reported for each sample in the Table 14 and Table 15.

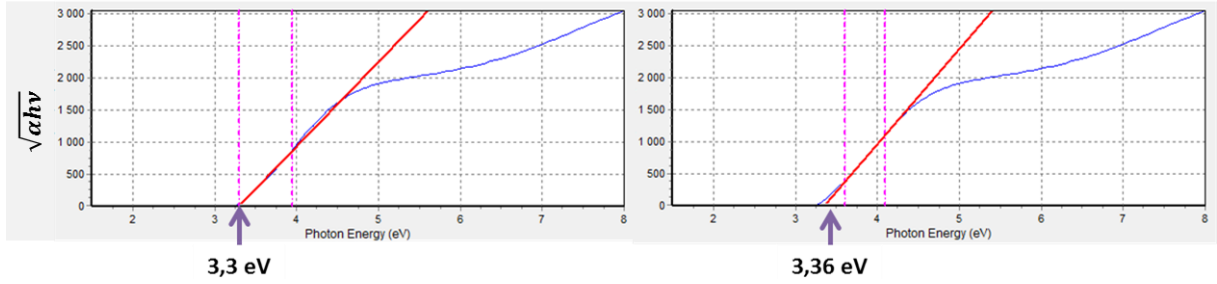


Fig. 70. Example of two boundary fits realized to evaluate the uncertainty on the determination of the optical gap of the TiO_2 layer deposited by IAD by vendor 1. E_g is estimated at 3.33 eV

5.2.2 Results

The general trend that has been observed in the past and reported in [43, 45, 42, 46] suggests that the intrinsic LIDT increases with the bandgap energy. The results presented in Fig. 71 mostly confirm this trend for each manufacturing process. However it seems not quite verified for the Al_2O_3 layer deposited by IAD by vendor 1, which has lower bandgap energy but higher intrinsic LIDT than the silica layer deposited by the same manufacturing process.

The results displayed in Fig. 71 further suggest that the influence of the manufacturing process on the optical gap energy is different for each material. The IAD layers by vendor 2 (red) exhibit the highest and lowest estimated optical gap energy for hafnia and silica, respectively. We observe a different trend for the layers coated by IAD by vendor 1 (orange) for which the hafnia optical gap energy is the lowest of the hafnia layers but the silica optical gap is in the range of other silica optical gaps. Fig. 71 also demonstrates that although the fabrication process has a large influence on the intrinsic LIDT, it only marginally affects the estimated value of the optical bandgap energy. All the optical bandgaps are indeed in the 5.5 to 6 eV range for hafnia, and 6.5 to 7.5 eV for silica.

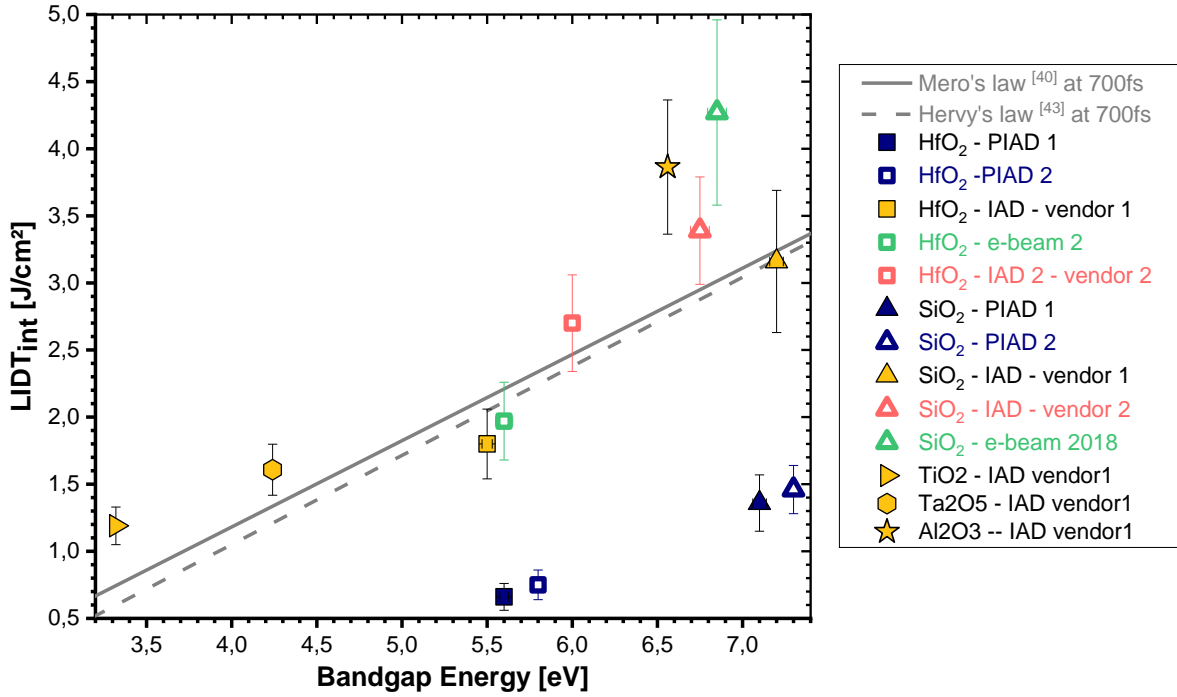


Fig. 71. Intrinsic LIDT as a function of the bandgap energy for hafnia (squares) and silica (triangles) samples deposited by PIAD (blue), IAD by vendor 1 (orange) and by vendor 2 (red), e-beam (green) compared to prediction rules taken in [43, 46]

Nota on Fig. 71: With the width of the scale for the bandgap energy, the uncertainties on the bandgap energy are hidden under the thickness of the points.

It seems that there is no general trend coming from our set of samples. One should note that Gallais *et al.* [42] observed a confirmation of the Mero's trend for multiple materials and deposition methods. This confirmation was reported in Fig. 41.(a) in chapter 3 (which was extracted from [42]). In Fig. 71, we observe a huge dispersion of the hafnia and silica intrinsic LIDT values.

To conclude on the existence of a specific law for each deposition process more materials for PIAD, IAD by vendor 2 and e-beam manufacturing process should be considered. Therefore, at this stage, it is not possible to establish a general relationship between the intrinsic LIDT and the optical gap energy alone. Moreover, such law would be laser damage setup dependent as difference in the LIDT values between various laser damage setups is observed [102]. The bandgap energy characterization can provide clues on the selection of materials among the materials deposited by a single deposition process, but are not significant for selecting a given material fabricated with different deposition process.

In conclusion, both the manufacturing process and laser damage set-up need to be taken into account when establishing an empirical law linking the intrinsic LIDT with the optical gap.

5.3 Correlation to other optical signature

Laser-induced damage under sub-picosecond regime results mostly from a multiphoton absorption process [106]. The multiphoton absorption cross section is enhanced when intermediate states exist

[62, 107], which is supposed to trig damage threshold. We therefore investigate the absorption of the monolayers in the UV spectrum in order to probe the absorption characteristics of each material at energies below the optical gap (Tauc energy) as a function of the deposition technique.

5.3.1 Correlation to spectrophotometry measurement

Our first investigation of the absorption of the monolayers is performed by determining the absorption coefficient spectra with a simple spectrophotometer.

5.3.1.1 Procedure to determine the absorption coefficient spectra

5.3.1.1.1 Case of hafnia single layers

The transmission and reflection spectra of our set of samples are measured at near-normal incidence (8° incidence) in the range 200 to 700 nm with a Perkin Elmer lambda 950 Flex System spectrophotometer. The 8° incidence angle is the smallest that can be used in both the transmission and reflection modes with this spectrophotometer. The losses arising from absorption and scattering are then calculated from these transmission and reflection spectra *via* the relation $L = 1 - T - R$ where L represents the losses, T the transmission and R the reflection coefficients. An example of the losses spectra for hafnia layers is plotted in Fig. 72. In the spectral region where the losses can be higher than about 10%, namely below approx. 370 nm in Fig. 72, the optical scattering can be safely neglected and the losses will be considered to be only due to absorption, inducing $A = L$, where A is the absorption. Moreover, the uncertainty on the estimated absorption coefficient increases when the absorption becomes very low

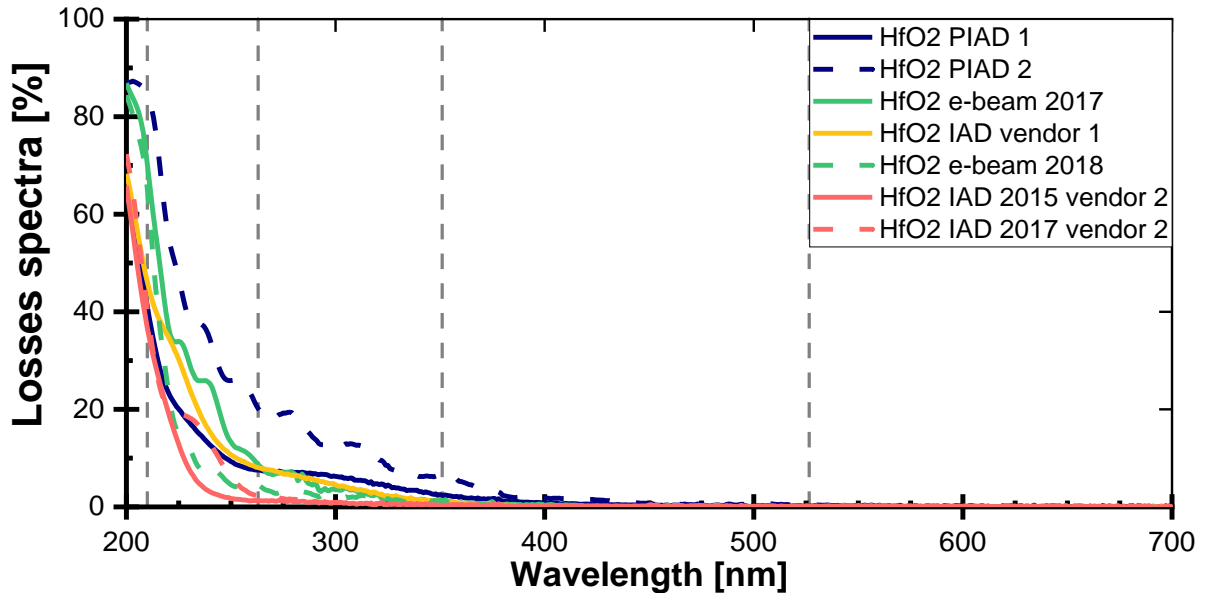


Fig. 72. Losses spectra for the hafnia monolayers between 200 to 700 nm. The dashed lines are here to guide the eye representing the wavelengths corresponding to 3, 4 or 5-photon for a 1053 nm laser

The hafnia samples referenced in the legend of Fig. 72 are sorted by increasing intrinsic LIDT values ($LIDT_{int,PIAD1} < LIDT_{int,PIAD2} < LIDT_{int,e-beam\ 2018} \dots$). From the sole consideration of these losses spectra, one can conclude that the HfO2 PIAD 2 sample has the highest losses for wavelengths below 300 nm and so the highest absorption above 15%. The losses values of the PIAD 2 layers are

approximatively twice the values of the PIAD 1 sample at 300 nm, whereas the intrinsic LIDT of both materials are quite similar. The influence of the thickness of the layers shall now be taken into account to compare absorption coefficients.

The absorption coefficient is calculated as $\alpha = -(1/h) \ln(L)$ with h the physical thickness of the layer and L the losses. The absorption coefficient spectra are plotted in Fig. 73 for hafnia layers. The spectral range 200-400 nm includes the three- to five-photon absorption spectral range. The dashed lines correspond to the wavelength of the three-photon (351 nm), four (263 nm) and five-photon (210 nm) absorptions.

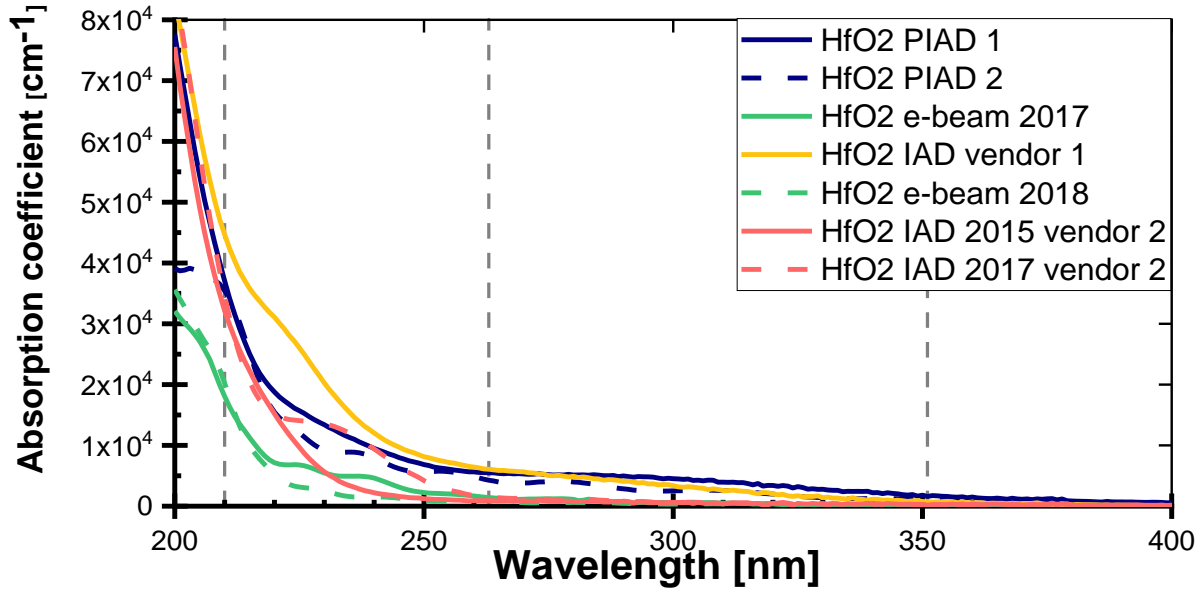


Fig. 73. Absorption coefficient of hafnia layer between 200 and 400 nm. The dashed lines are here to guide the eye representing the wavelengths corresponding to 3, 4 or 5-photon for a 1053 nm laser

The results shown in Fig. 73 for the hafnia layers indicate that the samples related to the highest $LIDT_{int}$ values exhibit the lowest values of the absorption coefficient in the three- to five-photon absorption spectral range (≈ 200 to 350 nm), while the samples related to the lowest $LIDT_{int}$ values exhibit the highest absorption.

5.3.1.1.2 Extension to other studied materials

We follow the same method for the rest of our set of samples and the final absorption coefficients are plotted in Fig. 74. The results displayed in Fig. 74 include the spectral region covering the 3, 4 and 5-photon absorption.

The absorption coefficient of the silica layers deposited by different deposition methods, displayed in Fig. 74.(a), exhibit lower values than the ones related to hafnia, and displayed in Fig. 73. Moreover, the SiO_2 layer deposited with IAD by vendor 2 in 2015 exhibits the highest absorption coefficient of the silica samples for the wavelengths below 240 nm. And, the absorption coefficient of the silica layer deposited with the same fabrication process in 2017 is lower for the whole spectral range, which reveals an evolution of the deposition process during these two years. Fig. 74.(b) presents the

absorption coefficient of other low absorbing materials, being two samples of magnesium fluoride, one of alumina and one prepared from the mixture of Sc_2O_3 and SiO_2 .

Finally, Fig. 74.(c) presents the absorption coefficient of various high index materials. The sample made from the mixture is displayed in both Fig. 74.(b) and (c) to facilitate the comparison between the two figures. Titanium and Tantalum are absorbing the UV photons. That is why the level of absorption for the TiO_2 , LaTiO_3 and Ta_2O_5 samples is considerably higher than the one observed for the other materials. Consequently the materials based on Titanium or Tantalum were not selected for entering in the composition of multilayer dielectric mirrors. The materials listed in the legends of Fig. 74(a), (b), (c) are sorted by order of increasing intrinsic LIDT values, similarly to Fig. 73.

Generally, a slight increase in the absorption can be observed for most of the materials starting around 351 nm. Defect states with their energy levels corresponding to this wavelength range can be populated via a three-photon absorption process and then, additional absorption from these states accordingly reduce the order of the multiphoton process required to support the electronic transitions up to the conduction band. All the materials also exhibit an increase of the absorption coefficient at 210 nm and below, which reveals the existence of a five-photon absorption process. These fundamental concepts suggest that increased absorption in the 200- to 350 nm spectral range could be associated with decreased damage thresholds since these intermediate states increase the probability for transition of ground-state electrons to the conduction band; therefore the damage-threshold electron density (formation of a plasma of electron in the conduction) can be reached at a lower laser fluence/intensity.

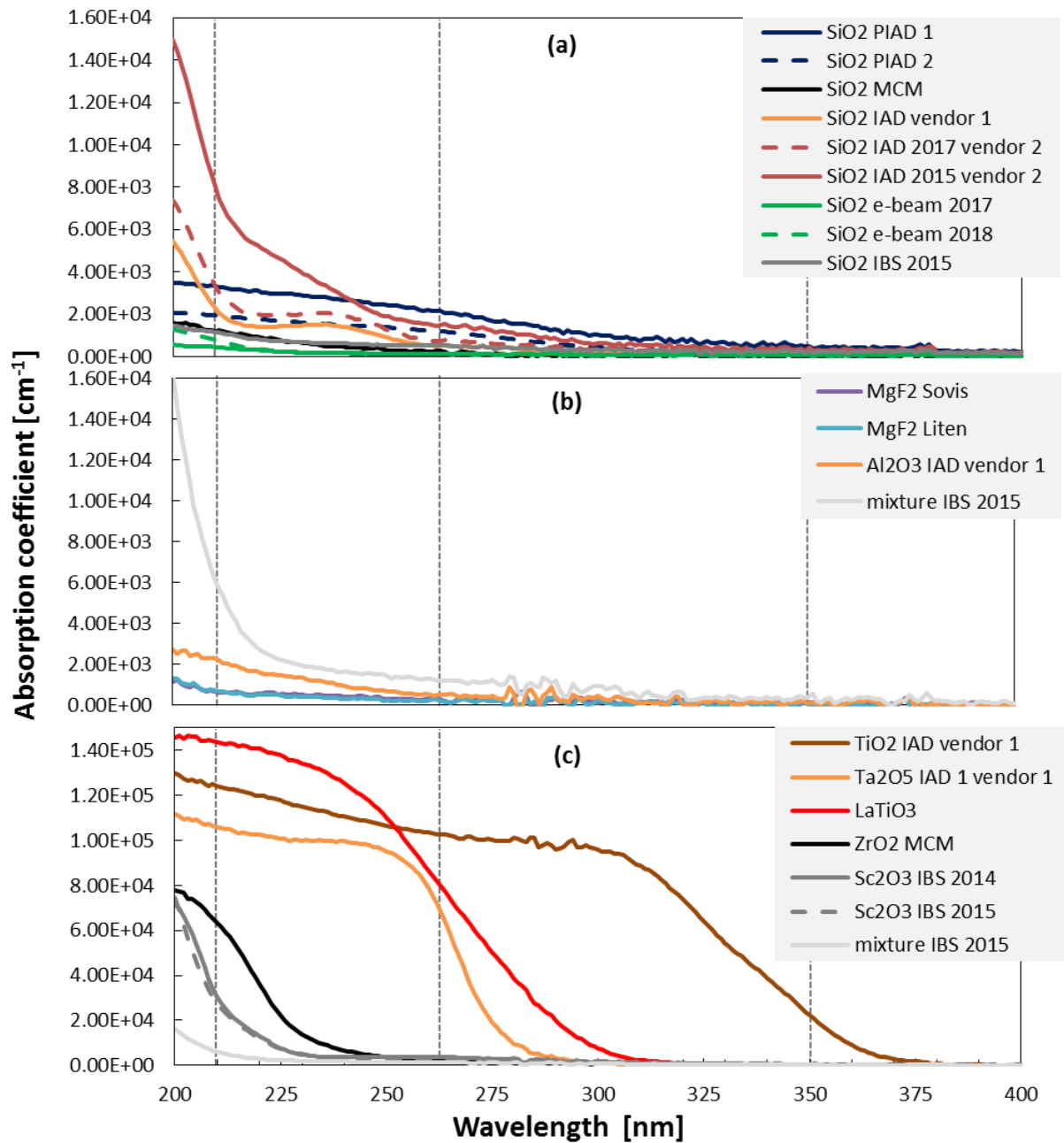


Fig. 74 Absorption coefficient of (a) silica, (b) other low absorbing materials and (c) variety of high index materials monolayers deposited on fused silica substrates. The dashed lines are here to guide the eye representing the wavelengths corresponding to 3, 4 or 5-photon for a 1053 nm laser

In Fig. 73 and Fig. 74, most materials with high absorption coefficients have low intrinsic LIDT values. This spectral characterization allows doing a macroscopic ranking of the materials and eliminating the materials with too high absorption coefficient.

5.3.1.1 Discussion

This trend is quantified in Fig. 75 and Fig. 76, which represent the absorption coefficient of high index monolayers at 351 nm and low index monolayers at 266 nm as a function of their intrinsic LIDT, respectively. The intermediate refractive index materials (the mixture and the Al_2O_3 layers) are presents on both figures. Considering the uncertainty on the thickness equal to ± 5 nm and the one

related to the reflection and transmission coefficients lower than $\pm 2\%$, one can conclude that the uncertainty of the absorption coefficient is in the order of $\pm 50 \text{ cm}^{-1}$.

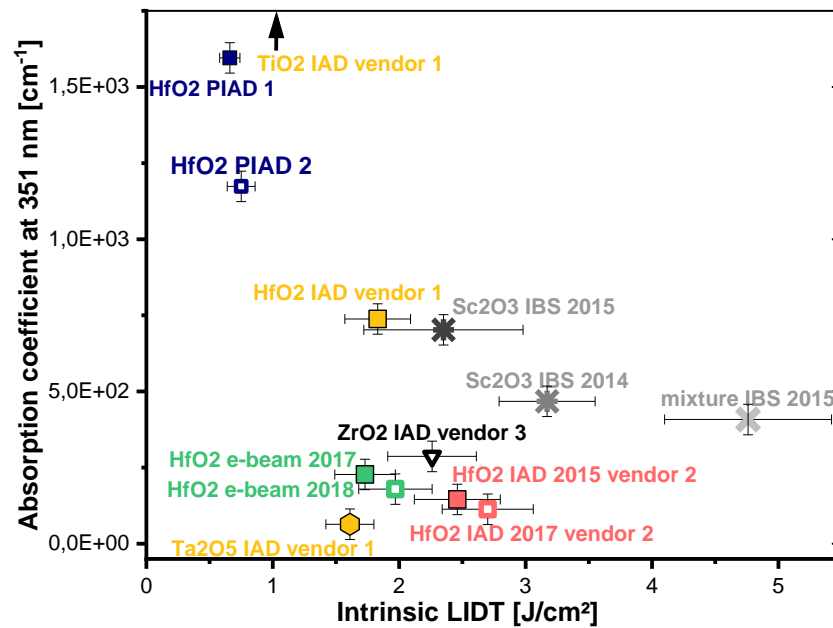


Fig. 75. Absorption coefficient at 351 nm for various high index materials (shapes of the symbols) deposited with various manufacturing process (colors)

On Fig. 75, one can observe that, for a given material, the layers that exhibit high absorption are characterized by low LIDT and reciprocally. The PIAD process exhibits important variations of the absorption coefficient. It is thus the deposition process that appears to be the less interesting for this kind of application. The TiO₂ absorption coefficient at 351 nm is one order of magnitude higher than the rest of the set of layers, it is then outside of the chosen scale.

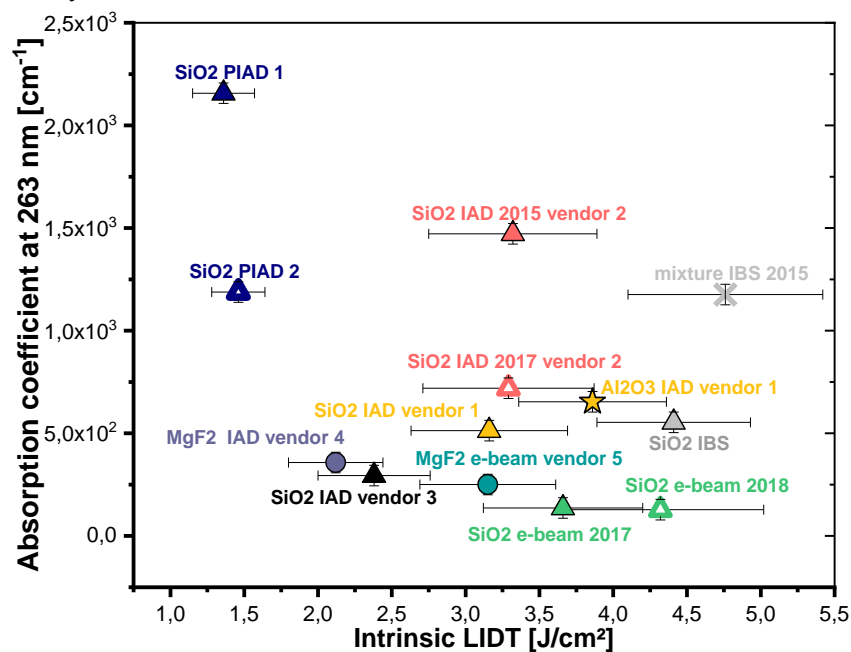


Fig. 76 Absorption coefficient at 263 nm for various low index materials (shapes of the symbols) deposited with various manufacturing process (colors)

As stated in the beginning of this chapter, in Fig. 76, the silica layers are represented by triangles, the magnesium fluoride layers by circles, the mixture by a simple cross and the alumina sample by a star. The distribution of the silica layers, except for the SiO₂ IAD deposited by vendor 2 in 2015, shows that the high absorbing layers exhibit low intrinsic LIDT values. It is possible that, for this outlier sample, the LIDT determination on a small area of the sample lead to an overestimation of the intrinsic LIDT value. The reflection and transmission coefficients are measured on a significantly larger area, which could confirm the presence of defects inside the coating that increase the absorption coefficient.

These results suggest the presence of a correlation between the absorption at energies below the optical gap and the intrinsic LIDT at 1053 nm, 800 fs laser pulses. It suggests the possibility to model the LIDT_{int} performance only based on the direct measurement of the absorption spectra in the spectral region below the optical gap. Such model could be used as in-situ diagnostic during the deposition process. In addition, the present spectral characterization of the UV absorption can already be used to perform a quick selection of the materials of interest deposited by a given deposition process, prior to submitting them to further accurate intrinsic LIDT determination.

With this characterization one can also qualify the typical range of variations of a deposition process for a given material. Thus, the deposition processes that exhibit variations higher than the uncertainties, like the PIAD technique between two samples of different thickness and same composition, or the IAD technique by vendor 2 between 2015 and 2017, should not be selected or only with caution.

The absorption characterization presented above is based on the approximation that when the losses are sufficiently high the scattering can be neglected. The deviation of some layers from the general trend observed might be due to a higher scattering contribution than expected.

5.3.2 *Correlation to photothermal absorption measurements*

For more precise characterization of the absorption and to further explore the above concept, photothermal absorption measurements in the UV at 355 nm were performed using a photothermal heterodyne imaging (PHI) system developed and installed at LLE.

5.3.2.1 Set-up description

The photothermal absorption technique described in [108, 109, 110] and in Fig. 77 is based on a pump-probe approach. The 355 nm pump beam modulated at 410 Hz and the continuous 633 nm probe beam are collinearly combined on the entrance aperture of a high-numerical-aperture objective and focused onto the sample in an overlapping submicrometer spot. The transmitted probe beam is analyzed by a photodiode coupled with a lock-in amplifier where the output signal is proportional to absorption. For every characterization, we recorded several intensity maps by raster-scanning the sample over a $20 \times 20 \mu\text{m}^2$ area.

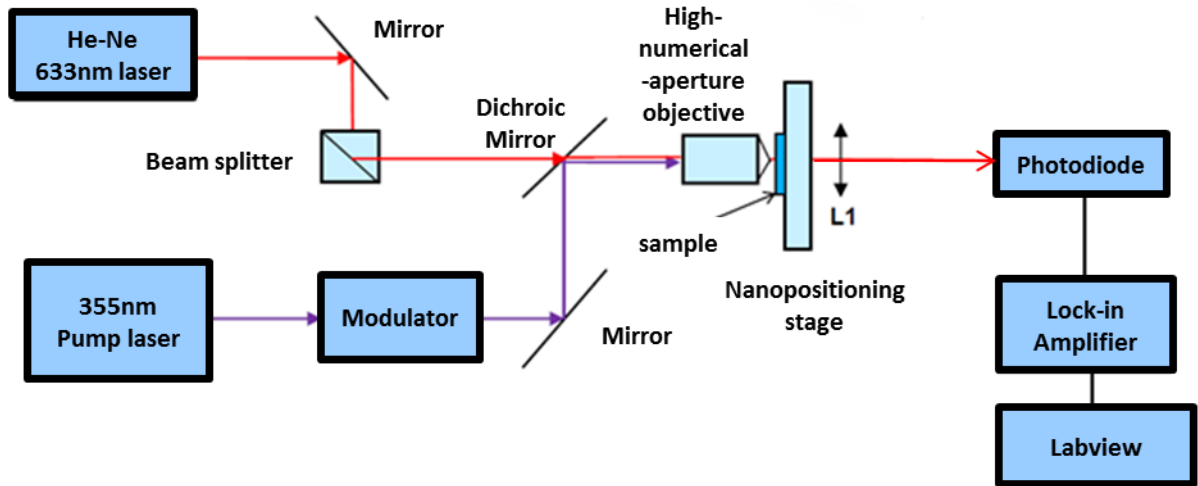


Fig. 77. Schematic of the Photothermal Heterodyne Imaging set-up installed at LLE, Figure taken from [110]

Those maps were homogeneous, as presented in the two examples of maps in Fig. 78, and an average value of every map for each sample was calculated. The photothermal absorption was normalized by the physical thickness of the layer. The results are displayed in Fig. 79

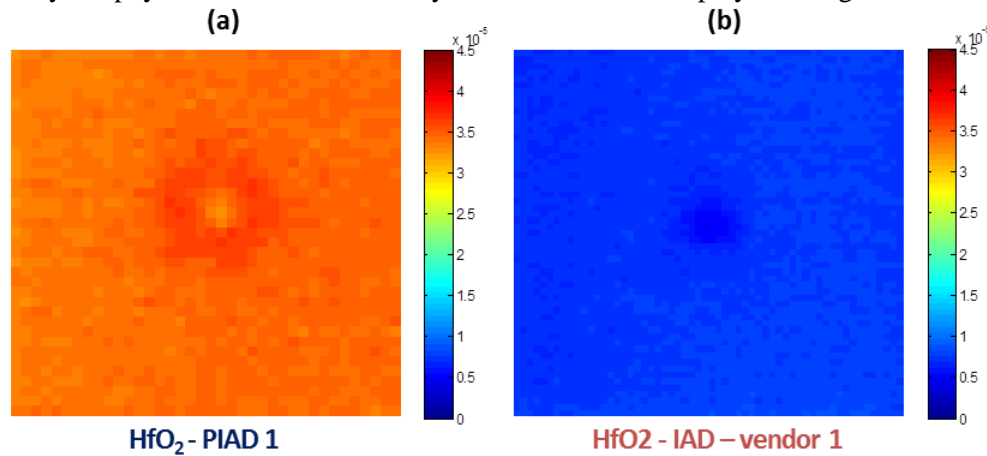


Fig. 78 Example of intensity $20 \times 20 \mu\text{m}^2$ maps recorded on two different hafnia samples. The color scale which is identical for both maps represents the level of PHI signal [V].

The circle in the center of the map in Fig. 78(a) is the trace left by the annealing effect induced by the pump laser spot during the alignment of the set-up. The uncertainty on the PHI signal is set at the noise level of this signal.

5.3.2.2 Results

The characterization of selected samples has been realized during exchanges at LLE.

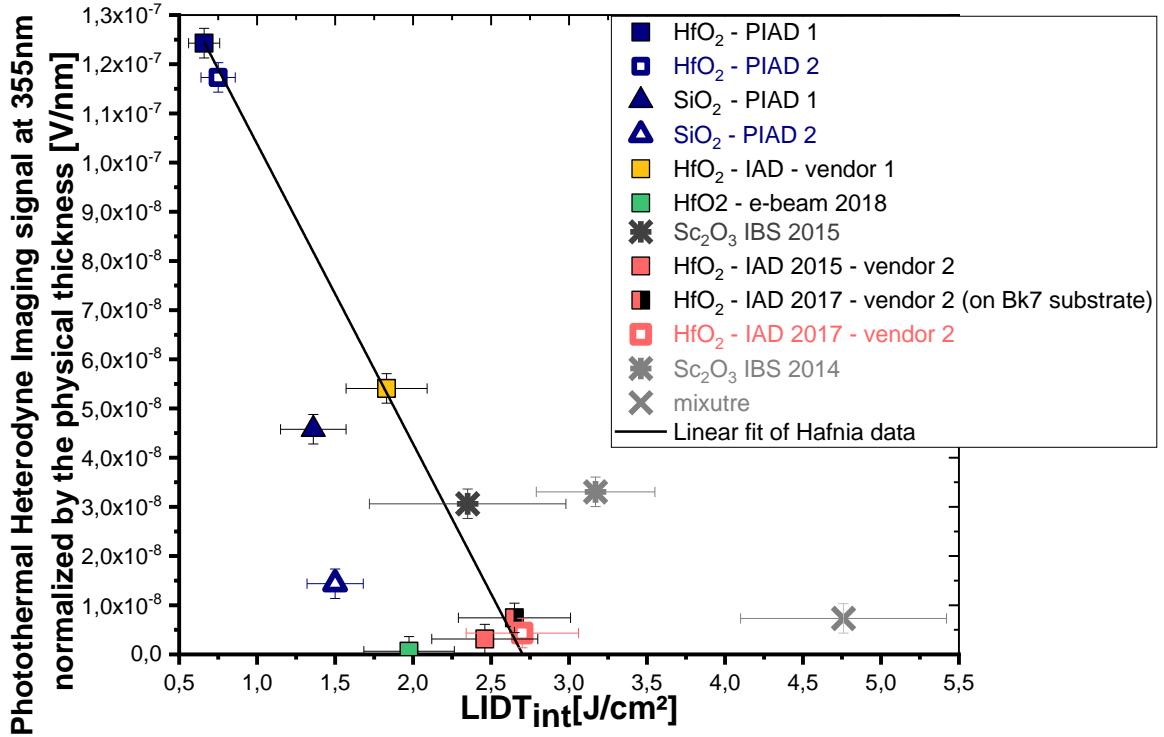


Fig. 79. Photothermal Heterodyne Imaging (PHI) signal at 355 nm normalized by the physical thickness as a function of the intrinsic LIDT for hafnia (squares), silica (triangles), scandia (8 branches crosses) and mixture (simple cross) samples.

The results shown in Fig. 79 indicate that the strength of the photothermal absorption in the samples depends on their deposition method. For the case of hafnia samples, the highest absorption at 355 nm is obtained for the two samples (PIAD 1 and 2) that also feature the lowest $LIDT_{int}$ at 1053 nm. On the other hand, lower absorption is observed for the IAD samples by vendor 2 that also feature the highest $LIDT_{int}$. The only divergence from this trend is for the hafnia sample deposited with e-beam, which exhibits the lowest photothermal absorption signal at 355 nm, barely above the noise level, but still its $LIDT_{int}$ is lower than the IAD samples from vendor 2 that exhibit slightly higher photothermal absorption. This behavior indicates that there are probably additional processes affecting the $LIDT_{int}$ that are not captured by the photothermal absorption technique when using a 355 nm pump. In fact, the absorption spectrum of the e-beam sample shown in Fig. 73 indicates that absorption at wavelengths above 266 nm, and corresponding to defect states that can be excited via three- or four-photon absorption, is very small, but it rapidly increases at shorter wavelengths to reach one of the highest absorption coefficient values at 210 nm, the wavelength corresponding to states that can be excited by five-photon absorption. This observation may suggest that complementary photothermal measurements at higher laser harmonics may be required for a more accurate assessment of the $LIDT_{int}$ using the photothermal absorption method.

The general trend observed in the hafnia samples is also observed for the silica samples. The number of data points for silica is limited since absorption of fused silica is very low and below the

detection limit of our instrumentation. Specifically, we were able to measure photothermal absorption for the PIAD samples only, which also exhibited the weakest $LIDT_{int}$ values.

The two Scandia layers exhibit comparable absorption which is not the case for their intrinsic LIDT. The uncertainty on the intrinsic LIDT of the layer deposited in 2015 is quite high and should be reduced by repeating the laser damage characterization on this sample. The absorption level of the mixture is lower than the one of the pure Scandia layer and higher than the one of the pure silica layer, the latter absorption was under noise level of the photothermal heterodyne imaging system.

A correlation between photothermal absorption at 355 nm and $LIDT_{int}$ at 1053 nm in short pulse seems to be observed for both hafnia and silica monolayers. This correlation could open novel routes toward not only an experimental screening of the sample of interest but also the quantification of intrinsic LIDT with a nondestructive method.

Remark on the research on a possible correlation to Luminescence measurements

Since the measurement of the absorption with the PHI system for the silica layer was most of the time impossible, we decided to also investigate the existence of a potential correlation between luminescence and intrinsic LIDT. However, we were not able to draw clear conclusions due to the significant intensity of the luminescence of the substrates. Indeed the luminescence maps performed with the same set-up than the photothermal absorption set-up at LLE [109, 110], were performed in transmission through the layer and the substrates. In the previous discussion, the contribution of the substrates was safely neglected due to the low level of absorption of fused silica substrates at 355 nm. In the present case, the luminescence due to the substrate was subtracted, but some uncoated substrates unexpectedly exhibited higher intensity of luminescence than coated ones. Consequently, the characterization was abandoned.

Conclusion of Chapter 5

To explain the dispersion of the intrinsic LIDT values, we first measured the optical gap of the layers. The results deviate from the laws previously presented in the literature suggesting the existence of a law specific for each manufacturing process (deposition method + manufacturer). Such laws should be considered carefully and only for a specific deposition process and a laser damage set-up. Finally, it means that the $LIDT_{int}$ cannot be predicted with the sole bandgap energy.

Further investigations have been conducted to understand what can affect the intrinsic LIDT values. A good correlation between the absorption in the UV and the $LIDT_{int}$ at 1053 nm was observed for hafnia, as well as other materials deposited as single layer. It confirms that the damage in sub-ps is the result of multiphoton absorption phenomenon. Further research are required to be able to determine a model that would predict the intrinsic LIDT with only absorption measurement and lead to the development of accurate nondestructive characterization.

The present absorption characterization with a spectrophotometer examined and already permits to realize a quick experimental screening of the best samples for laser damage test. This characterization of the absorption coefficient is especially interesting as it only requires a spectrophotometer.

Chapter 6 Design optimization

6.1	<i>Experimental validation of our algorithm: Optimization for air use</i>	118
6.1.1	Expected numerical LIDT results	118
6.1.2	Results	121
6.1.3	Intrinsic LIDT determination from multilayers	123
6.2	<i>Influence of the environment on multilayers dielectric mirrors</i>	124
6.2.1	Performance of the design for vacuum	125
6.2.2	Study of the potential Influence of the mechanical stress on LIDT	126
6.2.2.1	Stress variations with the environment for the three deposited designs	126
6.2.2.2	Evaluation of the possible impact of stress on the LIDT	127
6.2.3	Intrinsic LIDT determination in vacuum from multilayers	131
6.3	<i>Optimization of the Final design</i>	131
6.3.1	Expected numerical LIDT results	131
6.3.2	Results	133
6.3.2.1	For the optimized configuration	133
6.3.2.2	LIDT for p -polarization in ambient air	134
6.3.2.1	S-polarization results	136
Conclusion of Chapter 6		137

In chapter 3 was presented our home-made robust optimization algorithm to improve the LIDT of multilayer dielectrics coatings in the sub-ps regime based on materials properties extracted from the literature. Then, in chapter 4, several materials were experimentally characterized to retrieve the input parameters of this algorithm, namely the refractive index and intrinsic LIDT.

In the present chapter, this algorithm is submitted to experimental validation through the characterization of optimized designs of multi-layer dielectric mirrors, first for air use and finally for vacuum use. The optimizations were performed for the *p*-polarization since it is the limiting one. The electric field intensity in a MLD mirror is indeed always higher for the *p*-polarization than for the *s*-polarization, inducing a lower damage threshold for the *p*-polarization than for the *s*-polarization.

The chosen materials and manufacturing process to perform this experimental validation are the most available ones exhibiting good performances, namely SiO₂ and HfO₂ deposited with e-beam process.

6.1 Experimental validation of our algorithm: Optimization for air use

Our algorithm has been first applied with the aim at obtaining a high reflector ($R > 99\%$) at 1053 nm, 45° incidence for the *p*-polarization in ambient air. The laser-induced damage thresholds were retrieved from the 1-on-1 procedure performed at LLE in ambient air with an 800 fs pulse.

6.1.1 Expected numerical LIDT results

The input parameters of our algorithm are the refractive index and the intrinsic LIDT for both the high and low refractive index materials. These parameters were determined experimentally following the procedure described in chapter 4 on single layers and the results are reported in Table 16.

**Table 16. Input parameters in ambient air of the optimization algorithm:
refractive index and intrinsic LIDT of HfO₂ and SiO₂ deposited with e-beam**

	HfO ₂ - e-beam	SiO ₂ – e-beam
Refractive index in ambient air at 1053 nm	1.86	1.438
Intrinsic LIDT at 1053 nm and 800 fs [J/cm²] Determined at LLE on single layers ambient air	1.14±0.16	2.74±0.37

These two materials have lower refractive index than the bulk materials indicating the presence of a porosity of the layers. The relative humidity is then expected to have an influence on the coatings performances. The ratio between the two intrinsic LIDT is large around 2.4. This ratio is an indication on the importance of optimizing designs. In the case of a ratio around 1, the two intrinsic LIDT are equivalents. The balanced design will not be far from the QWOT design. Indeed, in this case, the thicknesses of the two outer layers required less adaptation so the laser-induced damage threshold of the two outer layers is equalized.

To assess the performance and validity of our algorithm, three different designs, counting the same number of layers, were fabricated and then laser damage tested.

- The first design is a *classical design* with 37 quarter-wave optical thickness (QWOT) layers: $(HL)^{18}H$.
- The second design is an Apfel based design, named *balanced design*, with the thickness of only the two outer layer optimized: $(HL)^{17}HyLxH$ (y and x are chosen so the Electric field intensity peak is shifted into the silica layer instead of the interface between the two outer layers).
- The last design is produced by the robust optimization algorithm. It is the design that maximizes the LIDT while being robust to manufacturing errors, named *LIDT max design*: $(HL)^{12}H(K)$, with (K) an alternation of 12 layers with optimized thicknesses.

The robust algorithm is used with the same settings than the example presented in chapter 3. The screening conditions for the numerical convergence of the algorithm are:

- reflectivity higher than 99%
- LIDT at least 5% higher than the one of the classical design, namely 1.27 J/cm^2 .

The manufacturing errors in the robustness tests are set to $\pm 3 \text{ nm}$ for the thicknesses, ± 0.03 for the refractive indexes and $\pm 0.08 \text{ J/cm}^2$ for the intrinsic LIDTs. The selected design here exhibits the highest LIDT value after the robustness screenings in nominal condition. This choice allows validating the capability of the algorithm to provide a design with a LIDT higher than a balanced design while being robust to manufacturing errors. It is essential to assess the performance and robustness of the selected design. To understand better how the so-called *robust* algorithm operates, the electric field intensity distribution of the classical, balanced and LIDT Max design are compared in Fig. 80.

In chapter 3 was presented another interesting design to study, this design produced by the algorithm and designated as *robust design* was the one that exhibit the highest LIDT under the final robustness selection criterion: a cumulative error. This design is not studied in a first time but will be fabricated and characterized in the case of vacuum use in 6.3.

Fig. 80 shows the electric field intensity distribution with the 12 outer layers of (a) the classical design (b) the balanced design and (c) the LIDT Max design. The red lines are guide for the eye to read the electric field maxima where the damage will occur. Fig. 80 (a) shows for the classical design the electric field intensity maximum is equal in the two outer layers and at 99%. For the balanced design, the thicknesses of the two outer layers are optimized, so the electric field intensity peak is shifted into the silica layer and the electric field maximum in the hafnia layer drops to 80%. When increasing more the thickness of the 2nd outer layer (silica layer), this maximum may decrease more but then the 3rd layer will still have a electric field maximum of 75% (lighter red line in Fig. 80 (b)) and this layer will be the one damaging. Finally, Fig. 80(c) shows that, for the LIDT Max design, the electric field intensity maxima of the 1st, 3rd and 5th outer layers is equalized around 63% for the p -polarization. Damage may occur at the depth of any of those maxima. The algorithm is able to bring a better numerical solution by balancing more layers and reducing the general electric field in the stack without significantly decreasing the reflectivity (only 0.2% reduction).

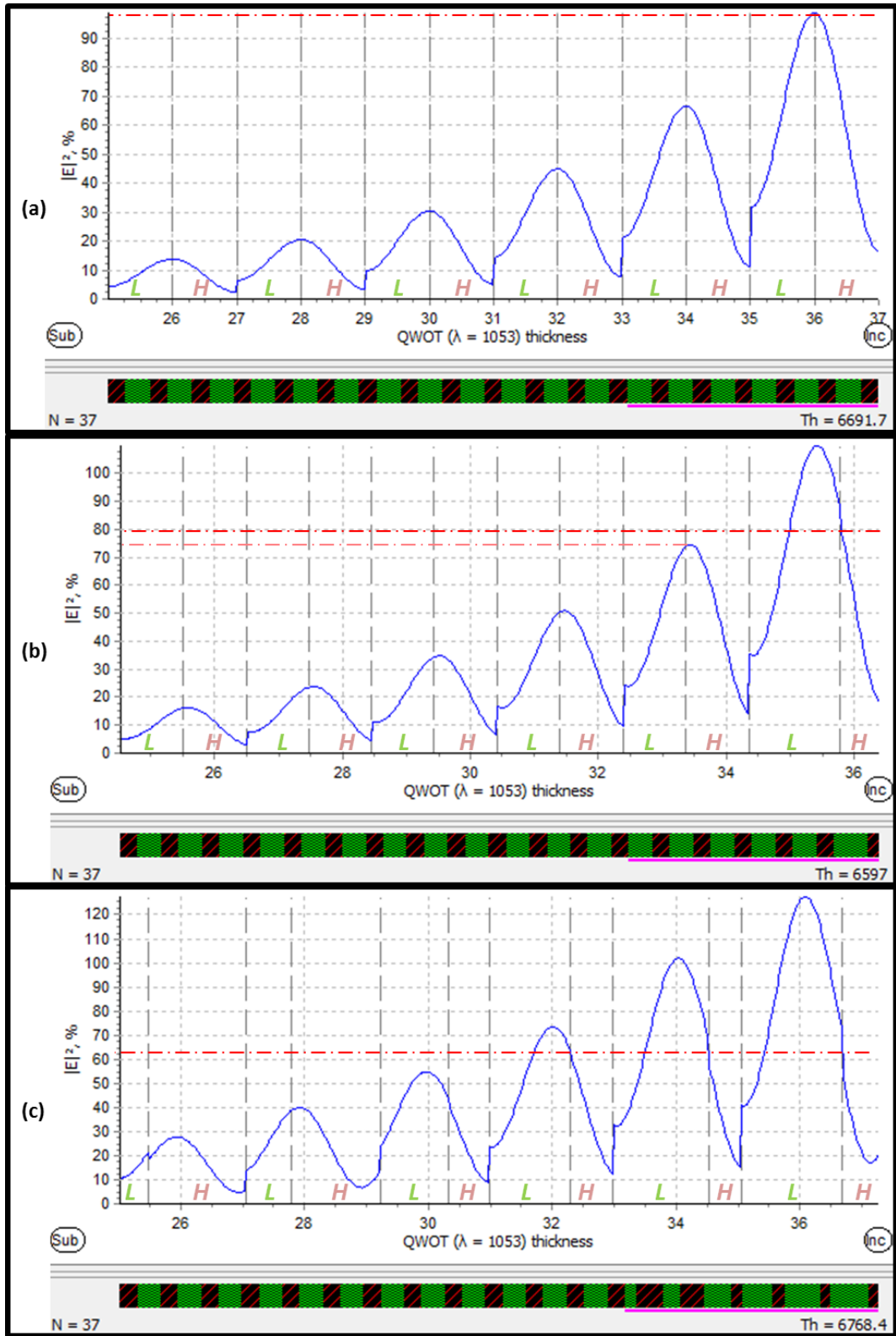


Fig. 80. Electric field intensity distribution for the p -polarization within the 12 outer layers of (a) the classical design (b) the balanced design and (c) the LIDT Max design (for which the thickness of those layers is optimized). The red lines are guide for the eye to read the Electric field maximum where the damage will occur.

The calculated performances of the three designs are reported in Table 17.

Table 17. Predicted LIDT performances at LLE in ambient air of all three designs

	Classical design	Balanced design	LIDT max design
Predicted reflectivity at 1053 nm	99.7%	99.7%	99.5%
Predicted LIDT In nominal conditions	1.21 J/cm ²	1.45 J/cm ²	1.80 J/cm ²
Improvement on the LIDT compared to classical design	--	+19%	+48%
LIDT in the case of cumulative manufacturing errors (Final robustness selection)	1.04 J/cm ²	1.08 J/cm ²	1.25 J/cm ²
Improvement on the LIDT compared to classical design in the case of a cumulative errors		+4%	+20%

The final robustness criterion corresponds to the case of a cumulative error on the three source of error. The LIDT Max design remains the design with the highest LIDT in either nominal and conditions and in the case of error, offering an improvement of 48% on the LIDT compared to the classical design in nominal condition and 20% in the case of a cumulative error.

6.1.2 Results

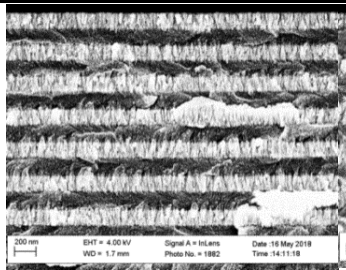
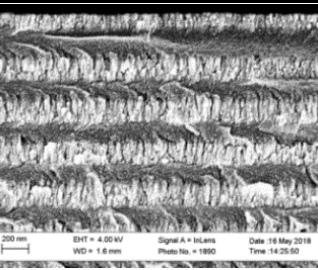
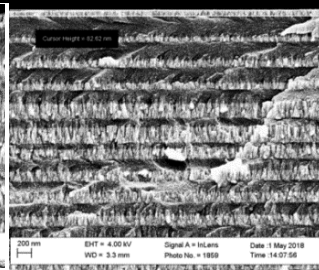
Once the three designs were coated, the following characterizations were performed: SEM observations of the profile of the designs, spectrophotometry measurements, 1-on-1 laser damage tests at 800 fs, 45° for both states of polarization.

The results are reported in Table 18. The SEM observations are used to verify the coated thicknesses of the layers for each design. The spectrophotometric measurement allows verifying if the expected reflectivity specification has been reached. The LIDT is measured under the specific conditions of optimization for each design.

The LIDT Max design exhibits the highest LIDT of 2.49 J/cm² which represents a 44% improvement compared to the classical design and around 9% improvement compared to the balanced design. The reflection of the three designs was measured to be higher than 99%, which is satisfying.

Although the ranking of these three designs is as expected from the calculation, the measured LIDT values of all three designs are about 45% higher than predicted LIDT from the single layers (Table 17).

Table 18. SEM pictures, reflectivity and LIDT performance of the 3 designs of interest

	Classical design	Balanced design	LIDT max design
SEM picture			
Reflectivity at 1053 nm, p -pol, 45°	99.8%	99.8%	99.7%
LIDT 1053 nm, p -pol, 800 fs, 45° ambient air At LLE [J/cm ²]	1.74±0.10	2.29±0.14	2.49±0.18
Improvement on the LIDT compared to classical design	--	+31%	+44%

This deviation from the predicted LIDT values can not to be attributed to manufacturing errors on the thickness or refractive index. Indeed, we have verified that the manufacturing error of the deposited layer thickness was less than 3%, thus in perfect agreement with the robustness test. In addition, the spectral responses of the deposited designs are close enough to the expected spectral response to indicate low errors on the values of the refractive index, as well as thickness.

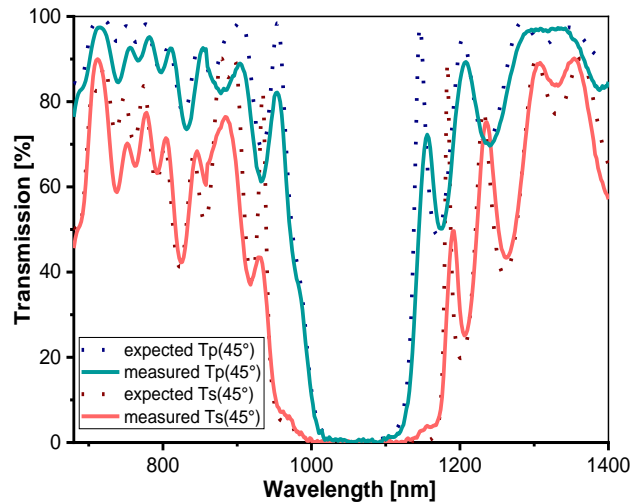


Fig. 81. Comparison between the predicted and measured spectral response of the LIDT Max design generated with the robust algorithm

Consequently, the difference between the measured and predicted LIDT values of the three designs are probably due to the underestimation of the intrinsic LIDT values of the two materials involved in the multilayer stack. More precisely, the intrinsic LIDT values of the materials in a multilayer stack seem to be different from the ones derived from single-layer characterization.

6.1.3 Intrinsic LIDT determination from multilayers

Thus, to verify this assertion, we decided to retrieve the values of the intrinsic LIDT directly from the three multilayers based on the procedure describe in Fig. 82.

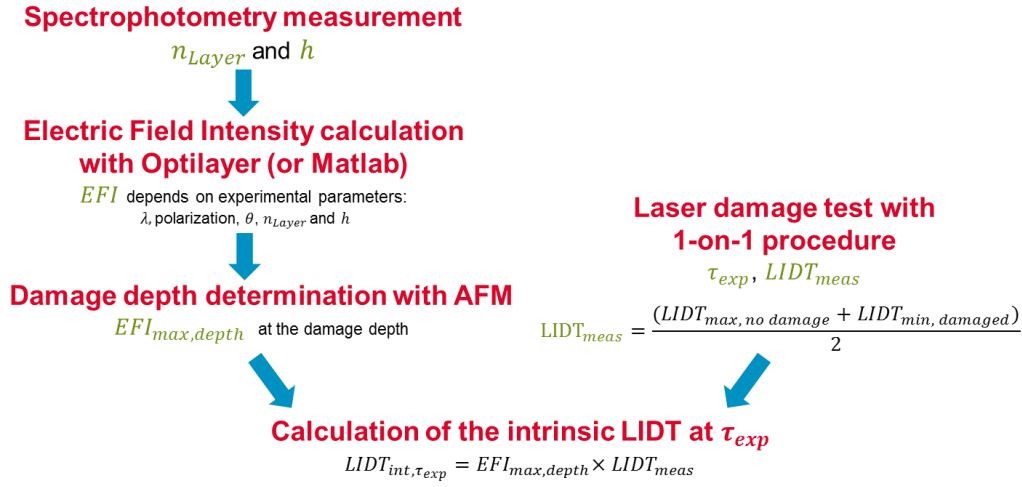


Fig. 82. Schematic of our procedure to determine the intrinsic LIDT from multilayers samples

The good agreement between the deposited and expected values of thickness and refractive index is first verified with the fit applied to the spectrophotometric data. Then, one can calculate the electric field intensity distribution. AFM measurements were performed on the damage sites to determine the damage depth. With this depth and the knowledge of the design, one can know which material is at the origin of the damage. The intrinsic LIDT of the damaging material is then estimated from the LIDT results and the value of the electric field intensity at the damage depth: $EFI_{max,depth}$. The $LIDT_{int}$ for hafnia and silica estimated from the three multilayers, reported in Table 19, are 15% higher for silica and 49% higher for hafnia than the ones determined with the single layers.

Table 19. Refractive index and intrinsic LIDT of HfO_2 and SiO_2 deposited with e-beam determined from the three multilayers

	HfO ₂ – e-beam	SiO ₂ – e-beam
Refractive index in ambient air at 1053 nm	1.86	1.438
Intrinsic LIDT at 800 fs[J/cm²]		
Determined at LLE on the multilayers	1.70	3.15
ambient air		

The discrepancy between the $LIDT_{int}$ values derived from either single layers or multilayers samples are higher than the ones estimated in the robustness test. The ratio between the $LIDT_{int}$ of the two materials is now 1.85.

The difference between the $LIDT_{int}$ values determined from single layers or multilayers samples could suggest that the $LIDT_{int}$ varies with the position of the layer and/or what is underneath the layer. These variations could be linked with the refractive index variations observed for porous layers within a stack. Indeed porous layers buried under the stack (near the substrate) could be denser than layers close to the incident medium. This densification and thus material properties variations are difficult to

quantify. This could also suggest that the difference between the intrinsic LIDT determined with single layer or multilayer varies with deposition method and would be smaller with denser deposition process. This would require to be verified by damage testing design deposited with other manufacturing process.

Even though, the characterization of the intrinsic LIDT with single layers needs to be performed, since it allows comparing the materials to one another and selecting the materials. Moreover the evaluation from single layers is underestimating which allows giving a bottom optimization value to expect when optimizing.

To increase the accuracy of the determinations of intrinsic LIDT on multilayers, not only the LIDT results for the *p*-polarization were used according the procedure described in Fig. 82, but also the LIDT results of the three designs for the *s*-polarization. These additional LIDT results are reported in the Table 20. The intrinsic LIDT values presented in Table 19 are in good agreement within the three design and different states of polarizations.

Table 20. LIDT performance of the 3 deposited designs for the *s*-polarization

	Classical design	Balanced design	LIDT max design
LIDT 1053 nm <i>s</i>-pol, 800 fs, 45°, ambient air [J/cm²]	2.38±0.13	3.61±0.21	3.15±0.20

As expected from the electric field intensity calculation, the LIDT values of the three designs are higher for the *s*-polarization than the ones reported for the *p*-polarization. Moreover, the ranking of the three designs is different for this polarization with the balanced design offering the best performance. This result highlights the importance of designing and optimizing a multilayer dielectric mirror for a specific polarization.

To conclude, the LIDT results reported in this paragraph demonstrate that our robust optimization algorithm works for the specific polarization it is aimed at. Even with unexpected variations of both materials intrinsic LIDT, the LIDT Max design performs better than the other designs for the conditions of use it was designed for. This optimization was undertaken for a *p*-polarized mirror used in ambient air.

6.2 Influence of the environment on multilayers dielectric mirrors

The MLD mirrors placed after the compression stage in Petal, which we aim at improving, are used in vacuum. We expect the vacuum environment to have 2 effects that can alter the LIDT value of the MLD mirrors: a change of the stress of the coating and a change of the refractive index induced by the porosity of the layers. We need to assess the influence of the environment on MLD mirrors. Firstly, we will test the performance in vacuum of our previously deposited designs to evaluate the impact of the environment on multilayer.

6.2.1 Performance of the design for vacuum

The three multilayer stacks previously discussed were laser damage tested in vacuum for the two states of polarization s and p , and the results are reported in Table 21. The LIDT values of the three designs in different conditions (see Fig. 83) show that the environment of test has an influence on the LIDT.

Table 21. Experimental LIDT characterized with p - and s - polarization in vacuum

	Classical design	Balanced design	LIDT max design
LIDT 1053 nm, p -pol, 800 fs, 45°, vacuum [J/cm ²]	1.41±0.08	2.15±0.20	1.51±0.08
LIDT 1053 nm, s -pol, 800 fs, 45°, vacuum [J/cm ²]	2.39±0.14	3.49±0.25	2.44±0.13

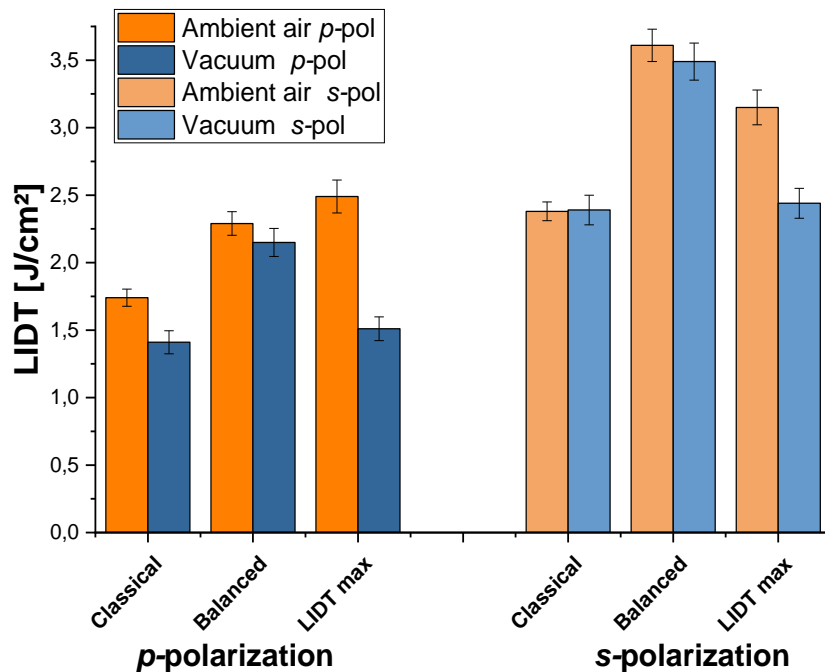


Fig. 83. Comparison of the LIDT values in either ambient air (orange) or vacuum (blue) for the three designs and the two states of polarization (p and s).

From Fig. 4, it is interesting to notice that the LIDT Max design optimized for the p -polarization in ambient air is no more the best design when operated under vacuum and the corresponding LIDT values fall down to the values of the classical design. The significant decrease of LIDT observed in this case between ambient air and vacuum can be due to refractive index variation or mechanical stress. Let's also notice that the variations of the LIDT between air and vacuum for the three designs are different. This could be due to the fact that i) the conditions of stress are probably very different depending on the designs, and/or ii) the robustness of each design to the refractive index variations induced by the environment are also different. The potential influence of mechanical stress on the LIDT will be evaluated in the next paragraph.

6.2.2 Study of the potential Influence of the mechanical stress on LIDT

Comparable variations of the LIDT values with the environment have already been reported for nanosecond pulses [111, 112]. The authors observed that denser coatings tend to be less inclined to exhibit these variations. Riede *et al.* [112] even stated that vacuum dehydration is affecting porous coatings, and increases the tensile stress, and generally lowers its LIDT. In addition, the application of compressive stress to e-beam coatings improves their performance (and vice versa for IAD). This assertion suggests that the difference in behavior of our three different designs is probably due to different stress conditions.

6.2.2.1 Stress variations with the environment for the three deposited designs

Consequently, we manufactured samples to address that potential effect. Stress witnesses were placed during the coating of the three different coating runs to characterize the intrinsic stress of the coatings. The witnesses are very thin Fused Silica substrates for which the sag is characterized before and after the coating. From these characterizations, one can retrieve the curvature induced by the coating to calculate the intrinsic stress σ using the Stoney's formula:

$$\sigma = \frac{Y_s \cdot h_s^2}{6(1-\nu_s)h_f R} \quad (6.1)$$

with Y_s the Young's modulus of the substrate, h_s / h_f the thickness of the substrate / film, ν_s the Poisson's ratio of the substrate and R the radius of the curvature of the sample.

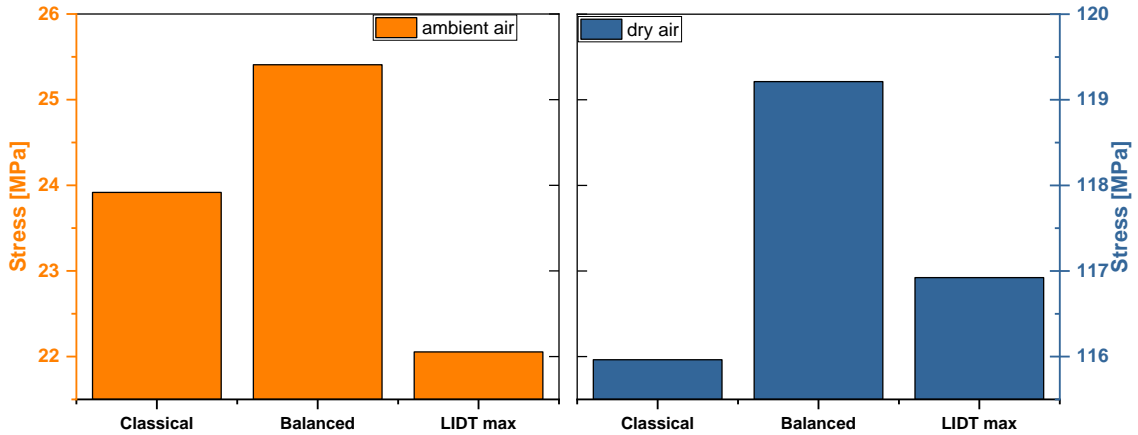


Fig. 84. Stress of the three stress witness representative of the three designs in ambient air, namely with 40% relative humidity (orange, left plot) and in dry air, namely with 0% relative humidity (blue, right plot)

The stress of the three designs increases from typically 24 MPa in ambient air to typically 118 MPa in dry air. More precisely, the increase of stress is 92 MPa for the classical design, 94 MPa for the balanced design, and finally 95 MPa for the LIDT Max design. This average behavior of having the tensile stress increasing can be linked with the reduction of the laser-induced damage threshold. The stress conditions of the three designs are not different. Consequently if stress was the major factor inducing LIDT variation with the relative humidity, the LIDT variation presented in Fig. 83 should be the same. This lead to think that stress has no effect or a limited one on the LIDT. To be sure of it, we

investigated the possible influence of the stress on the thin films LIDT in short pulse by damage tested mirrors samples placed under different external stress. The procedure and results are presented in the next paragraph.

6.2.2.2 Evaluation of the possible impact of stress on the LIDT

The specific question of whether stress can affect LIDT, without the environment consideration, has been the subject of a few studies and these studies were undertaken for laser damage threshold in nanosecond. Austin *et al.* [113] deposited $\text{MgF}_2/\text{SiO}_2$ mixture monolayers with varying proportions of the two materials and tested them for LIDT with a 1064 nm laser, with 30 ns pulses. They attributed the variations of LIDTs to the differences in stress of the films. More recently, Jensen *et al.* [114] presented more nuanced conclusions on the impact of stress onto multilayer, because the extent of the possible effect was slightly higher than the measurement error. The stress of the same multilayer $\text{Ta}_2\text{O}_5/\text{SiO}_2$ design was modified using different shapes of substrates, compensating layers or temperature treatment. All samples were laser damage tested at 1064 nm with 10 ns pulses.

To address this question in the sub-picosecond regime, laser damage tests were performed on the previously described classical design deposited on one side of rectangular slabs of either BK7 or fused silica (FS) while bending these slabs to induce different types of external stress. By using two different types of substrates and thus different Young modulus of those substrates, the intrinsic stress of the coating was expected to be different, giving more conditions of stress. The intrinsic stress of the coating was characterized using both BK7 and fused silica stress witnesses, as presented above. The stress values were verified by measuring the curvature of the rectangular samples before and after coating to retrieve the stress with an adapted Stoney's formula.

The rectangular slabs are bent with a “stress device” developed at CEA Cesta by Gingreau *et al.* [115] to investigate the potential influence of mechanical stress on the LIDT of silica vacuum windows such as the windows of the LMJ target chamber. This device presented in Fig. 85 consists in a frame and two metallic articulated flanges holding the rectangular sample under test; see Fig. 85(a). Stress is applied by tightening a screw that exerts a load on both articulated flanges, ensuring an equal stress distribution on both flanges; see Fig. 85(b). The sample takes a cylindrical shape. Three stress conditions have been used during this evaluation; see Fig. 85(c).

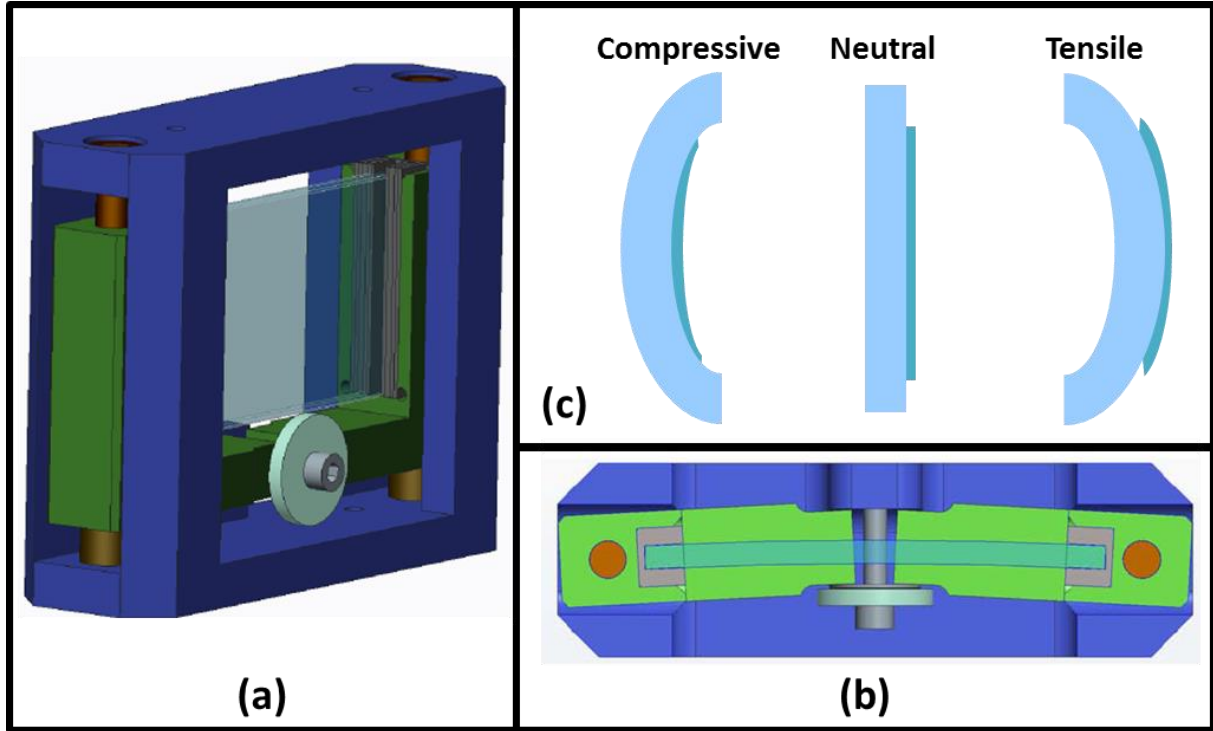


Fig. 85. Schematics of the stress device: (a) general view of stress device with a rectangular slabs placed (b) top view of the device when the slabs is bent by tightening the grey screw that exerts a load on both articulated green flanges (c) three different stress conditions used during the damage tests

External stress induced by the device is monitored *via* a Mesurex FC500N8-25 stress sensor located between the screw and the flanges. This sensor measures in Newton the strength of the load applied on the flanges. The sensor range is between 0 to 500N. Prior to the laser damage tests, a calibration performed by an interferometer is realized to link the strength measured with the radius of curvature of the surface of the slabs. This calibration is verified by repeating the operation with a mechanical displacement sensor placed at the center of the slabs measuring the displacement of the center of the slabs while applying different loads with the screw. A linear dependency is found between the applied load and the displacement of the center of the slabs. With a finite element modeling performed with Siemens NX Nastran 8.5 software it was shown [115] that the stress follows a linear variation with the displacement of the center of the slab. Considering these calibrations and finite element analysis, we are able to establish the two following scaling laws expressing the stress of the coating σ in MPa as a function of the applied load F in N for both types of substrates:

$$\text{For samples on BK7 substrates} \quad \sigma = 0.1052 \times F \quad (6.2)$$

$$\text{For samples on FS substrates} \quad \sigma = 0.1445 \times F \quad (6.3)$$

Consequently the maximal external stress measurable is 52.6 MPa for BK7 and 72.25 MPa for FS.

For this study, the stress device was installed on the DERIC samples carrier, see Fig. 86. The alignment, position at the waist of the Gaussian beams as well as the laser damage detection was verified before starting the laser damage tests.

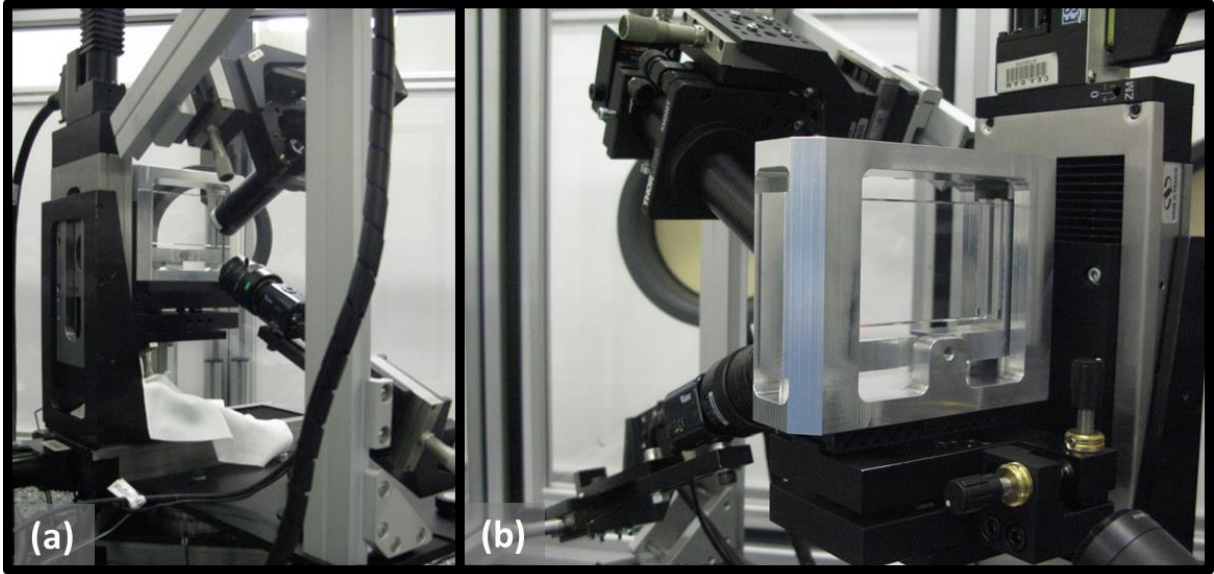


Fig. 86. Pictures of the stress device installed onto the DERIC sample carrier

The laser damage test sites are performed along the central axis of the samples. The first tests have been performed for the s and p states of polarization with no external stress applied; this configuration is designated as neutral in Fig. 85(c). Then the screw was tight with the coated side is facing the screw, meaning that when the screw is tightened the coated surface takes a concave shape. This puts the coating into compressive stress. The laser damage tests are performed again for both the s and p states of polarization. Then to perform the last stress configuration, corresponding to tensile stress, the sample was turned over in the frame, so the uncoated face is facing the screw. When the screw is tightened the samples and coatings takes a convex shape. The stress added to the coating is then a tensile stress; see Fig. 85(c). The stress device was also turned over so the beam is going through the coated face first. This operation was carefully realized so the coated face remains at the waist of the Gaussian beam.

Between each test configuration the stress was progressively relaxed and it was progressively applied too. We also waited for at least an hour before starting the damage tests for the sample to stabilize. All these tests were performed in ambient air with a relative humidity of 45%. To be sure, not to break the samples in the frame the maximal load applied was set to 192N for the BK7 and 136N for FS substrates. The resulting external stress applied to the coating for both stressed configurations is then 19.4MPa for the coating on BK7 substrates and it is 19.6MPa for the coating on fused silica substrate.

The LIDT results of the two classical designs deposited either on BK7 or FS substrates are presented in Fig. 87 for the s - (red) or p -polarization (blue) and the three different stress configurations: compressive stress, neutral and tensile stress.

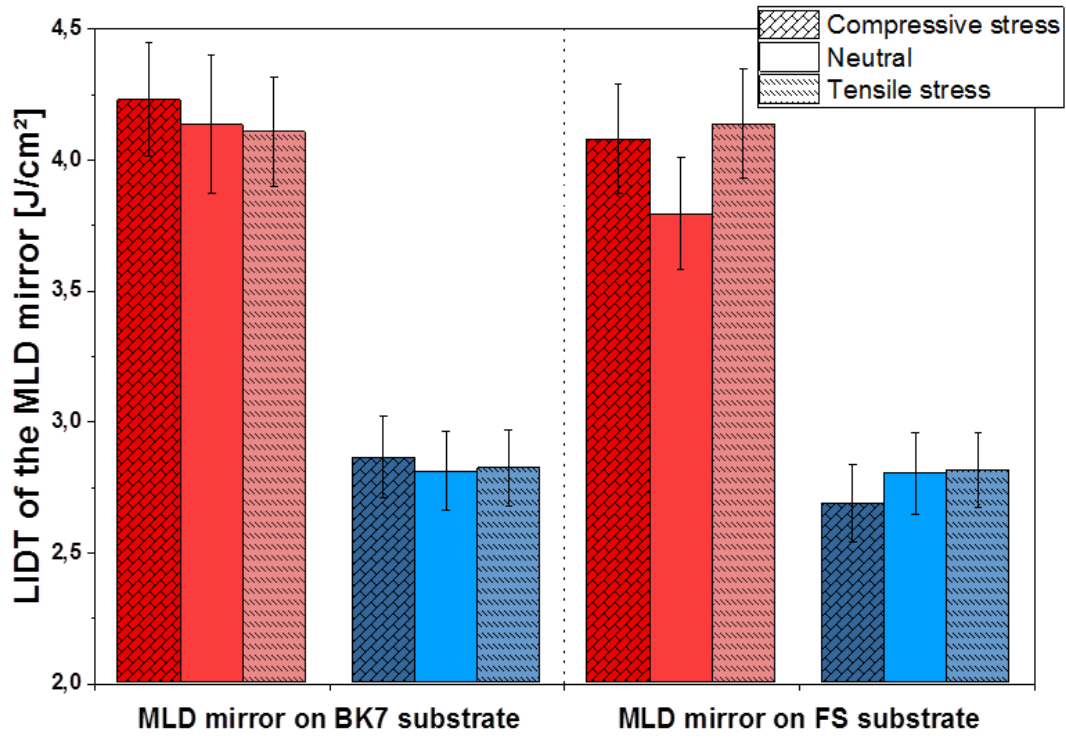


Fig. 87. LIDT of MLD classical design mirror deposited either on BK7 or FS substrates under the three different conditions of stress described in Fig. 85(c) for the *s*- (red) or *p*-polarization (blue)

At the neutral state of stress, the classical design deposited on a BK7 substrate sustains 18.9MPa tensile intrinsic stress and the classical design on the FS substrate has 23.9MPa intrinsic stress. When comparing the neutral LIDT results of the two samples, one can see that there is no difference for the *p*-polarization. Both samples exhibit a laser damage threshold of 2.8 J/cm². For the *s*-polarization, the classical design deposited on BK7 samples has a slightly higher value 4.13 ± 0.21 J/cm² than the samples with FS substrate 3.79 ± 0.21 J/cm², but the uncertainties bars are overlapping. Then the variation is not significant.

The external stress applied has the same magnitude than the intrinsic stress of the samples in ambient air Fig. 84. When an external compressive stress is applied, the resulting stress is around 0MPa for both samples in one direction. The LIDT slightly increases except for the *p*-polarization LIDT of the sample deposited on FS substrate. These variations are minor because included in the uncertainties. When applying a tensile external stress, the LIDT for the *p*-polarization remains identical to the neutral condition. For the *s*-polarization, the mirror on BK7 substrates exhibits identical LIDT than in neutral condition. The mirror on FS substrates exhibits higher LIDT than in neutral conditions with an external tensile stress applied, but the uncertainties bars are overlapping. This last observation is in contradiction with previous observation that tensile stress decreases the LIDT [112].

All the observed variations of the LIDT can be neglected regarding the uncertainties suggesting that there is no influence of the stress on the LIDT of MLD in the sub-picosecond regime in the stress range studied here. Therefore the variations of the LIDT between the ambient air and the vacuum (Fig.

83) for multilayer should be mainly attributed to the variation of the refractive index and not to the stress applied onto the layers.

6.2.3 Intrinsic LIDT determination in vacuum from multilayers

Considering the last conclusion, the intrinsic LIDT in vacuum is evaluated from the multilayers following the Fig. 82 procedure. The spectral response is measured with a spectrophotometer in dry air (because we are not able to do the measurement in vacuum). The vacuum refractive index will be approximated with the refractive index determined in dry air. The theoretical response of the designs using the refractive index determined dry air from the single layers are calculated and compared to the measured one. The deviations between the theoretical and measured responses are low so we can safely consider the average refractive index of the layers in dry air to be equal to the one of the single layers in the same environment. Based on these refractive indexes and the designs, the electric field intensity is calculated for each design.

The AFM measurement showed that for the vacuum LIDT tests, the limit damage occurs in the outer layer which is a hafnia layer. Consequently, with this method, we are only able to calculate the intrinsic LIDT of the hafnia: $LIDT_{int,H}=1.72 \text{ J/cm}^2$. This intrinsic LIDT of hafnia in vacuum is very close to the one determined in ambient air $LIDT_{int,H}=1.7 \text{ J/cm}^2$. This small variation with the environment of the intrinsic LIDT confirms the observations made above and in chapter 4 that the measured LIDT variation can be explained by refractive index variation. Then in the following optimization for vacuum, we considered the intrinsic LIDT of SiO_2 in vacuum to be equal to the one in ambient air $LIDT_{int,L}=3.15 \text{ J/cm}^2$.

Table 22. Refractive index and intrinsic LIDT for an environment similar to vacuum for HfO_2 and SiO_2 deposited with e-beam

	HfO_2 – e-beam	SiO_2 – e-beam
Refractive index in dry air at 1053 nm on the single layers	1.827	1.43
Intrinsic LIDT at 800 fs[J/cm²]		3.15
Determined at LLE on the multilayers Vacuum	1.72	(determined in ambient air)

Knowing these values we will be able to calculate, deposit and damage test the LIDT Max. and assess the potential influence of stress on LIDT.

6.3 Optimization of the Final design

In this present paragraph, we apply our optimization technique using the vacuum input parameters determined previous paragraph and thus determine a final design that could be later used on the Petal facility.

6.3.1 Expected numerical LIDT results

The settings of the robust algorithm (screening conditions and manufacturing errors) are identical to the ones presented in the first paragraph except for the screening on the LIDT which is now adapted to

vacuum with a target value of 1.48 J/cm^2 derived from the experimental LIDT value of the classical design in vacuum for the p -polarization. Among the billions of designs initially generated, 219 735 solutions were thus retained after the screening. With the robustness tests and the final robustness evaluation (with the cumulative error) only 332 designs were finally selected. The LIDT values of the 332 designs in the nominal conditions regarding their final robustness evaluations are plotted in Fig. 88. The LIDT values of the balanced design are superimposed to the plot to compare the performance of the design generated by the algorithm with the balanced design which is the common optimized design. The LIDT values of the classical design are below the scale of this figure and cannot be superimposed.

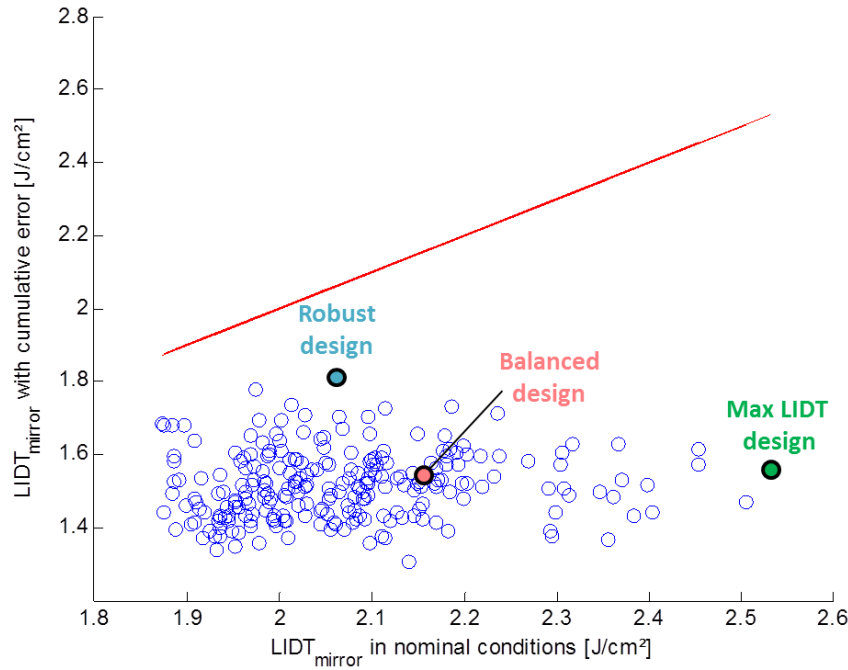


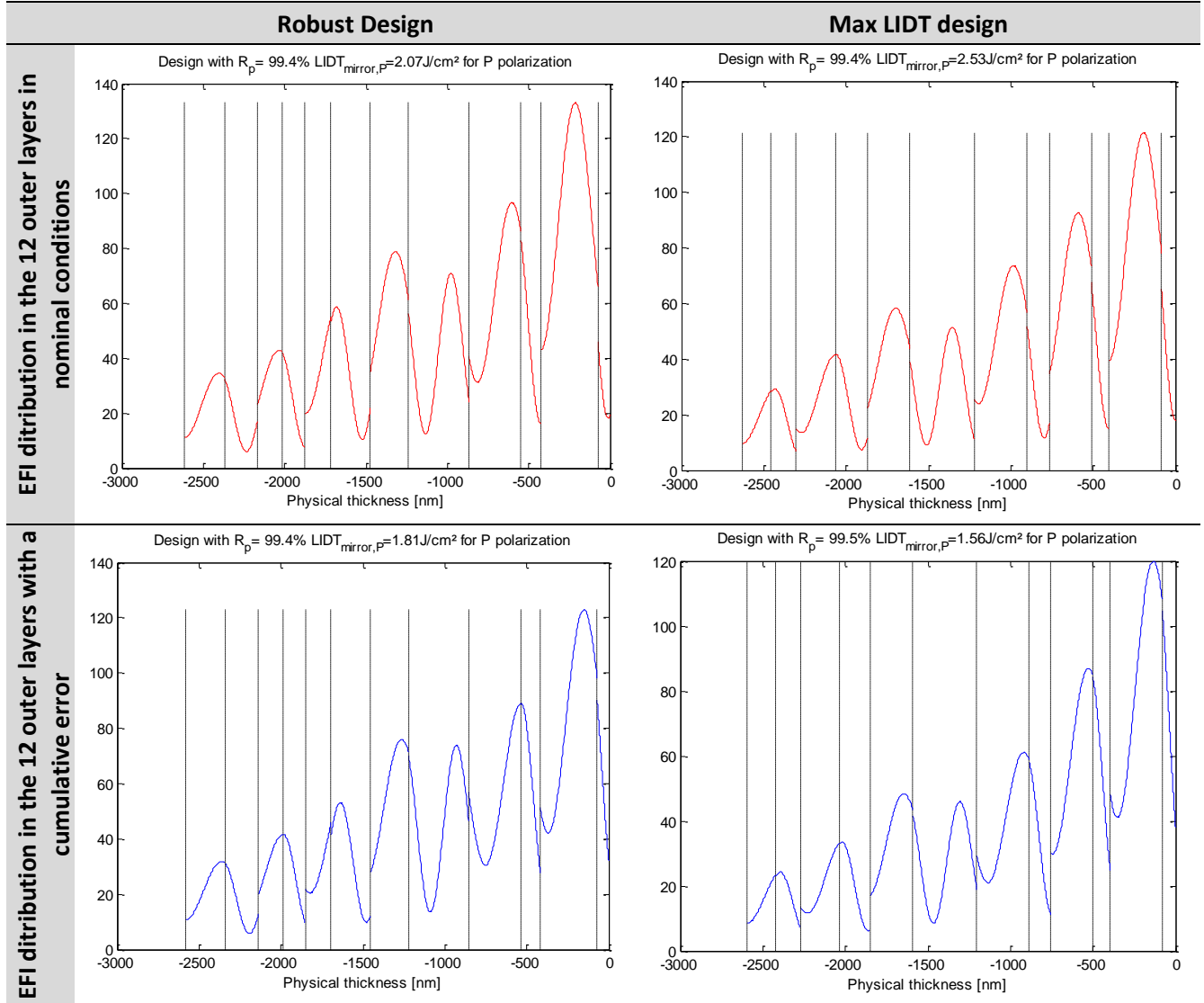
Fig. 88. LIDT performances in nominal condition (x-axis) regarding the LIDT performances with a cumulative error (y-axis) of the 332 optimized designs produced by the robust optimization algorithm and the balanced design. The red line is a guide for the eye which represents LIDT values equal in nominal condition and with a cumulative error.

With this representation, two designs distinguish themselves from the rest. The design that is called **robust design** (in blue in Fig. 88) exhibits a medium LIDT value of 2.07 J/cm^2 in nominal conditions but has the highest performance for the final robustness criterion 1.81 J/cm^2 , considering cumulative errors. The other design that is very interesting is the **max LIDT design** (in green in Fig. 88) that has a predicted LIDT value of 2.53 J/cm^2 in nominal conditions, which is considerably higher than the 1.41 J/cm^2 provided by the classical design. Under the worst conditions, its LIDT value drops to 1.56 J/cm^2 which is slightly above the screening condition on LIDT.

By depositing and testing the max LIDT design we were able to assess the interest of using the robust optimization algorithm. The results of the robust design will allow discussing the validity of the final robustness test evaluation. Is it more relevant to select the designs based on a cumulative error that is less likely to happen or would it be better to define another situation more likely to happen?

To compare these two designs, their electric field distributions in nominal condition or under cumulative error are plotted in Table 23.

Table 23. EFI ditribution in the 12 outer layers in nominal conditions or under cumulative error for the two selected designs for the *p*-polarization



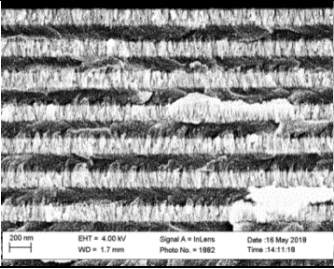
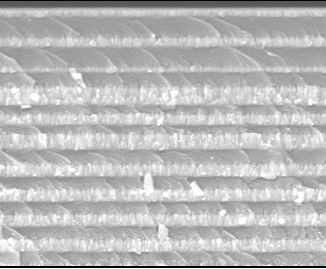
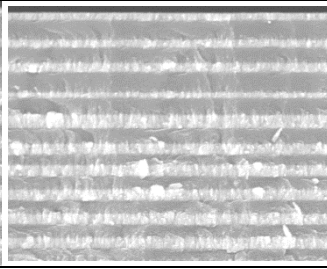
6.3.2 Results

Once the two selected design were coated, their reflectivity at 1053 nm was measured, along with 1-on-1 LIDT tests and SEM observations of the design profile.

6.3.2.1 For the optimized configuration

The results concerning the configuration the mirrors are optimized for are listed in Table 24.

Table 24. SEM pictures, reflectivity and LIDT values for the three designs under the configuration they are optimized for

	Classical design	Robust design	Max LIDT design
SEM picture			
Reflectivity at 1053 nm <i>p</i> -pol, 45° AOI	99,8 %	99,4 %	99,5 %
LIDT 1053 nm, <i>p</i> -pol, 800 fs, 45° vacuum [J/cm ²]	1.41±0.08	2.22±0.11	2.44±0.14
Improvement on the LIDT compared to classical design	--	+57%	+73%

The robust design exhibits a LIDT value of 2.22 J/cm² which is a little bit higher than the expected one, namely 2.07 J/cm². It suggests a slight underestimation of the intrinsic LIDT. The max LIDT design has a LIDT for the *p*-polarization of 2.44 J/cm² which is a little bit below the expected value of 2.53 J/cm². This latter variation is included in the uncertainty interval related to the LIDT determination. These results clearly validate the interest and efficiency of the optimization algorithm. The final improvement on the LIDT compared to a classical design performance in vacuum is 73% for the Max LIDT design which is considerable.

6.3.2.2 LIDT for *p*-polarization in ambient air

Table 25 displays the LIDT values obtained for the previous designs optimized for vacuum use for the *p*-polarization, but in ambient air. It clearly confirms that the designs optimized by our numerical approach are environment dependent. In particular, both the robust and Max LIDT designs exhibit in ambient air LIDT values lower than the classical one.

Table 25. LIDT performance of the deposited designs for other configurations

	Classical Design	Robust Design	Max LIDT design
LIDT 1053 nm, <i>p</i> -pol, 800 fs, 45° ambient air [J/cm ²]	1.74±0.11	1.25±0.08	1.35±0.07

When comparing all the five designs presented throughout this chapter LIDT values for the *p*-polarization in Fig. 89, the importance of the consideration of the environment in our algorithm is clearer.

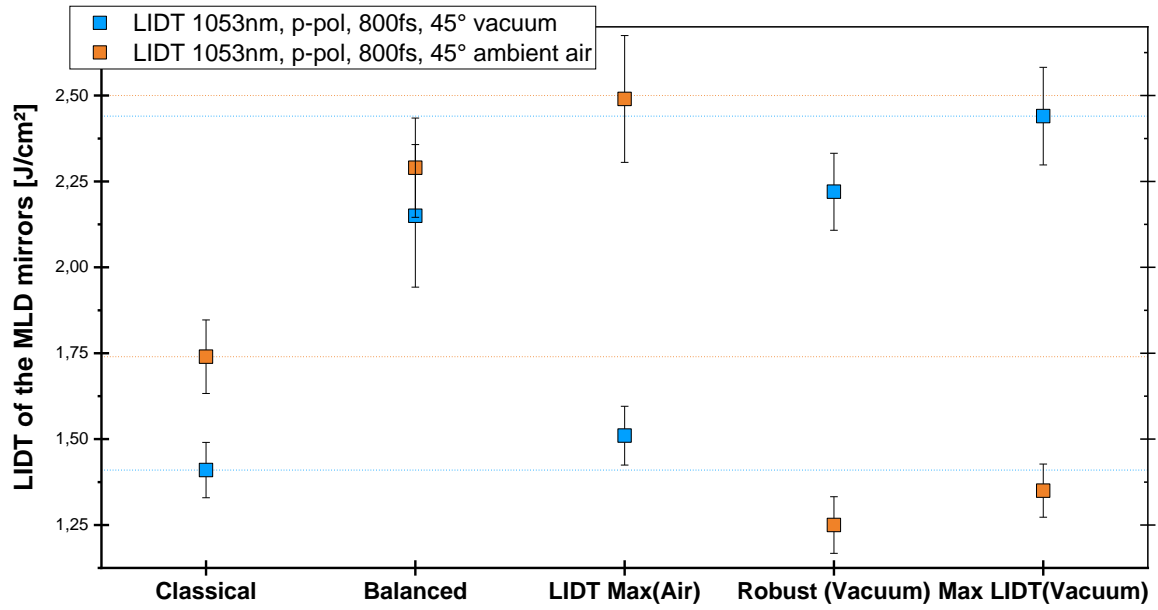


Fig. 89. Summary of the LIDT values for the p-polarization of the five deposited designs. The dotted lines are guide for the eye for the LIDT values of the classical design (starting point of this study) in both environment and the best LIDT values in both environments. The best LIDT values are exhibited by our two optimized design

The performances of the optimized designs for the environment it is designed for are good, but not for the other environment. With our current final robustness evaluation (which is a cumulative error), all of our designs are more robust than the balanced designs. However, when changing the environment, the balanced design is significantly less sensitive to the environment than the other designs. This is due to the fact that the variations of the refractive index with the environment are bigger than the error estimated in the robustness tests. Our robustness tests on the refractive index are aimed at mimicking manufacturing errors and not environmental changes. It could be a path of improvement for the algorithm to rethink the final robustness evaluation in order to consider environmental changes. The solution provided by such revised algorithm will be designed to exhibit high LIDT independently of the environmental variations.

This would be a path of improvement to consider only for manufacturer that are reliable regarding manufacturing errors. For manufacturer that has very varying process or that are more prone to experience manufacturing errors, the final robustness selection should remain the cumulative error one.

6.3.2.1S-polarization results

Table 26. LIDT performance of the deposited designs for *s*-polarization

	Classical Design	Robust Design	Max LIDT design
LIDT 1053 nm, <i>s</i> - pol, 800 fs, 45° vacuum [J/cm ²]	2.39±0.13	2.71±0.16	3.42±0.17
LIDT 1053 nm, <i>s</i> - pol, 800 fs, 45° ambient air [J/cm ²]	2.38±0.12	3.07±0.18	2.47±0.19

Table 26 presents the LIDT results for the *s*-polarization. The LIDT results of both designs are higher than the classical one for any type of environment. If we compare those values, with the LIDT for the *s*-polarization of the balanced design respectively 3.61 J/cm² in ambient air and 3.49 J/cm² in vacuum, they are not that good. However, the LIDT values of the balanced, robust or Max LIDT designs for the *s*-polarization are all higher than the one for the *p*-polarization. So if one of those designs is implemented on the transport of the Petal facility the mirrors that are expected to fail first should be the ones submitted to the *p*-polarization. It thus does not seem to be relevant to specifically optimize designs of mirrors for the *s*-polarization. Still some intensification of the beam might happen, bringing local higher fluence on those mirrors. To prevent such event, a specific optimization for the *s*-polarization is then required.

To conclude, our robust optimization algorithm has revealed it was environment dependent but very efficient to identify the best design for a given condition of operation and pair of material deposited with a specific manufacturing process. Next research will be focused at designing mirror optimized for the *s*-polarization and improving the algorithm so it can provide design that performs well in any environment. It should be noted that this final improvement will be valid for a specific manufacturing process. For each manufacturing process, the impact of the environment on single and multilayer should be evaluated to determine the refractive index ranges first.

Conclusion of Chapter 6

In this chapter is provided an experimental validation of the robust optimization algorithm presented in the chapter 3.

The first optimization based on the properties of the materials determined from single layers in ambient air respected the expected ranking but all the measured LIDTs were about 40% higher. This highlighted that it is more important to know the ratio between the intrinsic LIDT of both materials than having the accurate knowledge of the intrinsic LIDT of each materials. The determination of intrinsic LIDT from single layer allows classifying and selecting materials associated with specific manufacturing process. The characterization of a classical design in various environments allows determining intrinsic LIDT closer to the value observed in a multilayer stack. The refractive index has been observed to vary with the depth of the layer in the stack and so might the intrinsic LIDT.

The pair of materials used here hafnia and silica deposited with e-beam which yields porous layers that are sensitive to the environment (air vs vacuum) and relative humidity. Consequently, in a second section, we studied the effect of the environment on multilayer. The LIDT results of the three designs manufactured to operate in air use exhibited a drop of 20 to 40% in their LIDT values between ambient air and vacuum. The results showed that stress in the coating has a weak or even no influence on the laser-induced damage threshold in the test range. The variation of the LIDT with the environment is mainly due to the refractive indexes variations. The final environment of use has to be taken into account for the optimizations.

The final optimization for vacuum use provides an interesting final design that has a LIDT 73% higher than the classical design. The discussion on the robustness tests presents another criterion of selection of the manufacturer of the coating: their capability to deposit the design with few errors. The final robustness tests could be improved by being aimed at mimicking an environmental change. This would allow having a design with performance independent to the environment. This final improvement has to be considered only for manufacturing process that reliable toward manufacturing errors.

Conclusion

The main motivation of this PhD thesis was to improve the short pulse LIDT of the Petal transport mirrors by considering:

- other materials than the most ubiquitous HfO_2 and SiO_2
- other designs than the classical quarter-wave optical thickness design
- and/or various manufacturing processes

This objective has been fulfilled with the development of a new mirror design made of an alternation of HfO_2 and SiO_2 layers deposited with e-beam that exhibits a LIDT 73% higher than a classical design on samples. The chosen materials for our final design were HfO_2 and SiO_2 . Even if materials such as Sc_2O_3 have very high potential; they remain the pair of material with high performance and the most available for our kind of applications.

Firstly, we developed a numerical approach considering these paths of improvement and quantifying the potential increase that could bring the change of materials and/or designs. This numerical approach led to the conception and implementation of a robust optimization algorithm of design based on the LIDT in short pulse regime. This algorithm has been experimentally validated with the deposition and characterization of a mirror design that operates in ambient air and two other designs that operate in vacuum. Those optimized designs provided with our algorithm are significantly far from the classical quarter-wave optical thickness designs.

We also noticed that intrinsic LIDT values measured on single layer materials might not be directly transposable to intrinsic LIDT in multilayers composed of these materials. In order to accurately design an optimized design, we recommend laser damage testing multilayers with several test configurations (such as polarizations or angle of incidence) to determine the intrinsic LIDT of the chosen pair of materials. The variation between intrinsic LIDT determined on single layer or multilayers was found to be different and specific for each material and manufacturing process. The characterization on single layers is still primordial to select materials.

During this research, we highlighted that it is essential to consider and characterize materials associated with their manufacturing processes (deposition technique and manufacturer) rather than solely materials. Indeed all the hafnia and silica layers studied here exhibited significant discrepancy regarding their refractive index and intrinsic LIDT. We noted that this discrepancy of the intrinsic LIDT cannot be explained by bandgap energy variation as it is reported in the literature. However, we found that the intrinsic LIDT in the infrared in short pulse is linked to the absorption in the UV. A quick experimental screening to eliminate materials with too high absorption would be necessary. This ascertainment could pave the way for the development of a fast nondestructive characterization of the intrinsic LIDT of the materials with the establishment of a model expressing the intrinsic LIDT as

function of the absorption in UV. This is a very promising perspective, because the complete and accurate procedure to characterize intrinsic LIDT developed during this work is tedious and time consuming. Moreover, one should remember that all the general laws trying to correlate the intrinsic LIDT with other properties of the materials are laser damage setup dependent and should not be easily generalized to any laser damage setup.

Finally, part of this present work was focused on the effect of the relative humidity on the coating performance. On this topic, we assessed the effect of vacuum, dry air, and ambient air on the LIDT in sub-picosecond regime on single layers and then multilayers. We were able to link the LIDT variations between these three environments to refractive index variations and noted that the stress variation has a limited or no effect on the LIDT in short pulse in the tested stress range.

The results and methodology used in this work can be transposed to other topics and optical coatings. In the next section, we will present and discuss the future prospect of research on multilayer dielectrics used in high power laser facilities.

Perspectives on multilayer dielectrics components used in high power laser facility

1. Mirrors.....	141
1.1. Petal Transport Mirrors	141
1.2. Broadband chirped mirrors (15 fs)	142
2. Other optical functions	142
2.1. Polarizers	142
2.1.1. LMJ polarizers specification and designs	142
2.1.2. Aging effect: irreversible phenomenon	143
2.1.3. Effect of the relative humidity: reversible phenomenon	144
2.2. Petal gratings	145
Summary of the perspectives	146
Conclusion (français).....	147

In this present dissertation, an optimization of MLD mirrors based on LIDT in short pulse regime was presented. To perform this optimization, an algorithm was developed as long with a procedure to determine accurately the intrinsic LIDT from single layers and multilayers.

The robust algorithm and methodology developed and presented here can be applied and adapted to other areas of research on multilayers for high power facilities. In the present chapter, the next perspectives of research where this work can be used are presented. In a first paragraph we focused on the mirrors optical function, and in the following paragraph the consideration is broadened to other optical functions such as polarizers and gratings.

1. Mirrors

1.1. *Petal Transport Mirrors*

The first perspective of the research presented here is to implement it on Petal laser facility by manufacturing mirror with the developed design for the p -polarization and by developing a second design optimized for s -polarization.

In the present work, we aimed at increasing the laser-induced damage threshold initiation. Future research could be aimed at developing design robust to damage growth. It has been previously shown [98] that growth is more problematic for the s -polarization. Such addition on the present algorithm to control the growth would then be central when defining a design for the s -polarization.

As presented in Chapter 6, an improvement considered for our algorithm would be to change the final robustness selection into robustness toward environment change, mimicking the change from ambient air to vacuum. This improvement will allow having, if it is possible, a less-sensitive coating to the environment and relative humidity without considering other manufacturing process which could be tedious.

Consequently, another path to develop mirrors that are not sensitive to the relative humidity would be to use denser manufacturing process such as Ion Beam Sputtering. This will be done in the near future with the characterization of multiple oxides (HfO_2 , SiO_2 , TiO_2 , Ta_2O_5 , Sc_2O_3 , Al_2O_3 and a mixture of SiO_2 and Sc_2O_3) deposited with IBS and the development of a design of a mirror. IBS coatings turned out to be the highest LIDT single layer in our poll of samples with a SiO_2 layer that exhibits an intrinsic LIDT value of 4.41 J/cm^2 . This manufacturing process allows depositing Sc_2O_3 and mixture that has been shown to be of high potential in the numerical parametric study on materials (Chapter 3) and experimentally in Chapters 4 and 5. If the improvement of the LIDT provided by an optimized mirror deposited with IBS is high, it would be interesting to consider this deposition method to manufacture large coatings.

Finally, another aspect to control in the future on those mirrors design will be the ageing effect or the effect of external pollution on the coatings.

1.2. Broadband chirped mirrors (15 fs)

For pulse duration shorter than the one considered here, pulse duration of the order of magnitude of few femtoseconds, mirrors are expected to reflect a much larger spectral band. Those broadband mirrors need to be highly reflective on a 200 nm spectral range [116]. This induces the need to control the group delay dispersion of all the components of the spectra by adapting the design of the mirror. Our algorithm could be adapted to this topic by adding screening conditions on the broadband aspect and adding calculations of the group delay dispersion which is central to the challenges of chirped mirrors, while still aimed at increasing the laser-induced damage threshold in short pulses.

2. Other optical functions

The methodology used here could be adapted to the improvement of multilayer dielectric coatings with other spectral responses. Firstly, we will present issues on polarizers with the example of LMJ polarizers and then on gratings with the example of Petal compression gratings.

2.1. Polarizers

As addressed with the change of environment, the spectral stability can become a critical issue to control on multilayer dielectric coatings. It is also essential to guarantee that the coatings keep respecting their spectral specifications through time, in order to remain operational.

An ageing effect has been observed on the LMJ polarizers. As exposed in Chapter 1, Fig. 14 shows that the spectral response of the polarizers tends to shift toward longer wavelength after six years. This shift causes a severe transmission drop.

2.1.1. LMJ polarizers specification and designs

The specifications of the LMJ polarizers are presented in Table 27.

Table 27. Specification of the LMJ polarizers

Substrate	Angle of incidence	Size [mm]	Spectral specification for		LIDT* [J/cm ²]	Pulse length	Environment of use
			p- polarization	s- polarization			
Fused silica	Brewster angle 55,4°	415x710x25	>98% Transmission	<1% Transmission	12-14	3 ns	Dry Air

The current design of the polarizer is derived from a Bragg mirrors design. At normal incidence, both polarization of a Bragg mirror design are superimposed into one single spectral response. With the increase of the angle of incidence (from 0° to Brewster's angle), two areas are appearing and growing, one on each side of the central wavelength of the Bragg design, where the transmission is very high for *p*-polarization and still very low for *s*-polarization, see Fig. 90. This is the principle of a **polarizer**: being transparent for *p*-polarization and highly reflective for the *s*-polarization. Thin-film polarizers are thus designed on that principle. Additional layers are deposited to suppress the undesirable oscillations and have more flat spectral response. The best extinction ratio for a polarizer can be achieved by operating at the Brewster's angle. At this specific angle, there will be no reflection coming from the backside of the substrate in *p*-polarization.

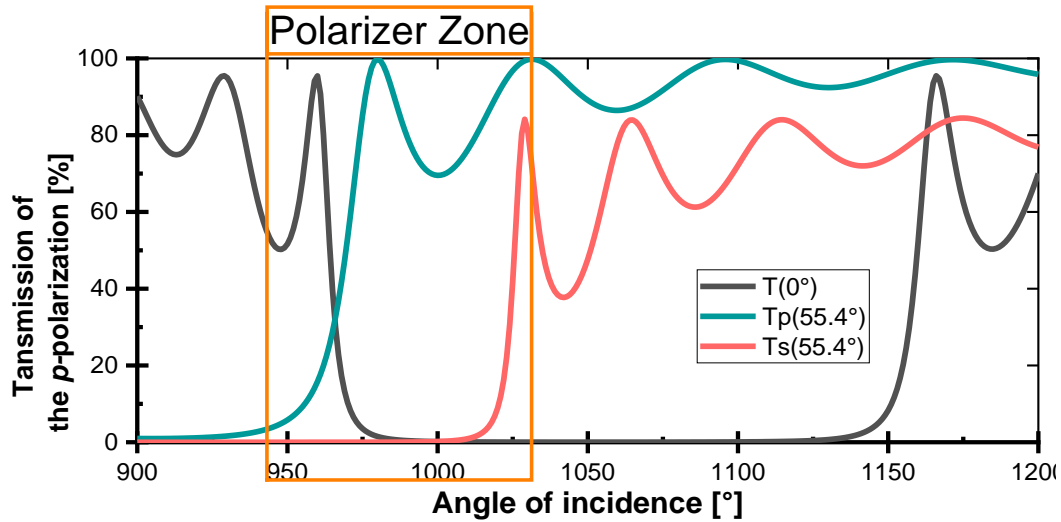


Fig. 90. Transmission of a classical (QWOT, quarter-wave optical thickness) mirror at 0° and Brewster's angle (55.4°) for p - and s -polarization. The red rectangle is here to highlight the creation of one of the two polarizer zones.

Due to their thinner spectral range than mirrors, polarizers are sensitive to spectral shifts. Those spectral shifts can be caused either by the relative humidity variations or by the ageing effect of the coating. These two phenomena are independent and cumulative, as illustrated with the example in Fig. 91. The spectral shift generated by the change of relative humidity is a fast and reversible phenomenon oppositely to the ageing effect that is slow and irreversible.

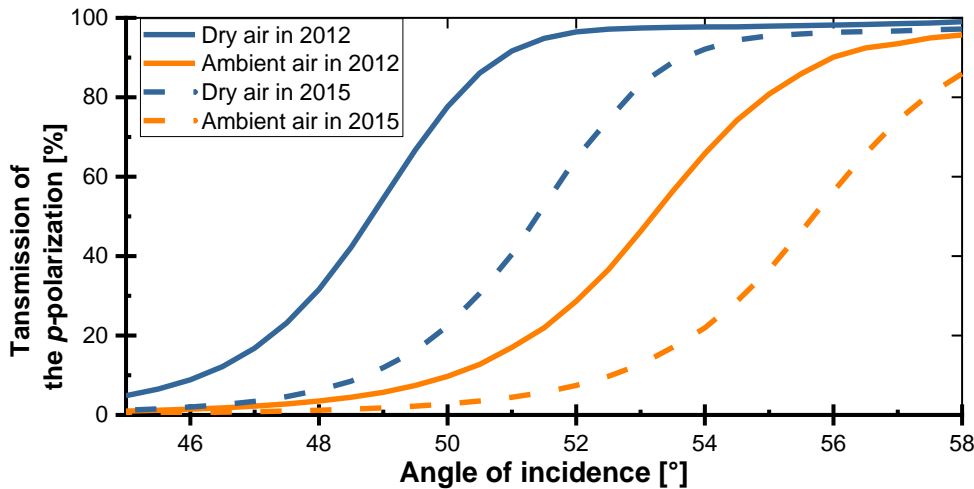


Fig. 91. Example of spectral shifts of the p -polarization transmission one polarizers with the ageing effect or the relative humidity of the environment

It would be interesting to develop a design robust to those spectral shifts or to consider other less sensitive materials than the currently used HfO_2 and SiO_2 materials deposited with Plasma Ion Assisted Deposition.

2.1.2. Aging effect: irreversible phenomenon

A similar approach to the one developed throughout all the work could be applied to the topic of ageing.

First, with a numerical approach we could assess and quantify the influence of the refractive index or thickness variations on the spectral shift of a polarizer. This would help determine if the spectral shift is due to refractive index variations or physical thickness variation (or both). It would also determine which materials are the most contributing to the effect.

Then with the development of the procedure to speed the ageing effect, one could characterize and compare the ageing of different materials associated with a specific manufacturing process. It is important to speed the ageing effect as nowadays the ageing is a slow process, taking years to be visible. Developing a procedure to accelerate the ageing of the films is currently under investigation. We tested multiple paths:

- placing/storing sample in different conditions of relative humidity and temperature,
- or under a high intensity of UV to probe the UV annealing effect on the coating
- or by investigation on the effect of the cleaning products.

Then with these experimental results we would be able to improve our robust optimization algorithm and develop new robustness tests aimed at mimicking the ageing effect. Finally with this new optimization algorithm we would be able to develop a new design that is resistant to ageing.

This ageing effect may be happening on all the coatings, Petal mirrors included. Thus, there is a need to understand the ageing of the films so in the future these transmission losses can be controlled and the improvement to the LMJ polarizer could be applied to the other multilayer coating that may age.

2.1.3. Effect of the relative humidity: reversible phenomenon

As addressed with the change of environment for the mirrors designs in Chapter 6, another important topic of the work is about the effect of the environment, or in other words the relative humidity of the environment, on the optical coating. Here the LMJ polarizers are used in dry air. Their effective refractive index and thus spectral response will change with the relative humidity of the air. The change of relative humidity from ambient air to dry air (or vacuum) causes a reversible shift of the spectral response toward shorter wavelengths this matches with a diminution of the optical thickness of the layers, as illustrated with the polarizers' example in the Fig. 92.

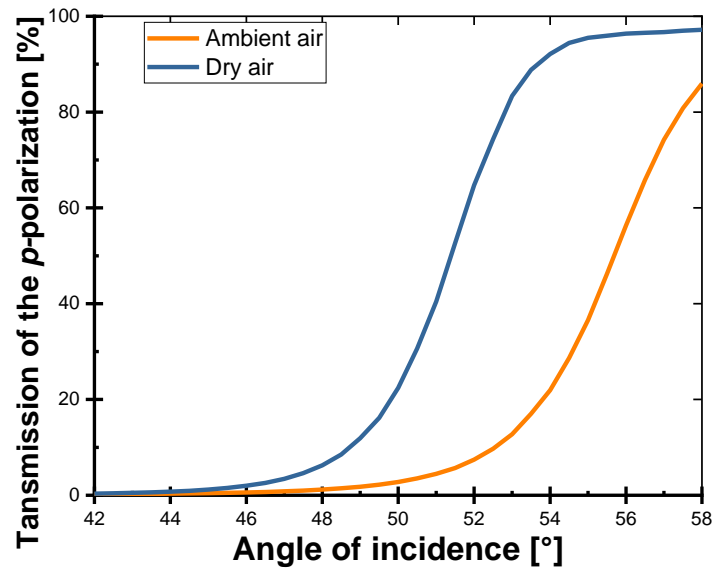


Fig. 92. Example of spectral shift with the relative humidity: Transmission of the p -polarization of a polarizer in ambient air (orange) with a relative humidity of 50% and in dry air (blue) with a relative humidity $\approx 0\%$

Controlling the relative humidity is not always an easy task. Thus the improvement of our algorithm (as suggested at the end of Chapter 6) to change the final robustness selection into robustness toward relative humidity change, mimicking the change from dry to ambient air, would be an interesting addition when selecting a polarizer design robust to ageing.

2.2. Petal gratings

Finally, the next components limiting the increase of power of Petal laser facility would be Petal compression gratings used in vacuum. Those gratings are compressing the amplified beam on Petal facility from few nanoseconds to few hundredth of femtosecond. The specifications of those gratings are presented in Table 28.

Table 28. Specification of the Petal compression gratings

Substrate	Angle of incidence	Size [mm]	Spectral specification for		LIDT* [J/cm ²]	Pulse length	Environment of use
			p -polarization	s -polarization			
glass	77.2	450 x420 x43	>99% Reflectivity from 1045 nm to 1061 nm		4	700 fs	vacuum

Those gratings are manufactured by etching a grating pattern on the outer layer of a MLD mirrors. It has been previously shown that the laser-induced damage threshold of those gratings is, as it has been shown for the Petal transport mirrors, depending on the electric field enhancement [117, 98]. Consequently all the work presented here (characterization procedure, intrinsic LIDT results on multiple material, algorithm) can be directly used. Moreover our algorithm associated with the calculation of the electric field intensity in the grating pattern can be applied to design new gratings resistant to manufacturing errors and with higher LIDT values.

A new PhD thesis should start on this topic of characterizing and improving laser-induced damage threshold of Petal compression gratings in 2019.

Summary of the perspectives

In the present section, we saw that the first perspective of this thesis will be to implement on the Petal facility our developed design. Then, our optimization algorithm can be improved to develop designs robust to laser damage growth or robust to relative humidity changes. It can also be adapted to develop broadband mirrors that require looking at the group delay dispersion. It is important to note that the optimization algorithm, as well as all numerical software, required accurate input parameters namely the optical materials properties. Thus the characterization procedures developed in this thesis and its results are indispensable for the application of this algorithm. That is why all the results provided here could help the improvement of the laser-induced damage threshold of Petal compression gratings.

More generally the methodology used here could be adjusted to deal with the ageing problem and spectral shifts with relative humidity that are currently experienced on LMJ polarizers.

Finally, to conclude, the characterization and optimization methods and experiences along with the experimental results presented through all of this dissertation can be used in future research on multilayer dielectric coatings for high power laser facilities. One should also remember the perspectives on metrology to develop a non-destructive characterization of the intrinsic laser-induced damage threshold by establishing a model from the absorption measurements; this was evoked in chapter 5.

And I am looking forward being part of this future and this research. ☺ ☺ ☺

Conclusion (français)

La motivation principale de cette thèse était d'augmenter le seuil de tenue au flux laser des miroirs de transport de Petal en considérant :

- de nouveaux matériaux
- de nouveaux designs d'empilement couches minces
- de nouvelles techniques de dépôts

Cet objectif a été atteint avec la conception, la fabrication et la vérification des performances de tenue au flux d'un miroir multicouches au design original constitué d'un empilement de couches minces de HfO_2 et SiO_2 déposées par évaporation. Ce miroir possède un seuil de tenue au flux laser 73% plus élevé qu'un miroir au design classique constitué des mêmes matériaux.

Nous avons développé, via une approche numérique très efficace et robuste, un nouvel algorithme de calcul permettant d'optimiser le design sur la base d'une évaluation chiffrée de l'amélioration du seuil de tenue au flux laser, tout en tenant compte des limitations apportées par les matériaux et leurs procédés de fabrication. Cet algorithme a été validé expérimentalement grâce à la caractérisation d'échantillons conçus et fabriqués de cette manière. Les architectures d'empilement des miroirs optimisés par notre algorithme sont significativement différentes de l'architecture classique aux couches d'épaisseur optique quart d'onde.

Grâce à ces échantillons de miroirs, nous avons également pu mettre en évidence que les valeurs de tenue au flux laser intrinsèque mesurées sur des échantillons monocouches n'étaient pas toujours identiques à celles des empilements multicouches. La différence entre les valeurs de tenue au flux laser intrinsèques déterminées à partir de monocouches ou multicouches est spécifique à chaque matériau et à chaque procédé de fabrication. La caractérisation à partir de monocouches reste cependant indispensable pour la sélection des matériaux qui composeront le miroir.

Au cours de ce travail de recherche, nous avons montré que le procédé de fabrication doit être pris en compte autant que le matériau lui-même. Nous avons en effet remarqué une forte dispersion des valeurs de tenue au flux laser intrinsèque ne pouvant être expliquée par des variations d'énergie de bande interdite des monocouches comme cela a été précédemment exposé dans la littérature. Cependant, nous avons trouvé une bonne corrélation entre les valeurs de tenue au flux intrinsèques en régime sub-picosecondes dans l'infrarouge et l'absorption dans le domaine de l'ultra-violet. Une sélection rapide et non destructive des matériaux à fort potentiel pourrait donc être faite à l'avenir en éliminant ceux ayant une absorption trop élevée dans l'UV. Cette perspective est très prometteuse, car la méthode de détermination complète et précise de la tenue au flux laser intrinsèque développée et utilisée au cours de ce travail est à la fois longue et difficile à mettre en œuvre.

Pour finir, une partie de ce travail était concentré sur l'effet de l'humidité relative sur les performances des traitements. Sur ce sujet, nous avons évalué l'effet du vide, de l'air sec (0% d'humidité relative) et de l'air ambiant (environ 50% d'humidité relative) sur la tenue au flux laser d'empilement en régime sub-picoseconde. Nous avons été capables de relier ces variations de tenue au flux laser entre chaque environnement aux variations d'indices de réfraction. De plus, nous avons observé que les variations de contraintes induites sur les matériaux par le changement d'environnement n'avaient aucun effet sur les variations de tenue au flux laser dans la gamme de contraintes testés.

Les résultats et méthodes utilisés au cours de ce travail permettent de définir les paramètres de fabrication des futurs miroirs de transport de Petal et sont transposables à l'amélioration d'autres composants optiques. Les perspectives de ce travail sont donc naturellement :

- la fabrication de miroirs de transport taille réelle pour Petal
- l'optimisation du design des miroirs large bande pour des utilisations dans le domaine femto-seconde
- l'optimisation du design des polariseurs pour prévenir le vieillissement des traitements
- l'amélioration de la tenue au flux laser des réseaux de compression de Petal utilisés sous vide.

References

- [1] Colin N. Danson, Constantin Haefner, Jake Bromage, Thomas Butcher, Jean-Christophe F. Chanteloup, Enam A. Chowdhury, Almantas Galvanauskas, Leonida A. Gizzi, Joachim Hein David I. Hillier, Nicholas W. Hopps, Yoshiaki Kato, Efim A. Khazanov, Ryosuke Kodama, Georg Korn, Ruxin Li, Yutong Li, Jens Limpert, Jingui Ma, Chang Hee Nam, David Neely, Dimitrios Papadopoulos, Rory R. Penman, Liejia Qian, Jorge J. Rocca, Andrey A. Shaykin, Craig W. Siders, Christopher Spindloe, Sándor Szatmári, Raoul M. G. M. Trines, Jianqiang Zhu, Ping Zhu, and Jonathan D. Zuegel. Petawatt and exawatt class lasers worldwide. *High Power Laser Science and Engineering*, 7(54), 2019.
- [2] T. H. Maiman. Simulated optical radiation. *Nature*, 187(4736):493–494, 1960.
- [3] Gerard A. Mourou, C L Labaune, M Dunne, N Naumova, and V T Tikhonchuk. Relativistic laser-matter interaction: from attosecond pulse generation to fast ignition. *Plasma Phys. Control. Fusion*, 49:B667 – B675, 2007.
- [4] C. Danson, D. Hillier, N. Hopps, and D. Neely. Petawatt class lasers worldwide. *High Power Laser Science and Engineering*, 3(e3):1–14, 2015.
- [5] LLNL. <https://lasers.llnl.gov/>.
- [6] Laboratory for Laser Energetics. www.lle.rochester.edu/omega_facility/omega seen in june 2019.
- [7] A. Casner, T. Caillaud, S. Darbon, A. Duval, I. Thfouin, J.P. Jadaud, J.P. LeBreton, C. Reverdin, B. Rosse, R. Rosch, N. Blanchot, B. Villette, R. Wrobel, and J.L. Miquel. LMJ/PETAL laser facility: overview and opportunities for laboratory astrophysics. *High Energy Density Physics*, 17, Part A:2 – 11, 2015. Special Issue: 10th International Conference on High Energy Density Laboratory Astrophysics.
- [8] Wanguo Zheng, Xiaomin Zhang, Wei Xiaofeng, Jing Feng, Sui Zhan, Zheng Kuixin, Yuan Xiaodong, Jiang Xiaodong, Su Jingqin, Zhou Hai, Li Mingzhong, Wang Jianjun, Hu Dongxia, He Shaobo, Xiang Yong, Peng Zhitao, Feng Bin, Guo Liangfu, Li Xiaoqun, Zhu Qihua, Yu Haiwu, You Yong, Fan Dianyuan, and Zhang Weiyang. Status of the sg-iii solid-state laser facility. *J. Phys.: Conf. Ser.*, 112(032009), 2008.
- [9] D. Strickland and G. Mourou. Compression of amplified chirped optical pulses. *Opt. Comm.*, 55(6):447–449, 1985.
- [10] L.J. Waxer, D.N. Maywar, J.H. Kelly, T.J. Kessler, B.E. Kruschwitz, S.J. Loucks, R.L. McCrory, D.D. Meyerhofer, S.F.B. Morse, C. Stoeckl, and J.D. Zuegel. High-energy Petawatt capability for the Omega laser. *Opt. Photon. News*, 16(7):30–36, 2005.
- [11] Laboratory for Laser Energetics. www.lle.rochester.edu/omega_facility/omega_ep/ seen in june 2019.
- [12] M. Koga, Y. Arikawa, H. Azechi, Y. Fujimoto, S. Fujioka, H. Habara, Y. Hironaka, H. Homma, H. Hosoda, T. Jitsuno, T. Johzaki, J. Kawanaka, R. Kodama, K. Mima, N. Miyanaga, M. Murakami, H. Nagatomo, M. Nakai, Y. Nakata, H. Nakamura, H. Nishimura, T. Norimatsu, Y. Sakawa, N. Sarukura, K. Shigemori, H. Shiraga, T. Shimizu, H. Takabe, M. Tanabe, K. A. Tanaka, T. Tanimoto, T. Tsubakimoto, T. Watari,

- A. Sunahara, M. Isobe, A. Iwamoto, T. Mito, O. Motojima, T. Ozaki, H. Sakagami, T. Taguchi, Y. Nakao, H. Cai, M. Key, P. Norreys, and J. Pasley. Present states and future prospect of fast ignition realization experiment (FIREX) with gekko and LFEX lasers at ILE. *Nuclear Instruments and Methods in Physics Research A*, 653:84–88, 2011.
- [13] N. Blanchot, G. Behar, T. Berthier, B. Busserole, C. Chappuis, C. Damiens-Dupont, P. Garcia, F. Granet, C. Grosset-Grange, J.-P. Goossens, L. Hilsz, F. Laborde, T. Lacombe, F. Lanièsse, E. Lavastre, J. Luce, F. Macias, E. Mazataud, J.L. Miquel, J. Néauport, S. Noailles, P. Patelli, E. Perrot-Minot, C. Present, D. Raffestin, B. Remy, C. Rouyer, and D. Valla. Overview of PETAL, the multi-Petawatt project in the LMJ facility. In *EPJ Web of Conferences*, volume 59, 2013.
- [14] N. Blanchot, G. Béhar, J.C. Chapuis, C. Chappuis, S. Chavardoine, J.F. Charrier, H. Coic, C. Damiens-Dupont, J. Duthu, P. Garcia, J. P. Goossens, F. Granet, C. Grosset-Grange, P. Guerin, B. Herbard, L. Hilsz, L. Lamaignère, T. Lacombe, E. Lavastre, T. Longhi, J. Luce, F. Macias, M. Mangeant, E. Mazataud, B. Minou, T. Morgaint, S. Noailles, J. Néauport, P. Patelli, E. Perrot-Minnot, C. Present, B. Remy, C. Rouyer, N. Santacreu, M. Sozet, D. Valla, and F. Lanièsse. 1.15 PW - 850 J compressed beam demonstration using the PETAL facility. *Opt. Express*, 25(15):16957–16969, 2017.
- [15] J.-L. Miquel, N. Blanchot, F. Lanièsse, E. Prené, and D. Batani. Applications de la ligne PETAL. *Chocs*, (49):91–100, 2019.
- [16] D.N. Papadopoulos, J.P. Zou, C. Le Blanc, G. Chériaux, P. Georges, F. Druon, G. Mennerat, P. Ramirez, L. Martin, A. Fréneaux, A. Beluze, N. Lebas, P. Monot, F. Mathieu, and P. Audebert. The Apollon 10 PW laser: experimental and theoretical investigation of the temporal characteristics. *High Power Laser Science and Engineering*, 4(e34):1–7, 2016.
- [17] Thalès. Record mondial : Le système laser le plus puissant au monde développé par thalès et ELI-NP a atteint une puissance record de 10 Péta Watts ! <https://www.thalesgroup.com/fr/group/journaliste/press-release/record-mondial-le-system-laser-le-plus-puissant-monde-developpe>, 2019.
- [18] ELI. <http://www.eli-laser.eu>.
- [19] Sergei Kühn, Mathieu Dumergue, Subhendu Kahaly, Sudipta Mondal, Miklós Füle, Tamás Csizmadia, Balázs Farkas, Balázs Major, Zoltán Várallyay, Eric Cormier, Mikhail Kalashnikov, Francesca Calegari, Michele Devetta, Fabio Frassetto, Erik M^oansson, Luca Poletto, Salvatore Stagira, Caterina Vozzi, Mauro Nisoli, Piotr Rudawski, Sylvain Maclot, Filippo Campi, Hampus Wikmark, Cord L Arnold, Christoph M Heyl, Per Johnsson, Anne L’Huillier, Rodrigo Lopez-Martens, Stefan Haessler, Maïmona Bocoum, Frederik Boehle, Aline Vernier, Gregory Iaquaniello, Emmanuel Skantzakis, Nikos Papadakis, Constantinos Kalpouzos, Paraskevas Tzallas, Franck Lépine, Dimitris Charalambidis, Katalin Varjú, Károly Osvay, and Giuseppe Sansone. The ELI-ALPS facility: the next generation of attosecond sources. *J. Phys. B: At. Mol. Opt. Phys.*, 50(132002), 2017.
- [20] Comprehensive Test Ban Treaty Observatory. www.ctbto.org.
- [21] The list Top 500. www.top500.org/lists/2018/11, November 2018.
- [22] CEA. www-lmj.cea.fr/fr/programme_simulation_16022011/airix.htm.
- [23] R. Betti and O. A. Hurricane. Inertial-confinement fusion with lasers. *Nature Physics*, 12, May 2016.

- [24] Mathilde Pfiffer. *Amélioration de la tenue au flux laser des composants optiques du laser Mégajoules par traitement chimique*. PhD thesis, Université de Bordeaux, 2017.
- [25] J. Zuegel, J. D. S. Borneis, C. Barty, B. Legarrec, C. Danson, N. Miyanaga, P. K. Rambo, C. Leblanc, T. J. Kessler, A. W. Schmid, L. J. Waxer, J. H. Kelly, B. Kruschwitz, R. Jungquist, E. Moses, J. Britten, I. Jovanic, J. Dawson, and N. Blanchot. Laser challenges for fast ignition. *Fusion Sci. and Technol.*, 49:453–482, 2006.
- [26] W. Theobald, W. Theobald, and to Complete. Initial cone-in-shell fast-ignition experiment on OMEGA. *Phys. Plasmas*, 18(056305), 2011.
- [27] J. Ongena, R. Koch, R. Wolf, and H. Zohm. Magnetic-confinement fusion. *Nature Physics*, 12:398–410, May 2016.
- [28] Laser Megajoule. *The Mégajoule Laser - leaflet*. CEA.
- [29] CEA. *Le Laser MégaJoule*. CEA, 2014.
- [30] Iso 21254-1 - laser and laser-related equipment - test methods for laser-induced damage threshold, 2011.
- [31] C. Martin Strickley. The laser damage meeting: early years. In *Proc. SPIE Laser damage in Optical Material 2018*, volume 1805, 2018.
- [32] M. J. Soileau. *Laser-Induced Damage in optical materials*, chapter Laser-Induced Damage Phenomena in Optics: a historical Overview, pages 3–9. CRC Press, 2015.
- [33] H. Angus Macleod. The early days of optical coatings. *J. Opt. A: Pure Appl. Opt.*, 1:779–783, 1999.
- [34] Laurent Gallais. *Métrologie de l'endommagement laser*. Technique de l'ingénieur, June 2010.
- [35] Semyon Papernov. *Laser-Induced Damage in optical materials*, chapter Defect-induced Damage, pages 25–75. CRC Press, 2015.
- [36] E. Lavastre, J. Iriondo, F. Tournemette, S. Bouillet, R. Parreault, L. Lemaître, and C. Rouyer. Study of downstream impacts induced by defects of sol-gel and antireflection layers in high power lasers. In *OSA Optical Interference Coating Conference 2019*, ThA.8, 2019.
- [37] E. G. Gamaly, A. V. Rode, B. Luther-Davies, and V. T. Tikhonchuk. Ablation of solids by femtosecond lasers: Ablation mechanism and ablation thresholds for metals and dielectrics. *physics of plasmas*, 9(3):949–957, 2001.
- [38] J. Jasapara, A. V. V. Nampoothiri, W. Rudolph, D. Ristau, and K. Starke. Femtosecond laser pulse induced breakdown in dielectric thin films. *Physical Review B*, 63(045117):1–5, 2001.
- [39] J. H. Apfel. Optical coating design with reduced electric field intensity. *Appl. Opt.*, 16(7):1880–1885, 1977.
- [40] Alexei A. Kozlov, John C. Lambropoulos, James B. Oliver, Brittany N. Hoffman, and Stavros G. Demos. Mechanisms of picosecond laser-induced damage in common multilayer dielectric coatings. *Sci. Rep.*, 9(607), 2019.
- [41] M. Mende, S. Schrameyer, and H. Ehlers. Laser damage resistance of ion-beam sputtered Sc₂O₃/SiO₂ mixture optical coatings. *Appl. Opt.*, 52(7):1368–1376, 2013.

- [42] L. Gallais and M. Commandré. Laser-induced damage thresholds of bulk and coating optical materials at 1030 nm, 500 fs. *Appl. Opt.*, 53(4):A186–A1966, 2014.
- [43] M. Mero, J. Liu, W. Rudolph, D. Ristau, and K. Starke. Scaling laws femtosecond laser pulse induced breakdown in oxide films. *Phys. Rev. B*, 71(115109):1–7, 2005.
- [44] L. V. Keldysh. Ionization in the field of a strong electromagnetic wave. *Sov. Phys. JETP*, 20(1307), 1965.
- [45] Benoit Mangote, L.aurent Gallais, Mireille Commandré, Mathias Mende, Lars Jensen, Henrik Ehlers, Marco Jupé, Detlev Ristau, Andrius. Melninkaitis, Julius Mirauskas, Valdas Sirutkaitis, Simonas Kicas, Tomas Tolenis, and Ramutis Drazdys. Femtosecond laser damage resistance of oxide and mixture oxide optical coatings. *Opt. Lett.*, 37(9):1478–1480, 2012.
- [46] A. Hervy, L. Gallais, G. Chériaux, and D. Mouricaud. Femtosecond laser-induced damage threshold of electron beam deposited dielectrics for 1-m class optics. *Opt. Eng.*, 56(1):011001–1–011001–8, 2017.
- [47] James Clark Maxwell. A dynamical theory of the electromagnetic field. *Phil. Trans. R. Soc. London*, 155:459, 1865.
- [48] Max Born and Emil Wolf. *Principles of Optics*. Cambridge, 7th (expanded) edition edition, 1999.
- [49] H. Angus Macleod. *Thin film Optical filters*. CRC press, 4th edition edition, 2010.
- [50] P H Lissberger. Optical applications of dielectric thin films. *Rep. Prog. Phys*, 33(197):197–268, 1970.
- [51] Florin Abelès. Sur la propagation des ondes électromagnétique dans les milieux stratifiés. *Ann. de Phys.*, 12 Série(t. 3):504–520, 1948.
- [52] Florin Abelès. Recherches sur la propagation des ondes électromagnétiques sinusoïdales dans les milieux stratifiés application aux couches minces. *Ann. de Phys.*, 5:596–640, 1950.
- [53] Florin Abelès. Recherche théoriques sur les propriétés optiques des lames minces. *Le journal de la physique et le Radium*, 11(7):307–309, 1950.
- [54] O. S. Heavens. Optical properties of thin films. *Rep. Prog. Phys.*, 23(1):1–64, 1960.
- [55] O. S. Heavens. *Optical Properties of Thin Solid Films Dover, New York*, chapter 4. 1965.
- [56] R. M. A. Azzam and N. M. Bashara. *Ellipsometry and polarized light*, chapter 4 "Reflection and Transmission of Polarized light by stratified planar structure", pages 269–363. 1977.
- [57] K. Ohta and H. Ishida. Matrix formalism for calculation of electric field intensity of light in stratified multilayered films. *Appl. Opt.*, 29(13):1952–1959, 1990.
- [58] W. H. Lowdermilk, D. Milam, and F. Rainer. Optical coatings for laser fusion applications. *Thin Solid Films*, 73:155–166, 1980.
- [59] J. B. Oliver, A. L. Rigatti, T. Noll, J. Spaulding, J. Hettrick, V. Gruschow, G. Mitchell, D. Sadowski, C. Smith, and B. Charles. Large-aperture coatings and for fusion-class and laser systems. In *OSA Optical Interference Coating Conference 2019*, ThA. 2, 2019.
- [60] C. J. Stolz, F.Y. Genin, T. A. Reitter, N. E. Molau, R. P. Bevis, M. K. von Gunten, D. J. Smith, and J. F. Anzellotti. Effect of SiO₂ overcoat thickness on laser damage morphology of hfo₂/SiO₂ brewsterTMs angle polarizers at 1064 nm. In *UCRL-JC-124875 PREPRINT*, 1997.

- [61] J. H. Apfel and J. S. Matteucci. The role of electric field strength in laser damage of dielectric multilayers. In *Boulder1976*, pages 301–309, 1976.
- [62] B. C. Stuart, M. D. Feit, S. Herman, A. M. Rubenchik, B. W. Shore, and M. D. Perry. Nanosecond-to-femtosecond laser-induced breakdown in dielectrics. *Phys. Rev. B Condens. Matter*, 53:1749–1761, 1996.
- [63] Andrius Melninkaitis, Tomas Tolenis, Lina Mazule, Julius Mirauskas, Valdas Sirutkaitis, Benoît Mangote, Xinghai Fu, Myriam Zerrad, Laurent Gallais, Mireille Commandré, Simonas Kicas, and Ramutis Drazdys. Characterization of zirconia- and niobia-silica mixture coatings produced by ion-beam sputtering. *appl. opt.*, 2011.
- [64] Benoît Mangote. *Tenue au flux des couches minces optiques en régime subpicoseconde*. PhD thesis, Aix Marseille III, 2011.
- [65] I. B. Angelov, M. Von Pechmann, M. K. Trubestov, F. Krausz, and V. Pervak. Optical breakdown of multilayer thin-films induced by ultrashort pulses at MHz repetition rates. *Opt. Express*, 21(25):31453–31461, 2013.
- [66] Martin Sozet, Stéphane Bouillet, Johan Berthelot, Jérôme Néauport, Laurent Lamaignère, and Laurent Gallais. Sub-picosecond laser damage growth on high reflective coatings for high power applications. *Opt. Express*, 2017.
- [67] History of Mirror. <http://en.m.wikipedia.org/wiki/mirror>, 2019.
- [68] Sabine Melchoir-Bonnet. *The Mirror: a history*. 2014.
- [69] Norbert Kaiser. Keynote presentation: New trends and developments in the field of optical interference coatings. In *OSA Optical Interference Coatings Conference*, 2019.
- [70] H. K. Pulker. *Optical interference coatings*, chapter Film Deposition Methods, pages 131–154. Springer, 2003.
- [71] C. J. Stolz, L. M. Sheehan, M. K. Von Gunten, R. P. Bevis, and D. J. Smith. Advantages of evaporation of hafnium in a reactive environment for manufacture of high-damage threshold multilayer coatings by electron-beam deposition. In *Proc. SPIE*, volume 3738, pages 318–324, 1999.
- [72] N. Kaiser and H. K. Pulker, editors. *Optical interference Coatings*. Springer, 2003.
- [73] K. H. Guenther. Microstructure of vapor-deposited optical coatings. *Appl. Opt.*, 23(21), 1984.
- [74] G. N. Strauss. *Optical Interference coatings*, chapter Mechanical Stress in Optical Coatings, pages 207–230. springer, 2003.
- [75] Matthew M. Braun and Laurent Pilon. Effective optical properties of non-absorbing nanoporous thin films. *Thin Solid Films*, 496:505–514, 2006.
- [76] Christopher J. Stolz, Raluca A. Negres, and Eyal Feigenbaum. Trends observed in ten years of thin film laser damage competitions. In *OSA Optical Interference Coating Conference 2019*, number ThA.1, 2019.
- [77] Bernard Cimma, Danièle Forest, Patrick Ganau, Bernard Lagrange, Jean-Marie Mackowski, Christophe Michel, Jean-Luc Montorio, Nazario Morgado, RenÃ©e Pignard, Laurent Pinard, and Alban Remillieux. Ion beam sputtering coatings on large substrates: toward an improvement of the mechanical and optical performances. *Applied optics*, 45(7), 2006.
- [78] M. J. Webber. *Handbook of Optical Materials*. CRC Press, 2003.

- [79] B. Wang and L. Gallais. A theoretical investigation of the laser damage threshold of metal multi-dielectric mirrors for high power ultrashort application. *Opt. Express*, 21(12):14698–14711, 2013.
- [80] D. Schiltz, D. Patel, L. Emmert, C. Baumgarten, B. Reagan, W. Rudolph, J. J. Rocca, and C. S. Menoni. Modification of multilayer mirror toplayer design for increased laser damage resistance. In *Proc SPIE*, volume 9237, page 6200Y, 2014.
- [81] G. Abromavicius, R. Buzelis, R. Drazdys, A. Melninkaitis, and V. Sirutkaitis. Influence of electric field distribution on laser induced damage threshold and morphology of high reflectance optical coatings. In 6720, editor, *Proc. SPIE*, volume 67200Y, 2007.
- [82] S. Chen, Y. Zhao, Z. Yu, Z. Fang, D. Li, H. He, and J. Shao. Femtosecond laser-induced damage of hfo₂/sio₂ mirror with different stack structure. *Appl. Opt.*, 51(25):6188–6195, 2012.
- [83] John Bellum, E. Field, D. Kletecka, and F. Long. Reactive ion-assisted deposition of e-beam evaporated titanium for high refractive index TiO₂ layers and laser damage resistant, broad bandwidth, high-reflection coatings. *Appl. Opt.*, 53(4):A205–A211, 2014.
- [84] H. Becker, D. Tovona, M. Sundermann, L. Jensen, M. Gyamfi, D. Ristau, and M. Mende. Advanced femtosecond laser coatings raise damage threshold. In *Proc. SPIE*, volume 9627, 2015.
- [85] S. Chen, Y. Zhao, H. He, and J. Shao. Effects of standing-wave field distribution on femtosecond laser-induced damage in HfO₂/SiO₂ mirror coating. *Chin. Opt. Lett.*, 9(8):083101, 2011.
- [86] D. Patel, D. Schiltz, P. F. Langton, L. Emmert, L. N. Acquaroli, C. Baumgarten, B. Reagan, J.J. Rocca, W. Rudolph, A. Markosyan, R. R. Route, and M. Fejer C.S. Menoni. Improvements in the laser damage behavior of Ta₂O₅/SiO₂ interference coatings by modification of the top layer design. In *Proc SPIE*, volume 8885, 2013.
- [87] J. B. Oliver, P. Kupinski, A. L. Rigatti, A. W. Schmid, J. C. Lambropoulos, S. Papernov, A. Kozlov, C. Smith, and R. D. Hand. Stress compensation in hafnia/silica optical coatings by inclusion of alumina layers. *Opt. Express*, 20(15):16596–16610, 2012.
- [88] M. Jupé, M. Lappschies, L. Jensen, K. Starke, and D. Ristau. Improvement in laser irradiation resistance of fs-dielectric optics using silica mixtures. volume 6403, page 64031A, 2006.
- [89] L. O. Jensen, M. Mende, H. Blaschke, D. Ristau, D. Nguyen, L. Emmert, and W. Rudolph. Investigation on SiO₂/HfO₂ mixture for nanosecond and femtosecond pulses. In SPIE, editor, *Laser Induced damage in Optical Material*, volume 7842, page 784207, 2010.
- [90] F. Demichelis, E. Mezzetti-Minetti, L. Tallone, and E. Tresso. Optimization of optical parameters and electric field distribution in multilayers. 1984.
- [91] A. V. Tikhonravov, M. K. Trubetskov, and G. W. DeBell. Application of the needle optimization technique to the design of optical coatings. *Appl. Optics*, 35(28):5493–5508, 1996.
- [92] A. V. Tikhonravov, M. K. Trubetskov, and G. W. DeBell. Optical coating design approaches based on the needle optimization technique. *Appl. Optics*, 46(5):704–710, 2007.
- [93] A. V. Tikhonravov and M. K. Trubetskov. *OptiLayer Thin Film Software Manual*. OptiLayer GmbH, 2015.
- [94] Yu Shi, Wei Li, Aaswath Raman, and Shanhui Fan. Optimization of multilayer optical films with memetic algorithm and mixed integer programming. *ACS Photonics*, 5(3):684 – 691, 2017.

- [95] J. B. Oliver. Impact of deposition-rate fluctuation on thin film thickness and uniformity. *Opt. Lett.*, 41(22):5182–5185, 2016.
- [96] JCGM. *Guide to the expression of uncertainty in measurement (GUM)*. 1st edition, 2008.
- [97] JCGM. *International vocabulary of metrology - Basic and general concepts and associated terms (VIM)*. 3rd edition, 2012.
- [98] Martin Sozet. *Étude de l'endommagement laser des composants réflectifs en régime sub-picoseconde*. PhD thesis, École centrale Marseille École Doctorale and Physique and et Sciences and de la Matière, 2016.
- [99] M. Sozet, J. Néauport, E. Lavastre, N. Roquin, L. Gallais, and L. Lamaignère. Assessment of mono-shot measurement as a fast and accurate determination of the laser-induced damage threshold in the sub-picosecond regime. *Opt. Lett.*, 2016.
- [100] M. Mero, B. Clapp, J. C. Jasapara, W. Rudolph, D. Ristau, K. Starke, J. KrÄ¼ger, S. Martin, and W. Kautek. *Opt. Eng.*, 44(051107), 2005.
- [101] A. A. Kozlov, S. Papernov, J. B. Oliver, A. Rigatti, B. Taylor, B. Charles, and C. Smith. Study of the picosecond laser damage in HfO₂/SiO₂ based thin-film coatings in vacuum. In *Proc. SPIE: Laser-induced damage in Optical Materials 2016*, volume 10014Y, 2017.
- [102] Laurent Lamaignère, Alexandre Ollé, Marine Chorel, Nadja Roquin, Alexei A. Kozlov, Brittany N. Hoffman, Stavros G. Demos, Laurent Gallais, and Andirus Melninkaitis. Round-robin measurement of optical coatings laser-induced damage threshold in the subpicosecond range. In *to be published in SPIE Laser-Induced Damage 2019 : annual symposium on optical materials for High-power lasers*, 2019.
- [103] Refractive index information website. <https://refractiveindex.info>, 2019.
- [104] M. Chorel, S. Papernov, A. A. Kozlov, B. N. Hoffman, J. B. Oliver, S. G. Demos, T. Lanternier, É. Lavastre, L. Lamaignère, N. Roquin, B. Bousquet, N. Bonod, and J. Néauport. Influence of absorption-edge properties on subpicosecond intrinsic laser-damage threshold at 1053 nm in hafnia and silica monolayers. *Opt. Express*, 27(10):16922–16934, jun 2019.
- [105] J. Tauc, R. Grigorovici, and A. Vancu. Optical properties and electronic structure of amorphous germanium. *phys. stat. sol.*, 15(627), 1966.
- [106] B. C. Stuart, M. D. Feit, S. Herman, A. M. Rubenchik, B. W. Shore, and M. D. Perry. Laser-induced damage in dielectrics with nanosecond to subpicosecond pulses. *Phys. Rev. Lett.*, 74:2248–2251, 1995.
- [107] L. A. Emmert, M. Mero, and W. Rudolph. Modeling the effect of native and laser induced states on the dielectric breakdown of wide band gap optical material by multiple subpicosecond pulses. *Journal of Appl. Phys.*, 108(043523), 2010.
- [108] S. Papernov, A. Tait, W. Bittle, A. W. Schmid, J. B. Oliver, and P. Kupinski. Near-ultraviolet absorption and nanosecond-pulse-laser damage in HfO₂ monolayers studied by submicrometer-resolution photothermal heterodyne imaging and atomic force microscopy. *Journal of Appl. Phys.*, 109(113106):1–7, 2011.
- [109] S. Papernov, M. D. Brunsmann, J. B. Oliver, B. N. Hoffman, A.A. Kozlov, S. G. Demos, A. Shvydky, F. H. M. Cavalcante, L. Yang, C. S. Menoni, B. Roshanzadeh, S. T. P. Boyd, L. A. Emmert, and W. Rudolph. Optical properties of oxygen vacancies in HfO₂ thin films studied by absorption and luminescence spectroscopy. *Opt. Express*, 26(13):17608–17623, 2018.

- [110] S. Papernov. Spectroscopic set-up for submicrometric resolution mapping of low-signal absorption and luminescence using photothermal heterodyne imaging and photon-counting techniques. *Appl. Opt.*, 58(14):3908–3912, May 2019.
- [111] L. O. Jensen, M. Jupé, H. Mädebach, H. Ehlers, K. Starke, D. Ristau, W. Riede, P. Allenspecher, and H. Schroeder. Damage threshold investigations of high-power laser optics under atmospheric and vacuum conditions. In *Boulder Damage Symposium XXXVIII: Annual Symposium on Optical Materials for High Power Lasers*, volume Proc. SPIE 6403, 2006.
- [112] Wolfgang Riede, Paul Allenspacher, Lars Jense, and Marco Jupé. Analysis of the air-vacuum effect in dielectric coatings. In *Boulder Damage Symposium XL Annual Symposium on Optical Materials for High Power Lasers*, volume 71320F, 2008.
- [113] R. R. Austin, R. Michaud, A. H. Guenther, and J. Putman. Effects of structure, composition, and stress on the laser damage threshold of homogeneous and inhomogeneous single films and multilayers. *Appl. Opt.*, 12(4):665–675, 1973.
- [114] L. O. Jensen, T. Bontgen, H. Kessler, and D. Ristau. Effects of film stress in laser-induced damage. In *Laser-Induced Damage in Optical Materials 2018: 50th Anniversary Conference*, volume Proc. SPIE 10805, 2018.
- [115] Clémence Gingreau, Thomas Lanternier, Laurent Lamaignère, Thierry Donval, Roger Courchinoux, Christophe Leymarie, and Jérôme Néauport. Impact of mechanical stress induced in silica vacuum windows on laser-induced damage. *Opt. Lett.*, 43(8):1706–1709, April 2018.
- [116] Simas Melnikas, Simonas Kicas, and Andrius Melninkaitis. Improved optical and resistance of broadband chirped mirrors. In *OSA Optical Interference Coating Conference 2019*, number ThB6, 2019.
- [117] J. Néauport, E. Lavastre, G. Razé, G. Dupuy, N. Bonod, M. Balas, G. de Villele, J. Flamand, S. Kaladgew, and F. Dessierouer. Effect of electric field on laser induced damage threshold of multilayer dielectric gratings. *Opt. Express*, 15(19):12508–12522, 2007.

Titre : Étude des traitements multicouches utilisés dans un environnement à très faible hygrométrie sur les installations laser de puissance

Résumé : L'amplification par dérive de fréquence démontrée en 1985 a permis la création d'installations laser en impulsions courtes tels que Petal (**P**etawatt **A**quitaine **L**aser). La montée en puissance de ces lasers est limitée par la résistance au flux laser des composants placés après la compression. L'objectif de cette thèse est d'améliorer la résistance au flux laser de ces composants qui sont des miroirs constitués d'empilement multicouches. Trois approches sont envisagées le changement de designs des empilements couches (nombre de couches minces, épaisseurs), de matériaux et/ou de procédés de fabrication. Une étude numérique a permis d'envisager théoriquement le changement de matériaux et/ou de design et de quantifier les améliorations possibles. Cette étude a conduit au développement d'un algorithme d'optimisation des designs qui requiert la caractérisation préalable des matériaux. Par conséquent, plusieurs matériaux déposés en monocouches par divers procédés ont été testés au flux laser et caractérisés optiquement. Les résultats obtenus montrent une forte dispersion qui ne peut être expliquée par des lois préalablement établies dans la littérature. Cependant, une bonne corrélation entre le seuil de tenue au flux laser intrinsèque dans l'infrarouge et l'absorption dans l'ultraviolet a été observée confirmant l'influence de l'absorption multi-photonique sur l'endommagement laser en impulsions courtes. Pour finir, l'ensemble de ces résultats expérimentaux combinés avec l'algorithme d'optimisation ont permis la fabrication d'échantillons de miroirs qui montrent augmentant le seuil de tenue au flux laser de 73% par rapport à des miroirs quart d'onde classiques.

Mots clés : couches minces, design multicouches, laser de puissance, endommagement laser, impulsion courte, propriété optiques

Title: Study of high damage threshold optical multilayer coatings used in very low hygrometry environment for fusion class laser system

Abstract: The chirped pulse amplification demonstrated in 1985 allowed the development of petawatt class laser such as Petal (**P**etawatt **A**quitaine **L**aser). The increase of power of those facilities is limited by the resistance to laser-induced damage of the optical components placed after the compression stage. The aim of this thesis is to improve the laser-induced damage threshold of those components which are multilayer dielectric mirrors. Three paths of improvement are considered the change of design (number of layers, thicknesses), of materials and/or deposition process. A numerical study allows evaluating the potential improvement brought by two of those paths. This led to the development of a design optimization algorithm that required the previous characterization of materials. Consequently, various materials deposited as single layers with different process were laser damage tested and optically characterized. The results show a wide discrepancy that cannot be explained by the laws exposed in the literature. However, a good correlation was found between the intrinsic laser-induced damage thresholds in the infrared with the absorption in the ultraviolet confirming the influence of the multiphoton absorption in the laser-induced damage mechanisms. Finally, those experimental results combined with the optimization algorithm allowed the development of mirror samples that exhibit laser-induced damage threshold 73% higher than one of classical mirrors.

Keywords: thin films, multilayer design, high power laser facilities, laser damage, short pulses, optical properties

UNITE DE RECHERCHE

[CEA CESTA, CS60001, 15 AVENUE DES SABLIERES, 33116 LE BARP CEDEX]
